University of California
Santa Barbara

Main-group halide perovskites: Structural & dynamical insights for photovoltaic performance

A dissertation submitted in partial satisfaction
of the requirements for the degree

Doctor of Philosophy
in
Materials

by

Douglas H. Fabini

Committee in charge:

Professor Ram Seshadri, Chair
Professor Michael L. Chabinyc
Professor Fred Wudl
Professor Song-I Han

September 2018

The Dissertation of Douglas H. Fabini is approved.

Professor Michael L. Chabinyc

Professor Fred Wudl

Professor Song-I Han

Professor Ram Seshadri, Committee Chair

May 2018

Main-group halide perovskites:

Structural & dynamical insights for photovoltaic performance

by

Douglas H. Fabini

to the teachers and educators in my life,
including my wonderful parents

Acknowledgements

There are so many people to whom I am immensely grateful: For mentorship, for friendship, for support, for introducing me to new friends, new passions, and new ways of looking at the world. Without you, this journey would likely not have been possible, and certainly not interesting.

First, to my advisor, Professor Ram Seshadri: Thank you for welcoming me into your group and fostering a supportive, stimulating, and intellectually challenging environment. Your curiosity and approach to seeking out and addressing scientific problems are inspiring. Thank you for our unplanned chats in your office, caffeinated and otherwise, and for teaching me to think more like a chemist. Thank you for encouraging me to identify, confront, and overcome my own intellectual biases and scientific myopia. Your willingness to and enthusiasm for sending me to conferences and workshops undoubtedly enriched my PhD experience, broadened my thinking, and introduced me to new friends and future collaborators. Lastly, thank you for showing by example how to carry oneself as a scientist, with integrity, inquisitiveness, and intensity. I look forward to many years of interacting as colleagues and friends.

Thank you to Professors Michael Chabinyc and Fred Wudl for serving both officially on my thesis committee and unofficially as my de facto co-advisors. Your perspectives, mentorship, scrupulous feedback, and frequent levity during our research meetings have been vital. Thank you for opening my eyes to ways to approach my research from outside my immediate field, and for constantly challenging my preconceived notions.

Thank you to the fantastic teachers I've had for classes in grad school: Professors Ram Seshadri, Anton van der Ven, Galen Stucky, Michael Chabinyc, Stephen Wilson, Craig Hawker, Chris van de Walle, Jim Speck, and Brad Chmelka. Thanks especially to Ram and Anton for helping me bridge the vast gulf between my previous discipline and

the world of materials in my first quarters at UCSB. Thanks also to Anastasia Patterson and Professor Omar Saleh, the best colleagues I could ask for when TA-ing.

I owe so much to the entire Seshadri group, past and present. To Anna Lehner, an immense thank you for your guidance and mentorship in my first year, and I look forward to seeing more of you and your family in Germany. Thank you to my indispensible cohort-mates, Clayton Cozzan and Hayden Evans, to Jason Douglas for your dry wit and for refusing to talk to me on the bus in the mornings, to the singular Mike Gaultois for hospitality, energy, and adventures during our brief coexistence in Santa Barbara. Thank you to Geneva Laurita, for beam-time bonding and for teaching me the dark arts of scattering, and to Leo Lamontagne for entertaining all of my tedious lab questions, for your undying devotion to the institution of Burrito Friday, and for keeping me honest. Thank you to Molleigh Preefer for our many conversations on science and life, houseplants and coffee, and for introducing the wonderful and shaggy Pixie Preefer to all of us. Thanks to Mitchell Koerner for your work on our research, for your drive to really understand things, and for helping me to challenge my scientific assumptions. Thanks also to Josh Bocarsly, Sam Teicher, Emily Schueller, Nicole Schauser for our many discussions and your generosity in helping troubleshoot all the 'wares (hard-, soft-, vapor-, etc.).

I'd also like to extend a huge thanks the Chabinyc group for taking me in as a group hanger-on, and to Anne Glaudell, John Labram, and especially Erin Perry for helping me get up to speed in the labs my first year, and for your solidarity in long hours with unruly and unstable thin films. I would also be remiss if I didn't thank John for bringing Iannucci films into my life.

To Costas Stoumpos and Professor Mercouri Kanatzidis, it's been a pleasure collaborating so consisently with you these last few years. Your ideas and input are so valuable and often orthogonal to the thinking on our end, and your samples are sec-

ond to none. Thanks also to Grant Alexander for including me in your work on such interesting heavy-metal halide phases.

Ting-Ann Siaw and Professor Song-I Han, thank you for an enjoyable and fruitful collaboration, and for bringing such a remarkable set of tools and expertise to bear on our research questions. Song-I, thank you also for serving on my committee and providing a critical and different perspective.

Thank you to Dan Olds and Kate Page for your immense help and your hospitality during experiments at the Spallation Neutron Source. Thanks also to all the staff and lecturers who put on the National School on Neutron & X-ray scattering, and to my new friends and colleagues with whom I shared the experience. Thank you to Professor Luis Echegoyen, David Buck, and Robert Cotta for welcoming us to El Paso and teaching us to make perovskite photovoltaics. Thank you to Professor Paresh Chandra Ray and the wonderful students, staff, and faculty at Jackson State University for a great conference and visit. Thank you to Professors Peter Blaha and Karlheinz Schwarz for a wonderful workshop and for your hospitality in Vienna. Thanks to Catherine Oertel for your feedback on drafts and for allowing me to contribute to one of your projects. Thanks to Jaye Harada and Tom Hogan for introducing me to the world of cryogenic measurements. Thanks also to Molleigh Preefer, Yue Wu, Matthew Cliffe, Fengxia Wei, and Sammy Shaker for some USDA Grade A travel companionship on our Ras al-Khaimah and Dubai adventures.

To all the staff of the MRL, thank you for creating such a community-within-a-community, and fostering a truly wonderful environment in which to do research. Thank you Joni, Sara, Claudia, Marisol, Mary, Samantha, Sylvia, and Mike. Thanks to Jerry Hu and Jaya Nolt for your tireless patience with my solid-state NMR questions, for teaching me so much, and for helping to troubleshoot hardware, sample preparation, and more. Thank you to Fuzzy Rogers for assisting with computing, to Guang

Wu for helping wrangle X-rays, to Tom Mates for extensive help with photoemission spectroscopy, and to Amanda Strom and Rachel Behrens for fantastic stewardship of the labs and your inimitable contributions to the culture and atmosphere of the MRL.

To Dotti Pak, Frank Kinnaman, and Julie Standish, I've so enjoyed the education and outreach programs put on by the MRL, and it's always a pleasure working with you. Also, to Wendy Ibsen, Marilyn Garza, Mike Maniscalco, and all the organizers and volunteers of FUSE, thanks for four years of homemade speakers, stinky unflavored jello, mind-bending science questions from middle schoolers, and the uncommon camaraderie that comes from trying to ensure that twelve year-olds play nice with magnets, chemicals, and lasers.

To my colleagues in GSDS, it has been such a pleasure working with you. Thanks especially to Wennie Wang, Niva Ran, Michael Swift, Menaka Wilhelm, Megan Butala, and Emre Discekici.

To my erstwhile officemates, Clayton Cozzan, Leo Lamontagne, Jack Zhang, Emily Wonder, David Kealhofer, and to the official-unofficial occupants of 2232, Victoria Steffes and Chris Freeze, thank you for entertainment, help, laughs, and for putting up with my various map-related shenanigans. And to Julija Vinckeviciute, Max Radin, and Harsha Gunda, thank you for receiving my unannounced drop-ins–I very much enjoy our chats about science, DFT, and life.

To my hiking and camping co-conspirators, but particularly to Anthony Rice, Jack Zhang, Santosh Raghavan, Sumit Singh, Rob Rhein, Dan Becerra, and Tobias Brown-Heft, thank you for unforgettable adventures (and more yet to come!). Thank you to my fellow concert, theater, and lecture junkies, Niva Ran and Rahul Sangodkar. Thank you also to Niva, Jack, Santosh, and Leah Kuritzky for introducing me to the infectious beats and thrilling moves of salsa and bachata. Thanks to Luca Galletti and Anna Kim, swimming partners extraordinaire—may we run into each other again, soon and often.

To Erin Perry, Colin Stewart, Menaka Wilhelm, and Alex Flood, you are awesome (and Alex, I haven't forgotten about Miami Vice).

To Corde Snell, it's been a joy reuniting with you here in Santa Barbara (how many "grades" of school have we been classmates now? Seventeen?). Thanks for keeping me grounded, and all the best wherever you land next.

Thank you to Leah Kuritzky, Greg Su, Rob Rhein, and Peter Mage for welcoming me into the community of the house, for late night debates, for evenings in the hot tub, for impromptu jam sessions and dance-offs, and for potlucks that inspire.

To Chris Freeze, your social energy is unparalleled and, thankfully for me at times, infectious. Your friendship means so much to me, and I know that we have many good times in our future.

To Julia Schneider and Matt Beale, would that we could have overlapped so much longer in the same place. All the best to you on your new adventures, and I look forward to more delicious meals, camping and bike rides, and aural experiences on vinyl.

Thanks to far-away friends, whom I can never see enough of, but who are so important to me. Thanks especially to Davie Nguyen, Navin Shekar, Ian Leighton, Josh Sokolski and Seren Moran, Dana Goin and Daniel Wolfe, Matt and Willa Bauer, Jay Taneja and Emily Kumpel, and Anna Brockway.

Lastly, to my incredible family: You mean the world to me, and I couldn't have done any of this without you. Mom, Dad, Ellen, Richard, Rachel, Lucca, Zoë, John, Emily, Adelaide, Tobias, Ryan, Allesy, Dick, Marisa, Laura, Skip, Matt, and Steph, thank you so much for your support, your encouragement, for summers at Henze Family Summer Camp, for watermelon log, for DIY sparklers, for visits to San Diego and Salt Lake City and Boston and Los Angeles, and for all the adventures that lie ahead. I love you.

Curriculum Vitæ
Douglas H. Fabini

Education

2018	Ph.D. in Materials University of California, Santa Barbara, USA
2011	B.S. in Mechanical Engineering (Highest Honors) University of California, Berkeley, USA

Publications

18. D. Fabini, M. Koerner, R. Seshadri, Screening valence-precise inorganic compounds for photovoltaic functionality based on ab initio optical and transport proxies *[working title]*, *in preparation*.
17. H. Evans, D. Fabini, J. Andrews, M. Koerner, M. Preefer, G. Wu, F. Wudl, A. Cheetham, R. Seshadri, Hydrogen bonding controls the structural evolution in perovskite-related hybrid platinum(IV) iodides, *Inorg. Chem.* **2018**, *in press*. [**doi**]
16. G. Alexander, D. Fabini, R. Seshadri, M. Kanatzidis, $AuPb_2I_7$: A narrow bandgap Au^{3+} iodide semiconductor, *Inorg. Chem.* **2018**, *57*, 804–810. [**doi**]
15. E. Schueller, G. Laurita, D. Fabini, C. Stoumpos, M. Kanatzidis, R. Seshadri, Crystal structure evolution and notable thermal expansion in hybrid perovskites formamidinium tin iodide and formamidinium lead bromide, *Inorg. Chem.* **2018**, *57*, 695–701. [**doi**]
14. D. Fabini, T. Siaw, C. Stoumpos, G. Laurita, D. Olds, K. Page, J. Hu, M. Kanatzidis, S. Han, R. Seshadri, Universal dynamics of molecular reorientation in hybrid lead iodide perovskites, *J. Am. Chem. Soc.* **2017**, *139*, 16875–16884. [**doi**]
13. G. Laurita, D. Fabini, C. Stoumpos, M. Kanatzidis, R. Seshadri, Chemical tuning of dynamic cation off-centering in the cubic phases of hybrid tin and lead halide perovskites, *Chem. Sci.* **2017**, *8*, 5628–5635. [**doi**]
12. E. Liu, C. Gang, M. Zeller, D. Fabini, C. Oertel, Ligand-induced variations in symmetry and structural dimensionality of lead oxide carboxylates, *Cryst. Growth Des.* **2017**, *17*, 1574–1582. [**doi**]
11. D. Fabini, J. Labram, A. Lehner, J. Bechtel, H. Evans, A. Van der Ven, F. Wudl, M. Chabinyc, R. Seshadri, Main-group halide semiconductors derived from perovskite: Distinguishing chemical, structural, and electronic aspects, *Inorg. Chem.* **2017**, *56*, 11–25. [**doi**]

10. D. Fabini, C. Stoumpos, G. Laurita, A. Kaltzoglou, A. Kontos, P. Falaras, M. Kanatzidis, R. Seshadri, Reentrant structural and optical properties and large positive thermal expansion in perovskite formamidinium lead iodide, *Angew. Chem. Int. Ed.* **2016**, *55*, 15392–15396. [**doi**]

9. D. Fabini(*), G. Laurita(*), J. Bechtel, C. Stoumpos, H. Evans, A. Kontos, Y. Raptis, P. Falaras, A. Van der Ven, M. Kanatzidis, R. Seshadri, Dynamic stereochemical activity of the Sn^{2+} lone pair in perovskite $CsSnBr_3$, *J. Am. Chem. Soc.* **2016**, *138*, 11820–11832. [**doi**] (*) *equal contribution*

8. H. Evans, A. Lehner, J. Labram, D. Fabini, O. Barreda, S. Smock, G. Wu, M. Chabinyc, R. Seshadri, F. Wudl, $(TTF)Pb_2I_5$: A radical cation-stabilized hybrid lead iodide with synergistic optoelectronic signatures, *Chem. Mater.* **2016**, *28*, 3607–3611. [**doi**]

7. D. Fabini, T. Hogan, H. Evans, C. Stoumpos, M. Kanatzidis, and R. Seshadri, Dielectric and thermodynamic signatures of low temperature glassy dynamics in the hybrid perovskites $CH_3NH_3PbI_3$ and $HC(NH_2)_2PbI_3$, *J. Phys. Chem. Lett.* **2016**, *7*, 376–381. [**doi**]

6. A. Lehner, D. Fabini, H. Evans, C.-A. Hébert, S. Smock, J. Hu, H. Wang, J. Zwanziger, M. Chabinyc, and R. Seshadri, Crystal and electronic structures of complex bismuth iodides $A_3Bi_2I_9$ (A = K, Rb, Cs) related to perovskite: Aiding the rational design of photovoltaics, *Chem. Mater.* **2015**, *27*, 7137–7148. [**doi**]

5. A. Lehner, H. Wang, D. Fabini, C. Liman, C.-A. Hébert, E. Perry, M. Wang, G. Bazan, M. Chabinyc, and R. Seshadri, Electronic structure and photovoltaic application of BiI_3, *Appl. Phys. Lett.* **2015**, *107*, 131109. [**doi**]

4. D. Fabini, Quantifying the potential for lead pollution from halide perovskite photovoltaics, *J. Phys. Chem. Lett.* **2015**, *6*, 3546–3548. [**doi**]

3. J. Labram, D. Fabini, E. Perry, A. Lehner, H. Wang, A. Glaudell, G. Wu, H. Evans, D. Buck, R. Cotta, L. Echegoyen, F. Wudl, R. Seshadri, and M. Chabinyc, Temperature-dependent polarization in field-effect transport and photovoltaic measurements of methylammonium lead iodide, *J. Phys. Chem. Lett.* **2015**, *6*, 3565–3571. [**doi**]

2. D. Fabini, D. Baridó, A. Omu, and J. Taneja, Mapping induced residential demand for electricity in Kenya, In *Proceedings of the 5th ACM Symposium on Computing for Development (DEV-5)*, San Jose, CA, USA, December 5–6, 2014, 43–52. [**doi**]

1. T. Clasen, D. Fabini, S. Boisson, J. Taneja, J. Song, E. Aichinger, A. Bui, S. Dadashi, W. Schmidt, Z. Burt, and K. Nelson. Making sanitation count: Developing and testing a device for assessing latrine use in low-income settings, *Environ. Sci. Technol.* **2012**, *46*, 3295–3303. [**doi**]

Abstract

Main-group halide perovskites:
Structural & dynamical insights for photovoltaic performance

by

Douglas H. Fabini

Among primary energy sources that do not generate carbon dioxide through the oxidation of fossil fuels, photovoltaics (PV)—which convert sunlight directly to electricity—are a promising approach. The solar resource is ample and well-characterized, pollutant emissions from PV power plants are negligible, and the technology is suited to nearly all climates and regions on earth. While the cost of solar electricity has plummeted in the last decade, further cost reductions and efficiency improvements in photovoltaic absorber materials may make this technology more accessible and ubiquitous.

To this end, there is much excitement about main-group halide perovskites, which have garnered intense research attention since 2009 when they were employed successfully in solar cells. These materials, which comprise main-group dications (Ge^{2+}, Sn^{2+}, Pb^{2+}), halide anions (Cl^{-}, Br^{-}, I^{-}), and large countercations (Cs^{+}, $CH_3NH_3^{+}$, $CH[NH_2]_2^{+}$) crystallized in the perovskite structure, combine excellent performance in PV and other optoelectronic applications with ease of preparation and abundant constituent elements. Despite some years of in-depth study, key fundamental questions and practical challenges remain. In particular, the remarkable properties of these systems confound the conventional wisdom of what constitutes a high-performance semiconductor, and the origins of these favorable properties remain a matter of significant debate. Concurrently, practical application of devices employing halide perovskites is

hampered by stability challenges, and the presence of lead in high-performing formulations raises significant neurotoxicity and environmental contamination concerns.

In this dissertation, we report research in three thematic areas aimed at resolving fundamental questions around the materials chemistry, crystal structure, and plastic crystal dynamics of these halide perovskites. In the first portion, the preparation and characterization of lead-free inorganic bismuth halides illustrate the importance of the electronic configuration of the main-group cation and of highly-connected, high-symmetry crystal structures to the favorable optoelectronic properties of the tin and lead halides. Subsequently, scattering experiments and ab initio calculations reveal an unusual and chemically-tunable form of dynamic disorder arising from an electronic instability associated with the main-group cations which affects thermal, dielectric, and electronic properties. Finally, a range of spectroscopic, computational, and scattering techniques are employed to establish the nature of molecular motion and its effects on the crystal structures of the high performance photovoltaic absorber, formamidinium lead iodide, providing critical context for the evaluation of hypotheses about the origins of the remarkable properties of these materials.

In an effort to understand the crystal chemistry of the halide perovskites, lead-free alkali bismuth iodides and the binary bismuth iodide are prepared in single crystal, bulk, and thin film forms, and their structures resolved via X-ray diffraction and ^{87}Rb solid-state nuclear magnetic resonance (NMR) spectroscopy. These phases are shown to exhibit strong optical absorption and suitable bandgaps for single junction and tandem solar cells, but photoemission spectroscopy and ab initio calculations based on density functional theory reveal valence band maxima that are deep relative to existing hole transport materials. This poor band alignment is demonstrated to be a consequence of relativistic stabilization of the Bi 6s orbital combined with reduced bandwidths from distorted Bi coordination environments, thus establishing the importance of the high-

symmetry structures seen for the divalent tin and lead halides.

X-ray total scattering studies reveal local off-centering of the main-group cations (Sn^{2+}, Pb^{2+}) within their coordination octahedra across the halide perovskites, reflecting a preference for lower symmetry coordination than that implied by crystallographic approaches. Taking $CsSnBr_3$ as an exemplar of the broader class of materials, ab initio calculations, photoluminescence measurements, and analogies to existing theory implicate the Sn $5s^2$ lone pair electrons (equivalently, the pseudo-Jahn–Teller effect) as the origin of this phenomenon, which we propose leads to enhanced defect screening, reduced thermal conductivity, and unusual temperature-dependence of the electronic bandgap. We further demonstrate control of the strength of this phenomenon in the hybrid tin and lead perovskites by chemical substitution on all sites of the crystal, with a lighter carbon-group dication, a lighter halogen, and a larger countercation all leading to more pronounced off-centering. This proximity to a polar phase boundary leads to an elevated lattice polarizability and suggests a possible mechanism for the formation of large polarons, which have been proposed as the origin of long-lived carriers and modest carrier mobilities in these materials.

As plastic crystals — which exhibit translational periodicity but orientational disorder — the hybrid organic–inorganic perovskites display a complex interplay between motion of the molecular cations and the structure of the surrounding anionic inorganic framework. High resolution X-ray diffraction reveals the complete phase evolution with temperature of formamidinium lead iodide, including an unusual reentrant pseudosymmetry at cryogenic temperatures arising from geometric frustration between the molecular symmetry and the favored ground-state tilting of the inorganic octahedra. Solid-state ^{1}H NMR and dielectric spectroscopies, calorimetry, ab initio calculations, and neutron total scattering establish the full temperature-dependent dynamics of molecular reorientation between 4 K and 400 K. Despite markedly different barriers

for molecular rotation compared to those in the homologous methylammonium lead iodide, both systems exhibit similar dynamics at room temperature. Together with the vastly different dipole moments for the two molecules, this result clarifies emerging hypotheses of polaronic transport and fugitive spin polarization, suggesting the primacy of the main-group–halogen sublattice, rather than the molecular cations, for defect-tolerant electronic transport.

Contents

Chapter 1

Introduction

Solar cells — which convert sunlight directly to electricity — are a promising technology for meeting humanity's energy needs without producing climate-altering carbon dioxide emissions. Once an expensive curiosity, solar panels can now be seen dotting the rooftops of homes and businesses in regions like California with abundant sunlight and relatively expensive incumbent electricity sources. And while costs for solar energy have come down significantly in the last decade, further efficiency improvements in solar cell materials can make this technology more accessible and widespread in more places.

Researchers have recently found that thin films of main-group halide perovskites can be employed to make cheap, efficient solar cells. However, their workings are poorly understood, and significant practical challenges currently prevent their use. The research described in this dissertation seeks to elucidate the relevant composition–structure–property relations governing these materials, resolve debate around the origins of unexpectedly favorable photovoltaic performance, and provide chemical design principles for the discovery of new defect-tolerant semiconductors.

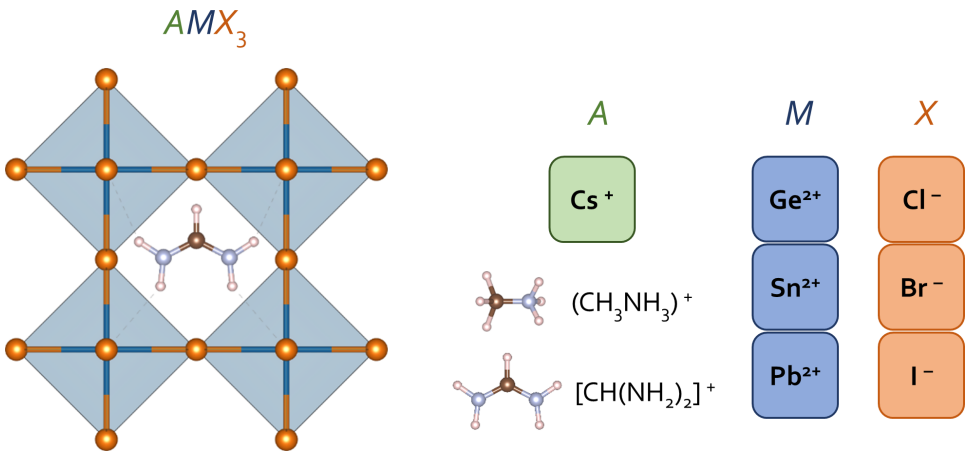

Figure 1.1: Graphical overview of the perovskite structure and typical compositions of main-group halide perovskites.

1.1 Structural & chemical overview

Main-group halide perovskites are materials of the general stoichiometry AMX_3 which adopt the structure of the mineral perovskite ($CaTiO_3$) and which contain main-group cations on the M-site, halide anions on the X-site, and large countercations on the A-site. An overview of the structure and most common compositions is provided in Figure 1.1. The main-group cations are octahedrally coordinated with halides, these octahedra are corner-sharing in all three dimensions, and the large voids formed by this anionic framework are filled and charge balanced by large alkali metal monocations or small molecular monocations. When the A-site cation is an organic molecule, such materials are known as "hybrid organic–inorganic" or simply "hybrid" perovskites.

The most intensely studied compounds in this family contain lead on the M site. Tin compounds are less studied, due to the tendency of the Sn^{2+} cation to further oxidize to Sn^{4+} in air. Germanium compounds are yet more sensitive to oxidation and very few reports of these exist.

Additionally, a number of derivative structures are possible, including ordered double perovskites and layered variants. Double perovskite halides, $A_2MM'X_3$,

may contain two different metals (e.g. $Cs_2Ag^{I}Bi^{III}Br_6$), a mixed valence metal (e.g. $Cs_2Au^{I}Au^{III}I_6$), or a tetravalent metal and a vacancy (e.g. $Cs_2Sn^{IV}\square I_6$). Layered variants include defect perovskites with ordered vacancies that break up the 3D framework along the [111] direction (e.g. $Rb_3Bi_2\square I_9$) and hybrid compounds with large organic cations that break up the layering of 2-D perovskite-like slabs along [100] (e.g. $[BA]_2[CH_3NH_3]_{n-1}Pb_nI_{3n+1}$; BA = N-butyl ammonium) and [110] (e.g. $[IoFA]_2[CH_3NH_3]_nSn_nI_{3n+2}$; IoFA = iodoformamidinium).

1.2 Historical perspective

While cesium lead halide perovskites were first prepared in the late 19th century, [1] their structures were not known until 1957, when they were additionally shown to be photoconductive. [2] Two decades later, the first hybrid organic–inorganic lead perovskites were prepared with the $CH_3NH_3^+$ (methyl ammonium) cation. [3] Starting in the late 1980s, [4] various layered derivatives were prepared and investigated for their excitonic properties, using bulky organic cations to template the self-assembly of quantum well structures. In the 1990s, excitement grew on reports of a tunable metal–insulator transition in certain layered compositions, [5] as well as the application of these phases in field-effect transistors. [6]

Fundamental study of the structural, dynamical, optical, and transport properties continued throughout the 1980s, 1990s, and 2000s, but it was the unexpectedly high performance of dye-sensitized solar cells employing $CH_3NH_3PbI_3$ and $CH_3NH_3PbBr_3$ that marked the genesis the field of perovskite photovoltaics. [7] Interest remained somewhat limited until demonstrations of all solid-state solar cells in 2012, [8, 9, 10] whereupon many researchers worldwide began investigating these materials, a situation which has only intensified since.

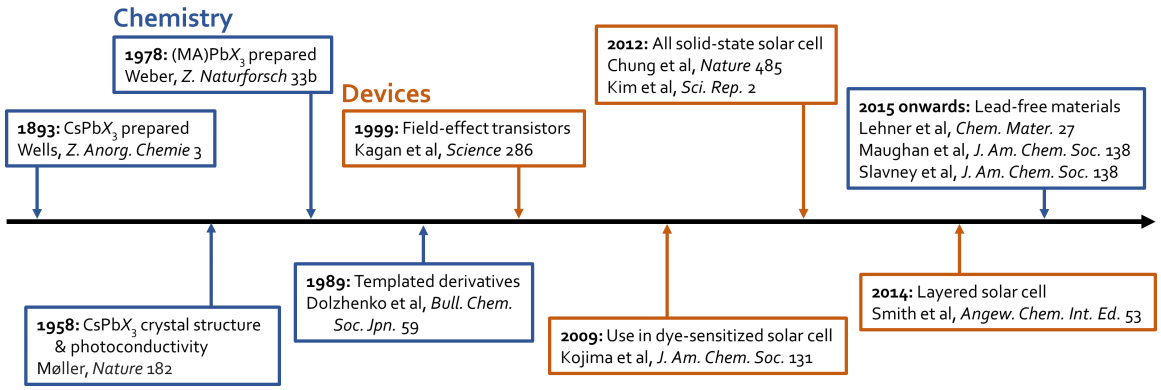

Figure 1.2: Abridged historical summary of the preparation and investigation of main–group halide perovskites for optoelectronic applications.

While there have been many consequential findings and demonstrations in the last half-decade, we summarize here briefly key contributions in examining new chemistries and exploring new applications. Known layered lead halide phases were revived for application as photovoltaic absorbers in an attempt to improve moisture stability. [11] Lead-free materials based on Sn(II), [12, 13, 14] Bi(III), [15, 16] Ge(II), [17] Sn(IV), [18] Te(IV), [18] Ag(I)/Bi(III), [19, 20] were prepared and investigated to address the toxicity of lead and correlate materials chemistry with optoelectronic properties. Other potential applications were explored, including light-emitting diodes [21, 22] and lasers [23, 24] (layered or nanocrystalline lead and tin halides), non-linear optics (germanium halides), [17] radiation detectors, [25] thermoelectrics, [26] and field-effect transistors. [27, 28, 29, 30]

This timeline is summarized in graphical form in Figure 1.2.

1.3 Practical challenges for application

While the halide perovskites exhibit promising performance for a range of optoelectronic functionalities, concerns about heavy metal toxicity and major challenges with their long-term stability hinder application. The range of compositions in this mate-

rials family have proven to exhibit varying levels of sensitivity to ambient moisture, oxidation, excessive heat, vacuum, and high fluences of blue/near-UV photons. Such degradation simultaneously greatly reduces the useful lifetime of devices and allows for the possible loss of highly toxic Pb^{2+} and Sn^{2+} to the environment in the form of slightly water-soluble lead and tin halides if solar cell encapsulants fail.

1.4 Open scientific questions

More fundamentally, the origins of the impressive performance of these materials remain unresolved. The halide perovskites differ substantially in composition, crystal structure, and electronic structure from the diamondoid group IV, III–V, II–VI, and I–III–VI_2 semiconductors that are typically regarded as high performance semiconductors and photovoltaic absorbers. In particular, the pronounced mechanical "softness" of the halide perovskites (and associated facile processability and degradation) are anomalous. Further, the halide perovskites appear to possess an unusual and compositionally robust defect tolerance. Conventional semiconductors are produced at great expense from high-purity precursors on specialized equipment in large, industrial foundries because impurities and imperfections are extremely detrimental to performance. On the other hand, halide perovskites can be prepared by undergraduate students in a standard chemistry laboratory. Surely, this results in many defects, and yet performance is relatively unaffected.

Perhaps most interestingly, this defect-tolerant behavior appears across the entire class of halide perovskites, suggesting a universal mechanism, rather than a fortuitous coincidence (such as a particular alignment of defect levels in a one or a few compositions). Several hypotheses have recently been put forth to explain this defect tolerance, as well as the unexpectedly modest carrier mobilities observed in experiment despite

high curvature electronic band edges from ab initio calculations. Two of these predominant hypotheses (of fugitive spin polarization, and polaronic transport) will be discussed presently in the context of the research reported here, but the field is far from consensus as of this writing.

1.5 Factors governing crystal structure evolution

1.5.1 Thermodynamic origin of thermal phase transitions

Many factors influence the atomic structure of solids, including local chemical bonding considerations, long-range Coulomb interactions, and entropic effects due to vibrations and configurational disorder. Consider the Gibbs free energy, which is minimized for a system in thermodynamic equilibrium with a bath at constant temperature and pressure (Equation 1.1, where G is the free energy, H is the enthalpy, p is the pressure, V the volume, T the temperature, and S the entropy).

$$G\left(T,p\right)=H\left(p\right)-TS=U+pV-TS \tag{1.1}$$

For solids, changes in volume are quite small, and the pV term can be ignored at ambient pressures. The phase behavior with temperature then reflects primarily a competition between energy minimization (the dominant term at low T) and entropy maximization (dominant at high T). For rigid structures, particularly those with covalent, directional bonding, few low-energy phonon modes and severe energetic penalties for distortions result in a single stable structure from the groundstate all the way to melting or sublimation. On the other hand, many metals (with metallic bonding and several nearly-degenerate stacking sequences) and ionic compounds (particularly those with ions "mismatched" in size relative to their packing) exhibit thermal phase tran-

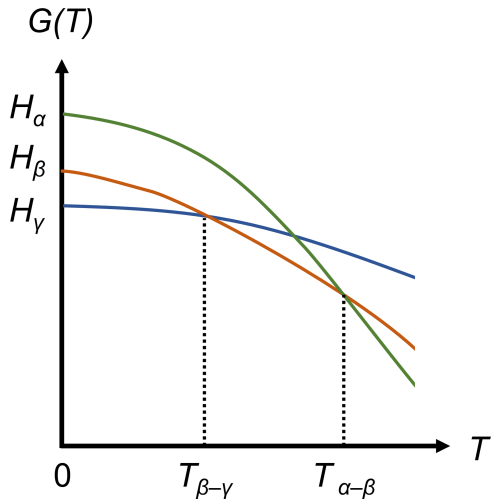

Figure 1.3: Gibbs free energy, $G(T)$ for a substance exhibiting different stable phases as a function of temperature due to differing vibrational, configurational, and electronic entropy contributions. The lowest enthalpy phase (γ) is the ground state, giving way to β- and α-phases with successively higher entropies. Phase transition temperatures are indicated.

sitions, where the lowest energy phase converts to successively higher energy phases with softer vibrations upon warming. An (isobaric) example of this free energy evolution is given in Figure 1.3.

1.5.2 Ionic size considerations: Goldschmidt's tolerance factor

The perovskite structure is known to accomodate a wide range of chemical compositions, in part because of the two cation sites of differing size and the flexibility of the structure to adopt a number of "tilted" configurations which improve coordination on the A-site for undersized cations.

Goldschmidt developed a simple criterion based solely on ionic sizes to predict whether a given composition will adopt the perovskite structure (Equation 1.2).[31] For $t > 1$, the A-site cation is too large, typically resulting in crystallization in lower-dimensional structure types. For $t < 0.71$, the cations are too similar in size, leading to other structure types. However, for $0.90 < t < 1$ and $0.71 < t < 0.90$, crystallization

as a cubic perovskite and a tilted orthorhombic/rhombohedral perovskite is predicted, respectively.

$$t = \frac{r_A + r_X}{\sqrt{2}\,(r_M + r_X)} \tag{1.2}$$

These soft octahedral tilt modes which maintain corner-connectivity are a consequence of the statics of the perovskite structure: Analysis of the structure as a collection of rigid frames [32] reveals that it is on the boundary between statically indeterminate (hyperstatic) and under-constrained, and these modes at the M and R points of the primitive cubic Brillouin zone have only higher-order, rather than Hookean, restoring forces. This fact, coupled with relatively long, weak metal–halogen bonds in the main-group halides, leads to large vibrational entropy contributions and many corresponding structural phase transitions at modest temperatures.

1.5.3 Covalency considerations: Lone pair stereochemistry

For main-group cations with lone pair electrons ($d^{10}s^0$ valence), their exists an instability to high symmetry coordination (e.g. ideal octahedral geometry) because of the degeneracy of low-lying excited states with appropriate symmetry (the pseudo-Jahn–Teller effect, or PJT). [33, 34] This is analogous to the PJT associated with d^0s^0 cations which drives ferroelectricity in certain transition metal oxides, like $BaTiO_3$. The strength of this instability is sensitive to the energy levels of cation and anion orbitals, as well as the degree of their spatial and energetic overlap. In particular, heavier main-group cations lead to a weaker instability (due to relativistic contraction and stabilization of the frontier s orbital), as do less electronegative anions. [35] In the solid state, this determines whether the cation will adopt the acentric coordination predicted from simple valence-shell electron pair repulsion (VSEPR) arguments, or whether the

energetic gain from the distortion is "washed out" by thermal motion.

In perovskites, this effect leads to a competition between distortions which remove the inversion symmetry of the dication (which tend to produce structures with long-range polar order) and the aforementioned distortions associated with octahedral tilting (which produce antipolar orderings of anions and A-site cations). The precise nature of this competition and its impacts on properties are the major focus of Chapters 5 and 6, though the crystallographic signatures and property effects are also implicitly observed in the results reported in Chapters 3, 4, and 8.

For a detailed background and discussion of the theory of lone pairs in the solid state, the reader is referred to the literature [36, 37, 38, 39, 35, 40, 41] as well as Chapters 5 and 6 of this dissertation.

1.5.4 Molecule–cage interactions in "plastic" crystals

"Plastic crystals" of rotating molecular units are a crystal at all temperatures in the translational sense. In an orientational sense, they are liquids at high temperature, with molecular units rotating rapidly in an uncorrelated fashion. At low temperatures, they may be an orientational glass or crystal, depending on whether the molecular rotations freeze-in in an ordered or disordered fashion. In some systems, an intermediate temperature state exists of strongly correlated molecular rotations. Plastic crystals often exhibit a range of phase transitions and order-disorder phenomena and are exemplars of the power of dynamical studies based on nuclear magnetic resonance (vide infra). The presence of molecular cations in the hybrid perovskites introduces additional complexity into their structure and lattice dynamics, and associated properties.

1.6 Brief background of key techniques

This section provides a brief overview of the core experimental and computational techniques employed in the research described in this dissertation.

1.6.1 Total scattering studies of local atomic structure

Crystallographic techniques based on the diffraction of radiation (X-rays, thermal neutrons, electrons) by periodic arrays of atoms have been used extensively for the last hundred years to establish the structure of crystalline matter. However, these approaches are necessarily limited to a description of "average" structure (long-range order) because only radiation scattered into the Bragg peaks is considered.

Deviations from perfect, static crystalline order cause some radiation to be diffusely scattered to general positions in reciprocal space ("underneath" and "between" Bragg peaks). These deviations occur from "dynamic" disorder, including thermal motion of atoms about their nominal, crystallographic positions, as well as from "static" disorder, such as the differing bond lengths present for different species on the same crystallographic site in substitutional alloys. This diffuse scattering is typically very weak compared to the Bragg scattering, and special experimental and analytical care must be taken to collect and interpret this information.

With respect to experimental setup, instruments optimized for simultaneous acquisition of Bragg and diffuse scattering for PDF analysis collect scattering deep into reciprocal space (large scattering vector, $Q = |\mathbf{Q}| = \frac{4\pi}{\lambda} \sin\theta$ for elastic scattering, where λ is the wavelength of incident radiation, and θ is the scattering angle), sacrificing Q-resolution in the process. Additionally, a careful "background" measurement must be collected to remove scattering from sample canisters and residual environmental gases and to correct for heterogeneities in detector efficiencies.

Once such corections are made, the one-dimensional pair distribution function (PDF), $G(r)$ is computed as the sine Fourier transform of the experimentally measured structure function, $S(Q)$, according to Equation 1.3, where r is the real-space atom–atom separation. The PDF represents the distribution of all pair-wise atom–atom correlation functions, weighted by the constituent atomic scattering factors of each pair correlation. Qualitatative analysis and quantitative modeling (by both "small-box" and "big-box" techniques) of PDFs then provides insights about "local" structure, offering a complementary approach to crystallographic techniques predicated on long-range periodic order and the Debye–Waller approximation.

$$G\left(r\right) = \frac{2}{\pi}\int_{0}^{\infty} Q\left[S\left(Q\right) - 1\right]\sin\left(Qr\right)dQ \tag{1.3}$$

1.6.2 Ab initio calculations of crystal properties via density functional theory

In recent decades, quantum mechanical calculations of the properties of condensed matter systems have proven an invaluable technique in chemistry, physics, and materials science. However, solution of the full, many-body Hamiltonian for the electronic and nuclear degrees of freedom in real solids remains intractable. A sequence of theoretical and practical advances have nonetheless demonstrated the value of approximate solutions based on density functional theory (DFT) and have enabled their widespread use. A brief, high-level overview of the theoretical framework, relevant approximations, and practical use of DFT for studies of the electronic structure and lattice dynamics of crystals follows.

Typically, the Born–Oppenheimer approximation is invoked, wherein the electronic and nuclear degrees of freedom are separated on the basis of the slow response of the

massive nuclei relative to the electrons. This approach, which by nature ignores vibronic coupling, allows the electronic system to be solved with fixed nuclear positions. Subsequently, the nuclear positions are iteratively found with classical electrostatics from the electronic charge density (Hellmann–Feynman forces).

Building on prior work of Thomas, Fermi, and others, Hohenberg and Kohn established two important theories that laid the foundation for DFT: 1) the external potential felt by the inhomogeneous electron gas is a unique functional of the electron density; and 2) the density which minimizes the total energy is the exact ground-state density. [42] Subsequently, Kohn and Sham developed the approximation of the many-body electron system as a single-particle (non-interacting) system with an effective (mean-field) potential. [43] The only term that is unknown in the Kohn–Sham formulation is the functional of density expressing the effects of electron exchange and correlation (XC), which if known, makes this greatly simplified formulation exact as it yields the same ground-state charge density as the real, interacting system. In reality, the "correct" XC functional is not known, and the design of such functionals that accurately reproduce the properties of real systems is an active area of research.

From a practical perspective, various XC functionals have been developed which trade increasing fidelity for increasing computational cost, and the use cases of the dominant functionals are well documented. Various aspects of the practical implementation of the Kohn–Sham formulation of DFT in periodic systems have been extensively developed, including plane wave basis sets, the use of pseudopotentials to obviate the need to represent core electrons with (spatially) rapidly varying wavefunctions, and the projector augmented wave formalism to compute properties which are sensitive to the all-electron density despite the use of pseudopotentials. Taken together, these various contributions result in a powerful tool for calculating the approximate electronic structure and lattice dynamics of crystalline solids without the need for system-specific

parameters or assumptions. Though not strictly first-principles because of the use of approximate XC functionals, due to this system-independent formulation, we will refer to these methods as "ab initio" methods throughout this dissertation.

1.6.3 Sub-GHz dielectric spectroscopy of semiconductors

The dielectric response, $\epsilon(\omega)$, of a substance — the electric polarization susceptibility under an applied electric field — is frequency-dependent, with the contributions of the various polarization mechanisms limited by their temporal dynamics. In the low frequency limit (a DC field), all polarization mechanisms contribute, resulting in the "static" dielectric constant, ϵ_0. In the high-frequency, "optical" regime, contributions from ionic polarization and the rotation of molecular dipoles are removed, leaving only the response of the electronic charge density under fixed nuclear positions, denoted somewhat misleadingly by ϵ_∞. At yet faster frequencies (near-infrared to ultraviolet), the dielectric response is dependent on the particulars of the electronic structure and permitted optical transitions, and is not considered here.

For typical inorganic semiconductors, the dielectric response of the crystal is nearly temperature-independent. However, both dielectrics close to polar phase boundaries (e.g. $BaTiO_3$) and plastic crystals with dipolar molecular ions (e.g. KCN) exhibit a strongly temperature-dependent response in the THz and slower regimes. Both of these phenomena are relevant to the hybrid perovskites, because the lone pair electrons cause a double-well potential for the dication, and the methylammonium and formamidinium countercations are polar. This discussion focuses on the latter consideration, as it dominates the dielectric response of the lead iodides presented here.

For a liquid of dipolar molecules, the static dielectric response is temperature-dependent in a manner similar to the magnetic susceptibility of a paramagnet, with

entropic factors competing with the energetically preferred alignment of dipoles to the applied field at finite temperatures. In the limit of non-interacting dipoles, this results in a Curie-like dielectric susceptibility, and the response of real materials can be understood as perturbations from this ideal behavior due to dipole–dipole interactions and steric considerations that hinder motion.

To first order, the dielectric response of the hybrid perovskites at ambient temperatures is the superposition of the response of the anionic inorganic framework and the response of a (hindered) dipolar liquid on the molecular sublattice. The dynamics of molecular rotation are not easily accessed in this regime, as they fall in the THz "gap" between routine electrical methods and routine infrared spectroscopies. At sufficiently low temperatures (10s to low 100s of Kelvin in the materials presented here), the reorientability of the dipolar molecular ions is frozen out due to molecule–cage interactions, so electrical approaches can directly probe this slowing. In particular, measuring the capacitance and loss of parallel-plate capacitors with the material of interest as the dielectric provides a straightforward means of probing the complex static dielectric response in this regime.

An illustrative example is given in Figure 1.4. The transition from a liquid-like state of molecular dipoles to a frozen state is dependent on the nature of the coupling between the dipolar molecules and their surrounding framework "cages." A cooperative mechanism between the molecules and the framework produces an abrupt freezing characterized by a sudden loss of the polarization term from dipole rotation and a first-order phase transition. On the other hand, a frustrated interaction (incompatible symmetries of molecule and cage) results in a more gradual slowing of molecular motion characterized by freeze-out of the molecular dipole response (and corresponding dielectric loss peaks due to resonance between dielectric relaxation and the probe frequency) at higher temperatures for higher frequencies. Further details and discussion

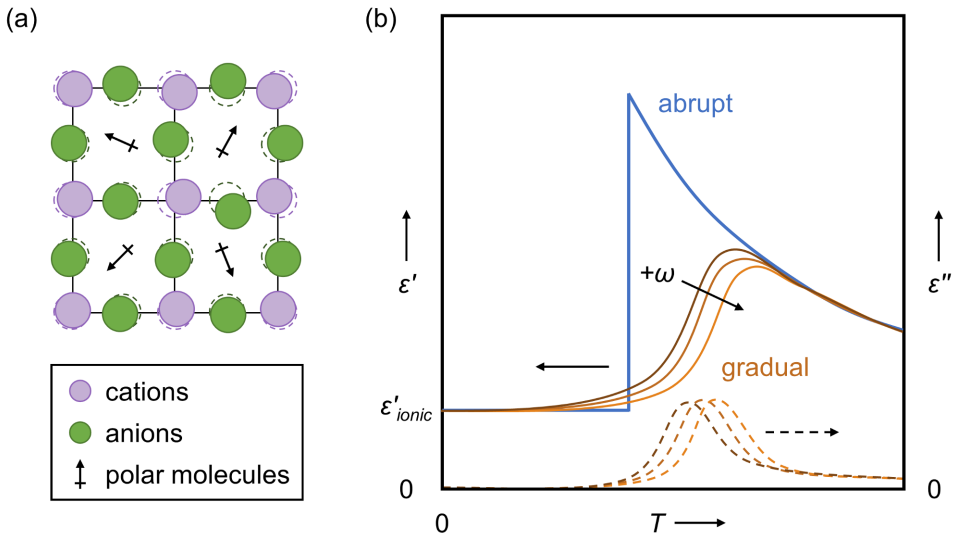

Figure 1.4: (a) A plastic crystal with dipolar molecular ions on a sublattice. (b) Schematic slow (Hz–MHz) dielectric response of such a crystal. At high T the dipolar molecules are liquid-like, with a roughly $\sim T^{-1}$ susceptibility. At low T, the dipole orientations are fixed, leaving only the response from ionic and electronic polarization. At intermediate T the response depends on the nature of the freezing of the dipole liquid sublattice, with details given in the text.

are given in Chapters 7 – 9.

Special care must taken in acquiring and interpreting dielectric measurements in the high-temperature, low-frequency limit as the effects of electronic conduction, ionic conduction, and polycrystallinity or other sample heterogeneity can obscure the intrinsic dielectric response of the bulk. These factors, collectively known as Maxwell–Wagner–Sillars polarization, [44, 45, 46, 47, 48] have been well understood for the better part of a century, but still cause confusion in some areas of the literature.

1.6.4 Relaxation effects in solid-state nuclear magnetic resonance (NMR) spectroscopy

Nuclear magnetic resonance (NMR) spectroscopy provides a powerful probe of the local environments of specific nuclei in solids, as well as of certain dynamic phenom-

ena. A general overview of NMR is omitted here, with focus instead placed on the use of longitudinal ("spin–lattice") relaxation measurements to study molecular motion in plastic crystals.

Due to the small magnetic moments of nuclei and correspondingly small Zeeman splittings of nuclear spin levels ($\ll 1$ meV at practical fields), coupling between the nuclear spin system and the bath is weak. Longitudinal relaxation occurs via phonons and localized vibrations, molecular rotation, diffusion and chemical exchange, paramagnetic impurities, and interactions with charge carriers. For effective energy transfer, these fluctuations must have spectral content near the Larmor frequency (much like the coupling of energy into a classical mass–spring–damper or other resonator). For instance, consider spin-1/2 nuclei on a vibrating lattice. Because the direct dipole-dipole interaction of nuclear spins is distance-dependent (r^{-6}), the annihilation (creation) of phonons at the Larmor frequency will effectively couple energy into (out of) the spin system from the reservoir of the lattice if the spins are colder (hotter) than the lattice. In the phonon density of states of most crystals, few modes exist in this energy range, so this "direct" process is actually exceedingly rare. More commonly a multi-phonon process occurs, where the difference between the modes is the Larmor frequency. Alternatively, in systems with soft localized modes such as molecular rotation or libration, the direct process may be an important contributor.

Longitudinal relaxation times, T_1, are typically measured by the saturation recovery or inversion recovery methods. The inversion recovery pulse sequence is presented in Figure 1.5a. A transverse π pulse is applied, followed by a variable delay time, a transverse $\pi/2$ pulse, and finally acquisition of the free-induction decay. This experiment is repeated for parameterized values of the variable delay time spanning multiple orders of magnitude which bracket T_1. To extract T_1, the integrated intensity of the NMR lines (for each nuclear environment or phase with unique relaxation behavior) at each delay

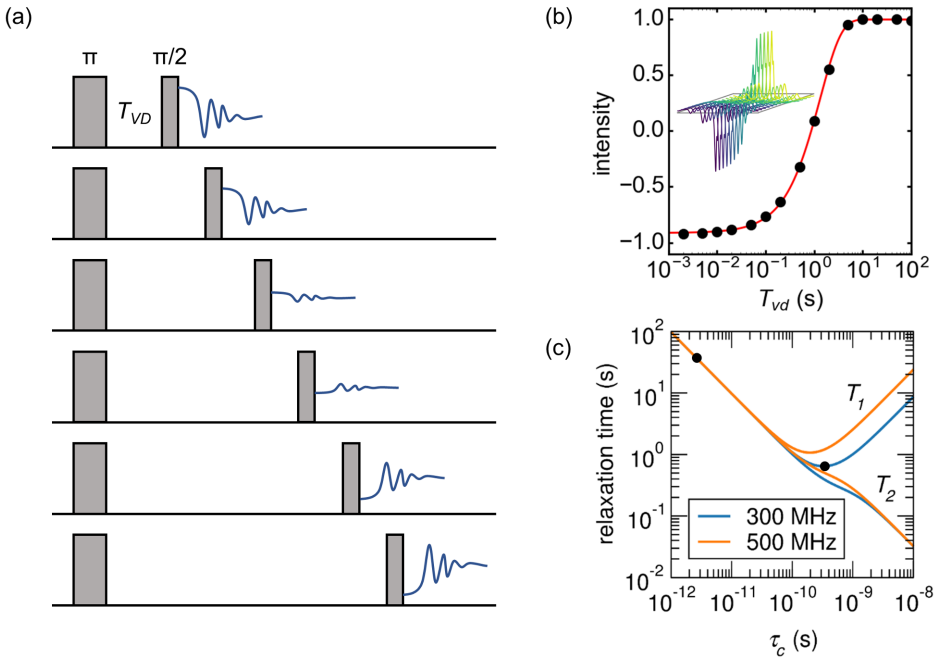

Figure 1.5: (a) Schematic view of the inversion recovery experiment used to measure NMR longitudinal relaxation time, T_1. T_{VD} denotes the parametrized variable delay time. (b) Example T_1 fitting for real inversion recovery experiments (spectra inset). (c) Dependence of longitudinal (T_1) and transverse (T_2) relaxation times on the autocorrelation time for molecular motion (τ_c) in the BPP model. Outside of the fast-motion regime ($\omega_0\tau_c \ll 1$) the relaxation times are field-dependent.

time is fit to Equation 1.4, where $M_z(t)$ and $M_{z,eq}$ are the longitudinal magnetization at time t and at equilibrium. A real example is given in Figure 1.5b for a sample with a single relaxation time.

$$M_z(t) = M_{z,eq}\left[1 - 2\exp\left(-\frac{t}{T_1}\right)\right] \tag{1.4}$$

Bloembergen, Purcell, and Pound ("BPP") formulated a simple theory for T_1 (as well as the transverse or "spin–spin," relaxation time, T_2) as a function of an internal time constant of motion and of longitudinal field (Eqn. 1.5). In the limit of a pure substance with isotropic molecular reorientation, they calculate T_1 and T_2 as a function of an autocorrelation time, τ_c, corresponding to the time it takes a molecule to rotate one

radian (Figure 1.5). This model has proven quite accurate for simple (pure) systems and provides qualitative insights for more complex ones. Notably, BPP theory predicts a monotonically decreasing T_2 with correlation time, while T_1 passes through a field-dependent minimum. This reflects the notion that spin–lattice energy exchange is most effective at the Larmor frequency, while two spins spending greater time in proximity will always serve to couple them more effectively.

$$\frac{1}{T_1} = C\left[\frac{\tau_c}{1+\omega_0^2\tau_c^2} + \frac{4\tau_c}{1+4\omega_0^2\tau_c^2}\right] \tag{1.5}$$

1.7 Permissions and Attributions

1. The content of Chapter 2 has previously appeared in reference [49]: D. Fabini, Quantifying the potential for lead pollution from halide perovskite photovoltaics, *J. Phys. Chem. Lett.* **2015**, *6*, 3546–3548, © 2015 American Chemical Society, reprinted with permission. I thank Prof. Ram Seshadri and Prof. Michael L. Chabinyc for helpful discussions.

2. The content of Chapter 3 is the result of a collaboration with Anna J. Lehner, Hengbin Wang, Christopher D. Liman, Claire-Alice Hébert, Erin E. Perry, Ming Wang, Guillermo C. Bazan, Michael L. Chabinyc, Ram Seshadri, and has previously appeared in reference [15]: A. Lehner, H. Wang, D. Fabini, C. Liman, C.-A. Hébert, E. Perry, M. Wang, G. Bazan, M. Chabinyc, and R. Seshadri, Electronic structure and photovoltaic application of BiI_3, *Appl. Phys. Lett.* **2015**, *107*, 131109, © 2015 AIP Publishing, reprinted with permission. We thank Prof. Jakoah Brgoch for fruitful discussions.

3. The content of Chapter 4 is the result of a collaboration with Anna J. Lehner, Hay-

den A. Evans, Claire-Alice Hébert, Sara R. Smock, Jerry Hu, Hengbin Wang, Josef W. Zwanziger, Michael L. Chabinyc, and Ram Seshadri, and has previously appeared in reference [16]: A. Lehner, D. Fabini, H. Evans, C.-A. Hébert, S. Smock, J. Hu, H. Wang, J. Zwanziger, M. Chabinyc, and R. Seshadri, Crystal and electronic structures of complex bismuth iodides $A_3Bi_2I_9$ (A = K, Rb, Cs) related to perovskite: Aiding the rational design of photovoltaics, *Chem. Mater.* **2015**, *27*, 7137–7148, © 2015 American Chemical Society, reprinted with permission. We thank Prof. Jakoah Brgoch for fruitful discussions.

4. The content of Chapter 5 is the result of a collaboration with Geneva Laurita, Jonathon S. Bechtel, Constantinos C. Stoumpos, Hayden A. Evans, Athanassios G. Kontos, Yannis S. Raptis, Polycarpos Falaras, Anton Van der Ven, Mercouri G. Kanatzidis, and Ram Seshadri, and has previously appeared in reference [50]: D. Fabini, G. Laurita, J. Bechtel, C. Stoumpos, H. Evans, A. Kontos, Y. Raptis, P. Falaras, A. Van der Ven, M. Kanatzidis, R. Seshadri, Dynamic stereochemical activity of the Sn^{2+} lone pair in perovskite $CsSnBr_3$, *J. Am. Chem. Soc.* **2016**, *138*, 11820–11832, © 2016 American Chemical Society, reprinted with permission. GL and HAE would like to thank Kevin A. Beyer (11-ID-B, APS) and Ashfia Huq (POWGEN, SNS) and GL and DHF would like to thank Katharine Page and Daniel Olds (NOMAD, SNS) for assistance and helpful discussions during beam line experiments. JSB acknowledges Min-Hua Chen and John C. Thomas for use of their phonon code.

5. The content of Chapter 6 is the result of a collaboration with Geneva Laurita, Constantinos C. Stoumpos, Mercouri G. Kanatzidis, and Ram Seshadri, and has previously appeared in reference [51]: G. Laurita, D. Fabini, C. Stoumpos, M. Kanatzidis, R. Seshadri, Chemical tuning of dynamic cation off-centering in the

cubic phases of hybrid tin and lead halide perovskites, *Chem. Sci.* **2017**, *8*, 5628–5635, Published by The Royal Society of Chemistry, reprinted with permission. GL and CCS would like to thank Hayden A. Evans, Kevin A. Beyer and Karena W. Chapman for assistance and helpful discussions during beam line experiments.

6. The content of Chapter 7 is the result of a collaboration with Tom Hogan, Hayden A. Evans, Constantinos C. Stoumpos, Mercouri G. Kanatzidis, and Ram Seshadri, and has previously appeared in reference [52]: D. Fabini, T. Hogan, H. Evans, C. Stoumpos, M. Kanatzidis, and R. Seshadri, Dielectric and thermodynamic signatures of low temperature glassy dynamics in the hybrid perovskites $CH_3NH_3PbI_3$ and $HC(NH_2)_2PbI_3$, *J. Phys. Chem. Lett.* **2016**, *7*, 376–381, © 2016 American Chemical Society, reprinted with permission. DHF thanks Geneva Laurita for helpful discussions and Jaye K. Harada for assistance with dielectric measurements.

7. The content of Chapter 8 is the result of a collaboration with Constantinos C. Stoumpos, Geneva Laurita, Andreas Kaltzoglou, Athanassios G. Kontos, Polycarpos Falaras, Mercouri G. Kanatzidis, and Ram Seshadri, and has previously appeared in reference [53]: D. Fabini, C. Stoumpos, G. Laurita, A. Kaltzoglou, A. Kontos, P. Falaras, M. Kanatzidis, R. Seshadri, Reentrant structural and optical properties and large positive thermal expansion in perovskite formamidinium lead iodide, *Angew. Chem. Int. Ed.* **2016**, *55*, 15392–15396, © 2016 John Wiley & Sons, Inc., reprinted with permission. We thank Professor Anthony K. Cheetham FRS for illuminating discussions.

8. The content of Chapter 9 is the result of a collaboration with Ting Ann Siaw, Constantinos C. Stoumpos, Geneva Laurita, Daniel Olds, Katharine Page, Jerry G. Hu, Mercouri G. Kanatzidis, Songi Han, and Ram Seshadri, and has previously ap-

peared in reference [54]: D. Fabini, T. Siaw, C. Stoumpos, G. Laurita, D. Olds, K. Page, J. Hu, M. Kanatzidis, S. Han, R. Seshadri, Universal dynamics of molecular reorientation in hybrid lead iodide perovskites, *J. Am. Chem. Soc.* **2017**, *139*, 16875–16884, © 2017 American Chemical Society, reprinted with permission. We thank Prof. Catherine Oertel for her useful suggestions.

Chapter 2

Quantifying the potential for lead pollution from halide perovskite photovoltaics

2.1 Results & discussion

[1]Hybrid organic-inorganic lead halide perovskites with the general formula $A\mathrm{Pb}X_3$ (where $A = [\mathrm{CH_3NH_3}]^+$ or $[\mathrm{HC(NH_2)_2}]^+$ and $X = \mathrm{Cl}^-$, Br^-, or I^-) have attracted substantial research attention of late because of the great promise they display in solution-processed photovoltaic (PV) devices. PV devices employing these materials as the active component currently display efficiencies in excess of 20%. [55] The pace at which these high efficiencies have come about is remarkable given that the first report of these materials in this application appeared only in 2009. [7] However, significant technological challenges remain in the realm of stability and potential lead

[1]The contents of this chapter have substantially appeared in reference [49]: D. Fabini, Quantifying the potential for lead pollution from halide perovskite photovoltaics, *J. Phys. Chem. Lett.* **2015**, *6*, 3546–3548, © 2015 American Chemical Society, reprinted with permission.

toxicity. The presence of lead in these materials raises substantial concerns regarding widespread application. Life cycle analyses considering a broad range of material and energy inputs and environmental impacts are beginning to appear for these materials. [56, 57]. A recent report by Hailegnaw *et al* in this journal investigates the mechanism and magnitude of lead loss from $CH_3NH_3PbI_3$ PV cells via exposure to water, as may happen if a PV module breaks, and considers the implications for lead pollution. [58]

In this Viewpoint, I attempt to quantify the total lead content of halide perovskite PV that would be required to supply current electricity needs in the United States as an indicator of the upper bound on possible lead pollution during the service life of this technology. This figure is compared with select historical and current sources of lead pollution in the U.S. Based on the crystal structure of $CH_3NH_3PbI_3$, typical device geometries, and forward-looking assumptions about PV performance, I find a lead intensity (total lead content per unit electricity produced) of 38 μg/kWh, as detailed below. This corresponds to a total lead content of 160 t/yr for all U.S. electricity generation. Consequently, if 1% of PV modules were to break while deployed, 1.6 t/yr of lead could leech into the surrounding environment. Though it is beyond the scope of the current work, lead pollution generated during PV module manufacture and disposal or recycling must also be considered. Furthermore, lead pollution is but one of many environmental and resource factors in evaluating the suitability of a new PV technology, including other toxic pollutants, impacts on land use and water resources, greenhouse gas emissions, energy payback times, and abundance of material inputs [56, 59, 60].

A comparison with select lead pollution sources and lead-containing products is summarized in Figure 2.1. In 1973, before the phase-out of leaded automotive gasoline, direct air emissions of lead from automobiles were estimated to be 200,000 t/yr. [61] In 2011, air emissions from leaded aviation fuel, processing of metals, and electricity generation from fossil fuels were reported to be 440 t/yr, 120 t/yr, and 35 t/yr,

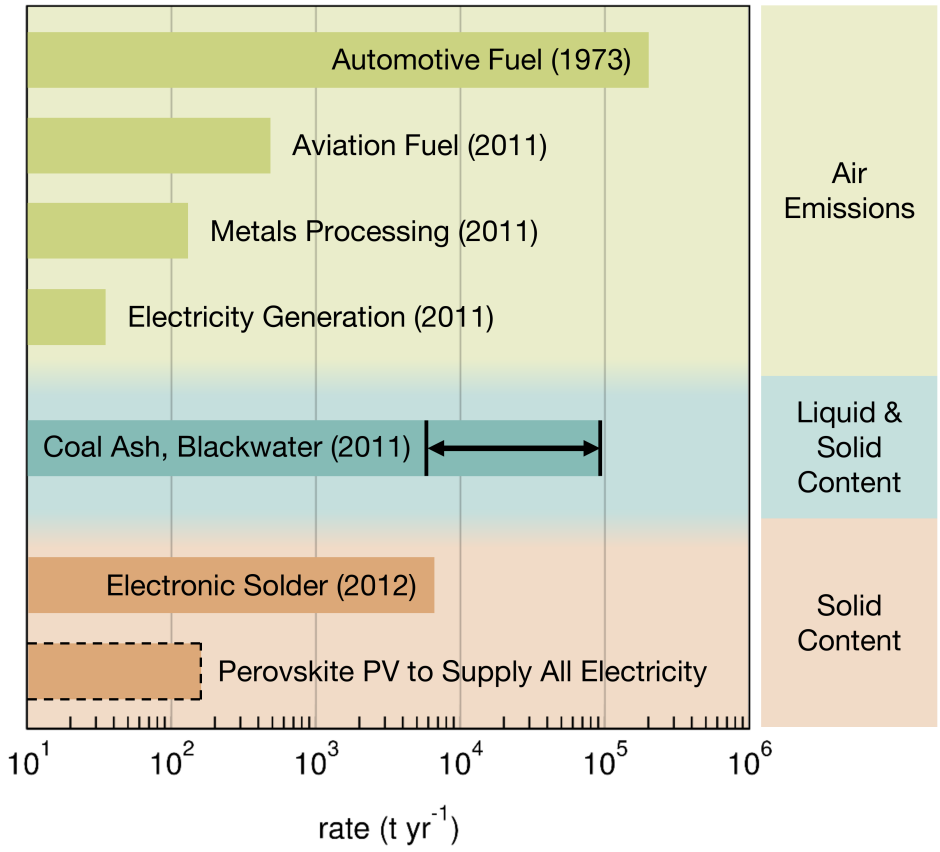

Figure 2.1: Select U.S. lead emissions sources [61, 62], lead content of coal wastes [63, 64, 65] and electronic solder produced in the U.S., [66] and hypothetical lead content of perovskite photovoltaics (PV) to supply the entire U.S. electricity sector. [67, 68, 65] All quantities are in metric tons per year.

respectively. [62] Additionally, while figures are not directly reported, I calculate that between 5,900 t/yr and 93,000 t/yr of lead are generated by the electric power sector during coal processing and combustion in the form of coal ash and blackwater. Lastly, in 2012, the lead content of electronic solder produced in the U.S. was reported to be 6,200 t/yr, [66] though the lead content of solder present in all electronic products in the U.S. is likely somewhat higher due to imports.

The chemical and physical forms of lead are of course markedly different in these contexts. Direct emission to the air provides a facile route for lead to end up in soil, on surfaces, and in food and water supplies. Coal ash and blackwater are not emitted directly to the air, but slurry impoundment ponds at coal processing plants and power stations have been the site of recent large-scale environmental disasters. [69, 70] In contrast, lead in halide perovskite PV is in the solid state, encapsulated, and specifically must remain there for the technology to be viable. The case of electronic solder is perhaps most analogous, though the quantity of lead appears to be substantially larger and the primary risk is associated with leeching from equipment improperly disposed of in landfills.

All technologies and processes present risks which must be weighed objectively against those associated with alternatives. In the case of leaded automotive gasoline, leaded solder for potable plumbing systems, and leaded paint, the lead pollution and toxicity burden is unacceptably high, and bans on these products have been in place for decades. In contrast, lead-acid batteries continue to be the standard for starting-lighting-ignition batteries in trucks and automobiles and are the primary source of recycled lead that makes up 91% of refined lead production in the U.S. [66] Effective regulation and management of manufacture, deployment, and disposal or reprocessing of technologies containing lead can significantly reduce the risks associated with these materials. In the case of halide perovskite PV, further study is required to determine

whether these risks can be mitigated to an acceptably low level. These are indeed challenging materials, but the picture that emerges from this analysis is that the potential for lead exposure from large-scale adoption of this technology is relatively modest when compared with other, existing technologies and practices.

2.2 Methods

The area density of lead in halide perovskite PV devices is calculated as

$$\sigma_{Pb} = \frac{N_{Pb}}{V_c} \times \frac{M_{Pb}}{N_A} \times l = 420\,\text{mg/m}^2\,,$$

where N_{Pb} and V_c are the number of lead atoms per unit cell and the unit cell volume, respectively, for the room temperature polymorph of $CH_3NH_3PbI_3$ [67], M_{Pb} is the molar mass of lead, N_A is Avogadro's number, and l is the absorber thickness (assumed to be 300 nm).

The lead intensity of energy produced from halide perovskite PV is calculated as

$$I_{Pb} = \frac{\sigma_{Pb}}{G\,T\,\eta\,C} = 38\,\mu\text{g/kWh}\,,$$

where G = 1 kW/m^2 is the nominal solar irradiation at the Earth's surface, T is the PV plant lifetime, η is the PV conversion efficiency, and C is the PV plant capacity factor. Here, the lifetime is assumed to be 25 yrs and the efficiency 25% (perovskite/c-Si tandem, or similar), reflecting the stringent reliability and performance requirements for widespread implementation of this new technology. The capacity factor encapsulates the geographic and temporal variation in solar irradiation, and is here assumed to be 20%, which is typical of fixed axis solar PV performance in the United States to date

[68].

The total lead content of enough halide perovskite PV to supply all U.S. electricity is calculated as

$$m_{Pb} = I_{Pb} \times E = 160\,\text{t/yr}\,,$$

where E = 14.01 quadrillion BTU is the net generation of electricity in 2011 (enough to supply all consumption plus transmission and distribution losses) [65]. Possible additional lead pollution from sources upstream in the supply chain, as in air emissions from additional lead smelting, are not captured here. These sources are assumed to be secondary in quantity to the lead present in PV cells themselves, and are likely more easily mitigated or contained than the potential pollution from geographically disperse lead-containing PV panels.

The lead content of U.S. coal wastes from electric power generation is calculated as

$$m_{Pb,coal} = c_{Pb,coal} \times C_{coal} = 5,900\,\text{t/yr} - 93,000\,\text{t/yr}\,,$$

where $c_{Pb,coal}$ = 7 μg/g $-$ 110 μg/g is the concentration of lead in coal [63, 64] and C_{coal} = 928.6 million short tons is the coal consumption of the electricity sector in 2011 [65]. This calculation assumes that all lead in the coal ends up in blackwater, bottom ash, and captured fly ash. In practice, a very small proportion escapes precipitators and filters and enters the atmosphere (compare the magnitude of air emissions from the power sector, 35 t/yr, with the original lead content of the corresponding coal, as calculated here). Additionally, some proportion of fly ash is repurposed as a partial substitute for Portland cement in concrete production or is used in embankments or other fill. This diversion of ash wastes is not captured here for lack of data, though the effect is likely to be significantly less than one order of magnitude.

Chapter 3

Electronic structure & photovoltaic application of BiI_3

[1] Rapid recent improvement in photovoltaic efficiency in hybrid lead halide perovskite materials has provided the impetus for understanding other, related main-group halide systems. Here we show that the closely related but less toxic bismuth iodide BiI_3 can show promising optoelectronic properties. Layered binary BiI_3 is used here as the active layer in solar cells. Experimental and computation studies of absolute band positions of BiI_3 are also presented, to help in the rational design of device architectures that would allow efficient charge transfer at the interfaces.

3.1 Introduction

Bismuth triiodide BiI_3 belongs to a family of layered heavy metal semiconductors with interesting anisotropic electronic and optical properties. [71, 72] Thin films and

[1] The contents of this chapter have substantially appeared in reference [15]: A. Lehner, H. Wang, D. Fabini, C. Liman, C.-A. Hébert, E. Perry, M. Wang, G. Bazan, M. Chabinyc, and R. Seshadri, Electronic structure and photovoltaic application of BiI_3, *Appl. Phys. Lett.* **2015**, *107*, 131109,

single crystals of BiI_3 have been investigated as hard radiation detectors [73, 74, 75, 76] and for X-ray imaging [77, 78, 79] due to the relatively wide band gap, high atomic numbers of the constituent elements, and high mass density. Additionally, BiI_3 can be solution-processed, which could facilitate large-scale, cost-efficient and flexible device fabrication. However, there appear to be few attempts to use BiI_3 in photovoltaic devices. The prior report of BiI_3 described its use as hole transport layer (HTL) in solar cells with a fullerene-based light absorber. [80] Clearly the potential of bismuth halides as photovoltaic absorbers and less toxic alternatives to the prominent hybrid lead halide perovskites [81] has not been fully explored.

The crystal structure of BiI_3 (space group $R\bar{3}$) [82] can be described as a slightly distorted hexagonally close packed lattice of I^- ions in which the metal cations occupy 2/3 of the octahedral voids of every other layer. Optical properties of BiI_3 have been extensively investigated. [83, 84, 85, 86, 87, 88] The band gap (E_g) values reported for BiI_3 span a large range and the nature of the transition has caused some discussion. It has been suggested that the strong absorption at temperatures above 77 K (E_g approx. 1.8 eV, see Figure 3.1a) can be interpreted as a direct transition, while at lower temperature the lowest energy transition has been attributed to an indirect transition. [83, 84, 88] More recently, the transition at room temperature has been assigned to an indirect gap by optical absorption spectroscopy. [89]

Density functional theory (DFT) has been previously used to elucidate the electronic band structure of BiI_3 and confirm the indirect nature of the transition, [89, 90] but only few recent studies [91, 89, 75, 90] apply spin orbit coupling, which is necessary in 6s systems. [85, 86] Most of those studies have been limited by the choice of using DFT within the local density approximation (LDA) or the generalized gradient approximation (GGA), which are known for poorly reproducing the band gaps of semiconductors. For photovoltaic applications, the knowledge of the absolute band positions is crucial

for successful rational device design.

Here we present the first study of the application of a bismuth halide as a photovoltaic absorber (active layer). The absolute band positions of BiI_3 are determined experimentally by optical (UV-Vis) absorption and ultraviolet photoelectron spectroscopy (UPS) and computationally by a super-cell method [92] which is also valuable for related complex lead halides. [93] We have used the screened hybrid functional of Heyd, Scuseria, and Ernzerhof (HSE) [94] to obtain reliable values. Additionally, the dielectric response including the dielectric tensors (ϵ^{∞}) and the Born effective charge tensors (Z^{*}) of BiI_3 are presented as indicators of incipient structural instability and dielectric defect screening. BiI_3 solar cells were fabricated with a dense TiO_2 electron transport layer (ETL) and two different polymer HTLs.

3.2 Results & discussion

The optical band gap of BiI_3 was determined by UV-Vis transmission of a film and diffuse reflection spectroscopy of a powder sample (Figure 3.1a, for details, see Supporting Information). From both measurement modes, the band gap was determined to be approximately 1.8 eV, which is in good agreement with values reported previously (e.g. 1.7 eV [89]). The band structure presented in the following illustrates that the direct and indirect transition lie very close together. The ionization energy (I), which is the position of the valence band maximum (VBM) with respect to the vacuum energy, was determined experimentally from UPS (Figure 3.1b) to lie between 6.0 and 6.3 eV for a range of measurements and samples (Table 3.1). Spectra were collected on thin film samples whose surface composition was confirmed by X-ray photoelectron spectroscopy (XPS, for details, see Supporting Information). This VBM level range is in good agreement with the value for the photoelectric work function of 5.8 eV reported

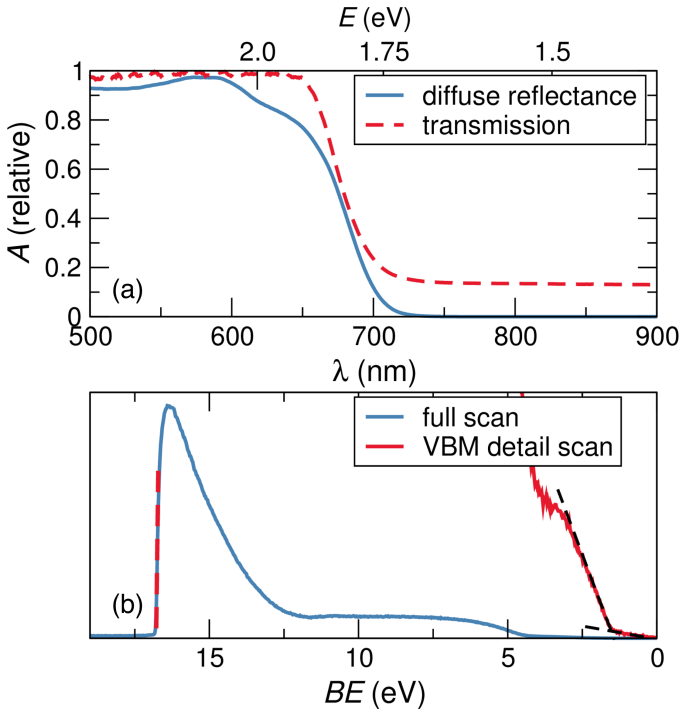

Figure 3.1: (a) Transmission and diffuse reflection UV-Vis and (b) UPS spectra of BiI_3. From the UPS data, the position of the valence band maximum (VBM) was determined by subtracting the energy difference between both edges of the spectral feature from the excitation energy ($h\nu = 21.22\,\text{eV}$). Figure prepared by Anna J. Lehner.

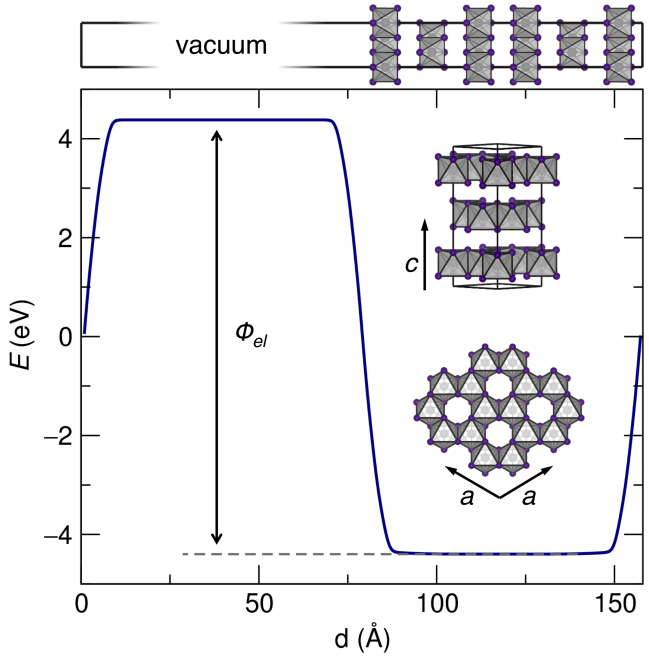

Figure 3.2: Absolute band position calculation (DFT method PBE+SOC) for BiI_3 ($R\bar{3}$, see insets) using a slab model with a half filled 1×1×4 super-cell (model shown at top). Φ_{el} is the difference between the vacuum energy and the average electrostatic potential of the crystal. Figure prepared by Anna J. Lehner.

Table 3.1: Experimental and calculated band gap (E_g) and ionization energy (I), calculated dielectric tensors (ϵ_{ij}^{∞}) and Born effective charge tensors (Z^*; $|e|$ on Bi^{3+}) of BiI_3.

E_g (eV)		I (eV)		ϵ_{xx}^{∞}	ϵ_{zz}^{∞}	Z_{xx}^*	Z_{zz}^*
exp.	calc.	exp.	calc.				
1.8	1.93	6.0 to 6.3	6.05	18.9	15.0	6.6	4.9

previously. [86]

To support the experiments, DFT calculations of the band structures, band gaps, and absolute band positions were carried out using the VASP Package. [95, 96] Spin-orbit-coupling (SOC) was included for all calculations. The input structure [82] was used without a structural relaxation step as the agreement between initial and optimized structure was poor due to inadequate description of the interlayer van der Waals interactions with the chosen method (see Supporting Information).

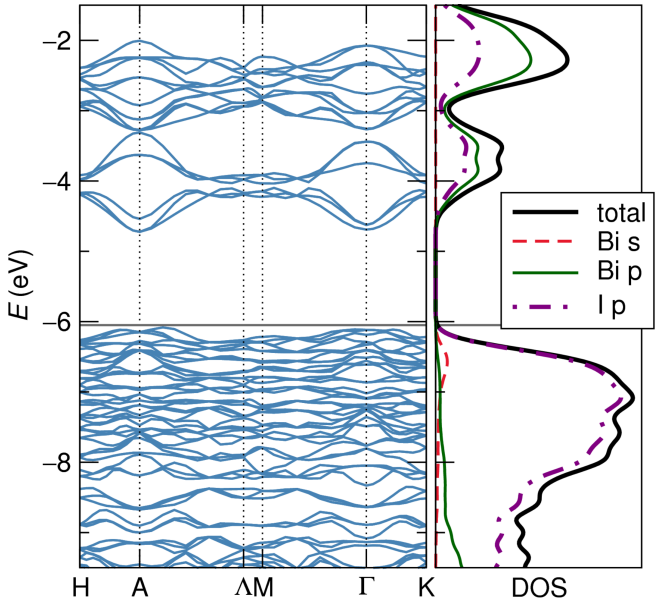

Figure 3.3: PBE+SOC band structure of BiI_3 ($R\bar{3}$) between the high symmetry points of the first Brillouin zone of a primitive hexagonal unit cell and HSE+SOC density of states (total DOS scaled). The position of the valence band maximum (VBM, horizontal line) was offset, based on slab calculations. Figure prepared by Anna J. Lehner.

In order to compare the calculated electronic structure of BiI_3 to other phases, the VBM was normalized by the average electrostatic potential (Φ_{el}) obtained from slab calculations. Thereby, the ionization energy (I) was calculated following $I = \Phi_{el} - E_F$, where Φ_{el} is the difference between the potential energy of the empty (approximating the vacuum) and filled (approximating the bulk material) sections of the super-cell used and E_F is the fermi energy of the single unit cell. The results are displayed in Figure 3.2 together with the BiI_3 crystal structure. As has been established in prior work, [93] Φ_{el} is rather insensitive to the exchange-correlation functional (PBE versus HSE) used as long as SOC is incorporated; thus the time-efficient PBE+SOC scheme was applied. It yields an excellent agreement with the experimental VBM and CBM (VBM+E_g = CBM) determination (Table 3.1). The band structure and the density of states, where the VBM was set to $-I$, are displayed in Figure 3.3. From the HSE+SOC calculations, the lowest energy transition is indirect (E_g 1.93 eV) between a point at approximately

$0.5\overline{A\Lambda}$ in the valence band (VB) and near A (energetically just marginally lower than Γ) in the conduction band (CB). However, the VB band dispersion is so small that the direct excitation requires only marginally more energy. The band dispersion of the CB is more pronounced suggesting a smaller effective mass of electrons compared to holes in BiI_3. Correspondingly, the mobility of electrons has been reported to be 30 times higher than for holes. [97]

While the room-temperature structure of BiI_3 exhibits no signs of a stereo-active Bi^{3+} 6s lone pair, it is inherently apt to undergo lone-pair-induced (ferroelectric) structural distortions. [90] The Born effective charge tensors (Z^*) have been used previously to probe such incipient structural instabilities. [98] The calculated Z^* tensors on Bi^{3+} for BiI_3 of 4.9 to 6.6 (Table 3.1) are significantly elevated compared to the nominal charge, which could be due to a substantial covalent interaction between Bi 6p and halogen p states. [91] Large static dielectric constants and Born charges were suggested to indicate effective screening of defects and impurities which would otherwise trap charge carriers. [99] Therefore we propose that the relatively high Z^* of BiI_3 reported here and previously [91, 90] may be correlated with favorable transport properties.

The results of the experimental and computational absolute band determination of BiI_3 are shown in comparison with the related binary PbI_2 (2H-polytype) and $CH_3NH_3PbI_3$ in Figure 4.7. The CBM of the electron transport layer (ETL), anatase TiO_2, and VBM of the HTL, PTAA, were included because they are commonly used contact materials in solution-processed solar cells. [81] As a fortuitous match, the VBM and CBM of the hybrid perovskite *MA*PbI_3 happen to be very well aligned with the displayed ETL and HTL energy levels allowing for an efficient transfer of both electrons and holes away from the absorber material. For BiI_3 however, while the CBM is well aligned with the TiO_2 CBM for efficient electron injection, the VBM is too

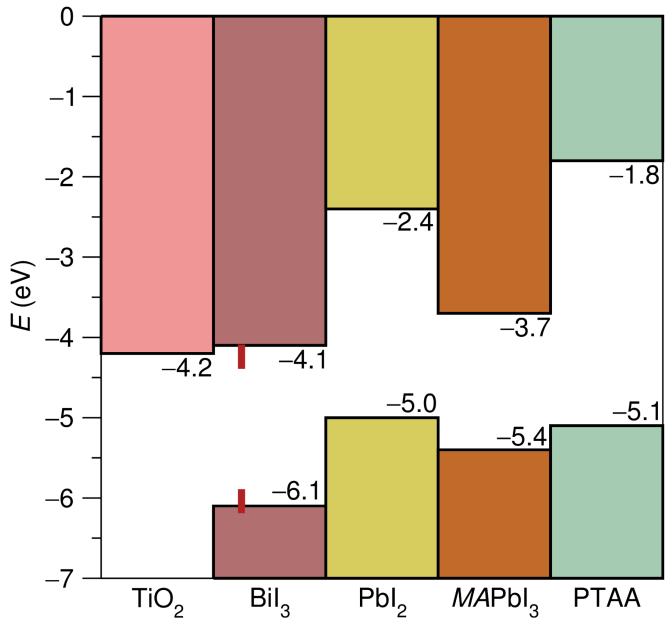

Figure 3.4: Band positions derived from DFT calculations (PBE+SOC) carried out on slab models for anatase TiO_2, [93] BiI_3 (this work) and 2H-PbI_2, [93] compared to experimental values for BiI_3 (indicated by vertical bars as a range, for the UPS experiments carried out here). For added comparison, the experimental band positions of *MA*PbI_3 [100] (*MA* = CH_3NH_3), and PTAA [101] are also displayed. Figure prepared by Anna J. Lehner.

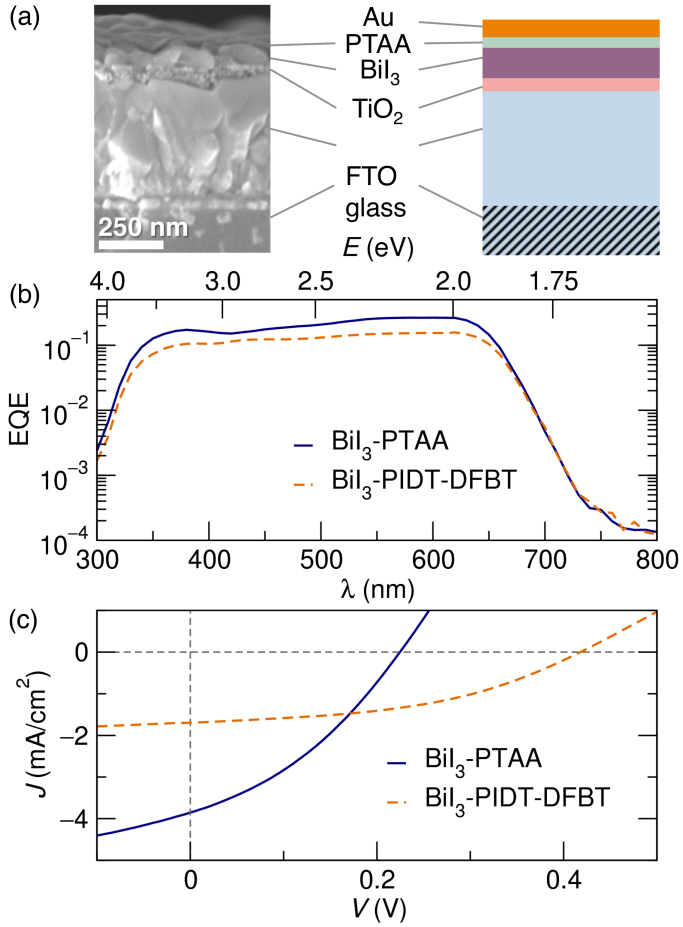

Figure 3.5: BiI_3 solar cell devices using PTAA or PIDT-DFBT as the HTL. (a) SEM cross section and schematic device architecture, (b) external quantum efficiency and (c) JV traces of the assembled devices. Figure prepared by Anna J. Lehner.

far below the VBM of PTAA and other common hole transport materials, potentially limiting of the open circuit voltage and thus power conversion efficiency (PCE).

To evaluate the potential of bismuth halides for photovoltaic application experimentally, solar cells with BiI_3 absorber layers were fabricated in a planar heterojunction structure (Figure 3.5a). Thin films were deposited onto fluorine-doped tin oxide (FTO) on glass under ambient conditions resulting in the final device structure glass/FTO/d-TiO_2/BiI_3/HTL/Au, with the HTL being either the poly-triarylamine PTAA [102] or the poly-indacenodithiophene-difluorobenzothiadiazole PIDT-DFBT [103] (for details see

Table 3.2: Photovoltaic properties of BiI_3-polymer devices: open circuit voltage V_{oc}, short circuit current J_{sc} (from JV or EQE measurements, respectively), fill factor FF, power conversion efficiency PCE.

Device	V_{oc} (V)	J_{sc} (mA/cm^2)		FF	PCE
		from JV	from EQE	(%)	(%)
BiI_3-PTAA	0.22	3.85	3.79	35	0.30
BiI_3-PIDT-DFBT	0.42	1.70	2.39	45	0.32

Supporting Information), and approximately 100 nm thick BiI_3 layers. Upon illumination, charge carriers can be generated within the BiI_3 layer and at the heterointerface with the ETL TiO_2. The photogenerated electrons are extracted through the TiO_2 layer and the holes are extracted through the organic layer.

The heterojunction solar cells studied here display sub-1 % efficiency, but demonstrate that BiI_3 can be used as the active layer in solution-processed solar cells. Representative current density-voltage (JV) characteristics and external quantum efficiency (EQE) spectra of the solar cell devices are presented in Figure 3.5b,c and device parameters are summarized in Table 3.2. The EQE spectra of the devices cover the visible spectrum with a sharp absorption onset around 700 nm, which is in good agreement with the BiI_3 optical band gap close to 1.8 eV. It is interesting to note that the low-energy Urbach tail of the EQE of BiI_3 is steep and does not show much structure, potentially suggesting little disorder-induced broadening. [104] The open circuit voltage (V_{oc}) was low as was expected due to the alignment of the transport levels of BiI_3 with the ETL and the HTL (Figure 4.7). When the deeper VBM polymer PIDT-DFBT is used as the HTL instead of PTAA in the BiI_3 devices, both V_{oc} and FF were improved although a decrease in the J_{sc} was observed. The relatively good quantum efficiency (20% in the PTAA devices) suggests that absorption across the spectrum and charge generation are relatively efficient and therefore improvement of the contacts is likely the best strategy for increasing the PCE of BiI_3 devices.

In summary, working planar heterojunction solar cells using BiI_3 as the light absorber have been presented (PCE 0.32%). The first generation devices exhibit promising quantum efficiencies (EQE 20% in devices with PTAA). The absolute band positions of BiI_3 have been determined both experimentally by UV-Vis and UPS spectroscopy and computationally by DFT slab calculations with excellent agreement. The relatively low PCE and open circuit voltages of 0.42 V arise from the poor match of the low lying VBM of BiI_3 relative to the VBM of the hole transport layers used. Carrier transfer between active layers could be improved by using HTLs with deeper VBMs.

Chapter 4

Complex alkali bismuth iodides $A_3Bi_2I_9$ for optoelectronic application

[1] Ternary bismuth halides form an interesting functional materials class in the context of the closely related Pb halide perovskite photovoltaics, especially given the significantly reduced toxicity of Bi when compared with Pb. The compounds $A_3Bi_2I_9$ (A = K, Rb, Cs) examined here crystallize in two different structure types: the layered defect-perovskite $K_3Bi_2I_9$ type, and the $Cs_3Cr_2Cl_9$ type. The latter structure type features isolated $Bi_2I_9^{3-}$ anions. Here the crystal structures of the ternary iodides are redetermined and a corrected structural model for $Rb_3Bi_2I_9$, as established by single crystal X-ray diffraction and solid state ^{87}Rb nuclear magnetic resonance (NMR) spectroscopy and supported by Density Functional Theory (DFT) calculations is presented. A variety of facile preparation techniques for single crystals, bulk materials, as well as solution-processed thin films are described. The optical properties and electronic structures

[1] The contents of this chapter have substantially appeared in reference [16]: A. Lehner, D. Fabini, H. Evans, C.-A. Hébert, S. Smock, J. Hu, H. Wang, J. Zwanziger, M. Chabinyc, and R. Seshadri, Crystal and electronic structures of complex bismuth iodides $A_3Bi_2I_9$ (A = K, Rb, Cs) related to perovskite: Aiding the rational design of photovoltaics, *Chem. Mater.* **2015**, *27*, 7137–7148, © 2015 American Chemical Society, reprinted with permission.

are investigated experimentally, by optical absorption and ultraviolet photoemission spectroscopy, and computationally by DFT calculations. Absolute band positions of the valence and conduction bands of these semiconductors — with excellent agreement of experimental and calculated values — are reported, constituting a useful input for the rational interface design of efficient electronic and optoelectronic devices. The different structural connectivity in the two different structure types, somewhat surprisingly, appears to not impact band positions or band gaps in a significant manner. Computed dielectric properties, including the finding of anomalously large Born effective charge tensors on Bi^{3+}, suggest proximal structural instabilities arising from the Bi^{3+} $6s^2$ lone pair. These anomalous Born effective charges are promising for defect screening and effective charge carrier transport. The structural, electronic, and optical properties of the complex bismuth iodides are to some extent similar to the related lead iodide perovskites. The deeper valence band positions in the complex bismuth iodides points to the need for different choices of hole transport materials for Bi-iodide based solar cell architectures.

4.1 Introduction

Heavy metal halide semiconductors have been intensely investigated over the last decades, due to their rich structural chemistry and interesting optical and electronic properties. Recently, photovoltaic applications of tetrel halides such as Ge, [17] Sn, [14, 105] and most prominently Pb halide perovskites [106, 81] have attracted tremendous interest. In comparison, the optoelectronic properties of bismuth halides have been the focus of many fewer studies. The simple iodide BiI_3 has been investigated for applications such as hard radiation detection, [73, 74, 75, 76] X-ray imaging, [77, 78, 79] and for solar cells as hole transport material. [80] Recently, some of us

have demostrated that BiI_3 can be used as the active layer in photovoltaic devices. [15] Hybrid organic-inorganic bismuth halides have been studied regarding their rich structural variety [107, 108] and in some cases optical properties. [109, 110, 111] Despite their much simpler composition, the optoelectronic properties of the ternary inorganic bismuth halides, with their most common family being the enneahalogenidometallate phases $A_3Bi_2X_9$ (A = K, Rb, Cs, or Tl; X = halide), have not been explored as extensively. Here we focus on the heavy alkali metal bismuth iodides $A_3Bi_2I_9$ for which the crystal structures have been reported: A = K, [112] Rb, [113] and Cs [114]. While the phase transitions in the Cs compound have been well-studied, [115, 116, 117, 118] only one report each for the K and Rb salt are to be found.

It is typical for the extensive family of $A_3M_2X_9$ structures that A and X atoms are closest packing and the M atoms occupy $2/3$ of the octahedral X_6 voids. [119, 120, 116] Two main structure types of $A_3M_2X_9$ can be distinguished, the ones with hexagonal close packing and the ones with cubic close packing of A and X. For the bismuth iodides of the former group, isolated $Bi_2I_9^{3-}$ ions result as pairs of face-sharing Bi-I octahedra (*e.g.* $Cs_3Cr_2Cl_9$ type $Cs_3Bi_2I_9$) and for the latter, defect-perovskites, corrugated layers of Bi-I octahedra are present (*e.g.* $K_3Bi_2I_9$). As the 6s lone-pair-bearing Bi^{3+} is isoelectronic to the tetrel dications and soft or polarizable just as Pb^{2+}, the bismuth halide crystal chemistry is similar to the lead halide perovskites: rich structual diversity is observed, including distortion, vacancies, and various modes of aggregation of the MX_6 octahedra. [107] However, Bi^{3+} exhibits a stronger tendency to form structures of lower dimensionality of the metal halide units than Pb^{2+}. Recently, the closely related caesium antimony iodide $Cs_3Sb_2I_9$ has been investigated as solar cell absorber layer and the electronic structure of its polymorphs has been calculated by density functional theory (DFT). [121] In contrast, the investigation of the properties of inorganic bismuth halides has been limited to some work reporting optoelectronic properties

[122, 123, 113, 124, 125] and so far as we can discern, apart from a few calculated parameters for $Cs_3Bi_2I_9$, [126] there are no computational studies of the electronic band structures available. Clearly complex bismuth halides are an interesting family of potentially solution-processable compounds, whose potential as an alternative to toxic lead halides is far from fully explored.

Here we present a combined, systematic experimental and computational study of some complex bismuth iodides, in an attempt to correlate crystal structure, electronic structure, and spectroscopic properties within this interesting materials class. Absolute band positions are derived using spectroscopic and DFT methods as a foundation for the rational design of device interfaces. From the DFT band structure calculations, we discuss band dispersion and bonding character, as well as dielectric response properties as indicators of charge carrier transport. We find the structural, electronic, and optical properties of the complex bismuth iodides to be somewhat similar to the related lead iodide perovskites. The deeper valence band positions in the complex bismuth iodides calls for different choices to be made for hole transport materials in Bi-iodide based solar cell architectures. In the two different structural types reported here, the distinct structural connectivity appears to not impact band positions or band gaps in a significant manner. However, band dispersions are significantly different for the two.

4.2 Methods

4.2.1 Materials preparation

All chemicals were purchased and used as supplied: BiI_3 (Strem 99.999%), HI 57% aqueous solution (Sigma-Aldrich 99.95%), KI (Sigma-Aldrich 99.998%), RbI (Strem 99.8%), and CsI (Strem 99.999%). The following solvents were used in their anhy-

drous forms: ethanol (Sigma-Aldrich 99.995%), acetonitrile (Sigma-Aldrich 99.8%), diethyl ether (Sigma-Aldrich, 99.0%), and N,N-dimethylformamide (Sigma-Aldrich 99.8%). Red $K_3Bi_2I_9$ crystals of relatively poor quality for single crystal X-ray diffraction were obtained by heating a stoichiometric mixture of the binary iodides in an evacuated sealed fused silica ampoule, following a previously reported protocol. [113] High quality crystals of $Rb_3Bi_2I_9$ and $Cs_3Bi_2I_9$ were obtained through solvothermal reactions. In a typical preparation, the stoichiometric mixture (300 mg) of the iodides BiI_3 and RbI, or CsI, respectively, were suspended in Ethanol (6 cm^3) and heated to 120°C in a pressure vessel (Parr autoclave with 23 cm^3 Teflon liner) for 6 h followed by a slow (5°C/h) cooling to room temperature. Red prisms (A = Rb) or red hexagonal platelets (A = Cs) were isolated by filtration. All materials can be kept in dry air for many days (A = K) to months (A = Cs), before significant crystal degradation and decomposition into the crystalline starting iodides occurs.

Bulk powders of the ternary iodides were prepared by stirring the binary iodides in the stoichiometric ratio in CH_3CN (2 cm^3 for 200 mg of product) for 5 h at room temperature. For the K and Rb salts, the resulting red solution was concentrated under vacuum until little solvent was left over the forming precipitation which was then filtered off. The Cs analogue was filtrated directly from the stock solution. The salts were washed with diethyl ether and their phase purity was confirmed by powder X-ray diffraction. As an alternative new route to the pure $A_3Bi_2I_9$ salts, high-energy ball-milling of AI and Bi_3 in a 3:2 ratio (10 min for 200 mg) using tungsten carbide vials and balls in a Spex SamplePrep 8000D Dual mixer/mill was successfully applied.

4.2.2 Characterization methods

X-ray diffraction data on powder samples (PXRD) was recorded for the K and Cs salts over the 2θ scattering angle range of 6° to 70° using Cu-Kα radiation (Philips X'Pert MPD diffractometer). For the Rb salt (sample diluted with 40w% cubic BN, Alpha Aesar), PXRD data using high-resolution synchrotron radiation was recorded on beamline 11-BM at the Advanced Photon Source, Argonne National Laboratory at 295 K with an average wavelength of $\lambda = 0.458996$ Å. For $K_3Bi_2I_9$ and $Cs_3Bi_2I_9$ samples, the agreement with published crystal structure models (A = K [113], Cs [114]) was confirmed by Rietveld refinements using TOPAS-Academic V5. [127]. X-ray diffraction on single crystals was performed using a Bruker Kappa APEX II diffractometer with a sealed tube Mo-Kα X-ray source. Single crystal samples were mounted onto Nylon loops and fixed with two component epoxy glue. For $Rb_3Bi_2I_9$ a full data set was collected at room temperature by sampling a fraction of the Ewald sphere with 0.5° ω steps, while only lattice parameters were determined for the K and Cs salts. The cell refinement, data reduction, correction, and integration were peformed using Bruker's SAINT/SADABS software [128, 129] The structure was solved with Direct methods using SHELXS-97 and the refinement was done using SHELXL-2014. [130, 131] We used the program VESTA [132] for the graphical representation of the crystal structures and the thermal ellipsoids where plotted using ORTEP-III [133]. For additional crystal structure data see Supporting Information; further details of the crystal structure investigation may be obtained from FIZ Karlsruhe, 76344 Eggenstein-Leopoldshafen, Germany (fax: (+49)7247-808-666; e-mail: crysdata(at)fiz-karlsruhe(dot)de), on quoting the deposition number CSD-430179. Experimental densities were determined for cold-pressed pellets on a MicroMeritics AccuPyc 1340 pycnometer by performing sensitive volume (by He gas displacement) and mass measurements.

A ^{87}Rb solid state magic angle spinning nuclear magnetic resonance (MAS NMR) single pulse experiment was performed for polycrystalline $Rb_3Bi_2I_9$ on a Bruker AVANCE III 800 MHz (18.8 T) standard bore spectrometer operating at 261.81 MHz with a 2.5 mm zirconia rotor system at a spinning frequency of 30.0 kHz. In order to enhance the signature of the quadrupolar interactions in the spectra, ^{87}Rb triple-quantum magic angle spinning (3QMAS NMR) experiments were performed on a Bruker Avance III HD 400 MHz (9.4 T) WB solid-state NMR spectrometer operating at 130.92 MHz with a 4.0 mm double resonance MAS probe head spinning at 12.5 kHz. Chemical shifts were referenced to a 1 molar aqueous $Rb(NO_3)$ solution using solid RbCl at 127 ppm [134] as a secondary reference. The single pulse experiment was performed with a $\pi/12$ excitation pulse of 0.62 μs using a 3 s relaxation delay, which was optimized for quantitative analysis, a 2.05 ms acquisition time, and an accumulation of 448 scans. The 3QMAS experiment was carried out using a three-pulse MQMAS sequence with a z-filter and the following parameters: an excitation pulse of 4.2 μs, a conversion pulse of 1.4 μs and a weak central transition selective 90° pulse of 20 μs. A States-TPPI phase sensitive detection in the F1 dimension was employed. The quadrupolar central transitions of the ^{87}Rb NMR spectra were simulated and analyzed with the Line Shapes module within the Topspin 3.2 software of Bruker BioSpin.

Scanning electron microscopy (SEM) images of thin film samples sputtered with gold/palladium to limit charging were collected using a FEI XL40 Sirion FEG digital scanning microscope in backscattered electron imaging mode. Optical spectra in the UV-Vis range from 220 to 800 nm were recorded using a Shimadzu UV3600 spectrometer in diffuse reflection on powder samples which were spread thinly onto compacted $BaSO_4$ powder. Diffuse reflection data were converted using the Kubelka-Munk transformation implemented in the spectrometer's software. Band gaps were extracted from Tauc plots [135, 136] of the Kubelka-Munk transformed reflection data assuming al-

lowed direct or indirect lowest energy transitions depending on the results from our DFT calculations. A Kratos Axis Ultra XPS/UPS instrument was used for X-ray and Ultraviolet Photoelectron Spectroscopy (XPS and UPS). Samples were prepared by drop-casting and spincoating from dimethylformamide or acetonitrile solution as thin films on 10×10 mm pieces of silicon wafers onto which 20 nm of chromium and 90 nm of gold had been deposited by thermal evaporation under high vacuum (10^{-7} torr). Material was removed from one edge of each sample via swabbing with chlorobenzene to expose the gold layer. Nickel tape was used to electrically connect the exposed gold on the top of the substrates to the airtight sample holder which was loaded in a glove box (N_2, $\leq$1 ppm O_2). For XPS, a monochromated Al-Kα source (180 W) was used under ultrahigh-vacuum conditions (10^{-8} torr). Survey scans were collected with a step size of 500 meV, a pass energy of 160 eV, and a dwell time of 150 ms. For UPS, a helium I radiation source was used with a gate bias voltage of -9 V. Photoelectrons at the 0° takeoff angle were collected at 600 W (6 kV, 10 mA) with a pass energy of 5 eV and a step size of 25 meV. Survey scans were collected once with a dwell time of 150 ms. Detailed scans near the valence band maximum (VBM) were collected with a dwell time of 600 ms and were repeated 3 times. The position of the VBM was determined from UPS spectra as the energy increment between the left and right edges of the spectral feature, subtracted from the incident photon energy (21.22 eV).

4.2.3 Computational methods

The DFT computational study of the electronic band structures, including absolute band positions, was carried out using the Vienna *ab initio* Simulation Package (VASP) [137, 138, 139, 95]. VASP implements density functional theory in the Kohn-Sham formulation, using a plane wave basis and the projector-augmented wave formalism

(PAW). [140, 96] Input structures were taken from the literature for $K_3Bi_2I_9$ [113] and $Cs_3Bi_2I_9$, [114] and from this work for $Rb_3Bi_2I_9$. For a better comparability of the band structures, the monoclinic phases were transformed to the space group setting $P2_1/c$ and the corresponding high-symmetry points were selected for the corresponding conventional Brillouin zone [141]. All ternary compounds were optimized using the Perdew-Burke-Ernzerhof (PBE) exchange and correlation functional [142] until the residual forces were less than 0.01 eV/Å on each atomic site. The resulting crystal structures exhibited 8 to 10% increased volumes compared to the experimental input structures, which lies withing the acceptable range of errors of the applied method. The energy cut-off of the plane wave basis set was 500 eV. A Gamma centered k-mesh grid with a minimum of 20 k-points was employed with the convergence criteria set at 0.01 meV. The band structures were calculated using PBE including spin-orbit coupling (SOC) in order to locate the band gap, but for more accurate band gap values and density of states (DOS), a screened hybrid functional (HSE06) [94, 143] with SOC was employed.

Absolute band positions for the ternary compounds were obtained by aligning the s-like states of Bi in $A_3Bi_2I_9$ from HSE+SOC DOS calculations to the corresponding levels of BiI_3 as derived by a slab calculation [92] of a $1\times1\times4$ half-filled supercell (PBE+SOC, see our previous work [93] for computational details). Born effective charge tensors (Z^*_{ij}) on Bi^{3+} and high-frequency (ion-clamped) dielectric constants (ϵ^{∞}_{ij}) were calculated as reported previously. [93] Calculations of those dielectric response parameters for the related binary iodides PbI_2 [93] using different computational schemes revealed that PBE+SOC is sufficient to reproduce values very close to the more accurate but computationally much more demanding HSE06+SOC. In the present work however, PBE without SOC was applied for the monoclinic systems to reduce computation time. Computations of the NMR observables for two structure models of $Rb_3Bi_2I_9$, this work's

model in $P2_1/n$ and the Pc model reported by Sidey *et al.* [112], were performed with the plane wave and PAW-based QUANTUM ESPRESSO package [144] together with the QE-GIPAW extension. QE-GIPAW computes the magnetic shielding at each nucleus using the gauge-including projector augmented wave formalism, [145, 146] and the electric field gradient at each nuclear site using standard PAW expressions. [147] PAW atomic datasets for Rb, Bi, and I were used based on the set recently published by Jollet, Holzwarth, and Torrent, and generated with the ATOMPAW code to create files suitable for QUANTUM ESPRESSO. [148, 149] Cut-off radii of 2.30, 2.90, and 2.30 Bohr were used for Rb, Bi, and I respectively; these are short enough that no PAW sphere overlap occurred. The PBE exchange and correlation functionals were used in all cases and the structures were computed with the experimental atomic positions and no subsequent optimization. Complete convergence required a planewave cut-off energy of 80 Ry (1088 eV) and a reciprocal point grid spacing of 0.02 $Å^{-1}$; however, as these values led to prohibitively large calculations for chemical shielding on the $Rb_3Bi_2I_9$ system, the values reported here were computed with a cut-off energy of 20 Ry (272 eV) and reciprocal point spacing of 0.04 $Å^{-1}$. To check that these more modest values were sufficient, we computed the chemical shieldings for the rubidium alkali salts at both the fully converged levels and at the more modest levels used here, and found that the shift orderings were still correctly represented and that the systematic error of the PBE functional for chemical shielding calculations was essentially unchanged. This result means that our computation of observables for $Rb_3Bi_2I_9$, even at modest convergence criteria, is useful for establishing experimental peak assignments and for differentiating between different potential crystal structure models.

4.3 Results & discussion

4.3.1 Materials preparation and structure

In this work we have established a variety of new facile preparation routes for the ternary bismuth iodides $A_3Bi_2I_9$ (A = K, Rb, Cs). By reacting the corresponding binary iodides in stoichiometric ratio in organic solvents at room temperature or simply ball-milling them, high purity materials were obtained. Previously, methods for growing single crystals, typically at high temperatures from the melts, have been reported. [115, 112, 113] We have found that single crystals of up to 1 mm can also be obtained at very mild solvothermal conditions in ethanol at 120°C for A = Rb, Cs. As the solubility of the ternary bismuth iodides decreases rapidly with increasing counter cation size, the Cs salt could be isolated directly by filtration of a acetronitrile solution of the starting iodides. For the isolation of powders of the K and Rb salts, the solution was concentrated under vacuum prior to filtration. Thin films were deposited from organic solvents by drop-casting or spin-coating. In future work, the procedures must be carefully optimized to improve microstructure, grain orientation and film quality, but generally the solution-processibility makes this family of heavy metal halides very appealing for technological applications. In this work, the crystal structures were determined for powder and single crystal samples and optoelectronic properties were examined for powders (UV-Vis) and thin films (XPS, UPS), respectively.

The stability in ambient atmosphere has been monitored by PXRD on as-prepared polycrystalline powder samples. With increasing size of the counter cation, the salts kept well for hours (K) to months (Cs) in ambient air, which is considerably longer than the extremely oxidation sensitive Sn^{2+} iodides or the moisture sensitive Pb^{2+} iodides would withstand. Exploring the effects of other factors on the stability, such as different

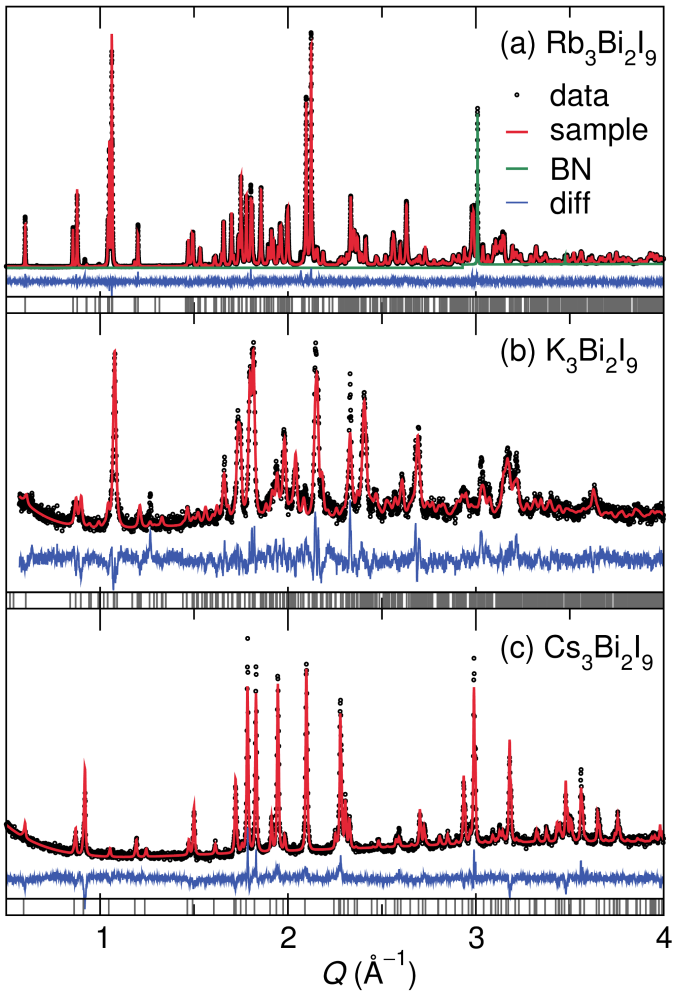

Figure 4.1: Powder X-ray diffraction and Rietveld refinements of $A_3Bi_2I_9$, A = (a) Rb (synchrotron data), (b) K, and (c) Cs (laboratory data). Figure prepared by Anna J. Lehner.

grain sizes and thus surface areas as a result of different preparation processes, will be an important future task. Our preliminary studies have confirmed that phase widths of mixed counter cations K-Rb, Rb-Cs, K-Cs exist in the $A_3Bi_2I_9$ phases. Taking into account not only the counter cation but also the variability of the central metal and halide, which has been previously explored only in some extent [150], this rich family of compounds offers a large variety of new interesting phases with tunable properties.

The crystal structures of the three ternary bismuth iodides $A_3Bi_2I_9$ (A = K, Rb, Cs)

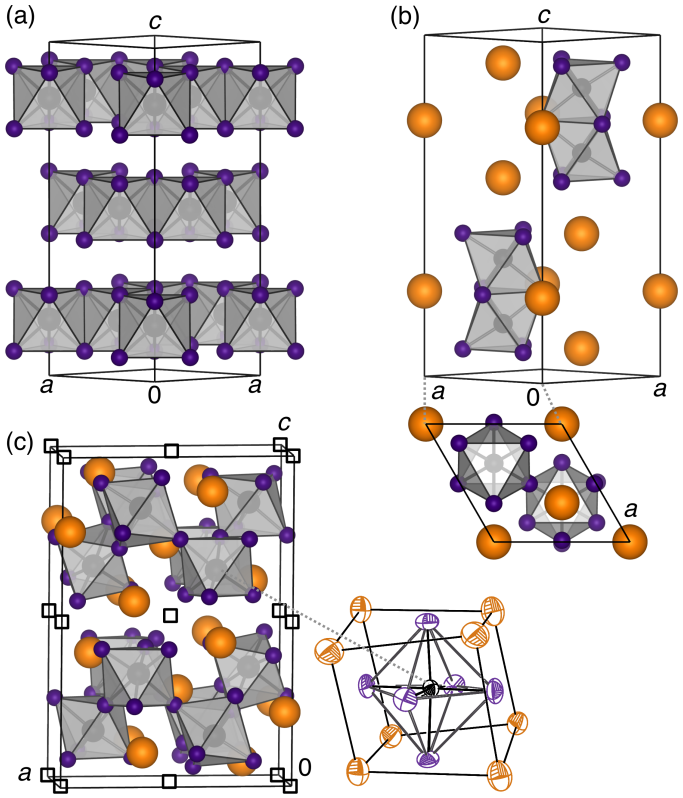

Figure 4.2: Crystal structures of (a) BiI_3 ($R\bar{3}$) [82], (b) $Cs_3Bi_2I_9$ ($P6_3/mmc$), [114] and (c) $Rb_3Bi_2I_9$ ($P2_1/n$) with empty squares marking the unoccupied metal positions of the perovskite aristotype. Small spheres represent I^-, large spheres are counter cations A^+, and spheres inside polyhedra are Bi^{3+}. The close relationship to the perovskite structure is obvious from the coordination environment of the BiI_6 octahedra (Ortep plot with ellipsoids at 80%). Figure prepared by Anna J. Lehner.

Table 4.1: Crystallographic parameters of $Rb_3Bi_2I_9$ with experimental densities derived from gas displacement pycnometry included for comparison.

Formula	$Rb_3Bi_2I_9$
Sample	single crystal
Structure type	$K_3Bi_2I_9$ [113]
Crystal system	monoclinic
Space group	$P2_1/n$
Unit cell (Å,°)	
A	14.6443(19)
b	8.1787(9)
c	20.885(2)
β	90.421(7)
V (Å^3)	2501.4(5)
Z	4
Density (X-ray) (g/cm^3)	4.82
Density (Pycnom.) (g/cm^3)	4.82(2)
X-ray λ (Å)	0.71073
Diffractometer	Bruker Apex II
T (K)	299(2)
Absorption coefficient	30.9
2Θ range (°)	3.4 to 56.8
No. measured reflections	18931
No. unique reflections	6269
R_{int}	0.0464
No. free parameters	127
Goodness of fit F^2	1.018
*R*1, *wR*2 ($I \geq 2\sigma(I)$)	0.0409 0.0879
*R*1, *wR*2 (all reflections)	0.0791, 0.1001
Residual e$^-$ density (e$^-$Å^3)	1.62 /−1.93

Table 4.2: Wyckoff positions, coordinates, and equivalent isotropic displacement parameters U_{eq} (Å^2) in the crystal structure of $Rb_3Bi_2I_9$ ($P2_1/n$).

Atom	Wyckoff site	x	y	z	U_{eq}
Rb(1)	4*e*	0.03098(9)	0.97581(2)	0.22393(8)	0.0622(4)
Rb(2)	4*e*	0.18643(1)	0.52117(2)	0.06266(8)	0.0721(4)
Rb(3)	4*e*	0.35098(1)	0.97172(1)	0.89373(8)	0.0692(4)
Bi(1)	4*e*	0.16689(2)	0.49351(4)	0.84409(2)	0.0276(1)
Bi(2)	4*e*	0.33675(2)	0.01025(4)	0.15456(2)	0.0278(1)
I(1)	4*e*	0.00492(5)	0.58289(1)	0.74634(5)	0.0602(3)
I(2)	4*e*	0.07209(5)	0.80753(9)	0.38965(4)	0.0458(2)
I(3)	4*e*	0.12109(5)	0.79317(9)	0.91443(4)	0.0457(2)
I(4)	4*e*	0.16975(5)	0.06654(1)	0.07954(5)	0.0541(2)
I(5)	4*e*	0.24235(5)	0.69155(9)	0.21872(4)	0.0433(2)
I(6)	4*e*	0.32991(5)	0.42761(1)	0.92177(4)	0.0524(2)
I(7)	4*e*	0.41596(6)	0.80249(9)	0.05562(4)	0.0465(2)
I(8)	4*e*	0.79932(5)	0.82268(9)	0.24451(4)	0.0451(2)
I(9)	4*e*	0.95328(5)	0.70836(9)	0.07647(4)	0.0448(2)

were examined by X-ray diffraction. Unit cell dimensions were derived from single crystal measurements and the phase purity was confirmed by Rietveld refinements of powder diffraction data (see Figure 4.1, Table 4.1, 4.2, and Supporting Information). For all three phases, the densities calculated from the structural data correspond nicely to the experimental densities which were determined by He gas displacement measurements (Supporting Information). For $K_3Bi_2I_9$ [113] and $Cs_3Bi_2I_9$ [114], an excellent agreement with previous crystal structure reports was obtained, while the redetermination of the structure of $Rb_3Bi_2I_9$ led to a new structure model with the space group $P2_1/n$ instead of the previously reported model in space group Pc [112]. From X-ray diffraction of $Rb_3Bi_2I_9$ single crystals, this space group could be clearly derived from the unit cell metrics (a = 14.6443(19), b = 8.1787(9), c = 20.885(2) Å, β = 90.421(7)°), the symmetry (Laue class 2/m) and the systematic zonal and serial extinction conditions ($h0l$ reflections only present for $h+l = 2n$, $h00$ reflections only present for $h =$

2*n*). The solution of the crystal structure using direct methods led to the expected composition with four formula units per unit cell and all atoms occupying general positions (Wyckoff sites 4*e*). Using anisotropic thermal displacement parameters, the structure model was refined to a good fit and reliable *R*1 value in few iterations. The final values of the positional and displacement parameters are listed in Table 4.2. Additional structural data as well as information about the transformation between the group subgroup pair $P2_1/c$ ($P2_1/n$) and Pc are included in the Supporting Information. It is likely that Sidey *et al.* [112] reported the $Rb_3Bi_2I_9$ crystal structure in the acentric space group *Pc* as a consequence of the crystal twinning in the crystal studied. The atomic positions and unit cell derived in this work are very similar to this previously published structure. In the following, the crystal structure of $Rb_3Bi_2I_9$ will be discussed in detail, while the structures of the isotypic $K_3Bi_2I_9$ [113], of $Cs_3Bi_2I_9$ crystallizing with the $Cs_3Cr_2Cl_9$ structure type [151], and the binary BiI_3 will be only touched on for comparison. The crystal structures discussed here are shown in Figure 4.2. Rhombohedral BiI_3 (Figure 4.2a) contains distorted BiI_6 octahedra, which are connected in honeycomb layers via three shared edges each. The anionic species in $Cs_3Bi_2I_9$ are isolated pairs of face-sharing BiI_6 ocahedra (Figure 4.2b). $Rb_3Bi_2I_9$ (Figure 4.2c) contains corrugated layers of corner-connected BiI_6 octahedra, the complex 2D anion ${}^2_\infty\{[BiI^t_3I^e_{3/2}]^{-1.5}\}$ written in Niggli nomenclature. The crystal structure can be described as distorted defect variant of the perovskite type (*AMX*$_3$), in which only two thirds of the octahedral M sites are occupied: $Rb(Bi_{2/3}\square_{1/3})I_3$. Every third M layer of the perovskite aristotype in [001] is depleted (Wyckoff sites 2a and 2b in the monoclinic unit cell). The ordered cubic close packing of Rb and I occurs in such a way that all BiI_6 octahedra are coordinated by eight Rb atoms in the arrangement of a distorted cube; the unit cell of the perovskite type. Wosylus *e*t al. have derived the symmetric group-subgroup relationships between the cubic perovskite and $Tl_3Bi_2I_9$ which is isotypic to our new model of $Rb_3Bi_2I_9$. [152]

The BiI_6 octahedra of the two crystallographic Bi sites are distorted with three shorter (2.93±1 Å) and three longer (3.20 to 3.25 Å) Bi-I distances, as it is observed for the K and Cs salts as well as for other complex bismuth iodides. [107] For all structure types the shorter Bi-I bonds involve terminal I sites while the longer bonds exist between Bi and μ_2 (or μ_3 for $Cs_3Bi_2I_9$) I atoms connecting multiple Bi sites. As this distortion is observed in all related structures, no matter if they contain lone-pair-bearing central metals or not (e.g. $Cs_3Y_2I_9$ [153]), we tentatively conclude that the structural distortion is not caused by a stereochemically active 6s lone pair on Bi^{3+}. For $Rb_3Bi_2I_9$, the Bi-Bi distances between corner-sharing BiI_6 octahedra are about 6.2 Å. For comparison, the bond lengths are about 4.0 Å in the Bi_2I_9 anions (face-sharing BiI_6) of $Cs_3Bi_2I_9$ and are about 4.4 Å in the layers of BiI_3 (edge-sharing BiI_6). The effect of the BiI_6 bonding mode in the different crystal structures on the optoelectronic properties and electronic structures will be discussed in the following sections. The iodide sites in $Rb_3Bi_2I_9$ are coordinated by a total of three to five metal sites, counting both Bi and Rb, while the bridging I sites (I1, I5, and I8) display the larger coordination numbers (CN). Due to the relatively small size of the Shannon ionic radius of Rb^+ (CN 6, 1.5 Å [154]) compared to I^- (CN 6, 2.2 Å [154]), the close packing between those ions is irregular, leading to the distorted and tilted BiI_6 octahedra. As a result, the coordination of the Rb cations by I anions is reduced from the cuboctahedral coordination (CN 12) of the perovskite aristotype *A* sites to CN 8 with Rb-I distances of up to 4.1 Å. The resulting tilting of BiI_6 octahedra is obvious in the decrease of the *M*-I-*M* bond angles from the ideal 180° angle in cubic perovskite aristotype to 147 to 153° in $Rb_3Bi_2I_9$ and even smaller angles for $K_3Bi_2I_9$, where the size mismatch of large I^- and small A^+ ions is more pronounced.

The RbI_8 coordination polyhedra can be described as heavily distorted bicapped trigonal prisms with similar volumes of about 94 $Å^3$ for all the three Rb sites (Figure 4.3). In the context of the complete structure, Rb1 sits inside the corrugated lay-

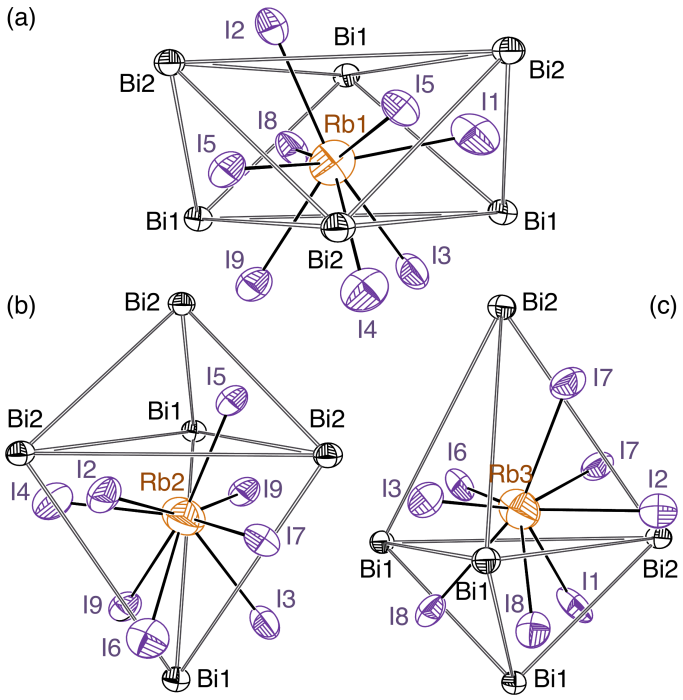

Figure 4.3: ORTEP plots (ellipsoids at 80% probability level) of the coordination environment of the three Rb sites (a) Rb1, (b) Rb2, (c) Rb3 in $Rb_3Bi_2I_9$ (all on Wyckoff positions 4*e*). Figure prepared by Anna J. Lehner.

Table 4.3: Absolute quadrupolar coupling parameters C_q, asymmetry parameters of the quadrupolar interaction η, absolute shielding σ, and isotropic chemical shift δ_{iso} (using RbCl as a reference at 127 ppm [134]) from DFT calculations and NMR experiments for $Rb_3Bi_2I_9$.

Structure	Site	C_q (MHz)		η		σ (ppm)	δ_{iso} (ppm)	
		calc.	exp.	calc.	exp.		calc.	exp.
$P2_1/n$	Rb1	2.6	2.1	0.91	1.0	1992	41	61
	Rb2	3.9	3.0	0.90	1.0	2016	17	41
	Rb3	3.4	2.8	0.70	0.5	2022	11	44
Pc	Rb1	4.3		0.83		2030	3	
	Rb2	4.3		0.95		1966	67	
	Rb3	3.9		0.43		2051	−18	
	Rb4	3.1		0.55		1962	71	
	Rb5	9.0		0.91		1973	60	
	Rb6	3.9		0.35		1988	45	

ers of BiI_6 octahedra, while Rb2 and Rb3 exhibit local environments similar to each other at the edges of those layers. Thereby, the volume of the trigonal antiprism of Bi sites surrounding Rb1 ($CN_{eff}(Rb1Bi_6)$ = 4.6) is about 50% larger than the volume of the trigonal bipyramids of Bi sites coordinating the Rb2 ($CN_{eff}(Rb2Bi_6)$ = 3.3) and Rb3 ($CN_{eff}(Rb3Bi_6)$ = 4.4) sites. Interestingly, the isotope ^{87}Rb is an NMR-active, quadrupolar (spin 3/2) nucleus with approximately 30% natural abundance, which can be probed to reveal the effects of the local structural environment. We examined the NMR signature of the Rb nuclei in $Rb_3Bi_2I_9$ by MAS NMR experiments in combination with DFT-simulation of the NMR observables in order to confirm our centrosymmetric structure model for $Rb_3Bi_2I_9$ as opposed to the previously reported non-centrosymmetric model.

The NMR spectrum of solid $Rb_3Bi_2I_9$ displays two main features which are broad and overlapping when recorded with a 400 MHz spectrometer (Figure 4.4). However, the 3QMAS experiment reveals clearly that there are three distinct sites which is in agreement with the three Rb sites of our crystallographic structure model. The traces

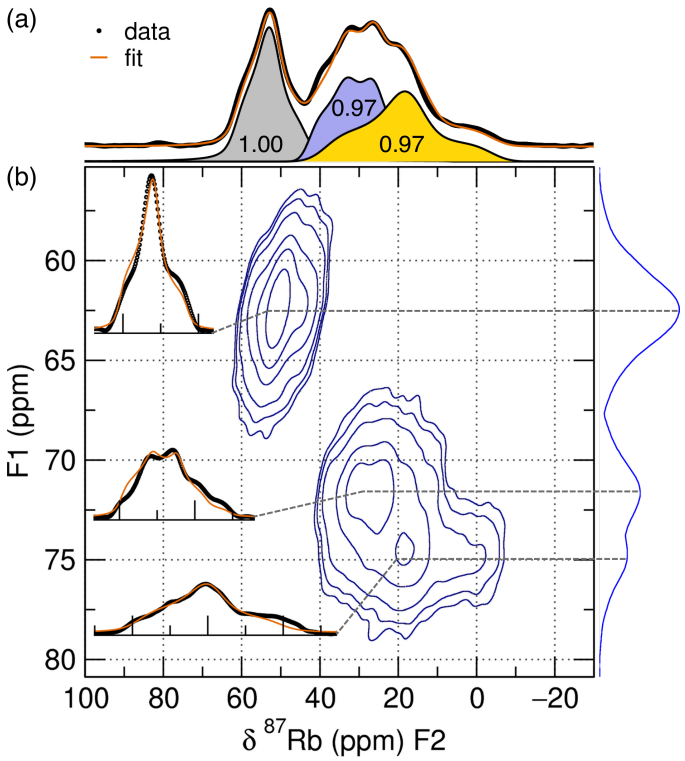

Figure 4.4: (a)^{87}Rb MQ-MAS NMR spectra of $Rb_3Bi_2I_9$ recorded at 130.92 MHz. The deconvolution of the 1D spectrum (b) into the three Rb sites (see Figure 4.3) with C_q, η, and δ_{iso} parameters derived from the fits of the individual traces (see Table 4.3) yields the expected integrated area ratio of 1:1:1 in good agreement. Figure prepared by Anna J. Lehner.

for each signal obtained from the 3QMAS measurement were fitted with a good agreement to extract NMR parameters which can be simulated by DFT-calculations: the isotropic chemical shift δ_{iso}, the absolute quadrupolar coupling parameter C_q, and the anisotropy parameter of the quadrupolar interaction η (Table 4.3). Using those parameters, the 1D spectrum could be deconvoluted with a decent fit into three signals (Figure 4.4a). As expected from the 1:1:1 crystallographic ratio, the integrated areas of those three signals are practically the same (site 1: 1.00, site 2: 0.97, site 3: 0.97). The DFT calculations of the NMR parameters (Table 4.3) allowed us to compare the NMR signature of our structure model in $P2_1/n$ directly to the non-centrosymmetric Pc structure published by Sidey *et al.* [112]. While the calculated chemical shifts for the $P2_1/n$ model are shifted systematically by approximately 25 to 30 ppm compared to the experimental values, the relative shifts differences between the sites are well reproduced. Including the expected shift from the second order quadrupole effect under Magic Spinning does not change this conclusion: using the computed values for C_q in addition to the total shielding again yields a predicted spectrum with two nearly overlapping sites shifted upfield from a third site about 35 ppm downfield. We can thus directly assign the most downfield signal to the Rb1 site (Figure 4.3a), based on the agreement of experimental and calculated isotropic chemical shift and quadrupolar parameters. As the C_q and η parameters can be calculated with much greater accuracy and reliability than the chemical shift, we use those to assign the signal observed at δ_{iso} = 41 ppm to the Rb2 site and the one at δ_{iso} = 44 ppm to the Rb3 site (Figure 4.3b,c). For the non-centrosymmetric structure model published in space group Pc, the six sites would give rise to six distinct ^{87}Rb signals spread over a spectral range of over 85 ppm (110 ppm after quadrupole effects are accounted for, see Table 4.3). This is obviously in stark contrast with our experimental results, which can most clearly be observed in the wide ppm-range section of the single pulse ^{87}Rb MAS NMR spectrum recorded at

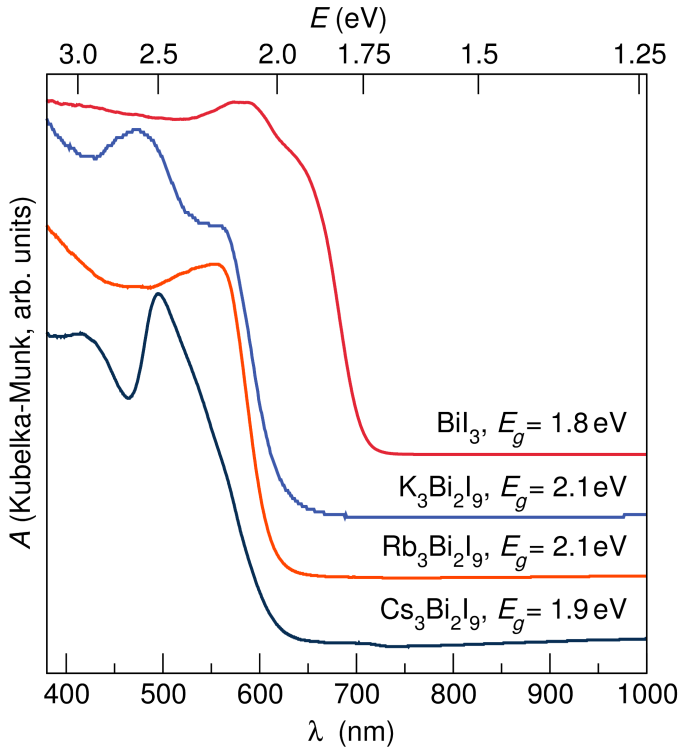

Figure 4.5: UV-Vis diffuse reflection spectra recorded on powder samples of $A_3Bi_2I_9$ and BiI_3 transformed into absorbance A. Band gaps were obtained using Tauc plots assuming direct gaps for A = K, Rb and indirect gaps for the remaining phases as predicted by DFT calculations (see Table 4.4). Figure prepared by Anna J. Lehner.

higher field (Supporting Information). Those results together with our crystallographic studies provide very strong evidence that the correct structure description of $Rb_3Bi_2I_9$ is our centrosymmetric one, which renders this salt strictly isotypic with $K_3Bi_2I_9$ [113] and $Tl_3Bi_2I_9$ [152] as has been hinted at previously [152].

4.3.2 Optical and electronic properties

The optical band gaps of $A_3Bi_2I_9$ (A = K, Rb, Cs) were derived from Tauc plots of Kubelka-Munk-transformed diffuse reflection UV-Vis data (Figure 4.5, Table 4.4). The absorption edge is located at approximately 2 eV for all three ternary bismuth iodides, while the binary exhibits a gap (E_g) of about 1.8 eV. In fact, the variation of the

$A_3Bi_2I_9$ band gaps determined with the given method only stems from the assumption of direct transitions for A = K, Rb, and an indirect transition for A = Cs as taken from the results of our DFT calculations. For the indirect gap $Cs_3Bi_2I_9$, a smaller band gap results from the Tauc method gap determination, while to the eye, the lighter alkali homologue salts appear a slightly darker red. Those E_g values are in excellent agreement with the values of 1.98 eV for A = Rb and 1.89 eV for A = Cs that were reported previously. [125] In the same study, the descending band gap magnitude of $A_3M_2I_9$ was correlated with ascending melting points and ascending average atomic numbers. Still, the counter cation, structure type, and thus connectivity mode and dimensionality of the BiI_6 octahedra have very little influence on E_g. The band gap of the layered polymorph of $Cs_3Sb_2I_9$ of around 2 eV [121] indicates that the variation of the central metal from Bi to Sb also does not have a strong impact on the magnitude of the gap. For the bismuthates, we observe that steepness of the edge, however, is greater for the layered structure types compared to the $Cs_3Bi_2I_9$ structure containing isolated anions. A steep edge is desirable, as for related lead halide perovskites a steep absorption edge has been correlated to little disorder-induced broadening and the absence of deep optically detectable states. [104]

The ionization energy IE, that is, the position of the valence band maximum (VBM) with respect to the vacuum energy, was determined for the $A_3Bi_2I_9$ phases by UPS measurements of thin film samples (see $K_3Bi_2I_9$ example in Figure 4.6 and Supporting Information for Rb and Cs salts). The sample surface composition was confirmed by XPS prior to recording the UPS spectra. We carried out between three and six UPS measurements of different thin film sample preparations for every compound to gauge the reproducibility and error of this method. The experimentally derived ionization energies are listed in Table 4.4. VBM determinations by UPS for these relatively wide gap semiconductors are not trivial: Insufficient film coverage leads to signals of the

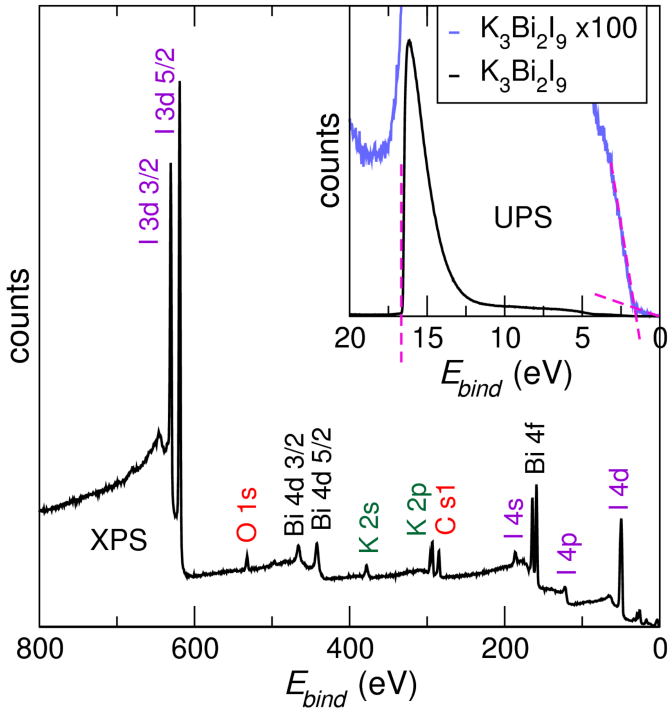

Figure 4.6: UPS (a) and XPS (b) spectra for $K_3Bi_2I_9$. From XPS data, the surface composition can be determined to $K_{2.84}Bi_2I_{8.95}$ which is in excellent agreement with the expected formula within the scope of the method. From UPS data, the position of the valence band maximum (VBM) was determined by subtracting the energy difference between both edges of the spectral feature from the excitation wavelength (He I lamp, 21.22 eV). Figure prepared by Anna J. Lehner.

Table 4.4: Experimental optical (from diffuse reflection UV-Vis) and calculated (DFT method HSE+SOC) band gaps E_g as well as experimental (from a range of UPS measurements) and calculated ionization energies of $A_3Bi_2I_9$ (A = K, Rb, Cs) and BiI_3.

Phase	E_g (eV)		IE (eV)	
	exp.	calc.	exp.	calc.
BiI_3	1.8	1.93	6.0 to 6.3	6.1
$K_3Bi_2I_9$	2.1	2.17	6.1 to 6.3	6.1
$Rb_3Bi_2I_9$	2.1	2.16	6.1 to 6.2	6.0
$Cs_3Bi_2I_9$	1.9	2.32	5.6 to 6.2	5.7

underlying Au layer being captured while measurements on too thick films suffer from charging, both potentially altering the outcomes. For samples with a range of non-detectable to small XPS signals of the underlying gold layer and no to slight charging observed during XPS measurements, the IE values for $A_3Bi_2I_9$ lie between 5.4 eV and 6.4 eV with variations of 0.2 eV to 0.8 eV for each compound.

4.3.3 Electronic structure calculations

In order to support our experimental work with a robust and relatively fast method of determining absolute band positions, we applied DFT calculations to estimate the band positions with respect to the vacuum level. For the binary BiI_3 as a computationally less demanding and closely related proxy, we conducted slab calculations [92] (PBE+SOC, computational details see our previous work [93]) using a half-filled $1\times1\times4$ super-cell to find the absolute VBM position. Details of these calculations have been reported elsewhere. [15] We then aligned deep s-like Bi states of the ternaries' DOS (HSE+SOC) to the corresponding BiI_3 states to obtain absolute VBM positions for all compounds (see Supporting Information).

The resulting calculated band positions are shown in Figure 4.7 for the ternaries $A_3Bi_2I_9$ (A = K, Rb, Cs) in comparison to BiI_3. Experimentally determined VBM positions and band gaps are represented as bars indicating a range of UPS measurements

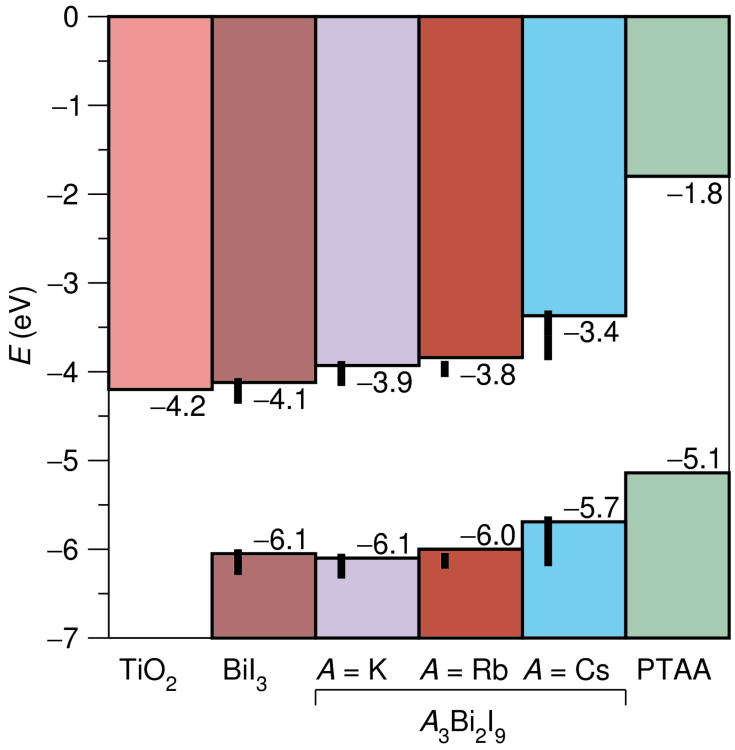

Figure 4.7: Band positions derived from DFT calculations (PBE+SOC), compared to experimental values (indicated by vertical bars as a range for the UPS experiments carried out here) for $A_3Bi_2I_9$ (A = K, Rb, Cs) and BiI_3. For added comparison, the experimental band positions of PTAA [101] and the calculated CBM of anatase TiO_2 [93] are also displayed. Figure prepared by Anna J. Lehner.

on different samples, the positions of the conduction band minima (CBM) were derived as CBM = VBM + E_g. In addition, the band positions of each of a commonly used electron and hole transport material for heavy metal halide photovoltaic devices, anatase TiO_2 and Poly-arylamide PTAA [102], are included. Here, taking into account the broad spectral absorption in the optical range, we suggest using the bismuth halides as solar cell absorber layer instead of as previously reported as hole transport layer. [80] The calculated E_g and VBM values are listed in Table 4.4. The agreement of the calculated values to the experimental data ranges is remarkable, suggesting that our relatively fast method of deriving absolute band positions from slab calculations only for a relatively simple reference compound and only needing advanced level (HSE+SOC) single unit cell DOS can be an excellent screening tool. The calculated band gaps for the ternary iodides increase from 2.2 eV to 2.3 eV with increasing counter cation size. This trend is not in agreement with the experimentally determined gaps in this and previous work [125] which might be due to the fact that the Cs salt unit cell volume is relatively more overestimated during the DFT structure optimization compared to the lighter alkali metal homologues. The VBM levels for the 2D layered K and Rb bismuth iodides around -6.0 eV are very similar to the layered BiI_3, and thus the nature and size of the counter cation (or even its absence) does not seem to have be relevant to the VBM position as long as the dimensionality of the Bi-I-units remains the same. In comparison, the 0D $Cs_3Bi_2I_9$ exhibits a shallower level. The same trend was reported for the series of hybrid lead iodides ranging from the 3D perovskite $CH_3NH_3PbI_3$ to layered derivatives of decreasing perovskite slab thickness. [155] For the layered antimony homologue $Cs_3Sb_2I_9$, the ionization potential was also reported to be 5.7 eV. [121] Potentially this is due to competing effects: increased anion dimensionality deepening the VBM and the lighter Sb central cation raising the VBM again to the same level as for $Cs_3Bi_2I_9$. For the heavier homologue, Bi, with its more contracted s-like states, we

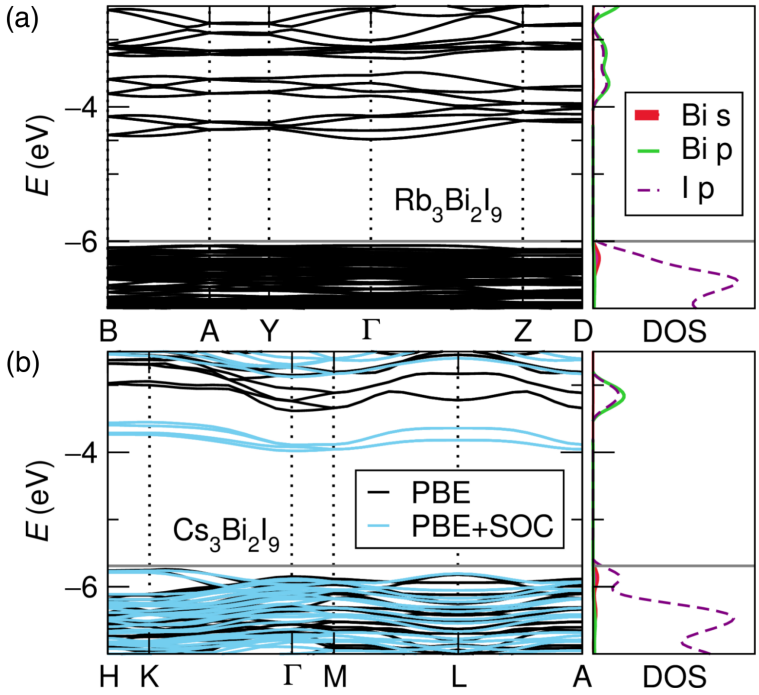

Figure 4.8: Band structure and partial density of states (DOS, HSE+SOC) of (a) $Rb_3Bi_2I_9$ ($P2_1/c$) and (b) $Cs_3Bi_2I_9$ ($P6_3/mmc$). The position of the valence band maximum (VBM, horizontal line) was offset based on slab calculations of BiI_3. The calculated band gaps (HSE+SOC) are direct at Γ for $A_3Bi_2I_9$ (A = K, Rb) and indirect between $0.75\overline{\Gamma K}$ in the valence band and Γ in the conduction band for $Cs_3Bi_2I_9$. Figure prepared by Anna J. Lehner.

expect less covalent interaction and thus less band dispersion in the region of the antibonding M(s)-I(p) interaction at the top of the valence band. However, the VBM levels of the complex bismuth iodides are considerably deeper than the related lead iodides (e.g. -5.4 eV for $CH_3NH_3PbI_3$ [100]). This creates a new challenges for the choice of hole transport layers for photovoltaic devices: the application of the commonly used polymers with VBMs not much below 5 eV would limit the open circuit voltage, and thus the power conversion efficiency.

For photovoltaic device construction, in addition to efficient solar light absorption and well-aligned transport band positions of the components, long charge carrier diffusion lengths are essential. In electronic band structures the curvature of the bands

is correlated with charge carrier effective mass and thus pronounced band dispersions can be indicative of high mobility. [156] Additionally, the band bonding character of heavy metal halides has been correlated with defect-tolerance. [126] As the band structures of the isotypic layered $K_3Bi_2I_9$ and $Rb_3Bi_2I_9$ phases are almost identical around the band gap, only the data for the Rb salt is included in Figure 4.8a for clarity. We will focus mainly on the comparison of the 2D vs 0D structure types for the examples of the Rb and Cs salt for the remainder of the discussion of computational results. For those layered salts, a direct band gap of 2.17 eV (K), or 2.16 eV (Rb) at Γ was obtained at HSE+SOC level of theory. The dispersion of the lowest conduction bands is moderate, while the top valence bands are very flat, indicating smaller effective masses for electrons compared to holes. For $Cs_3Bi_2I_9$ (Figure 4.8b), the valence band dispersion is larger while still relatively small compared to the related 3D halide perovskites [157]. From our HSE+SOC calculations, the band gap of $Cs_3Bi_2I_9$ (2.32 eV) is located between $0.75\overline{\Gamma K}$ in the valence band and Γ in the conduction band. From the comparison of the relatively flat band structures of the $A_3Bi_2I_9$ phases to highly dispersive ones of the 3D perovskites, [157, 93] one could conclude that the *M*-I-*M* bond angles rather than the connectivity mode have a strong influence on the band curvature and thus effective carrier masses and mobility: In the 3D perovskite structures, the near 180° *M*-I-*M* angles connecting the octahedra facilitate a better band overlap resulting in a better carrier transport through the metal halide lattice than in the defect-perovskites $A_3Bi_2I_9$ with Bi-I-Bi angles of around 150°. The $Cs_3Bi_2I_9$ and BiI_3 structures, with their shorter Bi-Bi distances due to face or edge-sharing octahedra, respectively, naturally exhibit even smaller Bi-I-Bi bond angles. The partial density of states plots show that the excitation across the gap occurs for all phases mainly from occupied I p states with a small contribution of Bi s states into empty Bi p + I p states.

In the homologous alkali antimony halides such as $Cs_3Sb_2I_9$ [121] and in the iso-

Table 4.5: Dielectric properties of $A_3Bi_2I_9$ salts including the high-frequency dielectric tensors (ϵ_{ij}^{∞}) and Born effective charge tensors (Z^*; $|e|$) on Bi^{3+}.

Phase	Method	ϵ_{xx}^{∞}	ϵ_{yy}^{∞}	ϵ_{zz}^{∞}	Z_{xx}^*	Z_{yy}^*	Z_{zz}^*
$Rb_3Bi_2I_9$	PBE	19.3	22.3	65.5	4.4	4.3	4.9
$Cs_3Bi_2I_9$	PBE	5.5		4.2	2.8	-	3.4
$Cs_3Bi_2I_9$	PBE+SOC	7.6		5.7	3.9	-	3.9

electronic tetrel halide perovskites [93, 158, 159, 160] the optical transition involves the same corresponding states and these materials' unique optoelectronic properties have been attributed in part to the effect of the ns^2 metal ions. For $CH_3NH_3PbI_3$, the strong p-character of the valence and the conduction band around the gap have been reported to lead to a high joint density of states, resulting in an unusually large optical absorption coefficient. [159] The combination of a direct band gap and p-p optical transitions in the 2D layered $A_3Bi_2I_9$ phases makes them very promising for next generation optoelectronics.

As discussed above, there are no obvious signs of stereochemical activity of the Bi^{3+} 6s lone pair in the studied $A_3Bi_2I_9$ structures. However, those phases are prone to undergo structural phase transitions as reported for $Cs_3Bi_2I_9$ [116, 117, 118], which could be potentially lone-pair-driven. Calculated Born effective charge tensors on the lone-pair-bearing atom and the dielectric constants have been used previously used to probe the lone-pair activity and proximal structural instabilities in heavy metal phases. [91, 99, 98, 161, 90, 158, 93] Interestingly, anomalously large Born tensors have also been suggested to indicate effective screening of defects and impurities which would otherwise be strong charge carrier traps, contributing to good carrier transport properties in heavy metal halides. [99, 158] The calculated Born tensors Z^* and high-frequency (ion-clamped) dielectric tensors ϵ_{ij}^{∞} for the 0D and 2D examples of $A_3Bi_2I_9$ are listed in Table 4.5. Comparing the two computational schemes (PBE vs. PBE+SOC)

used for $Cs_3Bi_2I_9$, it can be observed that including SOC increases the magnitude of ϵ_{ij}^{∞} as well as Z^* by ≈15%-40% due to reorganization of the band structure. However, it is clear that elevated Z^* values can be identified without applying the much more time-consuming SOC calculations. While for $Cs_3Bi_2I_9$, the Born charges are not significantly higher than the nominal charge, the layered defect-perovskite phase $Rb_3Bi_2I_9$ exhibits Z^* values of 4.3 to 4.9 on Bi^{3+}. Correspondingly, for BiI_3, a large in-plane Born charge on Bi^{3+} has been calculated and it was suggested to be correlated with the substantial covalent interaction between Bi 6p and halogen p states. [91] From this one can conclude that the 2D phases might be more defect-tolerant than the 0D bismuth halide phases. However, the applicability of Cs_2SnI_6 which contains isolated SnI_6^{2-} octahedra as a photovoltaic hole transport layer, [162] enforces our point that the structural influences on the optoelectronic properties of heavy main group metal halides are complex and even the phases with low dimensional bismuth halide units hold the potential for interesting future applications.

4.4 Conclusion

In the search for promising materials for optoelectronic applications, we look for band gaps that are well-matched with the excitation spectrum, efficient light absorption, and facile carrier transport. [126] Here we have investigated complex bismuth iodides $A_3Bi_2I_9$ (A = K, Rb, Cs) both experimentally and computationally. New facile preparation routes from organic solvents and by mechanical mixing are presented and initial thin film fabrication procedures are reported. From our preliminary observations, the chemical stability seems to be greater than for the related lead halides. Crystal structures were redetermined by X-ray diffraction, as the basis for advancing structure-composition-property relationships. For the layered defect-perovskite

$Rb_3Bi_2I_9$, we report an improved centrosymmetric structural model based on single-crystal diffraction and solid state NMR supported by DFT simulation of NMR parameters. The optical band gaps and absolute VBM positions were determined by UV-Vis and by ultraviolet photoemission spectroscopy, respectively. Band structures were calculated using the screened hybrid functional HSE, and including spin-orbit coupling for the band gaps, and slab-calculations for absolute band positions using the binary BiI_3 phase as a reference, that allowed other absolute band positions to be obtained. The excellent agreement between experimental and calculated values suggest that the methods employed here are a powerful tool for the rapid screening of semiconductors and the rational design of optoelectronic devices.

Key findings that resulted for the compounds studied are that the band gaps are around 2 eV and are rather insensitive to the counter cation and structure type. In addition, the VBM levels are significantly lower than for the widely used lead halide perovskite photovoltaics. Thus, for potential application in solar cells, in addition to the optimization of the film formation, a careful choice of the contacting hole transport materials will be necessary to match the band positions and enable high open circuit voltages. From the calculated band structures, the band gaps of the layered K and Rb salts are direct, while $Cs_3Bi_2I_9$ has an indirect gap. Direct gaps coupled with the high density of states with a strong p-character across the gap, as observed for the studied phases, are quite promising for effective light absorption. For the three phases, the band dispersion of the conduction and valence bands around the gap is moderate to small compared to the related perovskite halides, possibly as a result of the different relative arrangement of the BiI_6 octahedra. The calculated Born effective charges on Bi^{3+} are significantly elevated only for the layered $A_3Bi_2I_9$ and not for the 0D $Cs_3Bi_2I_9$. High Born effective charges are indicative of more efficient dielectric defect screening and thus potentially, better carrier mobility. Given the solution-processability and the

range of similar optoelectronic properties paired with a much lower toxicity compared to the lead halide perovskites, the structurally rich class of complex bismuth halides is a new promising class of materials for optoelectronic application.

Chapter 5

Dynamic Sn^{2+} lone pair stereochemical activity in perovskite $CsSnBr_3$

[1] Stable s^2 lone pair electrons on heavy main-group elements in their lower oxidation states drive a range of important phenomena, such as the emergence of polar ground states in some ferroic materials. Here we study the perovskite halide $CsSnBr_3$ as an embodiment of the broader materials class. We show that lone pair stereochemical activity due to the Sn s^2 lone pair causes a crystallographically hidden, locally distorted state to appear upon warming, a phenomenon previously referred to as emphanisis. The synchrotron X-ray pair distribution function acquired between 300 K and 420 K reveals emerging asymmetry in the nearest-neighbor Sn–Br correlations, consistent with dynamic Sn^{2+} off-centering, despite there being no evidence of any deviation from the average cubic structure. Computation based on density functional theory supports the finding of a lattice instability associated with dynamic off-centering of Sn^{2+} in its

[1]The contents of this chapter have substantially appeared in reference [50]: D. Fabini, G. Laurita, J. Bechtel, C. Stoumpos, H. Evans, A. Kontos, Y. Raptis, P. Falaras, A. Van der Ven, M. Kanatzidis, R. Seshadri, Dynamic stereochemical activity of the Sn^{2+} lone pair in perovskite $CsSnBr_3$, *J. Am. Chem. Soc.* **2016**, *138*, 11820–11832, © 2016 American Chemical Society, reprinted with permission.

coordination environment. Photoluminescence measurements reveal an unusual blue-shift with increasing temperature, closely linked to the structural evolution. At low temperatures, the structures reflect the influence of octahedral rotation. A continuous transition from an orthorhombic structure ($Pnma$, no. 62) to a tetragonal structure ($P4/mbm$, no. 127) is found around 250 K, with a final, first-order transformation at 286 K to the cubic structure ($Pm\bar{3}m$, no. 221).

5.1 Introduction

Inorganic and hybrid main-group halide perovskites have attracted significant attention of late for their excellent performance in optoelectronic applications, ease of preparation, and abundant constituent elements. [7, 9, 163, 164, 165, 166, 167] In addition to being investigated for use in radiation detectors and light emitting diodes, [25] the all-inorganic CsMX_3 (M = Ge, Sn, Pb; X = Cl, Br, I) perovskites offer an opportunity to understand the crystal chemistry of the divalent metal–halogen network without the added complexity introduced by the organic molecular ions present in the heavily studied organic–inorganic hybrids. [17, 168, 161, 169]

These materials are distinguished from tetrahedral semiconductors and from transition metal oxides in part by the presence of a s^2 lone pair on the divalent M-site cation. The lone pair gives rise to strong optical absorption near the bandgap and an unusual band structure, with the valence band comprising a mixture of cation s states and anion p states and three conduction bands comprised of cation p states. [161] A similar electronic structure gives rise to a lattice instability in divalent group IV chalcogenides [35] and monovalent group III halides. [99] Proximity to such a polar instability produces enhanced dielectric response and thus may contribute to effective screening of defects in semiconductors. [99, 170] Recently, a locally distorted state was reported in

rock-salt group IV chalcogenides (SnTe, [171] PbS, and PbTe [172]) upon warming on the basis of X-ray and neutron total scattering experiments, wherein the crystal retains long-range cubic symmetry, but the cations move off their nominal sites in a spatially or temporally incoherent fashion. This phenomenon has been referred to as *emphanisis*, meaning the appearance of something (a low symmetry state) from nothing (a high symmetry state) upon warming, in a manner that is contrary to most crystals that attain lower symmetries upon cooling. Based on chemical and thermodynamic arguments, the authors proposed lattice expansion-induced lone pair stereochemical activity as the mechanism for this unusual phenomenon, and in the case of SnTe found qualitative differences between this emergent high temperature phase and the ferroic low temperature phase. Following these reports, a number of articles have appeared, seeking to clarify the lattice dynamics and local structure of these materials based on ab initio calculations, [173, 174, 175, 176] extended X-ray absorption fine structure (EXAFS) spectroscopy, [177, 178] neutron scattering, [179, 174, 180] X-ray diffraction, [181] and piezoresponse force microscopy. [176] Most agree that a high degree of anharmonicity of the cation potential well exists within the region accessible at relevant thermal energies.

In contrast to systems that display such emphanisis, the typical phase evolution of polar insulators, including ferroelectric oxides, is from a centrosymmetric high temperature phase to a non-centrosymmetric low temperature phase (or sequence of phases) with spontaneous polarization. This conventional picture is true of materials with lone pair-bearing metals ($PbTiO_3$, $BiFeO_3$ with the lone pair on the A-site cations) [182, 183] and those without ($BaTiO_3$, $KNbO_3$). [184, 185] Local structure probes have revealed a more complex picture of the phase transitions in some of these materials, wherein disordered local cation displacements persist above the phase transition and average out crystallographically to a high symmetry structure model. [186, 187] Notably, these

disordered phases are emergent from a low temperature phase with ferroic displacements, rather than from a high symmetry undistorted phase, as has been proposed in the group IV chalcogenides.

The instabilities associated with lone pair-bearing $d^{10}s^2$ cations and empty shell d^0 cations in high symmetry environments are a consequence of the pseudo-Jahn-Teller effect, [33, 34] and predictors of ferroelectric instability based on simple chemical and geometric factors have been enumerated. [35] Based on these factors, we selected $CsSnBr_3$ for study as an exemplar of the delicate balance of structural tendencies in the main-group halide perovskites. In $CH_3NH_3SnBr_3$, the larger *A*-site cation expands the lattice and leads to coherent Sn^{2+} displacements in the orthorhombic phase [188] and to local displacements in the cubic phase. [189] In contrast, $CH_3NH_3PbBr_3$ shows no signs of coherent displacements in the low temperature phases [190] or local displacements in the cubic phase [189] due to the lowering of the Pb^{2+} lone pair levels associated with relativistic effects. This strong influence of the divalent cation is also evident in the iodides: The tendency for lone pair stereochemical activity is strong in $CsGeI_3$, resulting in a polar rhombohedral crystal structure with 3+3 Ge coordination at ambient temperatures, [17] while the high performance photovoltaic $CH_3NH_3PbI_3$ adopts orthorhombic, tetragonal, and cubic phases without coherent Pb^{2+} displacements [191] and shows no signs of local displacements at ambient temperature. [192] $CsSnF_3$, with strong lone pair stereochemical activity due to the hard fluoride anions, exists not as a perovskite, but rather as a salt of Cs^+ and $[SnF_3]^-$ pyramids. [193]

Here, we report the phase evolution of the halide perovksite $CsSnBr_3$ from 100 K to 420 K, including the first observation of a dynamic instability in the cubic phase ($T > 290$ K) characterized by local off-centering of Sn^{2+} cations at elevated temperatures. In other words, $CsSnBr_3$ displays emphanisis, in a manner very similar to the chalcogenides such as PbTe. These local distortions are evident in the pair distribu-

tion function obtained from neutron and X-ray total scattering studies between 300 K and 420 K. Ab initio calculations of lattice dynamics, electronic structure, and dielectric properties of $CsSnBr_3$ and related phases support this interpretation, and suggest that the s^2 lone pair electrons of the main-group cation are responsible for this instability. Photoluminescence measurements reveal a blue-shift of the bandgap with warming which becomes markedly more temperature-dependent in the cubic phase. We report the complete high resolution crystal structures for the cubic (300 K) and orthorhombic (100 K) phases of $CsSnBr_3$ from neutron and synchrotron X-ray powder diffraction, and for the tetragonal (270 K) phase of $CsSnBr_3$ from synchrotron X-ray powder diffraction. The structures of the tetragonal and orthorhombic phases demonstrate that at reduced temperatures, the tendency for Sn^{2+} to off-center is suppressed by the competing tendency for octahedral rotations that enhance electrostatic binding and increase the coordination of the undersized *A*-site cation. Ab initio calculations of the lattice dynamics of the orthorhombic phase confirm that it is the ground state structure, highlighting the categorical difference between the phase evolution of ferroelectric oxides and that of $CsSnBr_3$, where cation displacements exist only at elevated temperatures.

5.2 Methods

$CsSnBr_3$ was prepared by reacting $SnBr_2$ (Sigma-Aldrich, 20 mmol, 5.570 g) and CsBr (99.9 % Sigma-Aldrich, 20 mmol, 4.256 g) in a fused SiO_2 tube (13 mm OD, 11 mm ID), which was evacuated to 10^{-3} mbar and flame sealed. The silica tube was placed in a furnace and heated to 600° C over 6 h, held at this temperature for 3 h, followed by cooling down to ambient temperature over 3 h. The reaction resulted in a shiny black ingot of $CsSnBr_3$. The ingot was isolated by breaking the ampoule in a N_2-filled glovebox as a precautionary measure. The compound is air-stable and suffers

only surface damage when exposed to humid air.

High-Q resolution X-ray diffraction data were collected from 100 K to 300 K using the 11-BM beamline at the Advanced Photon Source (APS), Argonne National Laboratory (ANL) utilizing a calibrated wavelength of 0.45898 Å. The $CsSnBr_3$ sample (0.1 mmol, 27.8 mg) was transferred into a mortar and ground together with fused SiO_2 (0.9 mmol, 54 mg) into a homogeneous gray powder to reduce the absorption coefficient of the sample relative to the neat $CsSnBr_3$ material. The resulting powder was transferred to a fused SiO_2 capillary with a 0.5 mm OD and filled up to approximately 2 cm in height. Subsequently, powdered, fused SiO_2 was added and the capillary was evacuated to 10^{-3} mbar and flame sealed through the fused SiO_2 powder to prevent the loosening of the powder during evacuation and to ensure a more homogeneous sealing of the capillary. Time-of-flight (TOF) neutron diffraction data were collected at 100 K and 300 K on the POWGEN diffractometer at the Spallation Neutron Source (SNS), Oak Ridge National Laboratory (ORNL). The $CsSnBr_3$ ingot was broken into pieces, taking care to remove the top 1 mm to 2 mm that could be a potential source of impurities. Pieces of the ingot were transferred into a mortar and thoroughly ground to a fine powder. The powder was filled into a 6 mm vanadium can and was subsequently compressed tightly. The total mass of the sample for the neutron experiment was 4.381 g. The packed vanadium can was then sealed tightly under a N_2 atmosphere. Data were collected for a total time of 2 h on banks 2 and 4 with a central wavelength of the TOF neutrons chosen to be 1.066 Å and 2.665 Å, respectively. TOF neutron total scattering experiments were performed at 300 K and 420 K utilizing the Nanoscale Ordered Materials Diffractometer (NOMAD) at the SNS located at ORNL with a collection time of approximately 2 h to 4 h per sample. [194] The sample was the same as that for the POWGEN experiment. An empty 6 mm vanadium can was collected and subtracted as background. The pair distribution function (PDF), $G(r)$, was obtained by the trans-

formation of the normalized total scattering function, $S(Q)$, with a Q_{min} = 0.5 Å^{-1} and Q_{max} = 31.5 Å^{-1}. Synchrotron X-ray total scattering measurements were collected on the 11-ID-B beam line at the APS located at ANL with a photon wavelength of 0.1430 Å from 100 K to 420 K. A sample of fine powder, obtained by means described above, was transferred into a Kapton capillary (1.1 mm OD, 1.0 mm ID) tightly compacted to ensure the maximum packing fraction. Both ends of the capillary were sealed with epoxy and stored in a N_2 atmosphere prior to the measurement. Data were collected every 2 minutes upon cooling at a rate of 6 K min^{-1}. Corrections to obtain the $S(Q)$ and subsequent Fourier Transform with a Q_{max} of 23 Å^{-1} to obtain the $G(r)$ was performed using the program PDFgetX2. [195]

Rietveld refinements were carried out on the diffraction data to obtain the average crystallographic structure using the GSAS software suite with the EXPGUI interface. [196, 197] The local structure was investigated via analysis of the real-space PDF using the PDFgui software suite. [198] Correlated motion in the PDF was modeled using the *sratio* and *rcut* parameters, which account for effects on the PDF due to correlated motion of rigid structural units. An *rcut* value of 5 Å was specified, which corresponds to the approximate Br–Br distance in the $SnBr_6$. Crystal structures were visualized using the VESTA suite of programs. [132]

All calculations were performed with the Vienna Ab initio Simulation Package (VASP), [137, 138, 95, 139] which implements the Kohn-Sham formulation of density functional theory (DFT) using a plane-wave basis set and the projector augmented wave formalism. [140, 96] The generalized gradient approximation (GGA) was employed using the Perdew–Burke–Ernzerhof (PBE) exchange and correlation functional for total energy and electronic structure calculations, [142] and the PBEsol functional for calculations of phonon dispersions and dielectric properties. [199] In each case, calculations were performed from structures with lattice parameters relaxed with

the corresponding functional. Valence electron configurations were as follows: Cs, $5s^25p^66s^1$; Br, $4s^24p^5$; Sn, $5s^24d^{10}5p^2$; Pb, $6s^25d^{10}6p^2$; Ca, $3s^23p^64s^2$. Plane wave basis set cutoff energies and Γ-centered Brillouin zone sampling densities were chosen based on the convergence of total energy in structure relaxations (PBE: 500 eV cutoff, 8×8×8 Monkhorst-Pack sampling, [200] a =5.894 Å; PBEsol: 520 eV cutoff, 11×11×11 Monkhorst-Pack sampling, a =5.759 Å). For calculation of the electronic density of states, a denser 24×24×24 k-point mesh was employed. Born effective charge tensors, high frequency dielectric tensors, and static dielectric tensors (including local field effects) were calculated using density functional perturbation theory (DFPT). [201]

Energy surfaces for displacement of the divalent cation were calculated for both a primitive cell and a 2×2×2 supercell, wherein total energy per formula unit was evaluated as a function of rigid cation displacement along the high symmetry directions and of lattice parameter contraction or expansion. For the 2×2×2 supercell study, all symmetrically distinct combinations of high symmetry real-space displacement directions ($\langle 100\rangle$, $\langle 110\rangle$, $\langle 111\rangle$) and high symmetry reciprocal-space vectors (Γ, X, M, R) modulating the displacements from site to site were considered. The k-point density was kept the same for the supercell calculations.

The frozen phonon approach was employed to calculate the force constants for $CsSnBr_3$. Forces resulting from single atomic displacements (0.1 Å) were collected with VASP, and a least-squares fit between perturbations and collected forces was used to determine harmonic force constants. [202] The Born effective charges and dielectric tensors evaluated from DFPT were used to calculate the non-analytic correction for the dynamical matrix due to long-range Coulomb interactions. For the cubic phase, a 3×3×3 supercell (135 atoms) was used with a 4×4×4 Γ-centered k-point mesh, while for the orthorhombic phase, a 2×1×2 supercell (80 atoms) with a 4×6×4 Γ-centered k-point mesh was employed.

To screen candidate crystal structures for the low temperature phase of $CsSnBr_3$, symmetrized displacement modes associated with M_3^+ and R_4^+ irreducible representations of the M and R points of the first Brillouin zone in the parent $Pm\bar{3}m$ structure were found with the ISODISTORT [203] module of ISOTROPY (ISOTROPY Software Suite, iso.byu.edu). The 15 unique octahedral tilt systems as described by Howard and Stokes [204] were then enumerated through the application of the M_3^+ and R_4^+ displacement modes of the Br sublattice. Structural relaxations of all tilt systems were carried out in 2×2×2 supercells of the primitive cell with a 6×6×6 k-point mesh centered at the Γ point until the forces on atoms reached < 10 meV $Å^{-1}$. Symmetries of the relaxed structures were verified using the FINDSYM [205] module of ISOTROPY.

Differential scanning calorimetry was recorded on ground 5.9 mg sample using a DSC Q-2000 calorimeter from TA Instruments. The temperature was swept from 123 K to 323 K at a rate of 10 K min^{-1} for 2 cycles. Visible–near infrared photoluminescence spectra were recorded in a THMS600PS Linkam optical cell with a heating-freezing stage, under dynamic vacuum. The excitation beam (532 nm laser, 10 mW) was focused on the sample via a lens with a focal length of 75 mm in a quasi-backscattering geometry. Emitted light was analyzed in a double monochromator and detected with a photomultiplier.

5.3 Results & discussion

5.3.1 Average and local structure of cubic $CsSnBr_3$

Joint Rietveld refinements of the X-ray and neutron diffraction data at 300 K (Figure 5.1, Table 5.2) indicate the data is well described by the cubic space group $Pm\bar{3}m$ (no. 221) with Cs^+ in the $1a$ Wyckoff site at $(0, 0, 0)$, Sn^{2+} in the $1b$ site at $(\frac{1}{2}, \frac{1}{2}, \frac{1}{2})$, and Br^- in

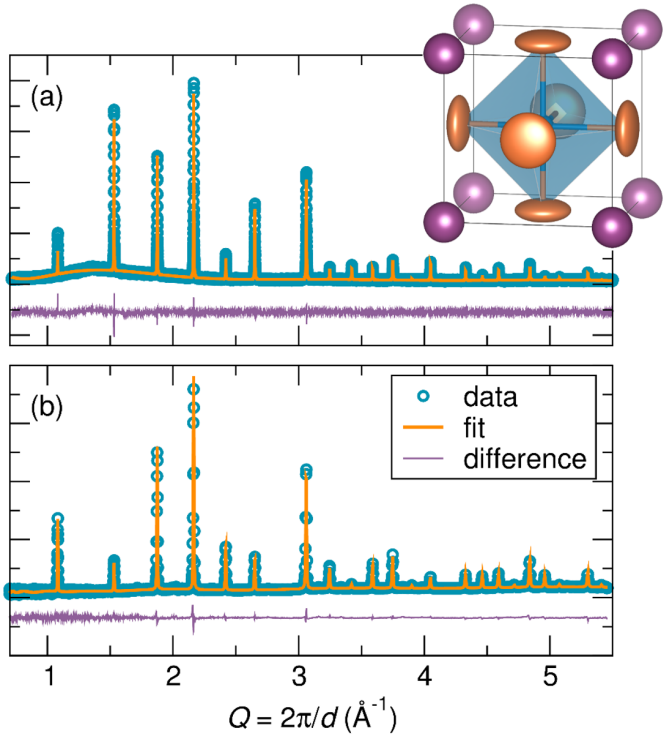

Figure 5.1: Fits obtained from the joint Rietveld refinement against $Pm\bar{3}m$ of (a) X-ray and (b) TOF neutron diffraction data collected at 300 K. Inset: analysis of the diffraction data indicates enlarged ADPs (shown at 90 % probability) on the Cs and Br sites. In particular, Br ADPs are anisotropically enlarged perpendicular to the Sn–Br bond, highlighting the presence of dynamic octahedral rotations in the flexible Sn–Br framework. Figure prepared by Geneva Laurita.

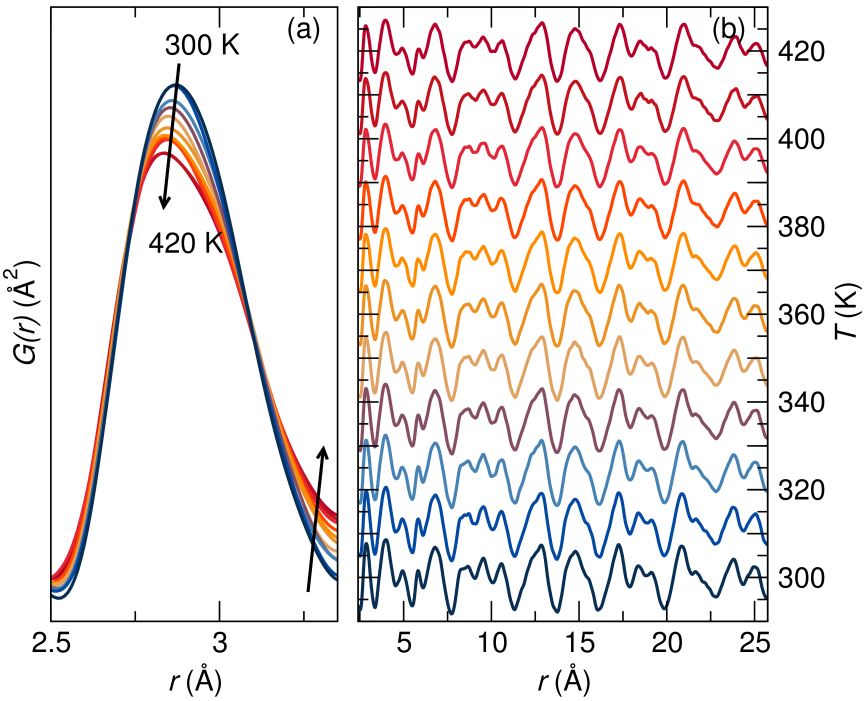

Figure 5.2: X-ray PDF data for $CsSnBr_3$ over a range of 300 K to 420 K. (a) Emergence of peak asymmetry in the Sn–Br correlation distance can be observed upon warming, while (b) the data over 2 Å to 20 Å indicate no apparent change over longer r correlations. Figure prepared by Geneva Laurita.

the $3c$ site at $(0, \frac{1}{2}, \frac{1}{2})$. The cation sites are modeled with isotropic atomic displacement parameters (ADPs, reported in U_{iso}), while the Br anions exhibit large anisotropic ADPs perpendicular to the Sn–Br bond of the $SnBr_6$ octahedral units, indicating a high degree of structural disorder of the Br atoms normal to the Sn–Br–Sn bonds. These large transverse displacements arise from the flexible nature of the partially covalent Sn–Br octahedral network, as well as the very low Cs–Br bond valence, and suggest there are dynamic octahedral rotations at this temperature.

A qualitative comparison of the X-ray PDFs between 300 K and 420 K reveals the emergence of a peak asymmetry of the first peak to high-r upon warming, which corresponds to the Sn–Br correlation in $CsSnBr_3$. However, no apparent changes in this temperature range can be distinguished over 2 Å to 20 Å as the data tends towards an

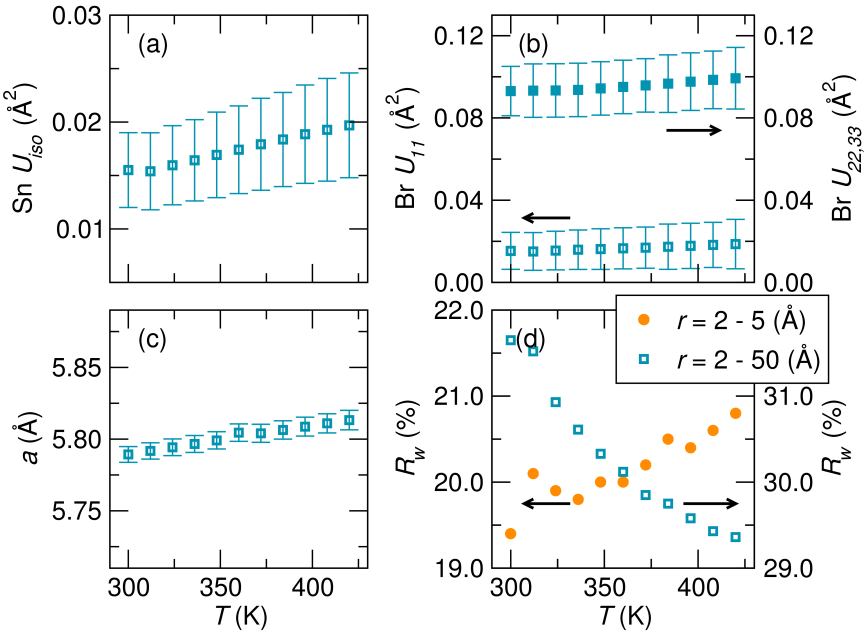

Figure 5.3: Select parameters obtained from fitting of the X-ray PDF at 420 K over a fit range of 2 Å to 5 Å (filled orange circles) and 2 Å to 50 Å (open blue squares) with structural model $Pm\bar{3}m$. (a) Sn isotropic and (b) Br anisotropic ADPs both increase with increasing temperature. (c) Comparison of the trend in lattice parameters with increasing temperature indicates an increase for the 50 Å fit due to thermal expansion. (d) R_w values obtained from the temperature series indicates a decreasing R_w with temperature over the 50 Å fit ($i.e.$ the cubic model becomes a better description of the long range symmetry with warming), whereas an increasing R_w is observed for the 5 Å fit ($i.e.$ the cubic model becomes a worse description of the local structure with warming). Figure prepared by Geneva Laurita.

average, crystallographic picture. Peak asymmetry of the first Sn–Br correlation can also be observed in the neutron PDF (Supporting Information).

Fits of the X-ray PDFs between 300 K and 420 K were performed against the $Pm\bar{3}m$ model obtained from the joint Rietveld refinement of the diffraction data at 300 K over ranges of 2 Å to 5 Å and 2 Å to 50 Å. Results are summarized in Figure 5.3. The ADP values obtained from the 2 Å to 5 Å fit were highly correlated and did not yield a stable refinement, and therefore only ADPs from the 2 Å to 50 Å fit are shown. In general, ADPs increase with temperature as expected due to increased thermal motion of atoms about their crystallographic sites. The Br ADPs remain anisotropic as was observed

in the Rietveld refinement. Due to the large transverse motion of the Br atoms with respect to the Sn–Br bond, the evolution of the lattice parameters over the 2 Å to 50 Å fit range was investigated. Similar large transverse motion of anions has been observed in ReO_3, which may be responsible for apparent negative thermal expansion in the material. [206, 207] However, lattice parameters exhibit an increase with temperature, following typical thermal expansion behavior. By looking at the R_w goodness-of-fit parameter, it can be seen that the R_w values against the cubic model show a decrease with increasing temperature over the 2 Å to 50 Å fit range. This indicates that the data is better described by a cubic space group as the temperature increases. This is in agreement with the average, crystallographic structure at these temperatures. However, the R_w values of the data over a 2 Å to 5 Å fit range *increase* with temperature, indicating the data is more poorly described by the cubic model as the temperature increases: The sample is locally deviating from cubic symmetry upon warming.

In the cubic $Pm\bar{3}m$ structure we would expect a single Sn–Br correlation in the PDF, and therefore does not capture the peak asymmetry as was illustrated in the 2 Å to 5 Å fits of the X-ray PDF data. Geometrical considerations of the local atomic interactions could help elucidate the origin of the observed asymmetry in the Sn–Br correlation. For example, the enlarged perpendicular anisotropic ADPs of the Br atoms could result in a distribution of Sn–Br correlations at and above the nominal Sn–Br bond distance, which would appear as peak tailing to high r. Alternatively, a rhombohedral off-centering of the Sn^{2+} (towards the face of the $SnBr_6$ octahedra along the [111] crystallographic direction) would result in two Sn–Br correlation distances. If this off-centering is dynamic, this could appear as an asymmetric peak at the nominal Sn–Br correlation distance.

To investigate the effect of anisotropic Br ADPs on the PDF, three $Pm\bar{3}m$ structural models were constructed and fit over a 2 Å to 5 Å range against the X-ray PDF at 420 K:

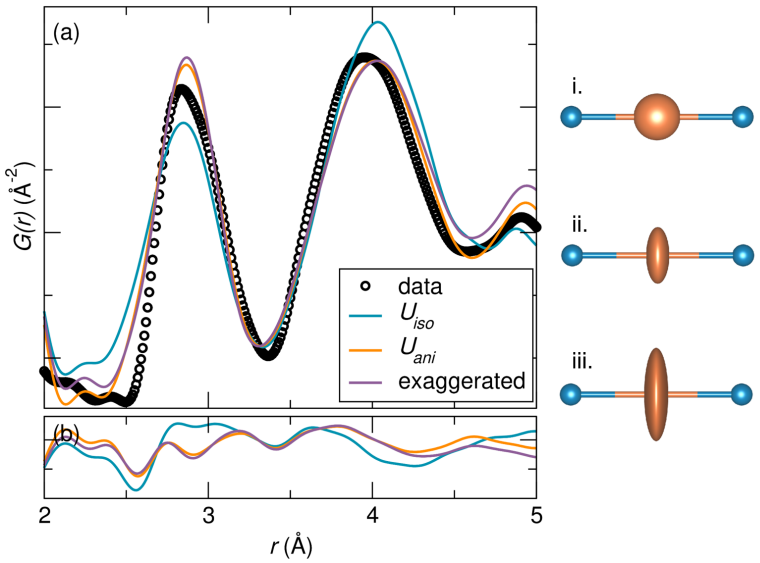

Figure 5.4: (a) Fits of the X-ray PDF at 420 K with three models of the Br ADPs in space group $Pm\bar{3}m$: isotropic ADPs (U_{iso}; $U_{11} = U_{22} = U_{33}$), anisotropic ADPs obtained from the joint Rietveld refinements of the average structure (U_{ani}; $U_{11} < U_{22} = U_{33}$), and exaggerated anisotropic ADPs (exaggerated; $U_{11} \ll U_{22} = U_{33}$). (b) Comparison of the difference curves for the fits of the three models indicates none are able to capture the peak asymmetry of the Sn–Br correlation at approximately 2.8 Å, but anisotropic ADPs are necessary to accurately model the second peak, comprised of Cs–Br and Br–Br correlations. Illustrations of the Sn–Br–Sn interactions in the three models are shown to the right: i. U_{iso}, ii. U_{ani}, and iii. exaggerated, with ADPs shown at 90% probability. Figure prepared by Geneva Laurita.

isotropic Br ADPs set to the U_{eq} value obtained from the 300 K Rietveld refinement (U_{11}=U_{22}=U_{33}= 0.107), anisotropic Br ADPs set to the values obtained from the 300 K Rietveld refinement (U_{11}=0.026; U_{22}=U_{33}= 0.1443), and anisotropic Br ADPs with an exaggerated perpendicular component (U_{11}=0.026; U_{22}=U_{33}= 0.4). For all three models the Br ADPs were held constant while other parameters (overall scale, lattice parameter, correlated motion, Sn U_{iso}, and Cs U_{iso}) were allowed to refine freely. It is observed that the anisotropic ADPs are essential for an accurate description of the second peak in the PDF, as this peak is dominated by Br-dependent correlations (Cs–Br and Br–Br). While the anisotropic ADPs do seem to do a better job of describing the first PDF peak by an effective shift in the central r-distance of the modeled Sn–Br correlation, they are unable to describe the observed asymmetry. This is indicative that the data cannot be explained by anisotropic ADPs alone; however, it must be recognized that this may be due to a limitation of PDFgui, which applies the harmonic approximation and thus generates Gaussian peak shapes. [208, 209] Therefore, if a harmonic approximation is assumed, a two-peak model, such as that of a rhombohedrally-distorted local symmetry, may provide a better description of this peak within the limitations of the analysis.

To model local Sn^{2+} displacement directions against the X-ray PDF data at 420 K, various crystallographic structures with prototypical ferroic displacements in perovskite materials were used: cubic $Pm\bar{3}m$ (no Sn^{2+} displacement), tetragonal *P*4*mm* (no. 99) (Sn^{2+} displacement along the $\langle 100 \rangle$ towards a corner of the $SnBr_6$ octahedron), orthorhombic $Amm2$ (no. 38) (Sn^{2+} displacement along the $\langle 110 \rangle$ towards an edge of the $SnBr_6$ octahedron), and rhombohedral $R3m$ (no. 160) (Sn^{2+} displacement along the $\langle 111 \rangle$ towards a face of the $SnBr_6$ octahedron). Starting structural models were obtained by transforming the refined cubic $Pm\bar{3}m$ structure into the various lower symmetry space groups, which were subsequently refined against the 300 K Rietveld

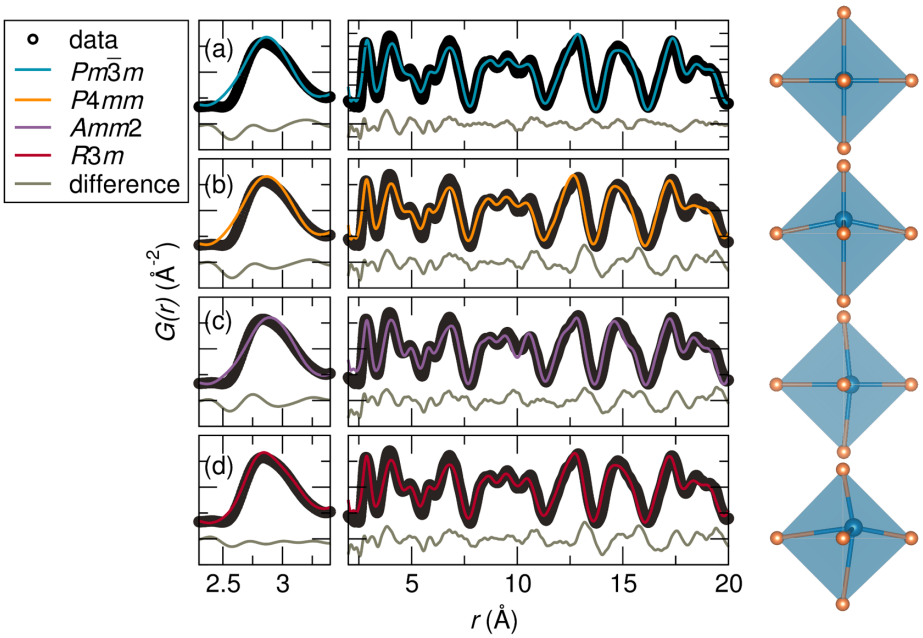

Figure 5.5: Fits of the X-ray PDF at 420 K against known prototypical ferroelectric perovskite space groups: (a) $Pm\bar{3}m$ (cubic, no Sn displacement), (b) $P4mm$ (tetragonal, Sn displacement along $\langle 100 \rangle$), (c) $Amm2$ (orthorhombic, Sn displacement along $\langle 110 \rangle$), and (d) $R3m$ (rhombohedral, Sn displacement along $\langle 111 \rangle$). A rhombohedral displacement of approximately 0.2 Å provides the best description of the asymmetric Sn–Br peak over a fit range of 2 Å to 5 Å, while cubic symmetry more accurately captures the features over a longer r-range (2 Å to 20 Å). Illustrations of the Sn^{2+} displacements in the $SnBr_6$ octahedra are shown to the right of each fit. Figure prepared by Geneva Laurita.

data. To avoid excessive correlations of parameters during the refinements of the PDF data, anisotropic Br ADPs were fixed to those obtained from the Rietveld fits, while other parameters were allowed to refine.

As previously seen in the 300 K to 420 K temperature series, the cubic space group does not describe the asymmetric shape of the first peak in the X-ray PDF at 420 K. A similar fit is obtained with the tetragonal $P4mm$ structure. Displacement of Sn^{2+} towards the corner of an $SnBr_6$ octahedron results in a narrow distribution of one short, four intermediate, and one long bond lengths, which effectively creates peak tailing to both high- and low-r of the main Sn–Br correlation. Similarly, a displacement of Sn^{2+} towards the edge of the octahedron results in a distribution of two short, two intermediate, and two long bond lengths, and once again does not describe the asymmetric shape. However, displacement towards the face of the octahedron results in three short and three long Sn–Br bond distances, which would appear as two peaks in the PDF. Indeed, over a 2 Å to 5 Å fit range, the rhombohedral model provides the best comparative fit to the data, capturing the peak asymmetry as a superposition of two Sn–Br correlations with a small r separation, corresponding to an Sn^{2+} off-centering of approximately 0.2 Å. This observed off-centering could arise from stereochemical activity of the $5s^2$ pair of electrons associated with Sn^{2+} driven by lattice expansion upon warming. The local rhombohedral distortion appears as two overlapping peaks, in contrast to that of the local rhombohedral distortion observed in $BaTiO_3$, [186, 210] where there are two distinct first correlation peaks. This is proposed to be an effect of dynamic displacement within the octahedra rather than the static displacement observed in $BaTiO_3$. This modeling approach limits the resulting local structure models to those of cation displacements along high symmetry directions. More complex stochastic approaches, such as those recently employed in understanding the nature of distortions in $BaTiO_3$, [211] suggest the way forward for bias-free determination of local distor-

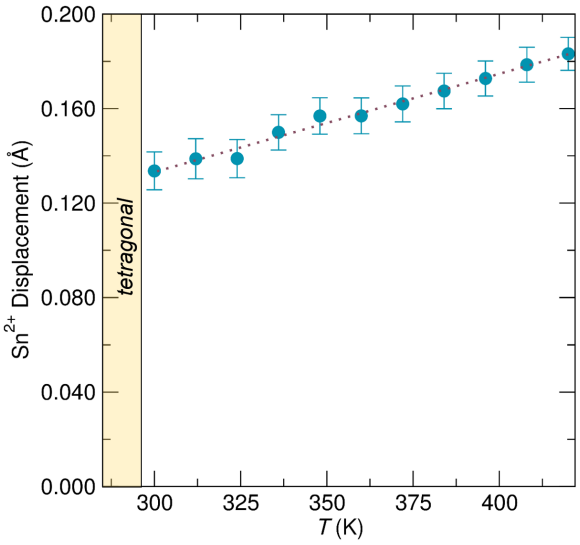

Figure 5.6: Evolution of Sn^{2+} displacement from the center of the $SnBr_6$ octahedron with increasing temperature as determined from fitting the X-ray PDF over a range of 2 Å to 5 Å against the rhombohedral $R3m$ model. Displacement from the center increases with increasing temperature. On cooling, the displacement does not reach zero (Sn^{2+} in the center of the octahedron) in the cubic phase due to the onset of a phase transition to a tetragonal structure at 286 K. Figure prepared by Geneva Laurita.

tions and their correlations, but are beyond the scope of this work. Nonetheless, our results do indicate that local Sn^{2+} displacements are the likely cause of the observed peak asymmetry at elevated temperatures, and that among the high symmetry directions, these displacements are preferentially along $\langle 111 \rangle$. This is also corroborated by DFT calculations as described in the next subsection.

The degree of Sn^{2+} displacement from the center of the $SnBr_6$ octahedron as a function of temperature was determined by refinement of the X-ray PDF data against the rhombohedral *R*3*m* model. Refinements were performed over a fit range of 2 Å to 5 Å and a temperature range of 300 K to 420 K. The degree of displacement is seen to increase with temperature, and attributed to enhanced stereochemical activity with expansion of the lattice. This is reported to drive a crossover from a local, lone pair-inactive state to a local, lone pair-active state in rock-salt tin and lead chalcogenides. [171] In contrast with the chalcogenides, the local displacement of Sn^{2+} in

cubic $CsSnBr_3$ does not appear to go continuously to zero displacement on cooling, and is instead suppressed discontinuously as the crystal undergoes a phase transition to a tetragonal structure at 286 K (*vide infra*).

5.3.2 Ab initio studies of cubic $CsSnBr_3$

Ab initio calculations of lattice dynamics, electronic structure, and dielectric properties of $CsSnBr_3$ are consistent with this propensity for off-centering of Sn^{2+} and confirm that these displacements are preferentially along $\langle 111 \rangle$. Additionally, comparison with isostructural but chemically distinct phases illustrates the importance of s^2 lone pair electrons in this coupled electronic–lattice instability. The electronic band structure and orbital-projected density of states, calculated at the PBE level with and without spin-orbit coupling (SOC), are presented in Figure 5.7. The PBE exchange and correlation functional is known to poorly reproduce excited state properties, and thus underestimate bandgaps. Apart from the magnitude of the bandgap, our results agree in the essential aspects with those of Huang and Lambrecht, from self-consistent quasiparticle calculations. [161] Similar to other inorganic main-group halide perovskites, the band structure is "inverted," with a single valence band with primarily Sn(s)–Br(p) anti-bonding character, and a triply degenerate (in the absence of SOC) conduction band minimum of primarily Sn(p) character. [161, 93]

The Sn^{2+} lone pair electrons are rather shallow relative to the Fermi energy. Strong overlap between occupied Sn(s) and Br(p) states produces a σ-like band at $\sim$4 eV below E_f and the σ^*-like valence band. This interaction pushes the antibonding Sn(s) states up in energy, bringing them close in energy to the unoccupied Sn(p) states, which tends to promote lone pair stereochemical activity. [36, 37, 38, 39, 41] Additionally, cross-gap mixing of cation (p) and anion (p) states is evident, which has been asso-

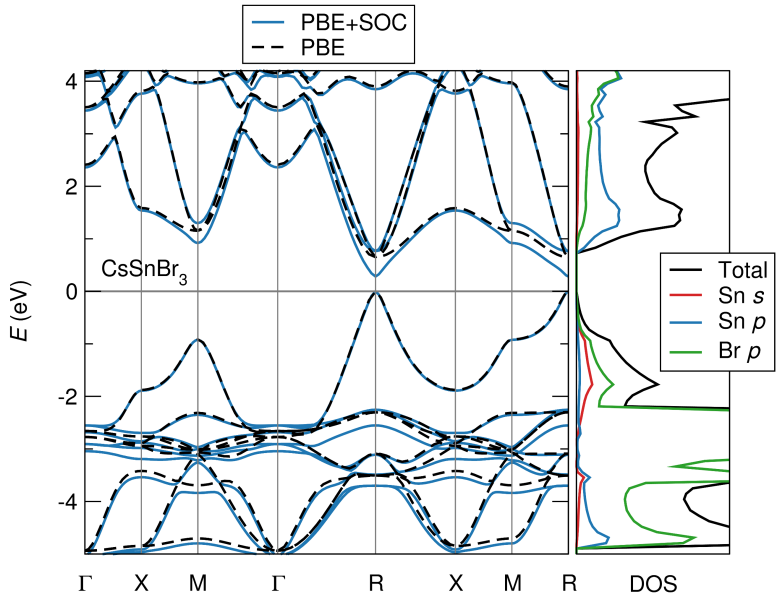

Figure 5.7: Electronic band structure and projected density of states (DOS) of $CsSnBr_3$, illustrating the "inverted" band structure typical of main-group halide perovskites. The valence band is formed from the antibonding interaction between Sn(s) and Br(p) orbitals. The regions near the conduction band minimum are triply degenerate in the absence of spin orbit coupling and are primarily derived from Sn(p) orbitals. The modest effect of spin orbit coupling is evident.

ciated with elevated Born effective charges, giant splitting between longitudinal and transverse optical modes (LO/TO splitting), and polar instability in perovskite oxides. [212, 213, 214, 215] Systems with these electronic features exhibit a strong electron–phonon coupling (and atomic displacement–polarization coupling), with implications for charge transport and defect tolerance. [99]

Comparison with isostructural $CsPbBr_3$ and $CsCaBr_3$ allows us to examine the influence of the s^2 lone pair electrons on the electronic structure and lattice dynamics: Pb^{2+} is predicted to have a lesser tendency for stereochemical activity due to greater relativistic stabilization of the lone pair, [35] and Ca^{2+} lacks a lone pair as it is fully oxidized to the electron configuration of Ar. The electronic band structures and densities of states of $CsPbBr_3$ and $CsCaBr_3$ are presented in the Supporting Information. The band structure of $CsPbBr_3$ is similar to that of $CsSnBr_3$, but the competing effects

of longer metal–Br bond length, reduced ionicity of metal–Br interaction, and stronger spin-orbit coupling result in a wider bandgap and larger carrier effective masses at this level of theory. The large electronegativity difference between Ca and Br causes $CsCaBr_3$ to be an insulator, with rather localized electronic states. We return to the comparison with these related phases presently.

Calculated Born effective charges and dielectric responses are also indicative of a polar instability, and are presented in Table 5.1. The Born charges of $CsSnBr_3$ and $CsPbBr_3$ are significantly elevated above the nominal divalent charge, consistent with substantial covalency and a large polarization response to ion displacement (or equivalently, a large force on the ions in response to electric fields). $CsCaBr_3$, in which the divalent cation lacks a lone pair of s^2 electrons, stands apart: The Ca^{2+} Born charge is much more similar to the formal charge for this highly electropositive cation, which implies the restoring forces are reasonably described by a simple ionic picture.

The same relative trend is present in the both the high frequency and static permittivities. There is a very large difference between the purely electronic and combined electronic–ionic dielectric response in $CsSnBr_3$, which is equivalent by the Lydanne-Sachs-Teller relation to a large LO/TO splitting. In the divalent group IV chalcogenides, Waghmare and coworkers have identified large LO/TO splitting as a strong predictor for lone pair stereochemical activity. [35] Du and Singh have identified a similar giant LO/TO splitting in the radiation detector TlBr (with similar electronegativity difference to Sn and Br) and have proposed this proximal instability as a mechanism for defect screening and robust carrier transport. [99] While the static dielectric constants of $CsPbBr_3$ and $CsCaBr_3$ are both substantial (due in part to the soft potential well for Cs^+ displacement, which is highly undercoordinated in the cubic phase, *vide infra*), they are much lower than that of $CsSnBr_3$. This is consistent with our prediction that $CsPbBr_3$ should be further from this off-centering instability [35] and that there is no

Table 5.1: Born effective charges (Z^*_M) of the central metal cation M^{2+}, high-frequency dielectric permittivity (ϵ_∞), and static dielectric permittivity (ϵ_0) for CsMBr$_3$.

	Z^*_M (e)	ϵ_∞	ϵ_0
$CsSnBr_3$	5.1	6.5	68.3
$CsPbBr_3$	4.3	4.8	22.1
$CsCaBr_3$	2.5	3.1	17.5

off-centering instability at all for $CsCaBr_3$ (all three systems exhibit an instability to octahedral rotations in the cubic phase due to the non-unity tolerance factors, but this is not reflected in the dielectric response because these modes do not contribute to the polarizability of the crystal).

Energy surfaces for displacement of the octahedrally coordinated divalent cation along the high symmetry directions for $CsSnBr_3$, $CsPbBr_3$, and $CsCaBr_3$ are given in Figure 5.8(a) as a function of lattice expansion or contraction. All directions are referenced to the parent cubic cell. Such calculations on a single formula unit necessarily imply a ferroic ordering of cation displacements. Nonetheless, important qualitative differences emerge, and we find that these features are robust in more complex supercell calculations (*vide infra*). As there is minimal band reorganization due to spin-orbit coupling (Figure 5.7), we omit this computationally costly correction for our lattice dynamical studies.

At the relaxed value of the lattice parameter ($\Delta a = 0\,\%$), we see simple potential wells for cation displacement, with $\langle 111 \rangle$ the softest directions. Upon lattice expansion, the potential wells in $CsSnBr_3$ and $CsPbBr_3$ soften substantially, taking on a highly anharmonic shape. Above a critical value of the lattice expansion ($\sim 2\%$ for $CsSnBr_3$, $\sim 4\%$ for $CsPbBr_3$), the energy minimum moves off of the nominal crystallographic site. Notably, for lattice parameters of a few percent over the relaxed value (consistent with the extremely large linear coefficient of thermal expansion, $\alpha_a = 35\,\mathrm{ppm\,K^{-1}}$, determined from real-space fitting to the $CsSnBr_3$ X-ray PDF) we observe energy minima at

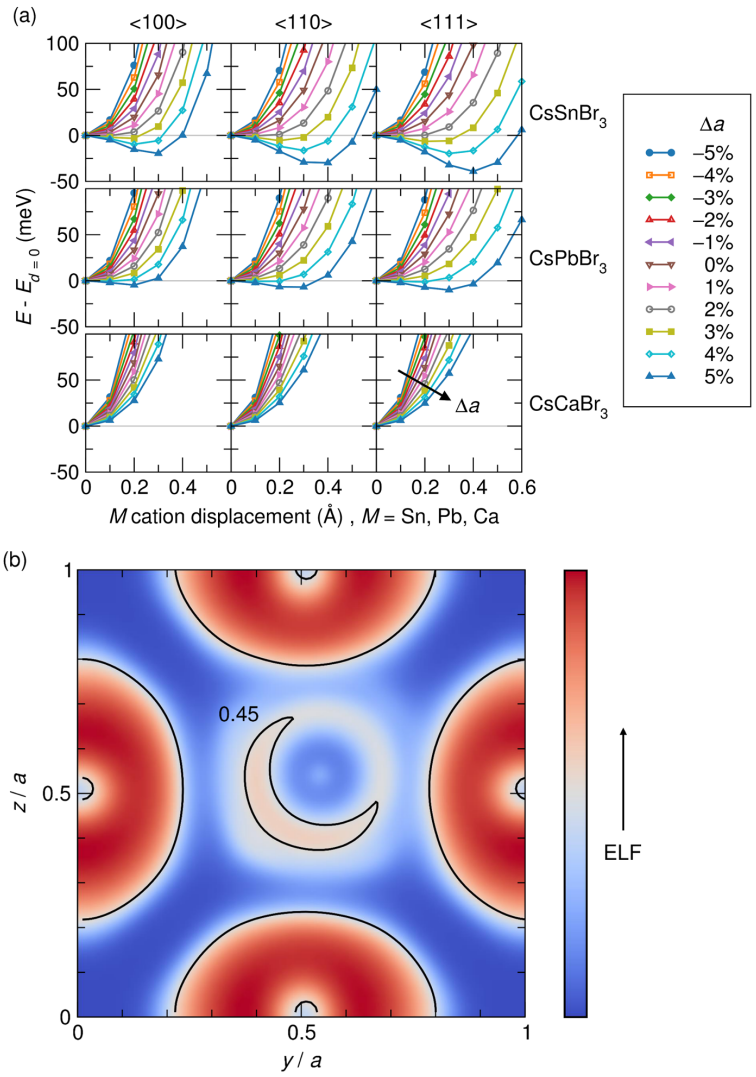

Figure 5.8: (a) Energy landscape for cation displacement in cubic CsMBr$_3$ along high symmetry directions at various compressed and expanded lattice parameters, $a = a_{nom}\,(1 + \Delta a)$. An instability is evident in $CsSnBr_3$ and $CsPbBr_3$: An energy minimum develops off the nominal crystallographic position upon lattice expansion. This effect is notably absent in $CsCaBr_3$, which lacks a lone pair of s^2 electrons. (b) The electron localization function (ELF) of $CsSnBr_3$ on a (200) slice of the unit cell (a plane through the nominal Sn site), with Sn^{2+} displaced 0.4 Å along [111] and Δa = 5 %, corresponding to the deepest well in (a). The contour at ELF = 0.45 shows clearly the localization of the $5s^2$ lone pair into a lobe opposite the direction of ion displacement. The regions of strong localization around Br^- are indicative of the non-bonding electrons in the Br p orbitals orthogonal to the sp hybridized Sn–Br bonds.

displacements on the order of tenths of an Angstrom, with depths on the order of k_BT. These displacements are well within the resolution of PDFs calculated from X-ray and neutron scattering, and are in essential agreement with the separation of the high-r shoulder and the main peak for the first Sn–Br correlation from experiment at elevated temperatures (Figures 5.2, 5.5). The shallow depth of the energy wells relative to the available thermal energy is consistent with these displacements being dynamic in nature. At the relaxed lattice parameter, cubic $CsSnBr_3$ and $CsPbBr_3$ are both proximate to an instability characterized by dynamic off-centering of the lone pair-bearing main-group cation. This instability can be activated by lattice expansion. $CsPbBr_3$ is further from this instability as expected from the lesser tendency for lone pair stereochemical activity of Pb^{2+}. [35]

Importantly, this feature is absent in the perovskite $CsCaBr_3$, which lacks a lone pair on the divalent cation. Ca^{2+} is chosen for comparison because of its identical ionic radius to Sn^{2+} in octahedral coordination, as calculated from bond valence sums in oxides. [216, 154] Because effective ionic size depends on the ligands, $CsSnBr_3$ and $CsCaBr_3$ have different relaxed lattice parameters. To ensure that a similar feature does not develop on further lattice expansion, calculations on $CsCaBr_3$ were carried out up to a lattice parameter of 10% over the relaxed value. No such feature developed, and the data is omitted from Figure 5.8(a) for clarity. There is no covalent driving force for Ca^{2+} displacements in cubic $CsCaBr_3$ because there are no lone pair electrons to mix with the orbitals of the ligands.

Visualization of electronic structure in real space via the electron localization function (ELF) provides additional information about the role of the lone pair in this lattice instability. The ELF is a real space scalar field which measures the spatially resolved effect of Pauli repulsion (essentially, the difference in kinetic energy between otherwise equivalent systems of fermions and bosons), and which may be used to classify

electrons as bonding, non-bonding, or core based on topological analysis. [217] A 2-D slice of the ELF of $CsSnBr_3$ along (200) is presented in Figure 5.8(b), for the case where Sn^{2+} is displaced along [111]. An asymmetric lobe of elevated localization opposite to the direction of cation displacement is indicative of the broken inversion symmetry of the lone pair that has become stereochemically active. In the undistorted case, the lone pair retains octahedral symmetry and the corresponding local maximum of the ELF occurs on a symmetric shell about Sn^{2+} rather than at a point away from the nucleus as it does here. The stereochemically active lone pair localizes as a lobe opposite the direction of cation displacement.

To investigate the importance of spatial coherence (ferroic ordering) of cation displacements, we consider high symmetry displacement patterns of Sn^{2+} in a $2\times2\times2$ supercell. The resulting energy surfaces are given in Figure 5.9 for an expanded lattice parameter ($\Delta a = 5\,\%$). The anion and *A*-site sublattices are rigidly fixed and all distinct combinations of high symmetry real-space cation displacement directions and high symmetry reciprocal-space vectors describing the spatial modulation of displacements are considered.

The Γ-like displacements are identical to the ferroic case presented above and are the most energetically favorable for all directions considered. For displacements along $\langle100\rangle$ and $\langle110\rangle$, other orderings where the sign of the displacements are modulated along vectors orthogonal to the displacements themselves are similarly favorable (100 X, 001 M, 101 X; no such scenarios are possible for $\langle111\rangle$ displacements). Thus, the dominant unfavorable interaction is the displacement of neighboring Sn^{2+} ions towards each other, suggesting that displacements are locally coherent (in fact, this feature may indicate a tendency for "chain-like" ordering of displacements, as in $BaTiO_3$ [218]). The potential well is sufficiently shallow relative to the available thermal energy that the cations do not localize and break global inversion symmetry, but rather explore this

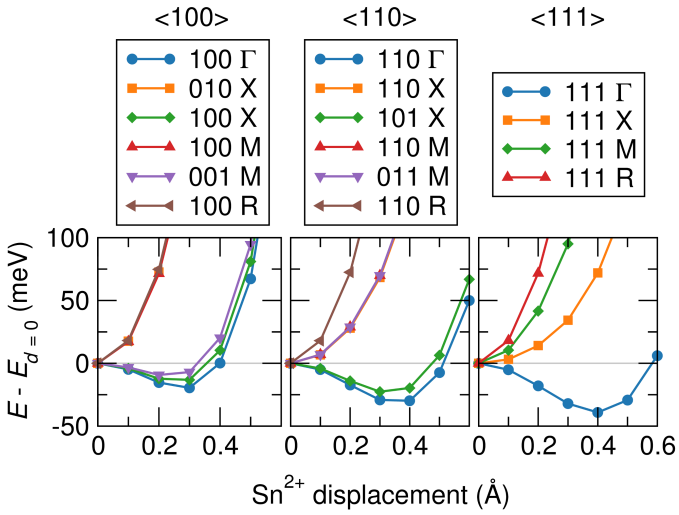

Figure 5.9: Energy landscape for symmetrically distinct high symmetry displacement patterns of Sn^{2+} for a 2×2×2 supercell, with expanded lattice parameter, $\Delta a = 5\,\%$. The nominal real-space directions of cation displacement are indicated, as well as the high symmetry reciprocal-space vectors describing the alternation of displacements from octahedron to octahedron along each of the cubic axes. Only Sn^{2+} is displaced; the *A* and *X* sublattices are unperturbed.

8-well potential dynamically (local minima along each of the ⟨111⟩ directions). Big box calculations that consider more complex displacement patterns (that is, reciprocal-space vectors other than only those at the Brillouin zone edges) may provide more information about the nature of fluctuating polar nanodomains, though we expect that such energy surfaces would be bracketed by the stiffest and softest curves presented in Figure 5.9.

5.3.3 Impact of dynamic off-centering on properties

In addition to its importance for our fundamental understanding of lone pair electrons in the solid state and the coupling between electronic structure and lattice dynamics, this dynamic lone pair stereochemical activity has significant implications for material properties and functionality. Indeed, any property which couples to the lattice will be influenced by the strong anharmonicity that emerges on warming.

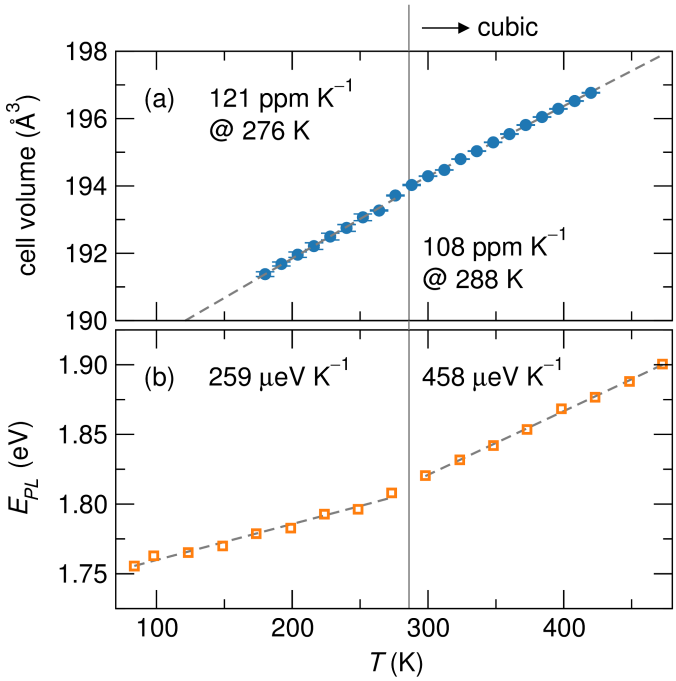

Figure 5.10: Experimental evolution of unit cell volume and photoluminescence (PL) emission peak energy, E_{PL}, with temperature. (a) The volumetric thermal expansion coefficient is 12% larger below the tetragonal–cubic transition than in the cubic phase, and is among the highest reported for any inorganic solid. [168] (b) The energy of the PL peak blue-shifts with temperature between 80 K and 480 K, consistent with the effects of volumetric expansion on the "orbital-inverted" electronic structure. The blue-shift becomes 77% more rapid in the cubic phase, despite the more gradual thermal expansion, suggesting a substantial contribution from dynamic Sn^{2+} displacements.

The experimentally observed cell volume, extracted from real-space fitting of the X-ray PDFs over the 20 Å to 50 Å range, and the temperature dependence of the photoluminescence (PL) emission peak energy is presented in Figure 5.10 (raw PL spectra are given in the Supporting Information). Of note, volumetric thermal expansion is extremely rapid (β = 121 ppm K^{-1} at 276 K, fully two-thirds the value for liquid Hg, and just smaller than that of $CsSnI_3$ [168]). This rapid thermal expansion may itself be a consequence of lone pair-induced anharmonicity. Upon warming to the cubic phase, β is somewhat reduced, possibly due to a negative contribution from dynamic octahedral tilts as in ReO_3 [206] and ScF_3. [219]

To understand the rapid blue-shift of the PL emission peak, we computed the electronic bandgap and band edge positions as functions of lattice expansion and Sn^{2+} displacement. The results, as well as a qualitative band diagram constructed from molecular orbitals, are presented in Figure 5.11. The bandgap of $CsSnBr_3$ widens on lattice expansion due to simultaneous narrowing and stabilization of both the valence and conduction bands, consequences of their antibonding character. This is in opposition to the computed behavior of $CsCaBr_3$ which, like group IV, III–V, and II–VI semiconductors, has a bandgap between bonding and antibonding states. Ferroic Sn^{2+} displacements along [111] are also seen to widen the gap by reducing orbital overlap from a maximum in the high symmetry state.

Experimentally, the PL peak (a proxy for the bandgap, barring abrupt changes in defect or excitonic levels) is observed to blue-shift with warming for all temperatures studied, as expected based on volumetric expansion and the underlying electronic structure. However, the blue-shift becomes 77% more rapid in the cubic phase, despite the reduced volumetric thermal expansion coefficient. Though inclusion of electron–phonon coupling is required for a comprehensive treatment of finite temperature effects, the magnitude of this trend suggests a substantial contribution from the local, dynamic Sn^{2+} displacements that are present in the cubic phase.

The anharmonic potential surface for cation displacement associated with emphanisis also gives rise to an elevated dielectric response, as we have calculated for the relaxed cubic cell in the previous section (the response should be substantially greater at finite temperatures, given the massive positive thermal expansion). In principle, the ionic part of the dielectric response can be tuned to be arbitrarily large by bringing the system to the brink of the ferroelectric transition. This can be achieved by alloying of a lighter halogen, a lighter carbon-group element, or a larger *A*-site cation such as methylammonium or formamidinium which will increase the propensity for lone pair

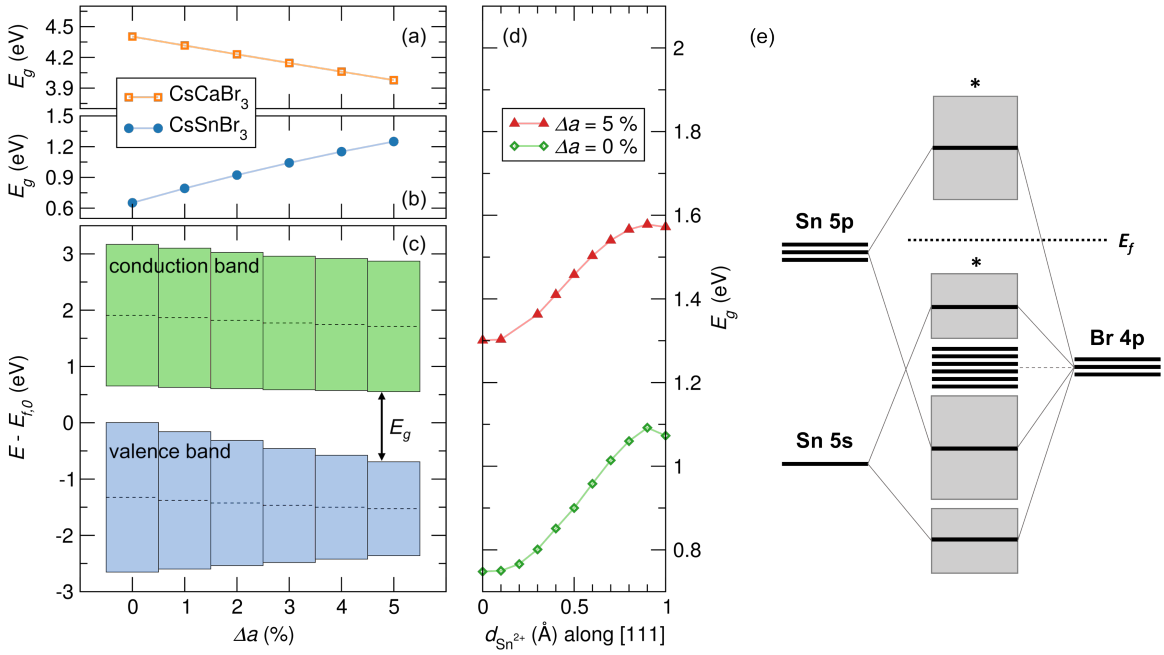

Figure 5.11: Evolution of the computed (PBE) bandgap, E_g, with lattice parameter expansion, Δa, for cubic (a) $CsCaBr_3$ and (b) $CsSnBr_3$. (c) Evolution of the $CsSnBr_3$ valence band and conduction band edges with lattice expansion, showing the simultaneous narrowing and stabilization of both bands due to weakened antibonding interactions. Band centers are indicated by dashed lines, and all are plotted on a common energy scale by aligning the energy of dispersionless Cs states. This is contrary to the bandgap evolution of tetrahedral semiconductors, [220] and of isostructural $CsCaBr_3$, which lacks an s^2 lone pair. (d) Evolution of the computed (PBE) bandgap with rhombohedral Sn^{2+} displacement in $CsSnBr_3$. Cation displacement serves to widen the bandgap, as has been calculated for frozen soft phonons in PbTe. [173] (e) Qualitative band diagram for 3-D corner-sharing $[SnBr_3]^{-1}$ octahedral network which reflects the calculated electronic structure in Figure 5.7.

stereochemical activity. [35] Because of the importance of defect screening for carrier transport, such tuning can be used to enhance carrier mobilities, as has been shown in pseudo-Jahn–Teller perovskite oxides. [170] In the high performance perovskite halide $CH_3NH_3PbI_3$, the large polarizability associated with the lone pair and with molecular reorientation may explain why carrier scattering is dominated by phonons rather than charged impurities. [221, 222, 223]

The details of charge transport in the halide perovskites remain mysterious, in particular the peculiar existence of extremely long carrier diffusion lengths [164, 224, 225] and lifetimes [226, 225] despite modest mobilities. [227, 228] Experimental and theoretical reports propose various mechanisms for reconciling these observations and the temperature dependence of carrier mobilities, including the formation of large polarons which increase carrier effective mass and protect against bimolecular recombination, [227] free carrier transport limited by acoustic [221, 223] or optical [229] phonons, and photon recycling. [167] The dynamic lone pair stereochemical activity we observe in $CsSnBr_3$ has implications for carrier recombination and transport in the halide perovskites beyond enhanced dielectric screening of charged defects. The short range spatial coherence of Sn^{2+} fluctuations suggested by our ab initio calculations implies the creation of polar nanodomains that will tend to separate electrons and holes in real space, thus reducing bimolecular recombination. [230, 231, 165] Additionally, Sn^{2+} displacements along certain directions split the otherwise degenerate conduction band minima in momentum due to the local symmetry-breaking. Such momentum-splitting, arising either from local distortions [232, 233] or spin-orbit coupling [234, 235] has been proposed to limit carrier recombination. [232, 234, 235] Further, the off-centering tendency of the divalent cation contributes to the lattice deformability, which would aid the formation of large polarons which may protect carriers from bimolecular recombination. [227]

Emergent anharmonicity in the phonon spectrum associated with lone pair stereochemical activity also has implications for phonon lifetimes and associated properties. The large fluctuating Pb^{2+} displacements in PbTe at elevated temperatures have been correlated with strong scattering of acoustic phonons and corresponding low lattice thermal conductivity, a fortuitous attribute for a high performance thermoelectric material. [236, 237, 238] One expects that the extremely low thermal conductivity of $CH_3NH_3PbI_3$ is in part due to this lone pair-driven anharmonicity. [239]

5.3.4 Competing instabilities at lower temperatures: Structural transitions

From laboratory X-ray diffraction, $CsSnBr_3$ is reported to undergo three successive phase transitions from the cubic perovskite structure upon cooling: to tetragonal $P4/mbm$ (no. 127) at 292 K, to $P42_12$ (no. 90) at 274 K, and to an undetermined monoclinic phase at 247 K. [240] The cubic to tetragonal phase transition has also been observed in ^{119}Sn Mössbauer, [241] ultraviolet photoelectron, and X-ray photoelectron spectroscopy. [242] Mössbauer additionally suggests a transition at approximately 260 K. While the cubic to tetragonal phase transition at 292 K is widely reported, [243, 240, 241, 242] the successive phase evolution upon cooling remain ambiguous.

High resolution Bragg scattering and differential scanning calorimetry (Supporting Information) reveal a first-order phase transition at 286 K and a continuous phase transition around 250 K. Candidate space groups for the low temperature (100 K) phase were screened with DFT as discussed in the methods section: The 15 unique octahedral tilt systems [204] were seeded with displacements of the Br sublattice and allowed to relax in a 2×2×2 supercell. Resulting energies, referenced to the cubic aristotype ($a^0a^0a^0$ in Glazer notation [244]), are presented in Figure 5.12. It is seen that the

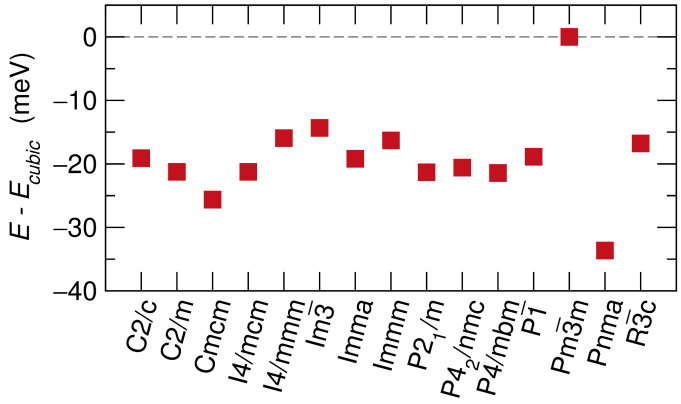

Figure 5.12: Total energy (per formula unit) of relaxed structures with the 15 unique octahedral tilt systems relative to the energy of the cubic $Pm\bar{3}m$ aristotype. The structure with $Pnma$ space group symmetry is substantially lower in energy than any other, suggesting a ground state structure with $a^-b^+a^-$ tilts. This model is confirmed by our Rietveld analysis of X-ray and neutron diffraction experiments (Figure 5.13). Figure prepared by Jonathon S. Bechtel.

structure with the $Pnma$ space group is lower in energy than any other tilt system, suggesting a ground state structure with $a^-b^+a^-$ tilts. Based on this screening, a joint Rietveld refinement was performed on the X-ray and neutron diffraction data at 100 K against the orthorhombic $Pnma$ (no. 62) structure with Cs^+ in the $4c$ Wyckoff site at $(x, \frac{1}{4}, z)$, Sn^{2+} in the $4b$ site at $(0, 0, \frac{1}{2})$, and Br^- in the $4c$ and $8d$ sites at $(x, \frac{1}{4}, z)$ and (x, y, z), respectively. The resulting fit and select crystallographic data are summarized in Figure 5.13(a), 5.13(b) and Table 5.2. Both sets of data are indexed and fit well by this structural model. ADPs are reduced in comparison to those of the higher temperature structures, and this indicates that the disorder is a dynamic, temperature-driven effect. Ab initio calculations of the phonon dispersion for this $Pnma$ phase (Supporting Information) reveal no unstable modes, suggesting that there is no further phase evolution on cooling below 100 K. Calculations of the bond valence sums (BVS) [245, 246] for Cs^+ in a 12-coordinate site using bond valence parameters extrapolated by Brese and O'Keeffe, [247] give BVS of 0.86 and 0.53 at 100 K and 300 K, respectively. Cs is severely under-bonded in the cubic phase, but combined Cs and Br displacements in

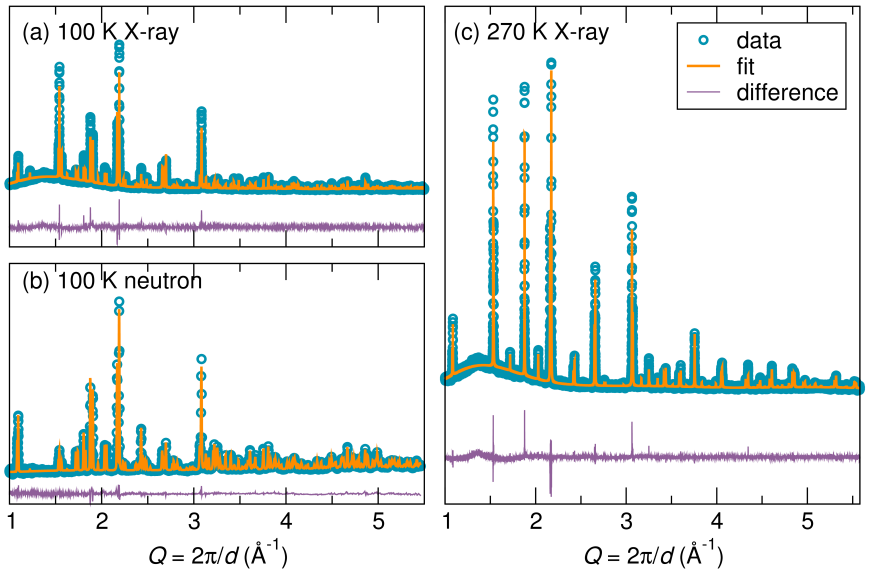

Figure 5.13: Fits obtained from the Rietveld refinements of the low temperature phases of $CsSnBr_3$. The joint refinement of the (a) X-ray and (b) TOF neutron diffraction data at 100 K indicates the data is well fit against orthorhombic $Pnma$. (c) Refinement of the X-ray diffraction data at 270 K shows the data is well fit with tetragonal $P4/mbm$. Figure prepared by Geneva Laurita.

the orthorhombic phase raise the BVS closer to the nominal value of 1, optimizing Cs coordination and stabilizing the $Pnma$ structure. Fits of the 100 K X-ray PDF data over a 2 Å to 5 Å range against the refined average $Pnma$ structure show the local structure of $CsSnBr_3$ is described well by this model (Supporting Information).

Rietveld refinement of the X-ray diffraction data collected at 270 K was performed against a structural model with space group $P4/mbm$ with Cs^+ in the $2c$ Wyckoff site at $(\frac{1}{2}, 0, \frac{1}{2})$, Sn^{2+} in the $2a$ site at $(0, 0, 0)$, and Br^- in the $2d$ and $4g$ sites at $(0, 0, \frac{1}{2})$ and $(x, y, 0)$, respectively. The resulting fit and select crystallographic data are summarized in Figure 5.13(c) and Table 5.2. Refinement against the $P4/mbm$ structure provided a reasonable fit of the data ($R_w = 9.21\,\%$). Refinement against the reported $P42_12$ structure [240] was performed, but yielded a poorer fit ($R_w = 9.58\,\%$) and is shown in the Supporting Information. Additionally, assignment of $P4/mbm$ space group symmetry is consistent with calculations of the preferred octahedral tilts for perovskite bromides

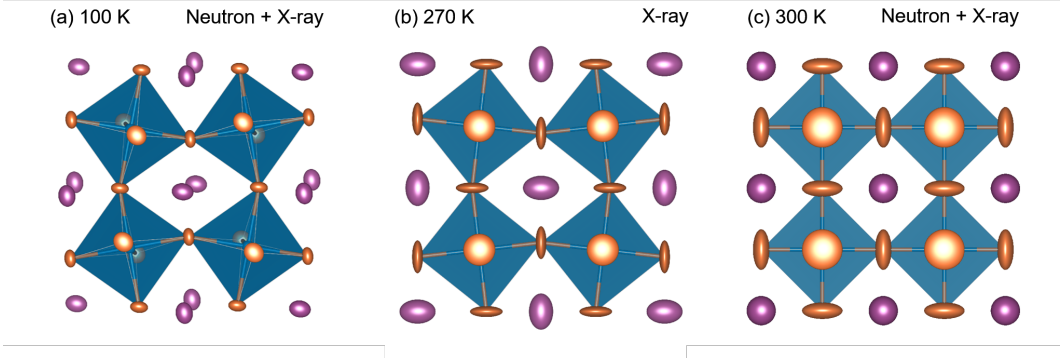

Figure 5.14: Evolution of the crystallographic structures of $CsSnBr_3$ upon warming from (a) orthorhombic $Pnma$ at 100 K, to (b) tetragonal $P4/mbm$ at 270 K, to (c) cubic $Pm\bar{3}m$ at 300 K. ADPs for all structures shown at 90 % probability. Figure prepared by Geneva Laurita.

[248] and with calorimetry (Supporting Information): The transition from $Pnma$ to $P4/mbm$ is allowed to be continuous under Landau theory, while $Pnma$ to $P42_12$ is not (ISOTROPY Software Suite, iso.byu.edu). As expected, the BVS for Cs (0.63 at 270 K) is intermediate to those in the cubic and orthorhombic phases.

Through the application of Rietveld analysis of X-ray and neutron diffraction data, it was determined that $CsSnBr_3$ adopts the following structures: orthorhombic $Pnma$ below 250 K, tetragonal $P4/mbm$ between 250 K and 286 K, and cubic $Pm\bar{3}m$ above 286 K. The successive phases are visualized in Figure 5.14. Upon cooling, the structure undergoes an in-phase rotation of the $SnBr_6$ octahedra about the *c*-axis corresponding to an $a^0a^0c^+$ tilt, which is consistent with calculations of the preferred octahedral tilts for perovskite bromides. [248] Additional out-of-phase rotation is observed at 100 K, corresponding to an $a^-b^+a^-$ tilt. In addition to the onset of rotational transitions, the isotropic ADP of Sn^{2+} is reduced upon cooling, implying the disorder around the crystallographic site is dynamic in nature and off-centering is suppressed at low temperatures. There is an observed increase in the Sn–Br bond lengths and decrease in the Sn–Br–Sn bond angles with cooling, indicating the degree of overlap between the Sn(p) and Sn(s)–Br(p) orbitals decreases as the structure undergoes the successive

Table 5.2: Select crystallographic data from the Rietveld refinements of powder synchrotron X-ray and neutron diffraction data of $CsSnBr_3$ at 100 K, 270 K, and 300 K.

Temperature (K)	100	270	300
Data sets	X-ray, neutron	X-ray	X-ray, neutron
Space Group	$Pnma$	$P4/mbm$	$Pm\bar{3}m$
a (Å)	8.1965(2)	8.1789(2)	5.8043(3)
b (Å)	11.5830(3)	8.17989(2)	5.8043(3)
c (Å)	8.0243(2)	5.8193(2)	5.8043(3)
Volume (Å^3)	761.82(3)	389.29(3)	195.546(5)
Sn U_{iso} (Å^2)	0.013(5)	0.024(2)	0.022(5)
Cs U_{11} (Å^2)	0.033(5)	0.082(5)	0.077(2)
Cs U_{22} (Å^2)	0.021(4)	0.082(5)	0.077(2)
Cs U_{33} (Å^2)	0.038(5)	0.057(8)	0.077(2)
Cs U_{12} (Å^2)	0.0	-0.032(9)	0.0
Cs U_{13} (Å^2)	-0.008(4)	0.0	0.0
Cs U_{23} (Å^2)	0.0	0.0	0.0
Br1 U_{11} (Å^2)	0.033(4)	0.090(9)	0.02(2)
Br1 U_{22} (Å^2)	0.010(3)	0.090(9)	0.148(3)
Br1 U_{33} (Å^2)	0.042(4)	0.018(9)	0.148(3)
Br1 U_{12} (Å^2)	0.0	0.0	0.0
Br1 U_{13} (Å^2)	-0.007(4)	0.0	0.0
Br1 U_{23} (Å^2)	0.0	0.0	0.0
Br2 U_{11} (Å^2)	0.020(2)	0.052(7)	–
Br2 U_{22} (Å^2)	0.032(2)	0.052(7)	–
Br2 U_{33} (Å^2)	0.023(2)	0.119(9)	–
Br2 U_{12} (Å^2)	0.0	0.041(8)	–
Br2 U_{13} (Å^2)	-0.008(2)	0.0	–
Br2 U_{23} (Å^2)	0.002(2)	0.0	–
Sn–Br1 (Å)	2.9245(7)	2.9096(9)	2.9021(5)
Sn–Br2 (Å)	2.927(3)	2.910(9)	–
Sn–Br1–Sn (°)	164.0(2)	180	180
Sn–Br2–Sn (°)	156.8(4)	167.0(5)	–
R_w (%)	5.48	9.21	4.31

rotational phase transitions. The reduction of orbital overlap results in less propensity for stereochemical activity of the Sn^{2+} lone pair, and thus less tendency for Sn^{2+} off-centering. Additionally, octahedral rotations bring the ions closer together, resulting in a larger electrostatic penalty for Sn^{2+} displacement. These observations illustrate the competing tendencies for lone pair stereochemical activity and octahedral rotations. At elevated temperatures, the former dominates, while the latter emerges upon cooling and suppresses off-centering of Sn^{2+}. A discussion of the competition between covalency and ionicity for the related perovskite $CsPbF_3$ is given by Smith and coworkers, [249] which displays both $a^-a^-a^-$ octahedral rotations and Pb^{2+} displacements in the low temperature phase. [250]

5.4 Conclusion

The main-group halide perovskite $CsSnBr_3$ exhibits competing tendencies for local Sn^{2+} off-centering and $SnBr_6$ octahedral rotations. Due to the presence of the $5s^2$ lone pair, an instability emerges in the cubic phase as the lattice is expanded on warming. This instability is characterized by dynamic off-centering of Sn^{2+} in its coordination environment and the localization of the stereochemically active $5s^2$ lone pair as a lobe opposite the direction of cation displacement, providing evidence of emphanisis in this material. These displacements occur preferentially along $\langle 111 \rangle$ and likely exhibit some short-range coherence. While this locally distorted state is "crystallographically hidden" (the only clue being elevated thermal displacement parameters for Sn^{2+} when refined in a high symmetry environment), it is evident in the pair distribution function as emergent asymmetry in the first Sn–Br correlation, and is corroborated by ab initio calculations of the lattice dynamics, dielectric properties, and electronic structure of the crystal. Similar calculations on isostructural $CsPbBr_3$ and $CsCaBr_3$ indicate that this

off-centering instability is present but weaker in $CsPbBr_3$, in accordance with existing theory of lone pair stereochemical activity, and is entirely absent in $CsCaBr_3$, which lacks a lone pair on the divalent cation. These local cation displacements drive a rapid blue-shift of the bandgap on warming which is observed in photoluminescence measurements. Upon cooling, $CsSnBr_3$ undergoes successive phase transitions driven by octahedral rotations, with the unit cell transforming from orthorhombic to tetragonal to cubic. In crystal structure models for the tetragonal and orthorhombic phases, reduced thermal displacement parameters for Sn^{2+} suggest that there are no coherent or local cation displacements that are not captured by the model: Lone pair stereochemical activity is suppressed by the octahedral rotations. The phenomenon is likely to be quite general and one would expect to observe emphanisis also in the cubic phases of $CsSnCl_3$ and $CsSnI_3$ with the strength of the effect increasing as the halogen atoms become lighter and more electronegative. [35]

The unusual structure evolution of $CsSnBr_3$ sheds further light on the role of lone pair electrons in extended inorganic solids. Chemical tuning to bring about this proximal instability in the halide perovskites offers a means to tailor the properties of these curious and promising semiconductors: By exploiting lone pair stereochemistry, it is possible to engineer lattice polarizability that enhances dielectric response and promotes polaron formation, thermal conductivity reduction, anomalous bandgap evolution with temperature, and possibly other functionalities.

Chapter 6

Chemical tuning of lone pair stereochemical activity in hybrid tin and lead perovskites

[1] Hybrid halide perovskites combine ease of preparation and relatively abundant constituent elements with fascinating photophysical properties. Descriptions of the chemical and structural drivers of the remarkable properties have often focused on the potential role of dynamic order/disorder of the molecular *A*-site cations. We reveal here a key aspect of the inorganic framework that potentially impacts electronic, thermal, and dielectric properties. The temperature evolution of the X-ray pair distribution functions of hybrid perovskites ABX_3 [$A^+ = CH_3NH_3$ (MA) or $CH(NH_2)_2$ (FA); B^{2+} = Sn or Pb; X^- = Br, or I] in their cubic phases above 300 K reveal temperature-activated displacement (off-centering) of the divalent group 14 cations from their nominal, centered sites. This

[1]The contents of this chapter have substantially appeared in reference [51]: G. Laurita, D. Fabini, C. Stoumpos, M. Kanatzidis, R. Seshadri, Chemical tuning of dynamic cation off-centering in the cubic phases of hybrid tin and lead halide perovskites, *Chem. Sci.* **2017**, *8*, 5628–5635, Published by The Royal Society of Chemistry, reprinted with permission.

symmetry-lowering distortion phenomenon, previously dubbed *emphanisis* in the context of compounds such as PbTe, is attributed to Sn^{2+} and Pb^{2+} lone pair stereochemistry. Of the materials studied here, the largest displacements from the center of the octahedral sites are found in the tin iodides, a more moderate effect is found in the lead bromides, and the weakest effect is seen in the lead iodides. The *A*-site cation appears to play a role as well, with the larger FA resulting in greater off-centering for both Sn^{2+} and Pb^{2+}. Dynamic off-centering, which is concealed within the framework of traditional Bragg crystallography, is proposed to play a key role in the remarkable defect-tolerant nature of transport in these semiconductors *via* its effect on the polarizability of the lattice. The results suggest a novel chemical design principle for future materials discovery.

6.1 Introduction

Inorganic and hybrid organic–inorganic halide perovskites ABX_3 [A^+ = Cs, CH_3NH_3 (MA), or $CH(NH_2)_2$ (FA); B^{2+} = Ge, Sn, or Pb; X^- = Cl, Br, or I] have attracted significant research attention of late due to their impressive optoelectronic performance, ease of preparation, and abundant constituent elements. Since the first application of hybrid lead iodides in photovoltaic (PV) devices in 2009, [7] the conversion efficiency of record perovskite PV cells has risen to over 20%, [251] and the field has broadened substantially to include the pursuit of lead-free materials, [14, 13, 121, 15, 16, 252, 253, 254, 255] bromides and mixed halides for light emission and detection applications, [21, 24, 23, 22, 256, 257] and layered perovskite-derivatives for enhanced stability. [11, 155, 258] However, key aspects regarding the origins of the remarkable functionality of these materials remain enigmatic. Among them are: Why do the low rates of carrier trapping and recombination [259, 221, 260, 256, 257] in these relatively soft,

solution-processed materials approach those of the best high purity III–V semiconductors, leading to long carrier lifetimes and long diffusion lengths? [164, 259] Why are carrier mobilities so modest, [221, 259, 228] relative to calculated carrier effective masses and typical scattering rates? In answering these questions, much attention has focused on the potential importance of the *A*-site organic molecular cations in the hybrid systems, [165, 261, 262] but recent reports suggest that all-inorganic analogues exhibit many of the same structural tendencies [50, 263] and favorable transport properties. [25, 264, 265, 266, 260]

A clue then to the unusual properties potentially lies in these systems being proximate in phase space (composition, temperature, pressure, strain) to symmetry-lowering distortions of the octahedral coordination environment of the group 14 divalent cation. The presence of this instability and the role that it may play in the properties of the perovskites have been hinted at in prior reports, [189, 93, 233, 50] but have not been explored in detail, nor have the impacts on the properties been fully considered. The strength of this effect is dictated by the stability of the ns^2 level of the isolated lone-pair bearing cation and the electronegativity of the halogen. In the case of the perovskites studied here, the Goldschmidt tolerance factor as influenced by the size of the *A*-site cation, and potentially, the shape of the *A* cation is also likely to play a role, providing guidelines for tuning these effects in a rational manner.

Main-group cations with a valence state that is two fewer than the group valence (e.g. Sn^{2+}, Sb^{3+}, Tl^{+}, Pb^{2+}, Bi^{3+}) possess the lone pair s^2p^0 electronic configuration and are prone to symmetry-lowering distortions associated with the pseudo- or second-order-Jahn-Teller effects. [33, 34] Heavier cations have deep ns^2 levels due to relativistic stabilization, reducing the strength of the on-site s–p hybridization. The higher energy of the ns^2 levels of lighter cations, as well as the mixing with anion p orbitals leads to stereochemical expression of the lone pair. [36, 38, 39, 35, 41] This is

exemplified in the AGeI$_3$ (A^+ = Cs, MA, FA) perovskite analogs, [17] where the strong tendency for activity of the s^2 electrons of Ge result in room-temperature structures with highly distorted Ge environments, that also happen to be polar. In contrast, the heavier Sn and Pb atoms form halide perovskite compounds that can crystallize with these cations in relatively regular octahedral environments.

The choice of ligand is also a key factor, with more electronegative anions resulting in greater interaction of anion p states with the orbitals of the cation and thus greater propensity for the off-centered coordination polyhedra associated with lone pair stereochemical activity. [35] When the propensity for lone pair stereochemical activity is not sufficiently strong relative to thermal energy to produce a ferroically distorted phase, uncorrelated, local off-centering displacements of the main-group cation can result. Such displacements have recently been observed to emerge from a high symmetry phase upon heating in rock-salt group 14 chalcogenides, [172, 179, 171] and have been termed *emphanisis*. This phenomenon leads to substantial anharmonicity of the lattice dynamics, contributing to the observed ultralow thermal conductivity important for thermoelectrics, [267] and has been a topic of intense interest since the first reports. [173, 177, 181, 174, 175, 180, 178, 176] Our recent work has shown a similar dynamic displacement of Sn^{2+} in CsSnBr$_3$ at ambient and elevated temperatures, [50] suggesting that an emphanitic local distortion of the metal halide network may also be present in the technologically important hybrid halide perovskites.

We show here that the tendency for symmetry-lowering local distortions of the group 14 cation coordination environment exists across the hybrid halide perovskites. Pair distribution functions for ABX_3 (A^+ = MA and FA; B^{2+} = Sn and Pb; X^- = Br and I) calculated from X-ray scattering at and above 300 K reveal temperature-activated, dynamic off-centering of the lone pair-bearing Sn^{2+} and Pb^{2+} cations that is not observed through traditional crystallographic techniques. This local off-centering is described by

displacements along ⟨111⟩, and we find the largest degree of off-centering in the lead-free tin iodides, a moderate degree in the lead bromides, and the smallest degree in the lead iodide compositions. This qualitative agreement with the chemical predictors of lone pair stereochemical activity as enumerated for the group 14 chalcogenides, [35] together with our prior *ab initio* studies of perovskite $CsSnBr_3$, [50] implicate the lone pairs as the driving force for this behavior. This phenomenon has profound implications on understanding the properties: Systems displaying this proximal instability exhibit strongly anharmonic lattice dynamics leading to an elevated static dielectric response that reduces carrier scattering, trapping, and recombination, [99, 170, 227] high coefficients of volumetric thermal expansion, [268, 168, 50, 53] and unusual temperature evolution of the bandgap. [50] The substantial lattice polarizability associated with this proximal instability is of particular importance as it may explain why carrier mobilities are limited by scattering from phonons rather than charged defects [221, 222, 223] and why carrier trapping and recombination rates are so low. [259, 221, 260] This additionally lends credence to the hypothesis of large polaron formation [227] that reconciles small carrier effective masses from band theory with the modest mobilities observed in experiment. Chemical control of this phenomenon, as demonstrated by the qualitative composition trends observed here, offers new design principles in the search for defect-tolerant semiconductors.

6.2 Methods

6.2.1 Materials preparation

The hybrid perovskites were prepared following modifications of previously reported procedures. [67] PbO and CH_3NH_3Cl were purchased from Sigma-Aldrich.

$HC(NH_2)_2Cl$ was prepared by stoichiometric addition of solid $HC(NH_2)_2(O_2CCH_3)$ in 37 % aqueous HCl, followed by rotary evaporation and washing with toluene to remove excess acetic acid. [53] Black SnO was prepared following a modification of the literature procedure. [269] Detailed procedures for the the preparation of polycrystalline samples of $CH_3NH_3PbI_3$, $HC(NH_2)_2PbI_3$, $CH_3NH_3SnI_3$, $HC(NH_2)_2SnI_3$, $CH_3NH_3PbBr_3$, and $HC(NH_2)_2PbBr_3$ can be found in the Supporting Information.

6.2.2 X-ray scattering data collection and modeling

For synchrotron total scattering measurements, samples of fine powder, obtained by means described above, were transferred into Kapton capillaries (0.81 mm OD, 0.8 mm ID) and tightly compacted to ensure the maximum packing fraction. Both ends of the capillaries were sealed with epoxy and stored in a N_2 atmosphere prior to the measurement.

Synchrotron X-ray total scattering measurements were collected on the 11-ID-B beam line at the Advanced Photon Source located at Argonne National Laboratory. 2D scattering data were collected on a Perkin-Elmer amorphous Si-based area detector. A photon wavelength of 0.2114 Å (58.66 keV) was used for $MAPbI_3$ (collected from 360 K to 300 K), $FAPbI_3$ (collected from 480 K to 300 K to ensure conversion from the yellow δ phase to the black perovskite phase, and verified by analysis of the reciprocal space data, shown in the Supporting Information at 360 K), $MAPbBr_3$ (collected from 360 K to 300 K), and $FAPbBr_3$ (collected from 360 K to 300 K). A photon wavelength of 0.1430 Å (86.70 keV) was used for $MASnI_3$ (collected from 360 K to 300 K) and $FASnI_3$ (collected from 360 K to 300 K) to avoid the Sn fluorescence edge at 29.21 keV. Data were collected every 2 minutes upon cooling at a rate of 6 K min^{-1}. Fit2D [270] was utilized to integrate the 2D data to 1D diffraction patterns. Corrections to obtain the

$S(Q)$ and subsequent Fourier Transform with a Q_{max} of 23 Å^{-1} and an r-grid of 0.01 Å to obtain the X-ray pair distribution function (PDF, $G(r)$) was performed using the program PDFgetX2. [195] These parameters were chosen to optimize the r-resolution while minimizing Fourier termination ripples satisfactorily for all samples across the series, and an example of the optimization process is shown in the Supporting Information for $FASnI_3$. Instrumental parameters used in the fits were Q_{broad} = 0.06 $\mathring{A}^{-1}$ and Q_{damp} = 0.01 $\mathring{A}^{-1}$ as determined from a CeO_2 standard.

For all samples the *A*-site cations have been modeled as a pseudo-atom with an equivalent scattering power (K for CH_3NH_3 and Mn for $CH(NH_2)_2$) placed in the center of the *A* site at (0,0,0) and given a large (between 0.2 and 0.4 Å^2) atomic displacement parameter (ADP). For all fit ranges, fits of the XPDF data were first performed against the cubic $Pm\bar{3}m$ model to obtain lattice parameters. The ADPs for the *A*- and *B*-site cations were refined isotropically, while ADPs for the halide atoms were allowed to refine anisotropically. The cubic space groups were subsequently transformed into the respective $I4cm$ and $R3m$ space groups using the "TRANSTRU" tool on the Bilbao Crystallographic Server. [271, 272, 273] Fits against the $I4cm$ model were first performed over an r-range of 2 Å to 25 Å. Lattice parameters were fixed to the transformed values from the cubic fit. The halide positions and anisotropic ADPs were allowed to refine, while *A*-site ADPs were fixed to those obtained from the cubic fit. *B*-site ADPs were fixed 0.008 Å^2. For fits against the remaining r-ranges (2 Å to 5 Å and all incremental fits), lattice parameters were fixed to the values obtained from the transformed structures, halide ADPs and displacements were fixed to the values obtained from the 2 Å to 25 Å fits while the *B*-site displacement in the $4a$ Wyckoff position $(0, 0, z)$ was allowed to refine. Fits against the $R3m$ model were first performed over an r-range of 2 Å to 25 Å. Lattice parameters were fixed to the transformed values from the cubic fit. The halide anisotropic ADPs were allowed to refine, while *A*-site ADPs were fixed

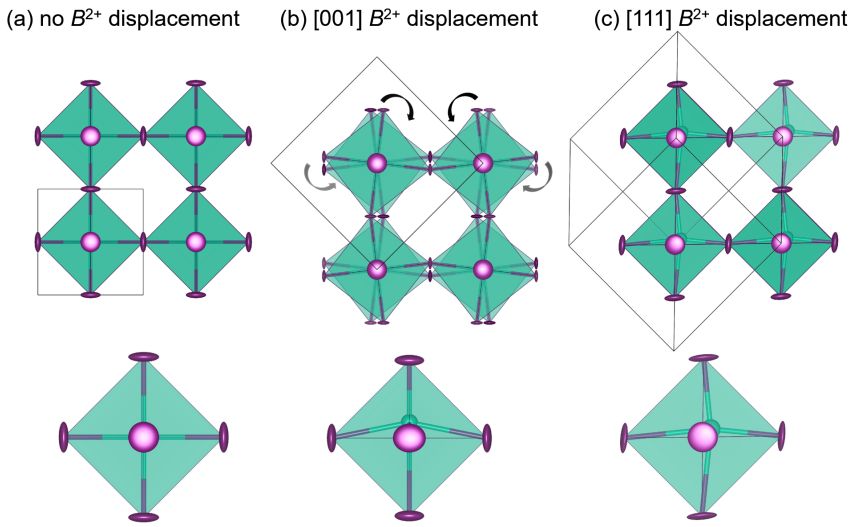

Figure 6.1: Crystal structures chosen to model the X-ray PDF data: (a) cubic $Pm\bar{3}m$ with no *B*-site off-centering or octahedral rotations, (b) tetragonal $I4cm$ with allowed *B*-site off-centering and static octahedral rotations, and (c) rhombohedral $R3m$ with allowed *B*-site off-centering and no octahedral rotations. Figure prepared by Geneva Laurita.

to those obtained from the cubic fit. *B*-site ADPs were fixed 0.008 Å^2. For fits against the remaining r-ranges (2 Å to 5 Å and all incremental fits), lattice parameters were fixed to the values obtained from the transformed structures, halide ADPs were fixed to the values obtained from the 2 Å to 25 Å fits while the *B*-site displacement in the $3a$ Wyckoff position $(0, 0, z)$ was allowed to refine.

6.3 Results & discussion

Dynamic octahedral rotations have been observed through local techniques at elevated temperatures in several halide perovskite systems [50, 233] which may be active in conjunction with dynamic off-centering of the *B*-site cations. To investigate the interplay between octahedral rotations and *B*-site stereochemical activity (and subsequent off-centering), three crystallographic models (Figure 6.1) were chosen to fit against

the X-ray PDF data over various r-ranges: cubic $Pm\bar{3}m$, which allows neither octahedral rotations nor *B*-site off-centering; tetragonal $I4cm$, which allows for simultaneous octahedral rotations and *B*-site off-centering along the c-axis; and rhombohedral $R3m$, which allows for no octahedral rotations but does allow for *B*-site off-centering along the [111] crystallographic direction. The space groups chosen to model the local symmetry of the PDF data were based on crystallographic structures with prototypical ferroic displacements in perovskite systems. In an effort to qualitatively describe the local structure, we have chosen known models that systematically lower the symmetry without drastically increasing the number or correlation of refined parameters. We have previously reported the $R3m$ structure as an approximate description of the dynamic off-centering of Sn^{2+} in $CsSnBr_3$ (in comparison to $Pm\bar{3}m$, $P4mm$, and $Amm2$ models), [50] while the local coexistence of rotations and Pb^{2+} off-centering described by $I4cm$ has been reported for crystallographically cubic $MAPbI_3$. [233]

The X-ray PDF data was analyzed from 300 K to 360 K (480 K for $FAPbI_3$), shown in Figure 6.2. The temperature at which the cubic perovskite phase is present varies for each composition: for $MASnI_3$ $T > 275$ K, [274] for $FASnI_3$ $T > 250$ K, [67] for $MAPbI_3$ $T >$327 K, [275] for $FAPbI_3$ $T > 285$ K, [53] for $MAPbBr_3$ $T > 237$ K, [275] and for $FAPbBr_3$ $T > 265$ K (unpublished reference). Therefore, quantitative studies were only performed in the known cubic phase regimes of each sample. Qualitatively, for all compositions the first *B*–I peak becomes broader and more asymmetric upon warming, and the effect is most pronounced for the Sn^{2+} samples. Peak broadening and asymmetry are expected to further increase with higher collection temperatures, which is evidenced in $FAPbI_3$, the only composition collected up to 480 K.

Fits against the X-ray PDF for each sample were performed carefully to avoid excessive correlation of the refined parameters, and the modeling is described in detail in the experimental section. To verify the samples are crystallographically cubic, the

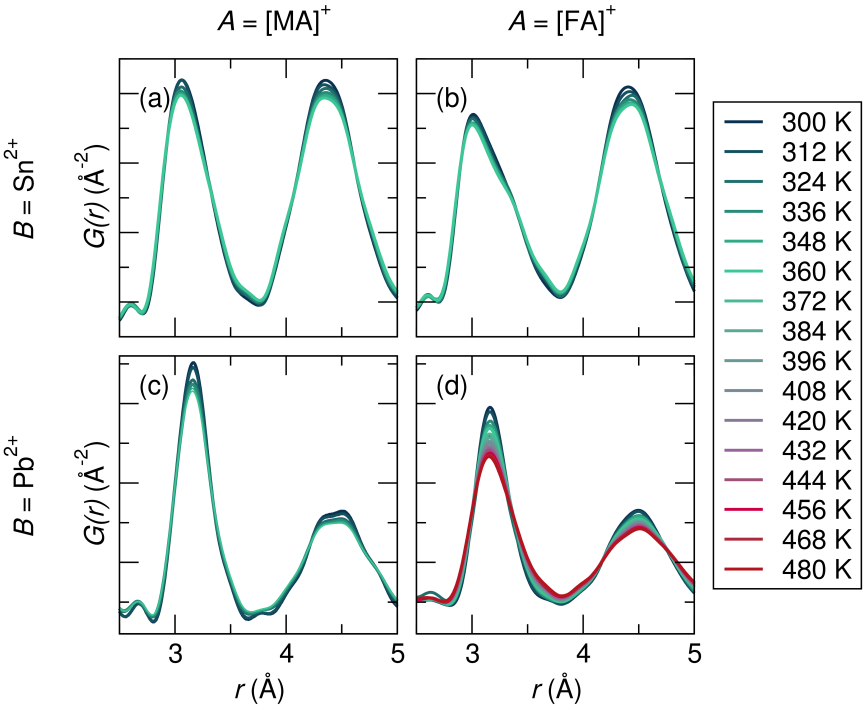

Figure 6.2: Overlay of raw X-ray PDF data collected over a range of 300 K to T_{max} for (a) $MASnI_3$ (T_{max} = 360 K), (b) $FASnI_3$ (T_{max} = 360 K), (c) $MAPbI_3$ (T_{max} = 360 K), and (d) $FAPbI_3$ (T_{max} = 480 K). Peak asymmetry of the first *B*–I correlation at approximately 3 Å is observed in all compositions, but is most pronounced in the Sn compositions. Figure prepared by Geneva Laurita.

X-ray PDF data were fit over an r-range of 10 Å to 25 Å against the cubic $Pm\bar{3}m$ model at the various reported cubic phase temperatures, and representative fits for each sample are shown in the Supporting Information. Reasonable goodness-of-fit (R_w) values (between 8 and 12 %) were obtained for all compositions, suggesting that the data are well described by expected cubic symmetry as we approach the average, crystallographic length scale. The corresponding reciprocal space data from the total scattering experiment, shown in the Supporting Information at 360 K, is additionally consistent with the cubic perovskite structure and does not indicate the presence of any impurity phases.

Fits of the X-ray PDF data at 360 K against the candidate space group models over a 2.0 Å to 5.0 Å range indicate the poorest fit for all samples against the cubic $Pm\bar{3}m$

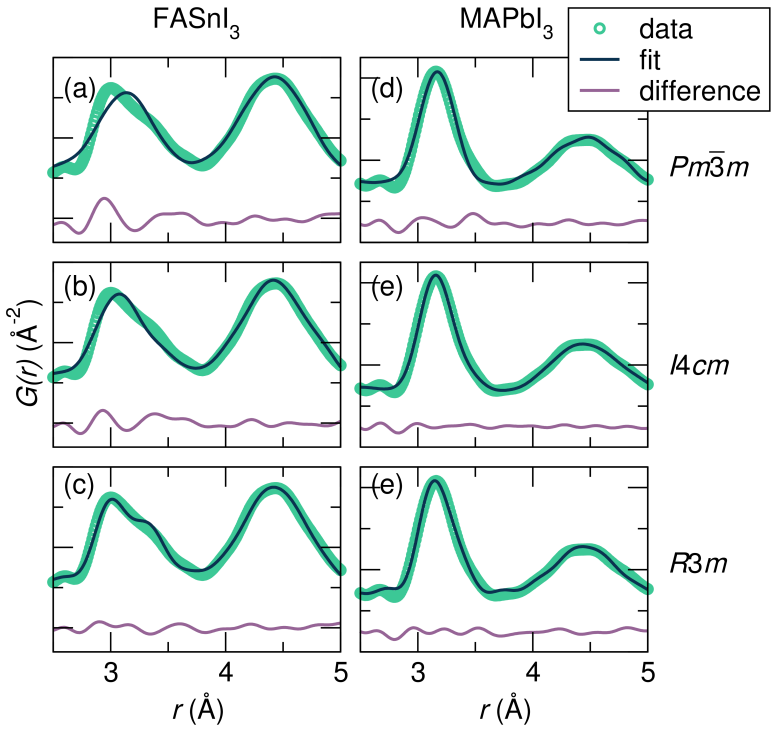

Figure 6.3: Fits of the X-ray PDF data at 360 K from 2.0 Å to 5.0 Å against the various space groups for representative samples $FASnI_3$ [(a) $Pm\bar{3}m$, (b) $I4cm$, and (c) $R3m$] and $MAPbI_3$ [(d) $Pm\bar{3}m$, (e) $I4cm$, and (f) $R3m$]. For both $FASnI_3$ and $MASnI_3$ (Supporting Information), the peak shape of the first Sn–I correlation is best captured by Sn off-centering along $\langle 111 \rangle$ as in the $R3m$ model, while $FAPbI_3$ and $MAPbI_3$ (Supporting Information) are equally well-described by both the $I4cm$ and $R3m$ models. Figure prepared by Geneva Laurita.

model. Fits for the most extreme cases, $FASnI_3$ (most distorted *B*–I peak) and $MAPbI_3$ (least distorted *B*–I peak), are shown in Figure 6.3. For both Sn^{2+} samples, the best description of the Sn–I correlation is described with the $R3m$ model, indicating off-centering best described by rhombohedral symmetry. It should be noted that the goodness-of-fit for the Sn^{2+} compositions are heavily influenced by the fit to the I–I correlations due to stronger scattering power of I vs. Sn (in comparison to I vs. Pb). This appears to result in a poorer fit in the Sn–I correlation of these samples; however, this does not change the result that the local symmetry of the Sn^{2+} compositions is best modeled with a rhombohedral off-centering of the Sn^{2+}. It should also be noted that

the use of anisotropic displacement parameters are necessary to fit the I–I correlation around 4.5 Å. However, the implementation of large anisotropic displacements of the halides perpendicular to the *B*–I bond does not account for the observed peak asymmetry of the first *B*–*X* correlation, even with highly exaggerated anisotropic components as we demonstrated for $CsSnBr_3$. [50] For both Pb^{2+} samples, a similar description of the Pb–I correlation is obtained with both the $I4cm$ and $R3m$ models. This indicates cation off-centering is present in the Pb^{2+} samples; however, it is minor compared to that of the Sn^{2+} samples, and complicated by a greater degree of correlation with the refined halide parameters. Regardless, the crystallographic cubic phase is an insufficient model of the local symmetry of the Sn^{2+} and Pb^{2+} coordination environment for all compositions.

To investigate the coherence length of distortions in the samples, 10 Å incremental fits of the PDF data at 360 K were performed (r-ranges = 1 Å to 10 Å, 5 Å to 15 Å, 10 Å to 20 Å, and 15 Å to 25 Å). R_w values of the fits against the various space group models as a function of r_{max} are shown in Figure 6.4. R_w values of the 2 Å to 5 Å fits are also plotted to illustrate the best representation of the local *B*-site coordination environment. It is observed for all samples that the cubic model quickly becomes the best description of the data as the incremental series progresses, even at an r-max of only 10 Å, and the R_w for the cubic fit continues to decrease with increasing r_{max}, further illustrating cubic symmetry as the fit range tends towards the average crystallographic structure.

In $CsSnBr_3$, we determined the presence of a dynamic displacement of the Sn^{2+} cation of approximately 0.2 Å along the [111] crystallographic direction at 420 K. [50] Fits of the local structure of the compositions studied herein indicate a similar local cation displacement. The presence of cation displacement with increasing temperature was investigated by fitting the temperature-dependent data of all samples against the $R3m$ model over a range of 2 Å to 5 Å, shown in Figure 6.5. Refined local struc-

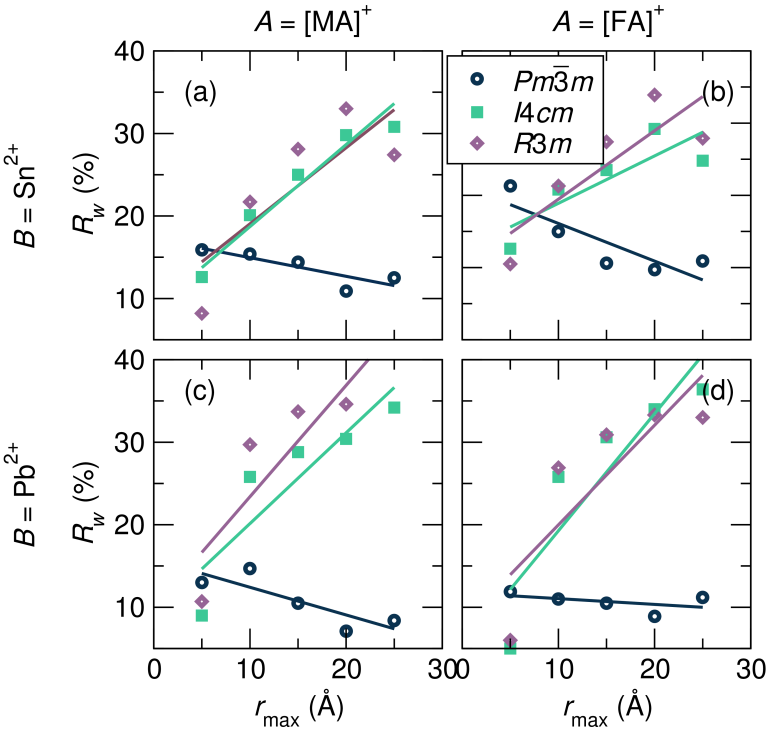

Figure 6.4: Goodness-of-fit parameters (R_w) as a function of r-max for 10 Å incremental fits of the X-ray PDF data at 360 K against the various space group models for (a) $MASnI_3$, (b) $FASnI_3$, (c) $MAPbI_3$, and (d) $FAPbI_3$. Models that allow *B*-site displacements ($I4cm$ and $R3m$) have lower R_w values with an r-max of 5 Å for all samples, while cubic $Pm\bar{3}m$ results in lower R_w values for all fits with r-max of 10 Å and above. Figure prepared by Geneva Laurita.

tures indicate large displacements are present for the Sn^{2+}-containing samples, while they are minimal in the Pb^{2+} samples. At 360 K the maximum displacement for each composition, from largest to smallest, is approximately 0.24 Å in $FASnI_3$, 0.22 Å in $MASnI_3$, 0.06 Å in $FAPbI_3$, and 0.01 Å in $MAPbI_3$. This goes with the expected trend of larger displacements in Sn^{2+} than Pb^{2+} due to larger relativistic effects in Pb and larger displacements with increasing lattice parameter from MA to FA. In addition to these cationic effects, the chemical identity of the anion and subsequent interaction between its orbitals with that of the of the *B*-site cation affects the propensity for stereochemical activity. Increasing the hardness of the anion (*i. e.* $APbBr_3$ instead of $APbI_3$) increases the interaction of the anion p states with the *B*-site s orbitals, [35] thus increasing the

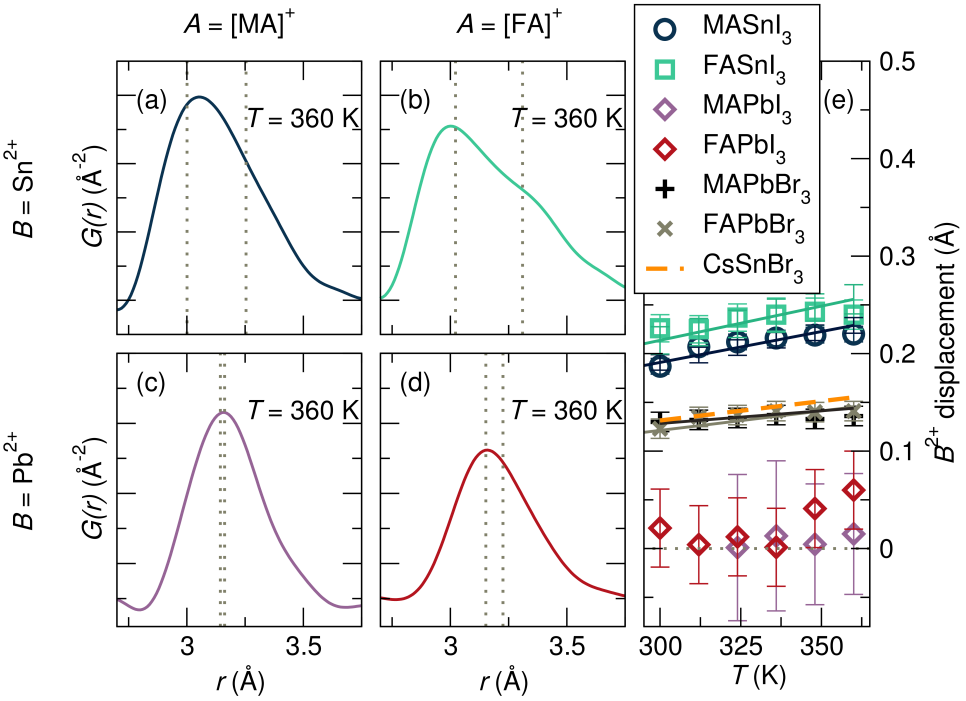

Figure 6.5: X-ray pair distribution functions for (a) $MASnI_3$, (b) $FASnI_3$, (c) $MAPbI_3$, and (d) $FAPbI_3$ at 360 K of the nearest *B*–I correlation. (e) Refined displacements of the *B*-site cation in space group $R3m$ as a function of temperature indicate large displacements for Sn^{2+} iodides and minimal displacements for Pb^{2+} iodides. Refined displacements for the $APbBr_3$ analogs indicate moderate off-centering. Reported Sn^{2+} displacements in $CsSnBr_3$ are overlaid for comparison. [50] Dashed lines in (a-d) indicate the distinct bond lengths extracted from modeling the local structure in space group $R3m$ ([111] displacement). Figure prepared by Geneva Laurita.

tendency for activity of the lone pair. Therefore, a larger rhombohedral distortion of Pb^{2+} should be observed in $MAPbBr_3$ and $FAPbBr_3$ in comparison to their iodide counterparts. Indeed, fitting of X-ray PDF data of $MAPbBr_3$ and $FAPbBr_3$ at 360 K against the $R3m$ model (Figure S6) indicates a Pb^{2+} displacement of approximately 0.15 Å. Based on the magnitudes of displacements resulting from the fits, it appears the identity of the *A*-site cation, which plays a role in the lattice parameter and influences octahedral rotations observed upon cooling, has the smallest effect on the stereochemical activation of the lone pair, and the composition of the *B*-site cation and *X*-site anion are the largest drivers for stereochemical activity of the s electrons, highlighting the importance of the

B–*X* cation–anion orbital interaction. However, the displacement magnitudes reported for $CsSnBr_3$ [50] are essentially indistinguishable from those we find for $MAPbBr_3$ and $FAPbBr_3$, suggesting that *A*-site shape may matter in addition to size, as one would expect greater displacements for Sn^{2+} than for Pb^{2+} given the same anion. We expect these chemical trends to be universal in the halide perovskite materials, even extending to the layered perovskites, which are known to exhibit distortions of the MX_6 octahedra. [276, 277, 278, 279], the dimensionality of layered perovskites may play an additional role in octahedral distortions and warrants further consideration.

6.4 Conclusion

We have shown through analysis of pair distribution functions calculated from X-ray scattering experiments that dynamic, temperature-activated *B*-site cation off-centering displacements occur at and above ambient temperature in the hybrid halide perovskites $MASnI_3$, $FASnI_3$, $MAPbI_3$, $FAPbI_3$, $MAPbBr_3$, and $FAPbBr_3$ as a consequence of lone pair stereochemical activity. The propensity for stereochemical activity can be tuned through chemical substitution on all sites of the ABX_3 perovskite structure: Substitution of a larger *A*-site cation (FA^+ for MA^+), a lighter *B*-site cation (Sn^{2+} for Pb^{2+}), and a harder anion (Br^- for I^-) all enhance the magnitude of these displacements. This tendency arises directly from the inherent instability of high-symmetry coordination for ns^2p^0 cations with significant impact on properties. [50]

Importantly, these observations are consistent with the emerging hypothesis that the remarkable defect-tolerance of these semiconductors is related to the lattice polarizability, and does not require the strongly dipolar $[CH_3NH_3]^+$ cation of the hybrid compositions. Recent reports have focused on the possibility of large [227] and small [280] polaron formation, and measurements of lifetimes and recombination constants

for both hot [262] and band-edge [260] carriers point to important differences and similarities across compositions. Zhu and coworkers find that hot carriers are much longer lived in $MAPbBr_3$ and $FAPbBr_3$ than in $CsPbBr_3$ and ascribe this to the dipolar molecular cations. [262] However, this ignores the negligible FA dipole moment (0.21 D) [165] compared to that of MA (2.29 D) [165] and the fact that, unlike the hybrid compositions, $CsPbBr_3$ is tilted (orthorhombic, $a^+b^-b^-$) rather than cubic at room temperature, [281, 25] which will affect lattice dynamics and polarizability both directly and via the suppression of lone pair stereochemical activity through reduced orbital overlap. In a separate report, Zhu and coworkers find extremely low trapping and recombination constants for band-edge carriers in all three compositions, suggesting the importance of the lead–halogen sublattice, rather than the molecular cations, for defect tolerance. [260] Additionally, the large static dielectric response of the halide perovskites is well known, [282, 161, 283, 284, 52, 53] and likely contributes to the effective screening of charged defects, [158] as has been postulated for thallium halides [99] and demonstrated for doped complex oxides. [170] Our findings are consistent with these ideas, suggesting the desired optoelectronic properties are in large part a consequence of the behavior of the metal-halogen network.

An analogous system where proximal instabilities impact transport properties may be seen in $SrTiO_3$. This d^0 system—which has attracted renewed attention in recent years because of the rich electrical transport phenomena doped variants display, particularly in thin film form [285]—is also subject to the off-centering instabilities due to second-order Jahn-teller effects. [34] However, due to the balance of size effects and the perovskite tolerance factor, the expected off-centering transition is pushed down to low enough temperatures that quantum fluctuations suppress any phase transition to a structure with distorted TiO_6 octahedra. [286] The dielectric constant is anomalously high however, resulting in unusual transport behavior in doped phases. [287, 288]

Most notably, polaronic effects, as in the halide perovskites, have been implicated in yielding a measured effective mass that appears larger than one would expect from band structure calculations. [289]

The elevated polarizability conferred by the proximal instability in Sn^{2+} and Pb^{2+} halide perovskites, together with the shallow nature of defect states due to the anti-bonding character of the valence band [290, 291, 126] and the possible separation of excited carriers in reciprocal space due to the spin-orbit interactions [292, 293, 235] are proposed to imbue these materials with their remarkable defect-tolerance. Actively profiting from the phenomena of proximal instabilities due to lone pairs offers a new paradigm for the chemical design of defect-tolerant semiconductors: Other compounds with lone pair-bearing ions in high symmetry environments may exhibit similarly favorable transport and recombination properties.

Chapter 7

Low temperature glassy dynamics in hybrid lead iodide perovskites

[1] Hybrid main group halide perovskites hold great technological promise in optoelectronic applications and present rich and complex evolution of structure and dynamics. Here we present low temperature dielectric measurements and calorimetry of APbI$_3$ [A = $CH_3NH_3^+$, $HC(NH_2)_2^+$] that suggest glassy behavior on cooling. In both compounds, the dielectric loss displays frequency-dependent peaks below 100 K characteristic of a glassy slowing of relaxation dynamics, with $HC(NH_2)_2PbI_3$ exhibiting greater glass fragility. Consistent with quenched disorder, the low temperature heat capacity of both perovskites deviates substantially from the $\sim T^3$ acoustic phonon contribution predicted by the Debye model. We suggest that static disorder of the *A*-site molecular cation, potentially coupled to local distortions of the Pb–I sublattice, is responsible for these phenomena. The distinct low temperature dynamics observed in these two

[1] The contents of this chapter have substantially appeared in reference [52]: D. Fabini, T. Hogan, H. Evans, C. Stoumpos, M. Kanatzidis, and R. Seshadri, Dielectric and thermodynamic signatures of low temperature glassy dynamics in the hybrid perovskites $CH_3NH_3PbI_3$ and $HC(NH_2)_2PbI_3$, *J. Phys. Chem. Lett.* **2016**, *7*, 376–381,

perovskites suggest qualitative differences in the interaction between the molecular cation and the surrounding inorganic framework, with potential implications for defect screening and device performance at ambient temperatures.

7.1 Introduction

Hybrid organic–inorganic main group halide perovskites of the form AMX_3 [$A = CH_3NH_3^+$, $HC(NH_2)_2^+$; $M = Sn^{2+}$, Pb^{2+}; $X = Cl^-$, Br^-, I^-] have attracted intense research interest for their performance in photovoltaic (PV) and other optoelectronic devices, coupled with ease of preparation, and abundance of their constituent elements. In particular, $CH_3NH_3PbI_3$ (methylammonium lead iodide) has been the subject of numerous recent investigations since the first report of its application in a PV device in 2009. [7] Recently, high performance PV devices incorporating $HC(NH_2)_2PbI_3$ (formamidinium lead iodide) have been reported. [294] For both compositions, many reports have focused on characterizing devices and understanding photophysical and electronic processes, while far fewer efforts have sought to develop a detailed description of crystal structure and disorder.

Due to the importance of local electric fields and defect screening for carrier separation and extraction in devices, much recent work has focused on the local dielectric environment in related lone pair-bearing main group metal halides [99, 93] and the relationship between long-range polarization and performance of field-effect transistors and PV devices employing $CH_3NH_3PbI_3$. [28, 27] In addition to its importance in phase transitions in hybrid perovskites [295, 190, 188, 67, 191], the *A*-site dipolar cation is an important determinant of dielectric properties. [282, 296] Accordingly, much attention has been paid to the dynamics of the disordered molecular cations in $CH_3NH_3PbI_3$. Early ^2H nuclear magnetic resonance (NMR) investigations of N-deuterated samples

indicate both rapid reorientation of the C–N axis with respect to the inorganic cage (hereafter, "tumbling") and rotation about the C–N axis (hereafter, "twisting") in the cubic and tetragonal phases, while only twisting remains in the low temperature orthorhombic phase. [297] Temperature studies of ^{1}H NMR spin-lattice relaxation times indicate the presence of cation twisting (activation energy 60 meV per molecule) in the orthorhombic phase and suggest rotational tunneling at temperatures below ∼70 K (first excited torsional state 23 meV above the ground state). [298] Based on calorimetry and infrared vibrational spectroscopy, three models of order–disorder transitions of the organic cation have been proposed, all of which imply a fully ordered organic cation in the orthorhombic phase. [275] Dielectric measurements indicate tumbling of the organic cation in the cubic and tetragonal phases and a Curie-Weiss-like temperature dependence of the real permittivity, consistent with a thermally inhibited net polarization of the molecular dipoles in the presence of an applied field. [282] Group theoretical analysis of quasi-elastic neutron scattering experiments suggests the presence of a four-fold rotation (tumbling, ∼5 ps at ambient temperature) and a three-fold rotation (twisting, ∼1 ps at ambient temperature) in the cubic and tetragonal phases, but only the three-fold rotation in the orthorhombic phase (slowing substantially to ∼4 ns at 70 K). [261] Weller et al. refined crystallographic structure models from neutron powder diffraction that indicate isotropic disorder of the organic cation in the cubic and tetragonal phases. [191] In the orthorhombic phase, they find that the molecular point group symmetry is compatible with the crystal site symmetry and all atoms can be localized. In their model, the organic cations are ordered antiferroelectrically in the [010] direction, with alternating C–N dipole orientations from cell to cell. Despite the nominal full ordering of the hydrogen atoms, they find large anisotropic atomic displacement parameters (ADPs) that are consistent with substantial librations of the organic cation even at 100 K. [191] Lee et al. perform ab initio computational

investigations of the orthorhombic phase which confirm the stability of the *trans* conformation of the organic cation and indicate hydrogen bonding between the amine-group hydrogens and the neighboring iodides of the inorganic cage. [299] Starting from the nominal structure of Weller et al. and fixing all other structure parameters, they find energy barriers (per molecule) of ∼70 meV, ∼190 meV, and ∼100 meV for three-fold rotation of the methyl group, amine group, and full molecule, respectively, implying that none of these modes are appreciably thermally populated in the orthorhombic phase. [299]

Far fewer reports of the structure and properties of $HC(NH_2)_2PbI_3$ exist to date. This compound exhibits polymorphism between a black perovskite phase and a yellow phase of 1-D chains at ambient temperatures, as well as further phase evolution on cooling. [67] We shall focus the remainder of our discussion on the perovskite phases. Trigonal structures for the ambient and intermediate temperature phases have been reported on the basis of laboratory single crystal X-ray diffraction. [67] The structure of the ambient temperature phase has recently been clarified via neutron powder diffraction, which suggests the cubic $Pm\bar{3}m$ perovskite aristotype and, correspondingly, a highly disordered molecular cation. [300] The structure of the low temperature phase below 140 K (transition temperature from differential scanning calorimetry, Supporting Information) has not been fully resolved.

An overview of the crystal structure of the low temperature phase of $CH_3NH_3PbI_3$ and the high temperature phase of both compositions is given in Figure 7.1. In light of the conflicting evidence from various experimental and theoretical treatments of the degree of ordering of the organic cation in the orthorhombic phase of $CH_3NH_3PbI_3$, here we employ dielectric spectroscopy and calorimetry to study the disorder of the polar molecular ion, and we extend our analysis to the closely-related and relatively underexplored $HC(NH_2)_2PbI_3$. We find in both compounds, frequency-dependent di-

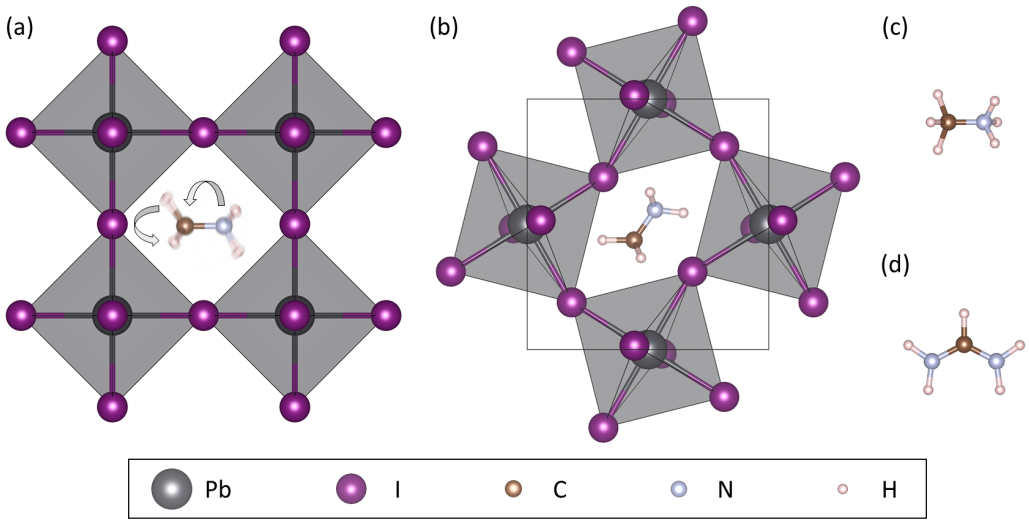

Figure 7.1: (a) High temperature cubic perovskite ($Pm\bar{3}m$) structure of $CH_3NH_3PbI_3$ (a = 6.31728(27) Å at 352 K) [191] and $HC(NH_2)_2PbI_3$ (a = 6.3620(8) Å at 300 K) [300] with highly disordered *A*-site cation. (b) Low temperature orthorhombic (*Pnma*) structure of $CH_3NH_3PbI_3$ at 100 K. Refined ADPs for the atoms of the organic cation remain large and anisotropic at this temperature. [191] Low temperature structures ($<$ 150 K) have not yet been reported for $HC(NH_2)_2PbI_3$. (c) Methylammonium ion, $[CH_3NH_3]^+$. (d) Formamidinium ion, $[HC(NH_2)_2]^+$.

electric loss peaks below 100 K characteristic of glassy slowing of relaxation dynamics. In $HC(NH_2)_2PbI_3$, the evidence points to greater glass fragility, perhaps due to the distinct shapes and dipole moments of the molecular cations. The low temperature heat capacity of both perovskites deviates substantially from the $C{\sim}T^3$ acoustic phonon contribution predicted by the Debye model. Some static disorder of the *A*-site molecular cation, potentially coupled to local distortions of the Pb–I sublattice, is suggested to play a role in these observed phenomena.

7.2 Methods

Single crystals of $CH_3NH_3PbI_3$ and polycrystalline samples of both compositions were prepared via previously reported methods. [67] Due to the slow spontaneous

conversion at ambient temperatures of the black perovskite phase of $HC(NH_2)_2PbI_3$ to the yellow phase of 1-D chains of face-sharing PbI_6 octahedra, [67] $HC(NH_2)_2PbI_3$ samples were fully converted to the perovskite phase just prior to measurement by heating in a glass vial with a hot air gun, with the phase purity confirmed by X-ray powder diffraction.

For dielectric measurements, pellets were prepared by grinding polycrystalline samples and cold-pressing to 9 tons in a 13 mm diameter cylindrical die. Indium contacts were applied via low temperature soldering in a parallel plate capacitor geometry. Capacitance–loss measurements were performed using an Andeen-Hagerling AH 2700A Ultra-precision Capacitance Bridge. The sample environment was controlled using a Quantum Design PPMS, over the temperature range of 1.8 K – 300 K. Real and imaginary components of relative permittivity were calculated using a parallel plate capacitor model.

Heat capacity measurements were carried out between 2.2 K and 150 K via relaxation techniques in a Quantum Design PPMS cryostat under high vacuum (9×10^{-6} torr). For $CH_3NH_3PbI_3$, a single crystal ($\sim$1.5 mm, 5.25 mg) was measured. For $HC(NH_2)_2PbI_3$, polycrystalline samples were ground, mixed with powdered iron (50.41% by mass, to enhance thermal conductivity, observed to be extremely low in both compounds as has been reported for $CH_3NH_3PbI_3$ [239]), and cold-pressed to 1 ton in a 3 mm $\times$ 9 mm die. The pellet was shattered, and a flat shard (4.48 mg) was measured. The background was subtracted by separately measuring a similarly prepared sample of the metal diluent (4.90 mg) at the same temperatures: the heat capacity of the composite sample was assumed to be a simple linear combination of that of the perovskite and that of the diluent.

7.3 Results & discussion

The complex permittivity across the full temperature range is presented in the Supporting Information and confirms the reported behavior of the $CH_3NH_3^+$ cation at the tetragonal–orthorhombic phase transition. [282] At higher temperatures, the intrinsic permittivity is obscured by ionic conductivity [28, 27, 301, 296] as well as interfacial and microstructural effects. [45, 46, 47] The low temperature complex permittivity is presented in Figure 7.2. Broad, frequency-dependent dielectric loss peaks are evident in both compositions, arising from the resonance of the probe with a dielectric relaxation process. Characteristic of glassy behavior, the dynamics slow by many orders of magnitude as the sample is cooled towards the glass transition. [302, 303, 304, 305] Importantly, the real part of the permittivity is minimally reduced as the relaxation is frozen out ($< 1\%$ for $CH_3NH_3PbI_3$, $< 7\%$ for $HC(NH_2)_2PbI_3$), suggesting that the relevant process does not involve significant reorientation of the C–N dipole axis. Though a wider spectral range is necessary to identify the functional form of the relaxation process and to model its temperature dependence, [303] we can readily conclude that at sufficiently low temperatures, both compositions exhibit a degree of static structural disorder. The feature seen in $HC(NH_2)_2PbI_3$ around 65 K is suppressed to varying degrees from sample to sample and may be due to extrinsic effects associated with impurities or sample preparation. Here, we focus our analysis on the most pronounced loss peaks (50 K to 80 K for $CH_3NH_3PbI_3$ and 40 K to 50 K for $HC(NH_2)_2PbI_3$). In addition to these frequency-disperse loss peaks, the frequency-independent feature at $\sim$13 K in the permittivity of $HC(NH_2)_2PbI_3$ suggests a structural phase transition that has not been reported.

The temperature-dependence of the relaxation dynamics is given in Figure 7.3. The glassy slowing is much more abrupt with temperature for $HC(NH_2)_2PbI_3$, suggesting

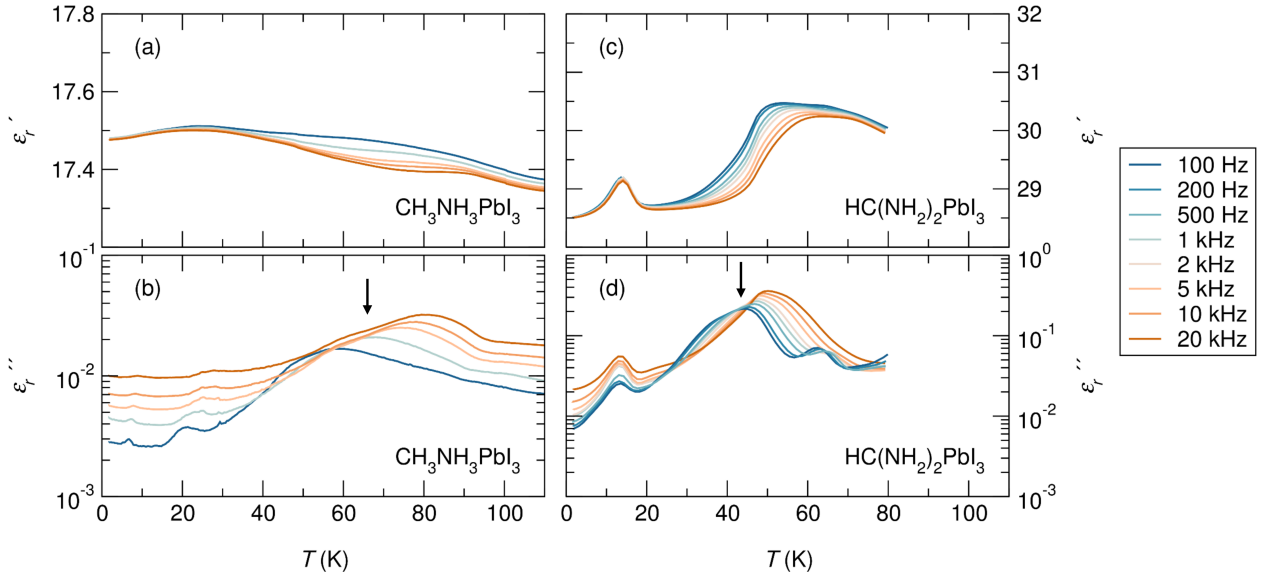

Figure 7.2: Low temperature detail of the real (ϵ_r') and imaginary (ϵ_r'') parts of the relative permittivity of polycrystalline (a,b) $CH_3NH_3PbI_3$ and (c,d) $HC(NH_2)_2PbI_3$ extracted from capacitance–loss measurements. Frequency-dependent dielectric loss peaks (↓) indicating substantial slowing of relaxation dynamics are observed in both samples. Additionally, a divergence in permittivity at 13 K for $HC(NH_2)_2PbI_3$ indicates a previously unreported structural phase transition.

that this compound exhibits more fragile glass dynamics, [303] an assertion which is corroborated by our calorimetry (*vide infra*). So-called "strong" glass-formers like SiO_2 exhibit substantial local structural similarity between the glass and the melt, while "fragile" glass-formers like toluene can take on a wide range of distinct configurations upon quenching and are often characterized by non-directional Coulomb or Van der Waals interactions. [303] The distinct dynamics observed in these two perovskites suggests that differences in molecular cation size, shape, and dipole moment give rise to qualitative differences in the mechanism of amorphization and the structure of the resulting statically disordered phases.

The heat capacities of both compositions are presented in Figure 7.4. As expected for soft crystals, the heat capacities rise rapidly with temperature and begin to level off as all phonon modes become appreciably populated. [306] The known $HC(NH_2)_2PbI_3$

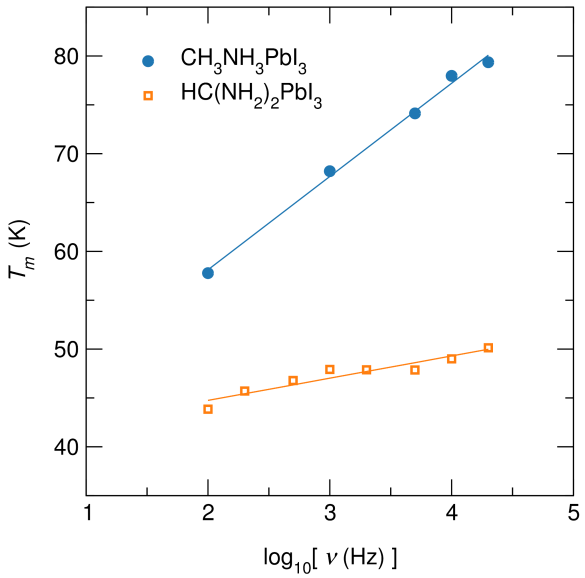

Figure 7.3: Temperature, T_m, of the low temperature dielectric loss peak versus probe frequency, ν. The stronger temperature dependence for $HC(NH_2)_2PbI_3$ suggests that this composition exhibits more fragile glass dynamics than $CH_3NH_3PbI_3$.

first-order phase transition at ∼140 K (Supporting Information) is poorly captured with our logarithmic temperature sampling. At 150 K, the heat capacities of both compositions are well below the high temperature limit of $36R$ (gas constant $R = 8.314\,J\ mol^{-1}\ K^{-1}$) predicted by Dulong and Petit for this crystal with a 12 atom formula unit. [306] Indeed, previously reported calorimetry of $CH_3NH_3PbI_3$ up to 360 K gives a constant heat capacity of $\sim 180\,J\ mol^{-1}\ K^{-1}$ in the cubic phase. We postulate that this corresponds to saturation of 21 or 22 of the 36 vibrational modes possible in this crystal: the 15 translational modes of the inorganic atoms and molecular center of mass, the 3 rotational modes of the full molecule, and 3 or 4 unidentified moderately soft intramolecular modes such as hydrogen wagging or independent methyl and amine group rotations about the C–N axis. A similar plateau of heat capacity up to 300 K at a slightly lower value of $\sim 170\,J\ mol^{-1}\ K^{-1}$ has been reported in the related $CH_3NH_3PbCl_3$, $CH_3NH_3PbBr_3$, [275] and $CH_3NH_3SnBr_3$. [307] We suggest that in these hybrid crystals, the heat capacity predicted from classical equipartition of energy is only

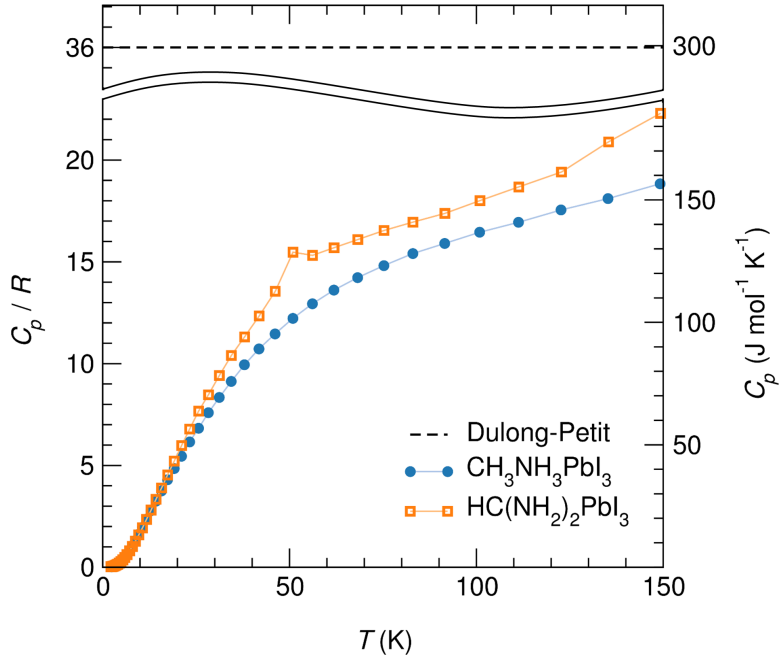

Figure 7.4: Low and intermediate temperature heat capacity of $CH_3NH_3PbI_3$ and $HC(NH_2)_2PbI_3$, scaled by the gas constant and in absolute units. Error bars are smaller than the markers for all points and are omitted. A glass transition in $HC(NH_2)_2PbI_3$ is evident between 46 K and 51 K while none is detectable in $CH_3NH_3PbI_3$, consistent with stronger glass dynamics in the latter compound. [303]

observed at temperatures well above the Debye temperature of the crystal because of rigid localized modes associated with the molecular ion.

Direct calorimetric evidence of the glass transition in $HC(NH_2)_2PbI_3$ is seen in the feature between 46 K and 51 K. This subtly enhanced heat capacity for the dynamically disordered state above the transition is not detectable in $CH_3NH_3PbI_3$, consistent with its stronger glass dynamics. [303] The apparent small discrepancy in glass transition temperature from the dielectric spectroscopy and from calorimetry is explained by sample temperature equilibration in the dielectric measurements as the sample was swept in the cooling direction for the dielectric data in Figure 7.2.

Examination of the low temperature heat capacity on a plot of C/T^3 versus T, shown in Figure 7.5, supports the hypothesis of glassy static disorder in both compo-

sitions. The heat capacity of the crystal deviates substantially from the $\sim T^3$ scaling predicted by the Debye model at low temperatures, as indicated by the low temperature "hump" in the C/T^3 versus T plot. [308, 309] Systems with glassy disorder are well-known to exhibit heat capacity in excess of that which can be attributed to acoustic phonons, though the exact origin of the corresponding "Boson peak" in the vibrational density of states is still an active area of research. [310, 311, 312] The modeled curves in Figure 7.5 for various Debye temperatures assume a single *A*-site atom rather than a molecule, a simplified model that nonetheless reflects the negligible occupancy of high frequency intramolecular modes at low temperatures. It is not possible to accurately determine Debye temperatures from these data: the heat capacities deviate substantially from the Debye model at low temperatures, and at intermediate temperatures the assumption of linear phonon dispersion is invalid for real crystals, particularly these hybrid systems with molecular ions.

The broader hump in C/T^3 for $HC(NH_2)_2PbI_3$ is consistent with our assertion that this compound exhibits greater glass fragility than $CH_3NH_3PbI_3$. [308] Liu and Löhneysen have compiled the maximum of C/T^3 and the corresponding temperature for a variety of amorphous and crystalline solids, and determined a scaling relation between these two parameters. [313] By comparison with their data, the hybrid perovskites measured here (parameters given in Table 7.1) fall in the region of polymeric and chalcogenide glasses. [313] Specifically, they are most similar by these metrics to poly(methyl methacrylate), polybutadiene, and Apiezon N Grease, [313] offering possible clues about the types of disorder and localized vibrational modes present in their ground state structures.

Careful examination of the literature suggests a degree of universality to this glassy behavior in hybrid main group halides and related materials. Similar low temperature dielectric loss dispersion has been reported but has not been adequately explained

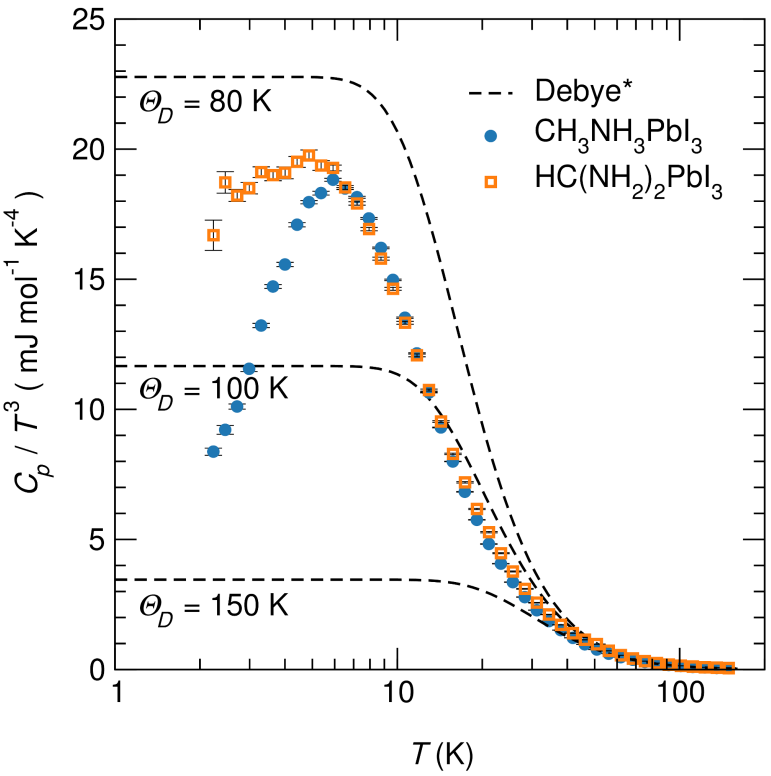

Figure 7.5: Heat capacity, expressed as C/T^3, of $CH_3NH_3PbI_3$ and $HC(NH_2)_2PbI_3$, illustrating deviation at low temperatures from the expected $C \propto T^3$ acoustic phonon contribution from the Debye model. *The heat capacities calculated from the Debye model assume the *A*-site cation is a single atom rather than a molecule, a simplified model that nonetheless accounts for the negligible activation of the stiffer rotational and vibrational modes of the molecule at low temperatures.

Table 7.1: Peak value, $P_c = (C/T^3)_{T=T_{max}}$, of the transformed heat capacity and corresponding temperature, T_{max}, for $CH_3NH_3PbI_3$ and $HC(NH_2)_2PbI_3$.

Sample	T_{max} (K)	P_c (μJ g^{-1} K^{-4})
$CH_3NH_3PbI_3$	5.92	30.4
$HC(NH_2)_2PbI_3$	4.87	31.2

for $CH_3NH_3PbBr_3$, $CH_3NH_3PbI_3$, [282] and $CH_3NH_3SnBr_3$. [307] In these materials, no glass transition is observed directly in calorimetry [275, 307] suggesting an entropic subtlety to the effect and correspondingly strong glass dynamics. Computational studies of $CH_3NH_3SnBr_3$ suggest many nearly degenerate possible ground state structures, [188] which implies a tendency towards glassy configurations. In the hybrid framework $(CH_3)_2NH_2Zn(HCOO)_3$, which adopts the perovskite structure and exhibits similar disorder-driven dielectric transitions to $CH_3NH_3PbI_3$, [314] glassy behavior and an associated memory effect have been observed via temperature-dependent ^{1}H NMR and low temperature calorimetry. [315] A glassy slowing of dynamics similar to those reported in this work is widely observed in "plastic crystals," which are composed of weakly interacting globular molecules that are orientationally or conformationally disordered. [316] We suggest that we may conceptualize the hybrid perovskites as a special case of plastic crystal, with a sublattice of isolated, disordered molecules embedded in an extended (and nominally ordered) inorganic framework. In contrast to conventional glasses that lose translational symmetry, quenched plastic crystals (such as the hybrid perovskites considered here) exhibit static local displacements and orientational disorder but maintain long-range translational periodicity of the molecular units. Recently, the analogy to plastic crystals has been identified and the possibility of orientationally glassy behavior has been predicted. [317] In the same work, a theoretical framework for treating the dynamically disordered cations and couplings between molecular rotations and lattice vibrations has been proposed. [317]

The precise mechanism behind this glassy disorder in APbI$_3$ is unclear. In $CH_3NH_3PbI_3$, early structural models based on transition entropies imply fully ordered molecular cations in the orthorhombic phase, [275] and ab initio calculations suggest high barriers to cation twisting about the C–N axis if the inorganic framework is rigidly fixed. [299] However, experimental evidence from quasi-elastic and elastic

neutron scattering suggests substantial dynamic disorder down to at least 70 K (the lowest temperature probed), [261, 191] and it is likely that rotational barriers could be lowered significantly in the presence of distortions of the soft Pb–I network. The same computational study suggests that freezing of a C–N axis twisting motion at an orientation off of a nominal three-fold alignment is energetically unlikely. [299] It is possible that more complex motions are important. A "wobbling-in-a-cone" libration has been identified in $CH_3NH_3PbI_3$ at room temperature ($\sim$300 fs) from 2-D vibrational spectroscopy, [318] and it is possible that similar motions persist in the orthorhombic phase. In light of the attractive interaction between the amine group hydrogens and the iodides of the inorganic cage, it is unlikely that such wobbling would ultimately freeze in an incoherent fashion unless it is accompanied by local distortions of the surrounding Pb–I framework. Low temperature analyses of the crystal structure have not been reported, and it is conceivable that the ground state of this material exhibits complex coupled disorder, perhaps including incommensurate modulation of the organic and inorganic sublattices. [319]

In the absence of low temperature crystal structure models for $HC(NH_2)_2PbI_3$, few mechanistic conclusions can be drawn for this composition. This material presents a prime opportunity for future study: compared to $CH_3NH_3PbI_3$, the effects of the larger molecule with a smaller dipole moment and multiple amine groups will be illuminating. The evidence presented here of low temperature glassy behavior provides new insights towards a complete description of crystal structure and disorder in this curious and promising family of materials.

Chapter 8

Structure evolution & reëntrant features in perovskite $CH(NH_2)_2PbI_3$

[1] The structure of the hybrid perovskite $HC(NH_2)_2PbI_3$ (formamidinium lead iodide) reflects competing interactions associated with molecular motion, hydrogen bonding tendencies, thermally activated soft octahedral rotations, and the propensity for the Pb^{2+} lone pair to express its stereochemistry. High-resolution synchrotron X-ray powder diffraction reveals a continuous transition from the cubic α-phase ($Pm\bar{3}m$, #221) to a tetragonal β-phase ($P4/mbm$, #127) at around 285 K, followed by a first-order transition to a tetragonal γ-phase (retaining $P4/mbm$, #127) at 140 K. An unusual reentrant pseudosymmetry in the β–to–γ phase transition is seen that is also reflected in the photoluminescence. Around room temperature, the coefficient of volumetric thermal expansion is among the largest for any extended crystalline solid.

[1] The contents of this chapter have substantially appeared in reference [53]: D. Fabini, C. Stoumpos, G. Laurita, A. Kaltzoglou, A. Kontos, P. Falaras, M. Kanatzidis, R. Seshadri, Reentrant structural and optical properties and large positive thermal expansion in perovskite formamidinium lead iodide, *Angew. Chem. Int. Ed.* **2016**, *55*, 15392–15396,

8.1 Introduction

Photovoltaic absorbers based on the hybrid perovskite $HC(NH_2)_2PbI_3$ (formamidinium lead iodide) and its alloys exhibit impressive performance, [251] but the description of the crystal structure of this material is incomplete. In addition to this technological motivation, [320] dense hybrid materials with 3-D inorganic connectivity and isolated organic molecular ions combine features of traditional inorganic solids and open framework materials, and their composition–structure relations are of fundamental interest.

The initial report of the preparation and characterization of $HC(NH_2)_2PbI_3$ proposed perovskite structures of trigonal symmetry for the α- and β-phases on the basis of laboratory single crystal X-ray diffraction, [67] while a subsequent report assigned the structure of the cubic perovskite aristotype for the α-phase from neutron powder diffraction. [300] The structure of the γ-phase has not been reported.

8.2 Methods

$HC(NH_2)_2PbI_3$ was prepared following a modification of the previously reported procedure. [67] 4.46 g (20 mmol) of PbO was dissolved in 15 ml of concentrated aqueous HI (57% w/w) and the solution temperature was raised and held to boiling (ca. 130° C). In a separate beaker, 2.08 g (20 mmol) of $(HC(NH_2)_2)(O_2CCH_3)$ or 1.61 g (20 mmol) of freshly prepared $HC(NH_2)_2Cl$ (prepared from $(HC(NH_2)_2)(O_2CCH_3)$ and concentrated HCl (37% w/w), followed by copious washing with toluene to remove excess acetic acid) [300] were dissolved in 5 mL of concentrated aqueous HI (57% w/w). The latter step was found to be necessary since commercially available $HC(NH_2)_2Cl$ is extremely hygroscopic and contains hydrolysis products. Addition of the $HC(NH_2)_2I$

solution to the PbI_2 solution resulted immediately in a fine black precipitate. The reaction was stopped after 5 min and the solution was filtered hot under vacuum to avoid co-precipitation of hydrated phases obtained for the cooled solution. During filtration, the black solid turns to yellow, completely converting over a period of 5 to 10 min. The yellow solid was transferred in a vacuum oven and heated at 120° C overnight, yielding a black solid that is stable for a period of 20 to 30 days before converting back to the yellow phase. Note that if the latter step is performed in an evacuated ampule under static vacuum, the black phase converts to the yellow one within 5 to 10 min. The obtained black material consists of the crystallographically pure α-phase of $HC(NH_2)_2PbI_3$. Yield: 9 to 10 g (70% to 80%).

High resolution synchrotron X-ray powder diffraction data were collected using beamline 11-BM at the Advanced Photon Source (APS), Argonne National Laboratory at a wavelength of 0.459200 Å. 50 mg of ground, yellow $HC(NH_2)_2PbI_3$ was packed and sealed into a 0.5 mm OD Kapton capillary. Complete conversion to the black perovskite phase was achieved in situ by heating initially to 490 K during data acquisition.

Candidate crystal structures for the phases of $HC(NH_2)_2PbI_3$ were generated using ISODISTORT (ISOTROPY Software Suite, iso.byu.edu). Le Bail and Rietveld analyses were performed using the GSAS software suite [196] with the EXPGUI interface. [197]

Photoluminescence measurements were performed on a Renishaw Invia spectrometer analyzing the backscattered filtered light emitted by a laser excitation at 785 nm. The samples were loaded into a THMS600PS Linkam optical cell under an inert Ar atmosphere. The incident beam was focused on spots of 5 μm^2. Power density was on the order of $\mu W\,\mu m^-2$, except above 433 K where the PL signal is very low and the incident power was raised to 0.12 mW μm^-2. PL spectra were recorded and averaged from five different spots at each temperature. The spectra from different spots have similar spectral characteristics but different absolute intensities, and spatial variation

of peak position is only 1 to 2 nm.

A flat plate capacitor was prepared by grinding black $HC(NH_2)_2PbI_3$ and cold-pressing to 3 tons in a 6 mm diameter cylindrical die (pellet thickness 2.54 mm) and applying indium contacts via low temperature soldering. Capacitance–loss measurements were performed in a Quantum Design PPMS DynaCool using an Andeen-Hagerling AH 2700A Ultra-precision Capacitance Bridge over the frequency range 100 Hz to 20 kHz.

8.3 Results & discussion

The disordered molecular cation, challenges associated with twinning in single crystals, and issues of pseudosymmetry led us to employ high-resolution synchrotron X-ray powder diffraction to follow the structure evolution of $HC(NH_2)_2PbI_3$ between 90 K and 490 K. The temperature-dependent scattering intensity around instructive low-angle Bragg peaks is given in Figure 8.1. The continuous α–to–β phase transition around 285 K is evident in the emergence of the 211 tetragonal peak and the splitting of the 200 cubic peak into the 002 and 220 tetragonal peaks on cooling. The first-order β–γ transition can be seen in the abrupt change in intensities and peak positions at 140 K (transition temperature from reported scanning calorimetry, which confirms the order of the transitions [52]). Remarkably, the 002 and 220 tetragonal peaks "fuse" in the γ-phase, while the 211 tetragonal peak remains, suggesting the possibility of a tetragonal phase with cubic pseudosymmetry.

Le Bail and Rietveld analyses of diffraction data confirm this hypothesis. In agreement with the results of Weller et al., [300] the α-phase is well described by the cubic $Pm\bar{3}m$ aristotype (a = 6.35788 Åat 299 K), as shown in Figure 8.2(a). For all phases, the *A*-site $[HC(NH_2)_2]^+$ cation has been modeled as a pseudo-atom with equivalent scattering power due to the dynamic disorder (vide infra) and limited sensitivity in the

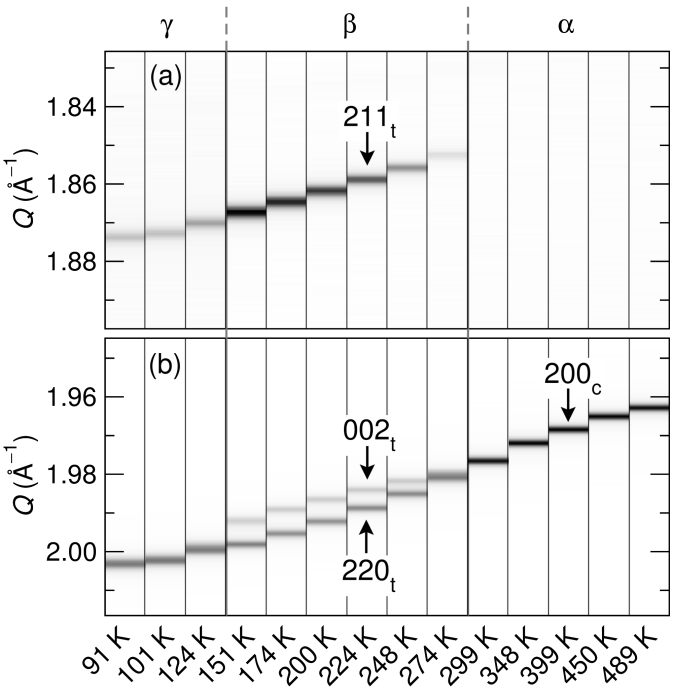

Figure 8.1: X-ray scattering intensity from $HC(NH_2)_2PbI_3$ around selected low-angle Bragg peaks between 90 K and 490 K, normalized to maximum peak intensity. (a) The 211_t tetragonal Bragg peak emerges upon cooling through a continuous phase transition around 285 K from the cubic α-phase to the tetragonal β-phase. (b) The 200_c cubic Bragg peak splits continuously on cooling due to the emergent tetragonality. A first order transition to the pseudo-cubic γ-phase with tetragonal symmetry occurs at 140 K. [52] The 002_t and 220_t tetragonal peaks "fuse" across the β–γ transition while the 211_t tetragonal peak remains.

X-ray experiment.

The structure of the β-phase is that of *P*4/*mbm* symmetry, with $a^0a^0c^+$ tilts in Glazer notation [244] (temperature-dependent structure parameters for all phases are provided in the Supporting Information). This in-phase uniaxial tilt pattern (Figure 8.2(b)) is in line with computational predictions of the preferred tilts for tetragonal perovskite iodides [248] and contrasts with the out-of-phase tilts observed in the tetragonal phase of $CH_3NH_3PbI_3$ [191] and many oxides. The anisotropy of the *A*-site atomic displacement parameters (ADPs) suggests preferential orientations for the molecular cation due to the tilting of the octahedra.

Remarkably, the structure of the γ-phase is also that of $a^0a^0c^+$ tilts with *P*4/*mbm* symmetry, as shown in Figure 8.2(c), though there are discontinuous changes in many structure parameters (vide infra) as required for such a first-order transition. Alternative structures exhibiting simple tilts that maintain 3-D octahedral connectivity [204] and that allow ferroic Pb^{2+} displacements [321] were screened and rejected based on unindexed peaks, absences of expected peaks, or both (details given in the Supporting Information).

Given this highly unusual phase evolution, we examined the temperature dependence of structure parameters from Rietveld refinement of diffraction data across the temperature range of 90 K to 490 K, as well as temperature-dependent optical and dielectric properties. The tetragonal lattice parameter ratio is given in Figure 8.3(a), and reflects the continuous emergence of tetragonality on cooling into the β-phase, as well as the reentrant cubic pseudosymmetry in the γ-phase.

The photoluminescence (PL) emission peak energy, E_{PL}, is given in Figure 8.3(b). E_{PL} blue-shifts with temperature in the α- and β-phases, consistent with the effects of thermal expansion on the unusual electronic structure as well as possible dynamic Pb^{2+} displacements. [50] E_{PL} plateaus above 370 K, a range which was not accessed in

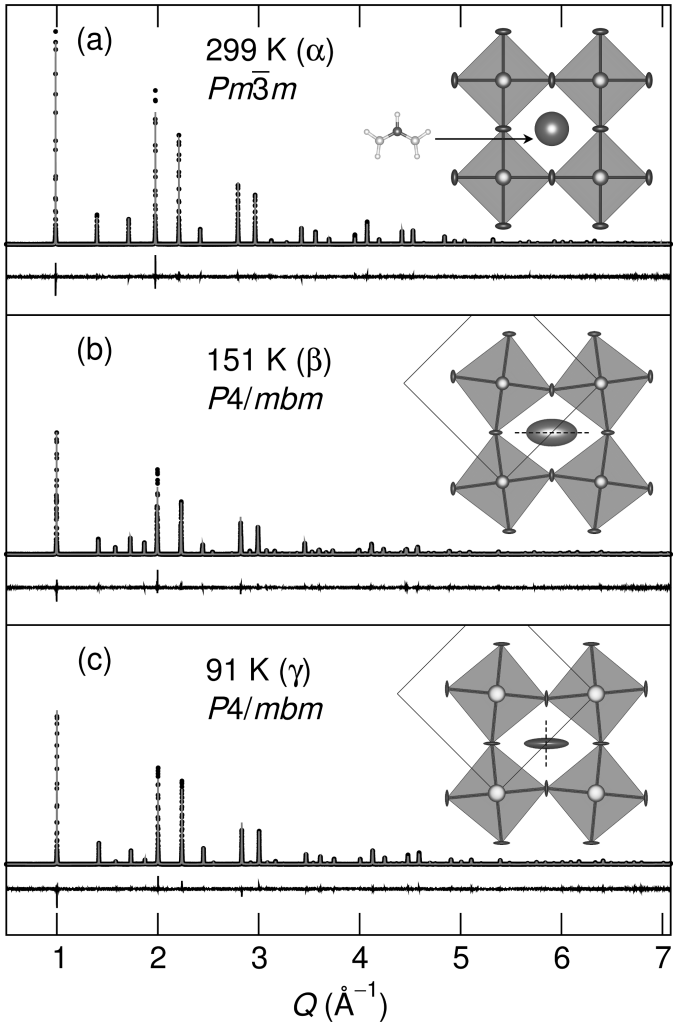

Figure 8.2: Rietveld refinement of X-ray powder diffraction and resulting crystal structures of the phases of $HC(NH_2)_2PbI_3$. Recorded scattering intensities are indicated by black dots, modelled intensities by grey lines, and difference curves are offset below. The *A*-site $[HC(NH_2)_2]^+$ cation is modelled as a pseudo-atom with the same form factor due to disorder and limited sensitivity in the X-ray experiment, and atomic displacement parameter (ADP) ellipsoids are visualized at the 50% level. (a) Cubic α-phase ($Pm\bar{3}m$, #221) at 299 K, $R_w = 12.4\%$. The formamidinium cation, $[HC(NH_2)_2]^+$ is illustrated. (b) Tetragonal β-phase (*P*4/*mbm*, #127) at 151 K, $R_w = 15.1\%$, viewed down the c-axis. (c) Tetragonal γ-phase (*P*4/*mbm*, #127) at 91 K, $R_w = 16.1\%$, viewed down the c-axis. Dashed lines in (b,c) indicate the unique axis of the *A*-site ADP ellipsoid.

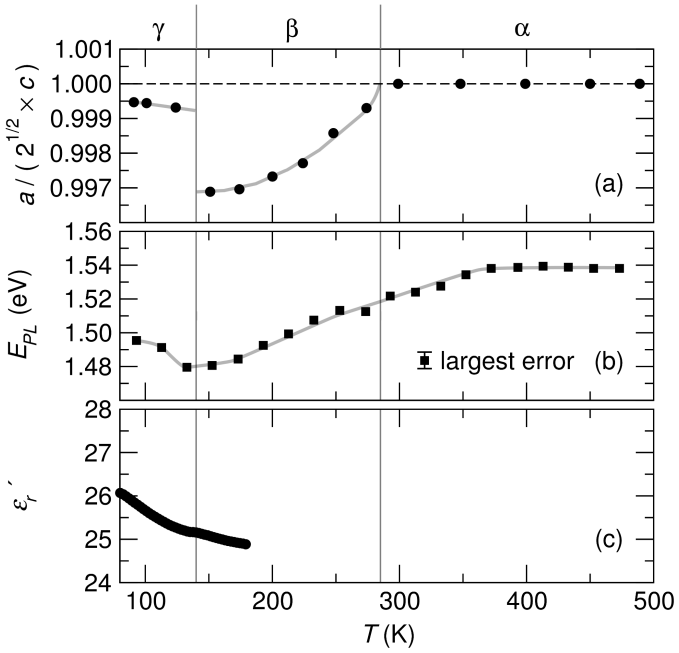

Figure 8.3: Tetragonal lattice parameter ratio, photoluminescence peak energy, and static dielectric permittivity of $HC(NH_2)_2PbI_3$. (a) The tetragonal lattice parameter ratio reflects the continuous α–β transition on cooling, as well as the reentrant cubic pseudosymmetry in the γ-phase. Error bars are smaller than the markers and are omitted. (b) The photoluminescence (PL) emission peak energy, E_{PL}, red-shifts on warming through the γ–β transition. In the β- and α-phases, E_{PL} blue-shifts with temperature, consistent with the effects of lattice expansion [50] on the unusual electronic structure of the main-group halide perovskites, and subsequently plateaus above 370 K. (c) Static dielectric permittivity, ϵ'_r, extracted from capacitance–loss measurements at 20 kHz. Despite a slight kink at the β–γ transition, ϵ'_r declines substantially with temperature in both phases, suggesting reorientation of the dipolar axis of the *A*-site cation is minimally inhibited even at these temperatures.

previous studies. On cooling through the β–γ transition, E_{PL} blue-shifts substantially, in agreement with existing reports. [322, 323] This is similar to the observed behavior at the tetragonal–orthorhombic transition in $CH_3NH_3PbI_3$, [323] where the blue-shift arises from reduced Pb–I orbital overlap due to the lowered symmetry, though in $HC(NH_2)_2PbI_3$ the blue-shift despite reduced tilting suggests crystallographically hidden disorder of the Pb–I network, though no disorder-induced emission broadening is apparent.

The static dielectric permittivity, ϵ_r', indirectly probes the rotational freedom of the polar axis of the molecular cation. [324] For the well-studied $CH_3NH_3PbI_3$, ϵ_r' rises on cooling in the tetragonal phase and drops abruptly through the tetragonal–orthorhombic phase transition, [282] as the severe tilting of the octahedra constrains the reorientation of the C–N axis. In contrast, ϵ_r' for $HC(NH_2)_2PbI_3$ has no discontinuity and continues to rise on cooling in the γ-phase (Figure 8.3(c)), suggesting minimally inhibited reorientation of the polar axis. The smaller value and reduced temperature dependence of ϵ_r' compared to that for $CH_3NH_3PbI_3$ are consistent with the smaller dipole moment for $[HC(NH_2)_2]^+$. The persistence of considerable cation motion in the γ-phase is in line with our previous observation of a glassy slowing of dynamics below 100 K in $CH_3NH_3PbI_3$ and $HC(NH_2)_2PbI_3$, with $HC(NH_2)_2PbI_3$ exhibiting greater glass fragility. [52]

The unit cell volume per formula unit, V, is given in Figure 8.4(a). A comparison of the volumetric thermal expansion coefficient, α_V, with those of other main-group halides and selected framework materials and liquids is given in Table 8.1. Fit over a temperature range of 200 K to 299 K, α_V is greater than $200\times10^{-6}\,K^{-1}$ ($R^2 = 99.8\%$). Thus, α_V for the β-phase is larger than that for liquid mercury [168] and appears to be nearly the largest for any extended crystalline solid near ambient temperature. It was recently reported that $\alpha_V = 220\times10^{-6}\,K^{-1}$ for the mixed *A*-site

Table 8.1: Volumetric thermal expansion coefficients, α_V, of $HC(NH_2)_2PbI_3$ and selected other compounds near room temperature.

Composition	Phase	T [K]	α_V [10^{-6} K^{-1}]	Reference
$HC(NH_2)_2PbI_3$	β (solid)	200–299	206–202	This work
$HC(NH_2)_2PbI_3$	α (solid)	348–489	100–98.6	This work
$CH_3NH_3PbI_3$	β (solid)	280	132	[268, 326]
$CsSnI_3$	γ (solid)	298	126	[168]
$Ag_3[Co(CN)_6]$	solid	276	121	[327]
Hg	liquid	293	182	[168]

$[CH_3NH_3]_{0.5}[HC(NH_2)_2]_{0.5}PbI_3$, though the precise temperature and fitting range are unspecified. [325] In the β-phase, linear thermal expansion is ≈60% greater in the ab-plane ($\alpha_a = 7.7\times10^{-5}\,K^{-1}$) than in the c-direction ($\alpha_a = 4.9\times10^{-5}\,K^{-1}$), suggesting anisotropic mechanical properties. While still large, α_V is substantially reduced in the cubic α-phase, consistent with a negative contribution from large amplitude dynamic octahedral tilts as in *A*-site vacant ReO_3 [206, 207] and ScF_3. [219]

The isotropic ADP for Pb, U_{iso}, is given in Figure 8.4(b), and increases monotonically with temperature. While the value is significantly elevated relative to typical values in oxides (partially a consequence of $6s^2$ lone pair-induced anharmonicity [50]), there are no discontinuities that would suggest crystallographic Pb^{2+} displacements that are not captured in our structure models for the low temperature phases.

The Pb–I–Pb octahedral tilt angle is given in Figure 8.4(c), and reflects the continuous α–β transition. In the γ-phase, the tilt angle jumps closer to linear, underscoring the unusual nature of this transition.

Iodine ADPs in the directions orthogonal to the Pb–I bonds, $U^{\perp}$, are given in Figure 8.4(d). Consistent with thermally-activated dynamic octahedral tilts, the values of $U^{\perp}$ decrease monotonically on cooling in the α- and β-phases. However, they increase significantly in the γ-phase, again consistent with disorder that is not captured by this crystallographic model. The discrepancy between ADPs for the two distinct I sites in

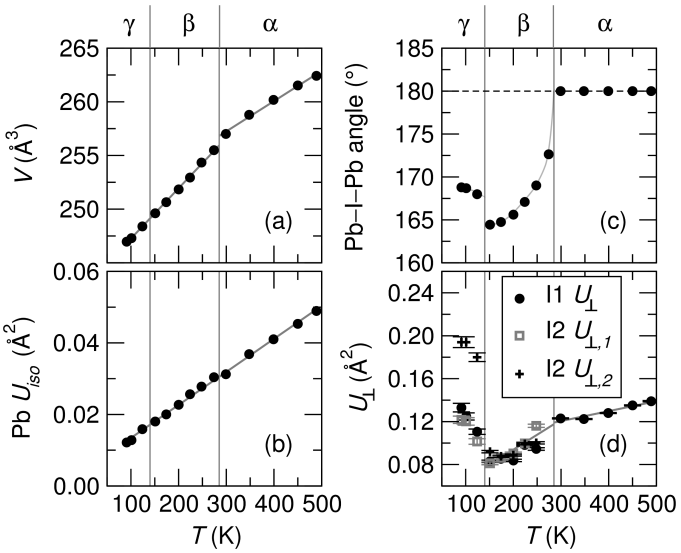

Figure 8.4: Selected crystallographic parameters for $HC(NH_2)_2PbI_3$. Error bars for (a)–(c) are smaller than the markers and are omitted. (a) The unit cell volume per formula unit, V, reveals unusually large volumetric thermal expansion coefficients ($\alpha_V = 203\times10^{-6}\,K^{-1}$ at 274 K). α_V is reduced in the cubic phase, consistent with a negative contribution from large amplitude dynamic octahedral tilts. [206, 207, 219] (b) The isotropic ADP for Pb, U_{iso}, is large compared to typical values in oxides but reveals no discontinuities associated with masked displacements in the tetragonal phases. (c) The Pb–I–Pb octahedral tilt angle reflects the continuous α–β transition, and jumps back toward linear through the unusual β–γ transition. (d) The ADPs for I in the directions orthogonal to the Pb–I bonds, $U^{\perp}$, decline monotonically with cooling in the α- and β-phases, consistent with reduced dynamic octahedral tilting. The increased values of the $U^{\perp}$ ADPs on cooling to the γ-phase suggest disorder that is not fully captured by this crystallographic model.

the γ-phase reflects parameter correlations that arise from Bragg peak overlap.

Together, the photoluminescence, iodine ADPs, and persistence of molecular motion in the γ-phase suggest complex (possibly modulated) disorder in this regime. This is supported by the observation of weak (intensity $<$0.5% that of the strongest Bragg peak) diffuse scattering features between $Q = 1.55\,\text{Å}^{-1}$ and $Q = 2.00\,\text{Å}^{-1}$ that are not indexed by any plausible space group symmetry. [204, 321] Nonetheless, the pseudo-cubic unit cell is unambiguous, and underscores the different N–H···I interactions between $CH_3NH_3PbI_3$ and $HC(NH_2)_2PbI_3$, where the diamine may hydrogen bond to halogens on both sides of the cage.

In summary, we find that this class of materials, already so fascinating on account of their outstanding functionality in photovoltaic devices, display fundamental properties that are surprising and even counterintuitive. The implications for technological applications are profound. For example, the very large volumetric thermal expansion creates substantial challenges in device applications. The atomistic origins of the reentrant structural and optical behavior deserve further scrutiny.

Chapter 9

Dynamics of molecular reorientation in hybrid lead iodide perovskites

[1] The role of organic molecular cations in the high-performance perovskite photovoltaic absorbers, methylammonium lead iodide ($MAPbI_3$) and formamidinium lead iodide ($FAPbI_3$), has been an enigmatic subject of great interest. Beyond aiding in the ease of processing of thin films for photovoltaic devices, there have been suggestions that many of the remarkable properties of the halide perovskites can be attributed to the dipolar nature and the dynamic behavior of these cations. Here, we establish the dynamics of the molecular cations in $FAPbI_3$ between 4 K and 340 K and the nature of their interaction with the surrounding inorganic cage using a combination of solid state nuclear magnetic resonance and dielectric spectroscopies, neutron scattering, calorimetry, and ab initio calculations. Detailed comparisons of the reported temperature dependence of the dynamics of $MAPbI_3$ are then carried out which reveal the molecular ions in the

[1] The contents of this chapter have substantially appeared in reference [54]: D. Fabini, T. Siaw, C. Stoumpos, G. Laurita, D. Olds, K. Page, J. Hu, M. Kanatzidis, S. Han, R. Seshadri, Universal dynamics of molecular reorientation in hybrid lead iodide perovskites, *J. Am. Chem. Soc.* **2017**, *139*, 16875–16884,

two different compounds to exhibit very similar rotation rates (≈8 ps) at room temperature, despite differences in other temperature regimes. For FA, rotation about the N···N axis, which reorients the molecular dipole, is the dominant motion in all phases, with an activation barrier of ≈21 meV in the ambient phase, compared to ≈110 meV for the analogous dipole reorientation of MA. Geometrical frustration of the molecule–cage interaction in $FAPbI_3$ produces a disordered γ-phase and subsequent glassy freezing at yet lower temperatures. Hydrogen bonds suggested by atom–atom distances from neutron total scattering experiments imply a substantial role for the molecules in directing structure and dictating properties. The temperature dependence of reorientation of the dipolar molecular cations systematically described here can clarify various hypotheses including large-polaron charge transport and fugitive electron spin polarization that have been invoked in the context of these unusual materials.

9.1 Introduction

The behavior of the organic molecular cations in the hybrid organic–inorganic main-group halide perovskites has attracted great attention in recent years, in part because the liquid-like disorder of this sublattice represents something of a novelty with respect to "traditional" semiconductors. [320, 256, 328, 329] These dense, hybrid materials are of both fundamental and applied interest. These systems occupy an underexplored region of the space of plastic crystals (which exhibit translational periodicity but orientational disorder) [316, 330, 331, 332] between better-studied molecular salts and open 3-D coordination polymers, and are likely to display complex couplings between microscopic, dynamic processes and macroscopic phase transitions. Further, understanding the molecule–cage interaction in these high performance semiconductors with potential optoelectronic applications [7, 10, 251] is essential for achieving full com-

positional control of the different material properties, as well as for the design and discovery of new functional materials.

Since the first preparation of the hybrid lead halide perovskites, [3] the behavior of the molecular cations has been studied by calorimetry, [275, 52] infrared spectroscopy, [333, 275, 318] dielectric spectroscopy, [282, 296, 52, 53, 334] Raman spectroscopy, [335] quasi-elastic and inelastic neutron scattering, [336, 261, 337, 338, 339] nuclear magnetic resonance (NMR) spectroscopy, [297, 295, 298, 340, 341, 342] isotopic substitution, [343] and ab initio methods, [299, 317, 344, 345, 346, 347] and these findings have been correlated to the structure evolution from crystallographic techniques. [67, 191, 300, 53, 325, 348, 349, 350] Most of these efforts have focused on MAPbX_3 (methylammonium lead halides; MA = CH_3NH_3, X = Cl, Br, I). In contrast, reports on $FAPbI_3$ (formamidinium lead iodide; FA = $CH[NH_2]_2$) have been less prolific, and understanding of the system remains incomplete in spite of the highly appealing photovoltaic performance of compounds with the formamidinium ion. [251]

The molecular cations have at times been invoked to explain all manner of confounding phenomena observed in these remarkable materials, including facile charge separation, [165] a high tolerance to intrinsic point defects, [227] persistent hot carriers, [262] and possible dynamic spin-splitting of the band extrema. [292] These hypotheses are somewhat misaligned with the growing body of evidence suggesting an important role for local distortions of the inorganic sublattice. [93, 336, 17, 50, 260, 233, 51, 263, 351, 279] Indeed, there are now numerous indications that the appealing optoelectronic properties of the hybrid perovskites are qualitatively matched by their all-inorganic analogues. [264, 265, 252, 260, 266, 352]

In order then to delineate the properties and functionality of the molecular cations from those of the inorganic framework, one must first complete the description of the structure and dynamics of each. To this end, we employ solid-state NMR, a technique

which is proved crucial for the study of plastic crystals. [316, 353, 297, 295, 298, 354, 355, 315, 356, 357] We complement the studies with neutron scattering, dielectric spectroscopy, calorimetry, and ab initio calculations to establish the behavior of the formamidinium ion and its coupling to the lattice in $FAPbI_3$ between 4 K and 340 K. Despite differences above and below room temperature, $FAPbI_3$ and $MAPbI_3$ are seen to exhibit very similar rates of molecular reorientation near 300 K. The unusual reentrant β–γ phase transition at 140 K reported in $FAPbI_3$ [53] is revealed to be a cascade of processes over a narrow temperature window, despite rather smoothly varying rotational dynamics. Below 100 K, molecular motion slows considerably, but the molecular geometry appears to be incompatible with the preferred ground state octahedral tilting pattern of the inorganic framework, leading to disordered freezing. Temperature-dependent pair distribution functions from neutron scattering suggest hydrogen bonds from the amine groups to the iodines of the surrounding cage, highlighting the role of the molecule in directing structure and modifying lattice dynamics and electron–phonon interaction. This work establishes important structural and dynamical details necessary for the evaluation of emerging hypotheses regarding the possible role of the molecular cations in the unusual and appealing optoelectronic properties of these hybrid materials.

9.2 Methods

$HC(NH_2)_2PbI_3$ samples for all experiments except neutron total scattering were prepared as described previously, [53] and $HC(ND_2)_2PbI_3$ samples were prepared following a modification of the previously reported procedure, as described below. [67] PbO and $HC(NH_2)_2Cl$ were purchased from Sigma-Aldrich. 10 M solutions of the $HC(NH_2)_2Cl$ in D_2O were prepared by dissolving 8.05 g of $HC(NH_2)_2Cl$ in 10 mL D_2O

and left standing for 24 h prior to use. 4.46 g (20 mmol) of PbO were initially dissolved in 15 ml of concentrated aqueous HI (57% w/w) and the solution temperature was raised and held to boiling (ca. 130° C) to afford a clear yellow solution. Addition of 2 mL of a 10 M solution of $HC(NH_2)_2Cl$ in D_2O resulted immediately in the precipitation of a fine black precipitate. The solution was stirred for 1 min and filtered hot under vacuum to avoid the exchange of the deuterium atoms with the hydrogen atoms. During filtration the black solid turns to yellow completely converting over a period of 5 to 10 min. The dry yellow solid produced 9 g (71% yield based on Pb) of crystallographically pure material.

Solid state ^{1}H NMR experiments and T_1 relaxation measurements under magic angle spinning (MAS) near ambient temperature were conducted on a 500 MHz (11.7 T) Bruker Avance NMR spectrometer with a Bruker 4 mm H/X/Y triple resonance MAS probe. Powdered samples were packed into a 4 mm zirconia MAS rotor and capped with a Vespel drive cap. For the black perovskite phase, the uncapped, packed rotor was first heated at ≈150° C under dynamic vacuum overnight to ensure complete conversion to the black phase and prevent subsequent degradation to the yellow phase, as described previously. [53] ^{1}H chemical shift was referenced to adamantane (1.71 ppm relative to TMS at 0 ppm). Longitudinal relaxation (T_1) experiments utilized the inversion recovery method. All gas flows (for MAS and temperature control) were dry nitrogen to reduce the risk of sample degradation to the yellow δ-phase, which appears to be hastened by moisture. Sample temperature was calibrated with the ^{207}Pb signal of lead nitrate [358] under the same MAS conditions, and the probehead was allowed to equilibrate for one hour at each temperature point before data acquisition.

Static solid state ^{1}H NMR experiments below 200 K were conducted in a 300 MHz (7.05 T) Bruker Avance DSX spectrometer equipped with a homebuilt NMR probe with slight modifications from descriptions in previous publications. [359, 360] The pow-

dered sample was packed in a Kel-F (CTFE) sample cup with inner and outer diameters of 5.3 mm and 7 mm, respectively, and height of 8 mm. After packing the sample cup, the sample cup was covered using a Kel-F cap, and immediately placed into the NMR probe for cryogenic cooling. The NMR probe is placed within a STVP-200-NMR cryostat (Janis Research Company) where a continuous flow of vaporized liquid helium is used to cool the entire NMR probe and sample. Temperature control is achieved with a combination of continuous cold helium gas flow and a resistive heater. The temperature is monitored with a Cernox sensor mounted on the cryostat at the sample position, while the heater output of the resistive heater was controlled with a PID algorithm in LabView that controls the voltage level of the resistive heater in relation to the desired temperature setpoint. The temperature is maintained at an accuracy level of +/–50 mK or better, depending on the temperature range. The probehead was allowed to equilibrate for 15 to 30 minutes at each setpoint before data acquisition, depending on the temperature step. Longitudinal relaxation experiments utilized the saturation recovery method. A small impurity of the yellow δ-phase was detected due to brief sample preparation in air, which was reflected in a second T_1 feature. To account for this, a constrained fitting routine was written in `python` utilizing the least-squares minimization package `lmfit` [361] which constrained the ratio of the black and yellow phase fractions (a fitting parameter) across all experiments for each non-consecutive day of data acquisition, while other parameters (relaxation times, amplitudes) were allowed to vary independently. The data were well modeled by this approach, and T_1 of the black phase was evident as the dominant contribution. The phase fraction of the yellow impurity phase ranged from 10% to 20% across the various non-consecutive days of the experiment. Cross-checking against the measured T_1 times for pure black $FAPbI_3$ (Figure 9.1) between 220 K and 340 K and pure yellow $FAPbI_3$ at 300 K (unpublished) ensured there was no amiguity in assigning the two T_1 features to the pertinent

polymorphs.

Dielectric spectroscopy was performed as described previously. [53] Heat capacity measurements across phase transitions were carried out via the pulsed dual-slope analysis method in a Quantum Design PPMS cryostat under high vacuum (9×10^{-6} Torr). Polycrystalline samples were ground, mixed with powdered iron (51.52% by mass, to enhance thermal conductivity), and cold-pressed to 1 t in a 3 mm $\times$ 9 mm die. The pellet was shattered, and a flat shard (5.00 mg) was measured. The background was subtracted by separately measuring a similarly prepared sample of the iron diluent (8.10 mg), and the heat capacity of the composite sample was assumed to be a simple linear combination of the two. For the rotational freezing region ($\approx$ 50 K), a T-rise of 30 K from 30 K was employed, and measured time constants were $\tau_1 \approx 25$ s, $\tau_2 = 0$ s (strong thermal coupling). For the β–γ transition ($\approx$ 140 K), a temperature rise of 50 K from 110 K was employed, and measured time constants were $\tau_1 \approx 54$ s, $\tau_2 = 0$ s (strong thermal coupling). All measurements were repeated three times.

Neutron total scattering experiments were performed on an N-deuterated sample using the NOMAD instrument (BL-1B) [194] at the Spallation Neutron Source at Oak Ridge National Laboratory. The as-prepared dried powders were transferred into a mortar and pestle and thoroughly ground to a fine powder. The sample was packed into a 6 mm diameter vanadium canister and sealed tightly under N_2 atmosphere. Measurements were performed in an approximately 1.5 cm cross-section neutron beam, and the detectors were calibrated with scattering data from a diamond powder standard prior to measurements. The sample temperature was first raised to 500 K to ensure complete conversion to the black perovskite phase, and subsequently cooled to 300 K and then 100 K. Approximate data collection times were 20 mins at 500 K and 2 hr each at 300 K and 100 K. Data were normalized against scattering data collected for a vanadium rod, container background was subtracted, and the merged total scattering

structure function was produced using the IDL codes developed for the NOMAD instrument. [194] Significant incoherent scattering necessitated hydrogen correction of the structure functions, following the procedure of Page and coworkers, [362] with the parameters $L = 0$, $u^2 = 0.05\,\text{Å}^2$ (the salient features of the PDFs shown in Figure 9.6 were found to be robust to variation of these parameters). Fourier transforms of the corrected structure factors were performed with Q_{min} =1.0 Å^{-1}, Q_{max} = 21.88 Å^{-1}. Hydrogen corrections [362] and the generation of PDFs were performed using custom `python` code. Simulated neutron PDFs for analysis were generated using the PDFgui software suite. [198]

Fourier difference maps were generated from high-resolution synchrotron X-ray powder diffraction experiments at beamline 11-BM of the Advanced Photon Source at Argonne National Laboratory that have been described previously. [53] The *A*-site molecule was removed from the crystal structure models from Rietveld refinement [53], and the residual charge density was calculated using the program GSAS [196] with the interface EXPGUI. [197] Results were visualized with VESTA [132] and custom `python` code.

Ab initio calculations of the molecule geometry and energy surfaces for molecular rotation were performed with the Vienna Ab initio Simulation Package (VASP), [137, 138, 95, 139] which implements the Kohn–Sham formulation of density functional theory (DFT) using a plane wave basis set and the projector augmented wave formalism. [140, 96] The generalized gradient approximation was employed using the revised exchange and correlation functional for solids of Perdew, Burke, and Ernzerhof (GGA–PBEsol). [199] For Pb, d electrons were included in the valence. The plane wave basis set cutoff energy (800 eV) and k-point mesh density (α-phase: $6 \times 6 \times 6$; β-,γ-phases: $4 \times 4 \times 6$, both Γ-centered Monkhorst–Pack sampling [200] for molecular rotations) were chosen based on convergence of the total energy.

To map the energy surfaces for molecular rotation, the structure of the isolated molecular cation was first relaxed in a $(16\,\text{Å})^3$ cube (to avoid interaction with periodic images) with a homogeneous neutralizing background jellium. Rigid rotations and translations of the molecule were then generated using Euler angle-based rotations in a custom `python` program, and the total energies evaluated with static DFT calculations. Lattice parameters and inorganic atom positions were fixed to those observed in experiment, [53] and deformations of the inorganic framework were not considered. The nominal orientations of the molecule are depicted in Figure 9.4, with the dipole axes (C–H) oriented ferroically from cell to cell (all parallel to c). For rotations about each principle direction of a coordinate system fixed to the molecule, a 2-D translation-rotation study was performed, and the minimum energy path for rotation was extracted.

9.3 Results & discussion

Solid state ^{1}H nuclear magnetic resonance (NMR) spin-lattice relaxation time (T_1) experiments were conducted at temperatures between 4 K and 340 K. 1-D spectra and relaxation times from 10 kHz magic-angle spinning (MAS) experiments above 220 K ($\omega_0 = 500$ MHz) are presented in Figure 9.1 (spectra for the yellow hexagonal δ-phase are provided in the Supporting Information for comparison). Due to the strong dipolar interactions associated with ^{1}H, it is not possible to resolve the three chemically distinct protons under achievable MAS speeds, as in an equivalent solution-state experiment. [325] As expected, the changes in the spectra with temperature are subtle, reflecting only temperature effects on spin polarization, slight broadening, and gradual changes in chemical shift. By fitting a single pseudo-Voigt function to the central peak (which comprises features from each of the chemically distinct protons, broadened by dipolar

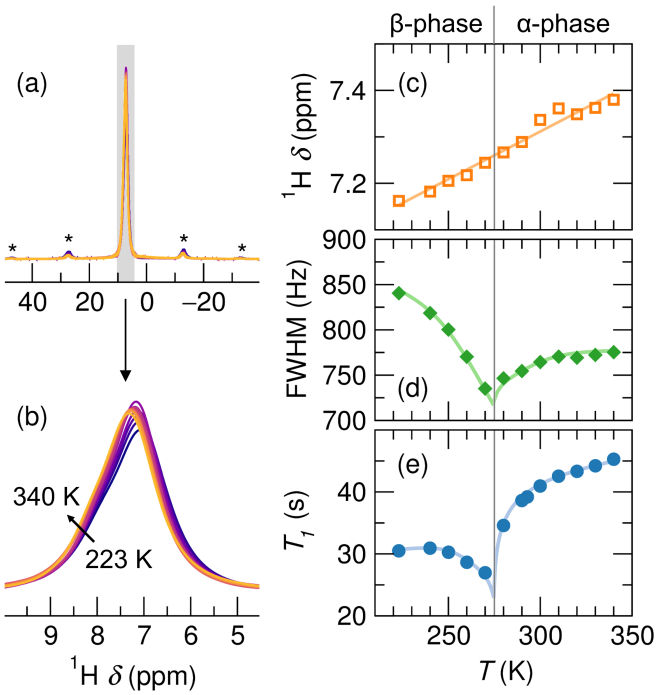

Figure 9.1: (a,b) Solid state ^{1}H NMR (10 kHz MAS) spectra of perovskite $FAPbI_3$ at temperatures near ambient. Asterisks indicate spinning sidebands. (c) Chemical shift and (d) peak width (full width at half maximum, FWHM) when the data are fit with a single pseudo-Voigt function. (e) Spin-lattice relaxation time (T_1) from inversion recovery experiments. The α–β phase transition is indicated. For (c-e), lines are to guide the eye only, and error bars are smaller than the markers and are omitted for clarity.

interactions and chemical shielding anisotropy), we observe that the protons become slightly more shielded on cooling (Figure 9.1c), consistent with lattice contraction and increased residence time near the electron-rich iodides of the inorganic cage as molecular motion slows.

The peak shape and T_1 are extremely sensitive to the onset of the otherwise subtle continuous α–β phase transition near 275 K (Figure 9.1d–e). The line broadening in the tetragonal β-phase suggests that molecular motions become anisotropic, consistent with the reduced site symmetry from X-ray diffraction. [53] Finally, we observe a hastening of spin-lattice relaxation due to critical fluctuations in the vicinity of the

transition.

1-D spectra from cryogenic experiments ($\omega_0 = 300\,\text{MHz}$) at selected temperatures between 4 K and 245 K are presented in Figure 9.2a. Absorption lines are extremely broad as MAS was not possible with this configuration. Increased shielding is observed on cooling (smaller apparent chemical shift changes are not significant owing to the challenge of precisely phase correcting such broad features), again consistent with lattice contraction and increased residence time of the protons near the electron-rich iodides of the inorganic cage as molecular motion slows. Lineshapes are very similar down to roughly 100 K, confirming that the molecule retains considerable motion into the disordered γ-phase, [53] unlike in the corresponding orthorhombic γ-phase phase of $MAPbI_3$. [191] Below 100 K, the signal broadens considerably as motion becomes too slow to average out dipolar interactions and chemical shielding anisotropy. Due to the presence of a small impurity of the yellow δ-$FAPbI_3$ polymorph detected after the cryogenic experiments, we cannot interpret conclusively the additional lineshape structure that emerges at 60 K and below. This impurity phase was accounted for in the extraction of spin-lattice relaxation times via a constrained fitting routine as detailed in the Methods section.

The motional slowing of the molecular cation suggested by the broadening of the NMR signal below 100 K is corroborated by dielectric spectroscopy and calorimetry, shown in Figure 9.2b–d. For the frequencies measured (100 Hz to 20 kHz) the static dielectric constant, ϵ_r', drops substantially over a ≈25 K temperature window as the dipolar axis of the formamidinium cation is restricted from reorienting. Concurrently, the dielectric loss tangent, $\tan\delta$, exhibits frequency-dependent peaks as the frequency of the AC probe resonates with the timescale of dielectric relaxation. [303] This glassy freezing of dipolar motion on cooling is in accordance with our prior report, [52] and in contrast with the abrupt loss of dipolar motion observed in dielectric measurements

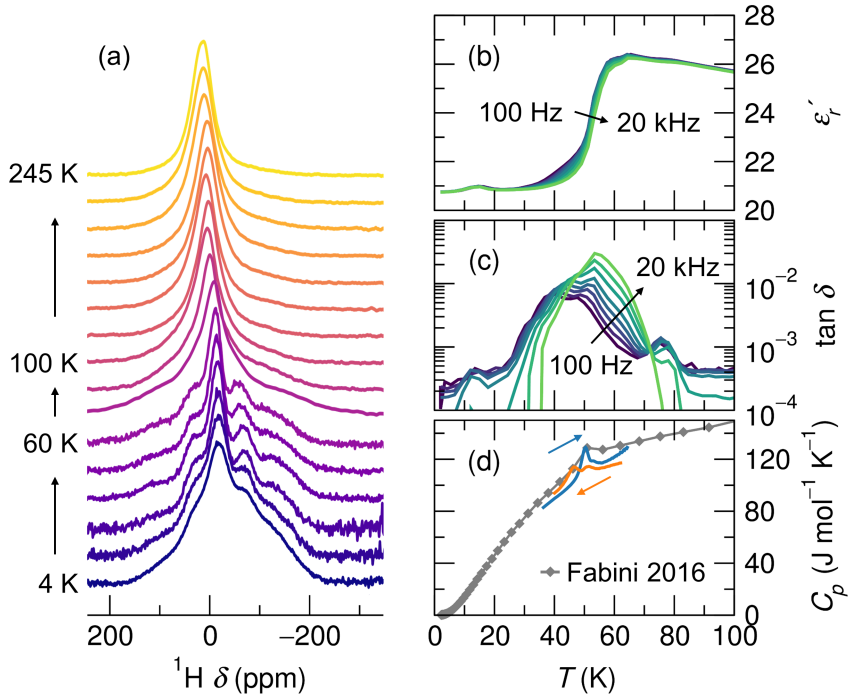

Figure 9.2: (a) Solid state ^{1}H NMR spectra of perovskite $FAPbI_3$ at selected cryogenic temperatures. (b) Real permittivity (ϵ_r') and (c) loss tangent ($\tan\delta$) from AC capacitance measurements. (d) Heat capacity (C_p) in the vicinity of the freezing of the molecular dipole from rapid warming (blue) and cooling (orange) sweeps, with prior measurements at fixed temperatures from the literature for comparison. [52] Detailed calorimetry and entropy analysis is provided in the Supporting Information.

of $MAPbI_3$ at the β–γ transition. [282, 296, 52, 334] Calorimetry about the motional freezing temperature reveals two closely spaced peaks in the heat capacity, C_p, with a total transition entropy too small to be that of an abrupt order–disorder transition (details in the Supporting Information), suggesting a gradual loss of motion precedes the phase transition on cooling.

^{1}H spin-lattice relaxation times in $FAPbI_3$, as well as those reported for $MAPbI_3$, [298] are displayed in Figure 9.3. For both compounds, excluding the known phase transitions, T_1 decreases on cooling until reaching a minimum, and subsequently increases on further cooling. This general temperature-dependence is consistent with relaxation of nuclear spins to the bath by dipole–dipole interactions that fluctuate due to molecular motion.

For $FAPbI_3$, the β–γ transition appears to be characterized by a small but abrupt increase in T_1 over a narrow temperature range (≈135 K to 138 K). Though this would seem to suggest a first-order transition as suggested previously, [52, 53] differential scanning calorimetry and relaxation calorimetry (Supporting Information) indicate that the transition is in fact a cascade of multiple events with no noticeable hysteresis, and a total transition entropy that is far too small to be a full order–disorder transition. This highlights the unusual nature of this reentrant disordered γ-phase with cubic pseudosymmetry, [53] and points to a more complex molecule–cage interaction in $FAPbI_3$ than in $MAPbI_3$, as suggested previously. [52]

Similarly, the behavior below 100 K is also more complex than that of $MAPbI_3$. Though scattering or complementary spectroscopies will be required to fully elucidate the structure and dynamics in this regime, we note that the intricate temperature-dependence of T_1 is consistent with the multiple sets of dielectric loss peaks observed above, the greater fragility of the glassy freezing for this composition, [52] and the predictions of frustrated ground states. [317, 344]

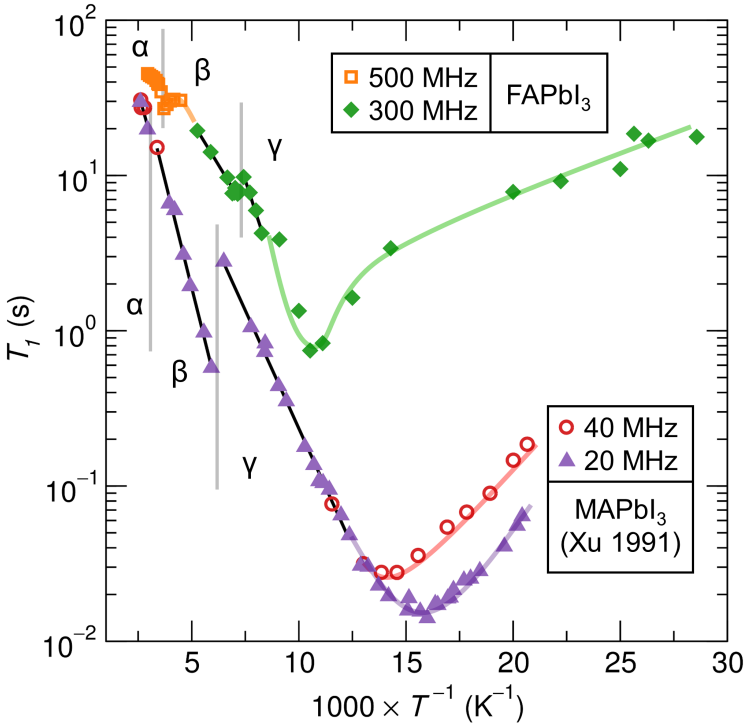

Figure 9.3: Temperature-dependence of ^{1}H spin-lattice relaxation times (T_1) for $FAPbI_3$, with those reported for $MAPbI_3$ for comparison. [298] Temperature ranges for the α-, β-, and γ-phase of each compound are indicated, and phase transitions are indicated by vertical gray lines. Black lines are Arrhenius fits for activation barriers in each phase. Colored lines are to guide the eye only. For $FAPbI_3$, error bars are smaller than the markers and are omitted for clarity.

The temperature-dependence of T_1 for $MAPbI_3$ is discussed at length in the original report. [298] Notably, there is a significant jump in T_1 on cooling to the γ-phase, which reflects a change in relaxation mechanism as the four-fold rotation about an axis perpendicular to the C–N bond is frozen out, but three-fold rotation about the C–N bond remains. [191, 261]

The framework of Bloembergen, Purcell, and Pound [363] has been widely used to interpret T_1 for solids wherein relaxation occurs by dipole–dipole interactions mediated by molecular motions involving the relevant nuclei. In such systems, the predicted T_1 is given in Equation 9.1, where $C = (3\mu_0^2\hbar^2\gamma^4)/(160\pi^2 r^6)$ is a lumped constant independent of correlation time and field strength. τ_c is the correlation time for molecular motion (the time to rotate through one radian), ω_0 is the Larmor frequency of the nucleus, μ_0 is the vacuum permeability, $\hbar$ is reduced Planck's constant, γ is the gyromagnetic ratio of the nucleus, and r is the dipole–dipole separation distance.

$$\frac{1}{T_1} = C\left[\frac{\tau_c}{1+\omega_0^2\tau_c^2} + \frac{4\tau_c}{1+4\omega_0^2\tau_c^2}\right] \tag{9.1}$$

In the "fast motion" limit ($\omega_0\tau_c \ll 1$), Equation 9.1 reduces to $\tau_c = (1/5C)T_1^{-1}$, so activation barriers, E_a, for molecular motion (assuming $\tau_c \approx \exp[-E_a/(k_BT)]$) may be extracted directly from the slopes in Figure 9.3. The activation barriers for the various phases of both compounds from ^{1}H NMR T_1 measurements are provided in Table 9.1, as well as those we predict from ab initio calculations of the energy surfaces for molecular rotations in $FAPbI_3$ (Figure 9.4, vide infra). Somewhat remarkably, given the simplifications made in modeling this high-dimensional problem (vide infra), the barriers we calculate are in excellent agreement with those from experiment for the α- and β-phases of $FAPbI_3$, though we cannot rule out the possibility of a fortuitous cancellation of errors. The underestimate of the activation barrier in the reentrant, pseudo-cubic

Table 9.1: Activation barriers (meV) for molecular rotation from ^{1}H NMR (exp.) and DFT (calc.) in the perovskite phases of $FAPbI_3$ and $MAPbI_3$. For all phases of $FAPbI_3$, the rotation is about an axis parallel to the N···N line (ϕ_3 rotations, by the notation of Figure 9.4). The behavior for $MAPbI_3$ is non-monotonic due to the change in relaxation mechanisms from four-fold rotations (α-, β-phases) to three-fold rotations about C–N (γ-phase).

	α-phase	β-phase	γ-phase
$FAPbI_3$ (exp.)	21	45	84
$FAPbI_3$ (calc.)	21	39	63
$MAPbI_3$ (exp.) [298]	95	110	60

γ-phase is consistent with our prior finding that the relatively high symmetry and small octahedral tilt angle apparent from crystallographic studies masks substantial local tilting disorder in this regime [53] which was not included in periodic DFT calculations.

Ab initio energy surfaces for molecular rotations in the perovskite phases of $FAPbI_3$ are displayed in Figure 9.4. Each curve represents a two-dimensional study of rigid translation and rotation of the molecule (no relaxation of atomic coordinates or unit cell parameters is permitted), but only the locus of points forming the minimum energy path is displayed. Rotations are about the three principal axes of a coordinate system fixed to the molecule, and the structures of the inorganic cage are fixed to those from experiment. [53] Van der Waals corrections are not included.

Barriers to all rotation modes are lowest in the cubic phase, and are sensitive to both lattice parameters and the degree of octahedral tilting. Rotations about an axis parallel to the N···N line (ϕ_3 axis) are the preferred mode in all phases, in agreement with a recent report of heterogeneous dynamics at 300 K from ab initio molecular dynamics. [344] As shown in Table 9.1, the activation barriers for ϕ_3 rotations are in remarkable agreement with experiment for the α- and β-phases, and a slight underestimate of the experimental value for the disordered γ-phase. Though a few meV higher in energy than the $\phi_1 = 0°$ orientation, the $\phi_1 = 90°$ nominal orientation significantly

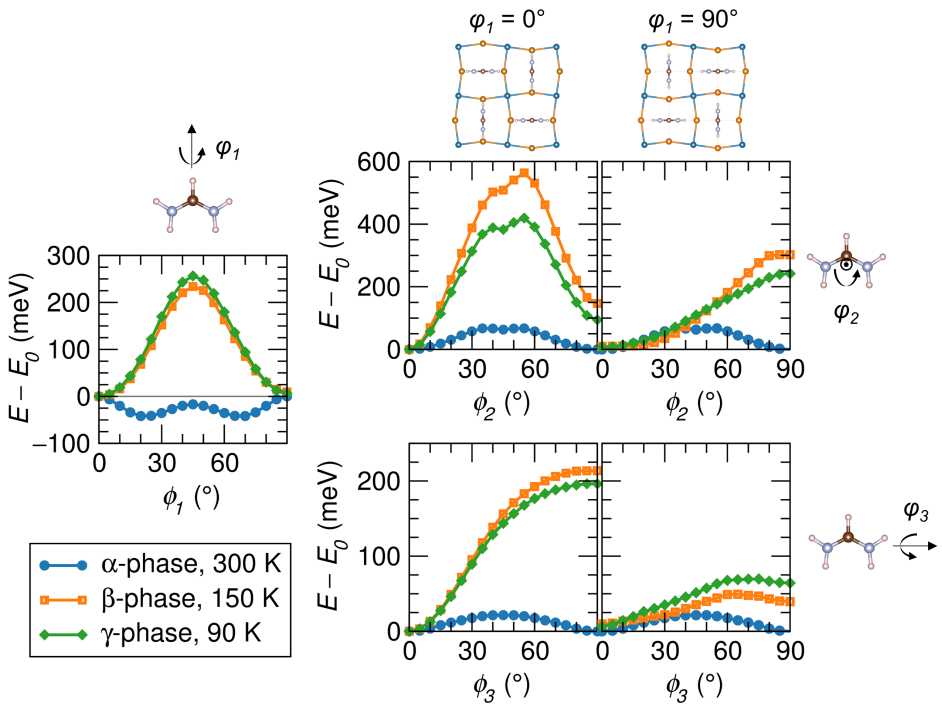

Figure 9.4: Lowest energy paths for molecular rotations in the three known perovskite phases of $FAPbI_3$, from density functional theory (DFT). Each curve represents a two-dimensional study of rigid translation and rotation of the molecule, but only the locus of points forming the minimum energy path are displayed. Energies are per formula unit. For each rotation mode about the principal axes of the molecule, the other two rotation angles are fixed (for ϕ_1 rotations, $\phi_2 = \phi_3 = 0$; for ϕ_2 rotations, $\phi_1 = (0,\, 90°)$, $\phi_3 = 0$; for ϕ_3 rotations, $\phi_1 = (0,\, 90°)$, $\phi_2 = 0$).

reduces barrier heights for ϕ_2 and ϕ_3 rotations, suggesting this configuration may be entropy stabilized. This hypothesis is corroborated by charge density analysis of X-ray diffraction experiments (Supporting Information).

Figure 9.5 shows the reorientation times for molecular motion, τ_{rot}, that result from fitting the ^{1}H spin-lattice relaxation times for $FAPbI_3$ and $MAPbI_3$ [298] within the framework described by Bloembergen, Purcell, and Pound. [363] Estimates of the dynamics reported from a number of other techniques are shown for comparison. Correlation times from fitting T_1 experiments, τ_c, are multiplied by the angle of rotation of the corresponding mode (e.g. $\pi/2$ for the four-fold rotations in α- and β-$MAPbI_3$) to obtain τ_{rot}. Note that some ambiguity remains in defining a consistent reorientation time across these various techniques.

The large discontinuity in τ_{rot} for $MAPbI_3$ at 165 K reflects the loss of four-fold molecular rotation in the orthorhombic γ-phase, as discussed above. For $MAPbI_3$, reorientation times from quasi-elastic neutron scattering over a wide energy-transfer and momentum-transfer range (5 ps at RT) are in general agreement with those from ^{1}H NMR (7 ps at RT) over much of the temperature range, [261] while those from a more limited experimental window estimate a slightly larger τ_{rot} at room temperature (14 ps). [337] For both compounds, room temperature estimates from ab initio molecular dynamics (2 ps to 4.3 ps) [191, 318, 344] are somewhat shorter than those from ^{1}H NMR (FA: 8 ps; MA: 7 ps). Among reported values, the estimate of τ_{rot} for $MAPbI_3$ from ^{14}N NMR experiments via a diffusion-on-a-cone model (108$\pm$18 ps) [364] is an outlier.

It appears that despite rather different energetic barriers for molecular motion in the two compounds, $FAPbI_3$ and $MAPbI_3$ coincidentally exhibit very similar rotational dynamics near room temperature. Above the glassy freezing in $FAPbI_3$ ($\approx$50 K) and above the β–γ transition in $MAPbI_3$ (165 K), these reorientation times are associated

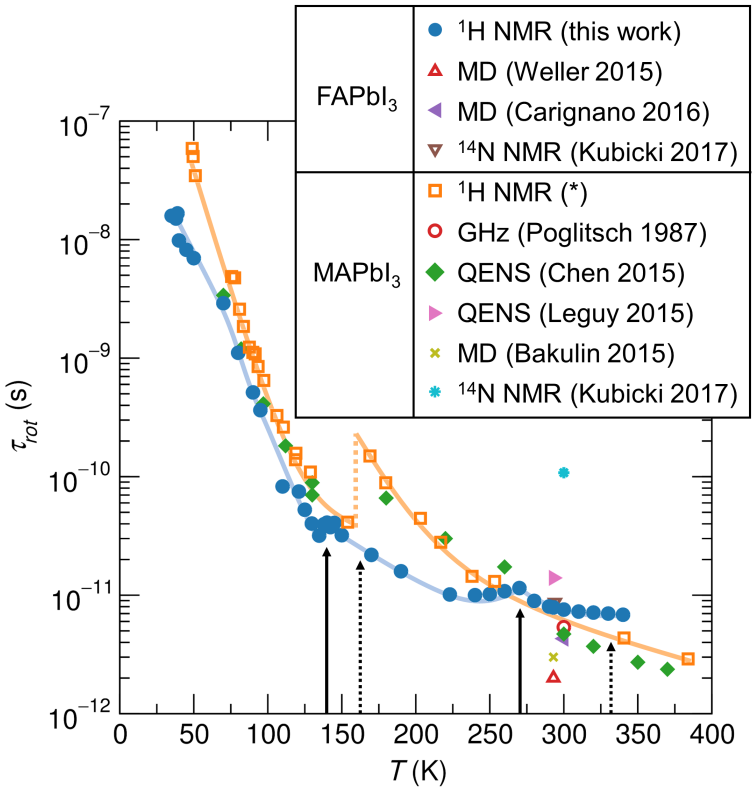

Figure 9.5: Temperature-dependence of the molecular reorentation time (τ_{rot}) in $FAPbI_3$ and $MAPbI_3$ modeled from ^1H T_1 using the model of Bloembergen, Purcell, and Pound. [363] Phase transition temperatures are indicated by solid ($FAPbI_3$) and dashed ($MAPbI_3$) arrows. Colored lines are to guide the eye only. (*) ^1H T_1 data for $MAPbI_3$ are taken from Xu and coworkers. [298] Reported reorientation times from GHz spectroscopy, quasi-elastic neutron scattering (QENS), ab initio molecular dynamics (MD), and ^{14}N NMR are presented for comparison. [300, 344, 364, 333, 261, 337, 318]

with modes that reorient the dipole axis of the molecules, which are intimately linked to dielectric properties, local electric fields, and dynamic symmetry-breaking. The coincident room temperature dynamics observed here in the two compounds suggest a need for further study of the molecular contribution to the full frequency-dependent dielectric response. With one exception, [333] reports in this area appear to be limited to ab initio calculation of the molecular dipole moments (MA: 2.3 D; FA: 0.2 D) [165] and to electrical [282, 296, 52, 53, 334] and optical [284] measurements of dielectric response which are far slower or far faster, respectively, than molecular reorientation. In particular, it is intriguing to consider if the differing barriers to molecular dipole rotation and differing dipole moments lead to important differences between $FAPbI_3$ and $MAPbI_3$ on timescales relevant to exciton dissociation, interaction of charge carriers with polar optical phonons or polarons, or momentum separation of excited electrons and holes due to possible dynamic Rashba–Dresselhaus effects.

Near room temperature (where T_1 is independent of field strength), the longer relaxation times in $FAPbI_3$ compared with $MAPbI_3$ despite similar dynamics suggest less effective spin-lattice relaxation, perhaps related to the reduced density of ^{1}H nuclei. Indeed, the ratio of the dipole–dipole distances obtained from fitting to the model of Bloembergen, Purcell, and Pound [363] ($r_{FA} = 2.35$ Å; $r_{MA} = 1.90$ Å), is nearly inverse to the ratio of the volumetric number density of H in the two compounds. As a matter of practice, the broad agreement between the results for $MAPbI_3$ from ^{1}H NMR and from QENS, techniques which both probe hydrogen but leverage distinct physics, confers a degree of confidence in our results and suggests the use of these methods for future studies of molecular motion in related compounds.

To further understand the molecule–cage interaction in $FAPbI_3$, we analyzed pair distribution functions at 100 K, 300 K, and 500 K from neutron total scattering experiments on an N-deuterated sample ($CH[ND_2]_2PbI_3$, to reduce the incoherent scattering

contribution from ^{1}H). One expects that substitution of D for H may impact the molecular moment of inertia as well as hydrogen bond strengths, [365] possibly modifying the evolution of structure [366, 188] and, concomitantly, of properties. [343] Isotope effects aside, the neutron pair distribution functions (NPDFs) shown in Figure 9.6 exhibit clear features associated with changes in molecular motion with temperature. By comparison with the reported X-ray pair distribution function (XPDF, which will have a negligible contribution from the weakly-scattering organic molecule) for hydrogenated $FAPbI_3$ [51] and the calculated NPDF for the isolated molecule (molecular geometry from DFT, see Supporting Information), we identify regions with substantial temperature dependence due to atom–atom correlations between the molecule and the inorganic framework.

Of particular note, the PDF is significantly enhanced and sharpened with cooling near ≈3.7 Å, consistent with a slowing of molecular motion. This distance corresponds to the N···I separation for hydrogen bonds between –Nsp^2H$_2$ donors and iodine acceptors from ab initio structure relaxations (3.6 Å to 3.7 Å, Supporting Information) and from the crystallographic database analysis of Steiner (3.66 Å). [367]

This evidence of molecule–cage correlations at distances consistent with hydrogen bonding suggests the importance of the molecule–cage interaction for correctly describing local structure and lattice dynamics. Indeed, local distortions enhanced by the molecules have recently been implicated in the anomalously large bandgaps of the hybrid perovskites relative to their all-inorganic counterparts, [368] and the hydrogen bonds in $MAPbI_3$ are suggested to play an important role in directing structure evolution more broadly. [299, 346, 347] It appears likely that standard methods for calculating phonon dispersions may fall short given the sensitivity of lattice stiffness to the particular ordering of molecular orientations (due to hydrogen bonding) and the overlapping timescales for molecular reorientation and phonons.

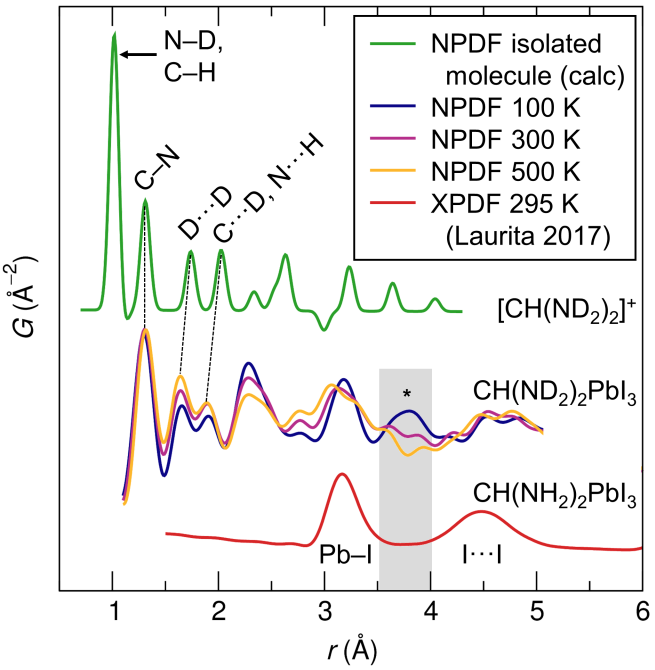

Figure 9.6: Neutron pair distribution functions (NPDF) for N-deuterated perovskite $FAPbI_3$ from neutron total scattering experiments, with the calculated NPDF for an isolated N-deuterated FA cation (molecular geometry from DFT, Supporting Information), and the reported X-ray pair distribution function (XPDF) [51] for comparison. (*) Particularly around ≈3.7 Å, which corresponds to N···I correlations (see Supporting Information, as well as Steiner's crystallographic database analysis of hydrogen bonding), [367] the NPDFs are significantly sharpened on cooling, consistent with a reduced reorientation rate of the molecule.

An overview of the evolution of crystal structure and molecular dynamics for the known phases of $FAPbI_3$ and $MAPbI_3$, as well as the activation barriers for molecular rotations in each, is displayed in Figure 9.7. This represents a synthesis of the results of this work with the findings of complementary prior reports. [298, 191, 261, 318, 52, 53, 344]

As $FAPbI_3$ is cooled, molecular motion slows and the inorganic octahedra tilt to improve coordination of the *A*-site cation and enhance electrostatic binding, but the molecular geometry appears to be incompatible with the preferred ground state octahedral tilting pattern. This leads to substantially more complex behavior in $FAPbI_3$ than in $MAPbI_3$, with a disordered pseudo-cubic γ-phase with persistent dipole motion, [53] followed by a fragile glassy freezing into a disordered ground state. [52] The activation barriers (above 100 K) for molecular rotation increase monotonically in each successive phase on cooling, reflecting lattice contraction and the increasingly confined local environment of the *A*-site as the degree of octahedral tilting increases. In the case of the disordered, pseudo-cubic γ-phase, the tilt angles increase only locally, but not crystallographically.

In contrast, as $MAPbI_3$ is cooled, the tetragonal β-phase exhibits a tilt pattern ($a^0a^0c^-$) that is unusual for perovskite bromides and iodides, [248] followed by a common orthorhombic tilt pattern ($a^+b^-b^-$) that somewhat easily accommodates the shape and hydrogen bonding tendencies of the MA cation in antiferrodistortive ordering. This last transition is accompanied by the loss of four-fold dipole reorientation, which drastically reduces the dielectric response and leads to a reduced activation barrier for rotation from ^{1}H NMR, since relatively facile three-fold rotations about the C–N axis become the dominant relaxation mechanism. While signatures of glassy freezing exist on cooling this compound below 100 K, they are significantly subtler than for $FAPbI_3$, [52] which comports with the findings presented here.

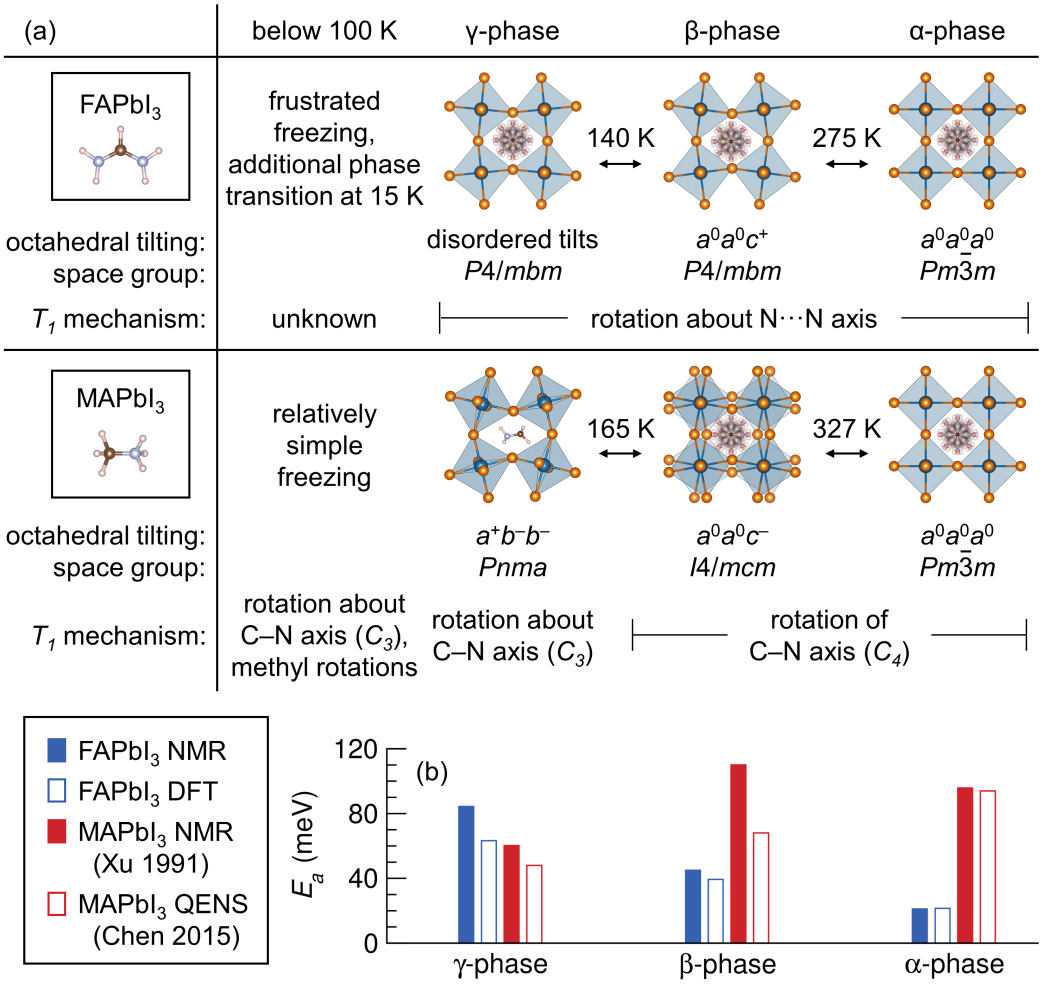

Figure 9.7: (a) Overview of the temperature evolution of crystal structure and molecular rotations for $FAPbI_3$ and $MAPbI_3$. Crystal structures and phase transition temperatures are taken from Weller and coworkers [191] and Fabini and coworkers, [53] while T_1 mechanisms and low temperature behaviors (<100 K) are synthesized from this work and prior reports. [298, 261, 318, 52, 53, 344] (b) Activation barriers for molecular rotation mechanisms that mediate spin-lattice relaxation for the known perovskite phases of $FAPbI_3$ and $MAPbI_3$. Values for $FAPbI_3$ are from this work, while those for $MAPbI_3$ are drawn from the literature. [298, 261]

9.4 Conclusion

With $FAPbI_3$ the closest end-member of the highest performing perovskite photovoltaic absorber solid solutions, establishing the dynamics of molecular motion is an important prerequisite for mechanistic explanations of the outstanding optoelectronic properties of these systems. We show via spectroscopy, scattering, calorimetry, and computation that despite differences in the details of the molecule–cage interaction in $FAPbI_3$ and the better-studied $MAPbI_3$, reorientation rates of the molecular dipole axis at room temperature are not significantly different in the two. Both systems coincidentally exhibit reorientation times on the order of 8 ps at ambient temperature, with weaker temperature dependence in $FAPbI_3$. For FA, rotations about an axis parallel to the N···N line are the preferred mode in all phases above ≈50 K. Incompatibility between the geometry of hydrogen bonding propensities of the molecule and octahedral tilting tendencies of the inorganic framework lead to a frustrated molecule–cage interaction. As the system is cooled, this frustration produces an unusual disordered phase with reentrant cubic pseudosymmetry followed by a glassy freezing into a disordered ground state. Hydrogen bonds between amine group hydrogens and the halogens of the surrounding cage underscore the importance of the molecular cation in directing structure evolution and modifying the electron–phonon coupling.

This work provides essential dynamical and structural information for resolving the key outstanding questions in the halide perovskite field: Namely, why are these solution-processed materials so insensitive to inevitable point defects and impurities; why are carrier mobilities so modest relative to the expectation from the low effective masses indicated from band theory; and how can strong optical absorption and extremely long carrier lifetimes fortuitously coexist? Because of the couplings between molecular motion and dielectric response, local electric fields, dynamic symmetry-

breaking, and electron–phonon scattering, any hypothesis which attempts to explain these (including those of large-polaron transport and of transient Rashba–Dresselhaus effects) must reconcile with this emerging understanding of molecular motions.

Time-resolved spectroscopic [369] and scattering [370] techniques may afford the opportunity to probe these promising semiconductors on time-scales relevant to the structural and electronic perturbations that are proposed to play a role in enhanced carrier lifetimes. [292, 336, 234, 227, 50, 262, 51, 263, 351] We hope that new results such as these may inform a key point of contention: Are the molecular cations simply larger monocations than any (non-radioactive) alkali metal (in a sense, "pseudo-francium") that serves to un-tilt the surrounding inorganic framework and improve orbital overlap, or are they indeed intimately linked to the remarkable functionality of these intriguing materials?

Chapter 10

Summary & Outlook

In just a few short years, the main-group halide perovskite research community has made incredible strides in developing new and better thin film deposition techniques, high performance solar cells, and previously unexplored optoelectronic and electronic devices. Additionally, there has been some measure of progress in characterizing the nature of carriers in these materials, investigating the mechanisms of degradation, and understanding the interfacial chemistry and energetics relevant to devices. But despite these fundamental and applied advances, no consensus has yet emerged regarding the origins of the curious combination of properties observed in these systems. Why are carrier lifetimes so long, and seemingly robust to preparation route and precise composition? Why are carrier mobilities so modest, when ab initio studies suggest high curvature band edges?

Further, new materials which fully mimic the favorable performance of the main-group halides have not been identified, either by explicit chemical design or by exploratory synthesis. Given the substantial (though not exhaustive) effort which has been applied in this direction, one is left to wonder if the features which imbue the perovskites with their remarkable properties are in fact unique — an improbable com-

bination of factors which are not reproduced in any other chemical or structural family.

It is towards these overarching questions — Are the main-group halide perovskites unique in their unusual properties? If so, why? And if not, what else is out there? — that the research efforts described in this dissertation have been addressed. Chapter 2 provides a brief illustration of the need for lead-free alternatives to achieve practical use of these materials. Chapters 3 and 4 explore the electronic structure and optoelectronic properties of isoelectronic bismuth(III) halides, revealing the importance of high-symmetry, extended connectivity for favorable band alignments and electronic transport. Chapters 5 and 6 demonstrate the existence of a chemically-tunable lattice instability across the halide perovskites and provide design rules to explicitly test the importance of lattice polarizability and local symmetry-breaking to the observed properties in these phases. Chapters 7 – 9 demonstrate the nature of molecular motion and its interaction with the surrounding inorganic framework in the high performance lead iodide PV absorbers. Chapter 8 additionally identifies an unusual disordered reentrant phase (and its associated optical properties) which arises due to a frustrated molecule–cage interaction upon cooling the underexplored formamidinium lead iodide ($FAPbI_3$). Chapter 9 additionally establishes the dynamics of molecular motion for $FAPbI_3$ over a wide temperature range and reports a critical analysis of the estimates of molecular motion times for methylammonium lead iodide ($MAPbI_3$) and $FAPbI_3$ from various techniques across the literature. These insights on the dynamics of molecular motion provide essential inputs for future scrutiny of hypotheses which seek to explain the origins of the favorable properties in these systems.

Though the field has not arrived at a consensus on these points, we summarize here the criteria which appear, based on the results described here as well as recent reports from other laboratories, to be important to the unexpected optoelectronic performance of the main-group halide perovskites.

First, the spatially-disperse, filled ns^2 orbitals (lone pair electrons) on the heavy main-group dications overlap strongly with the anion p orbitals. This results in a very wide valence band which leads to light hole effective masses and a valence band maximum which is suitable for hole transfer to existing hole transport layers. Were it not for these lone pair electrons, the electronic structure would qualitatively resemble that of compounds with $d^{10}s^0$ metals like perovskite $BaSnO_3$,[371] with deep, rather flat valence bands, and a single extremely dispersive conduction band.

Second (and related to the first point), the linear or nearly-linear covalent metal–anion connectivity in three dimensions afforded by the perovskite structure is important for electronic structure and transport, maximizing the metal s–anion p overlap in the valence band and the metal p–metal p interaction in the conduction bands and affording three dimensional band transport. Non-toxic ns^2 ions stable against further oxidation (Bi^{3+}, and to a lesser extent, Sb^{3+}) tend to adopt crystal structures with very different connectivity and more distorted metal coordination due to their different valence. Recently prepared $A_2M^{\mathrm{I}}\mathrm{Bi}^{\mathrm{III}}X_6$ elpasolites are an exception,[19, 20, 372] but these phases have a qualitatively different electronic structure unless the monovalent metal is highly toxic Tl^+ or oxidation-prone In^+.

Third, the substantial lattice polarizability (and resulting high static dielectric constant) increasingly appears to be related to defect tolerant transport. This suggestion was made some years ago for these materials,[93] and earlier still for thallium halides[99] and doped ferroelectric oxides.[170] The polarizability of the lattice is proposed to screen the Coulomb interaction among carriers and between carriers and charged defect complexes. This would reduce trapping and recombination rates, as well as reduce carrier mobilities because of the strong electron–phonon interaction, all of which are consistent with experimental observations. More recently, this hypothesis has been somewhat formalized using the framework of "large" polarons,[227] express-

ing the fact that this state is intermediate between a textbook rigid lattice and a strongly coupled system where carriers self-trap in such a localized manner that conduction proceeds by a hopping mechanism ("small" polarons).

With these factors in mind, a number of future research directions for materials chemistry emerge. First, despite the limitations discussed above, can clever design strategies produce lead-free double perovskites or perovskite-derivatives which qualitatively retain the electronic structure of the tin and lead halides, but with greater stability against moisture and oxidation? Second, can layered lead halides be prepared which combine improved stability with adequate performance for photovoltaic, light emission, and photodetection applications? Can the wide valence band width and reasonably shallow valence band maximum arising from the lone pair electrons be leveraged to make p-type transparent conductors from perovskite tin or lead chlorides or chloro-fluorides?

More broadly, are there other regions of chemical and structural space where "soft" semiconductors can be found, combining a polarizable lattice and favorable electronic structure? For instance, can transition metal cations with the d^0s^0 valence (also subject to a pseudo-Jahn–Teller [PJT] instability, though not due to a lone pair) be leveraged to prepare highly polarizable phases with favorable electronic transport? d^0 oxides are typically insulators, but perhaps there exist sulfides, selenides, phosphides, or arsenides which balance between the strength of the PJT effect from more electronegative anions and the semiconducting bandgaps likely to arise from softer anions.

The research described in this dissertation provides essential dynamical and structural information for the resolution of several outstanding questions in the halide perovskite field. In addition to the chemical explorations proposed above, the application of sophisticated time-resolved spectroscopic and scattering techniques may afford the opportunity to probe these curious semiconductors on time-scales relevant to the struc-

tural and electronic perturbations. We hope that these research results may inform key points of contention, including whether the molecular cations are simply larger monocations than any (non-radioactive) alkali metal ("pseudofrancium") that serves to un-tilt the surrounding inorganic framework and improve orbital overlap, or whether they are indeed intimately linked to the remarkable functionality of these intriguing materials.

Bibliography

[1] H. L. Wells, Über die cäsium–und kalium–bleihalogenide, *Z. Anorg. Chem.* **3**, 195–210 (1893) [doi].

[2] C. K. Møller, Crystal structure and photoconductivity of caesium plumbohalides, *Nature* **182**, 1436 (1958) [doi].

[3] D. Weber, $CH_3NH_3PbX_3$, ein Pb(II)-system mit kubischer perowskitstruktur, *Z. Naturforsch. B Chem. Sci.* **33**, 1443–1445 (1978) [doi].

[4] Y. I. Dolzhenko, T. Inabe, Y. Maruyama, In situ x-ray observation on the intercalation of weak interaction molecules into perovskite-type layered crystals $(C_9H_{19}NH_3)_2PbI_4$ and $(C_{10}H_{21}NH_3)_2CdCl_4$, *Bull. Chem. Soc. Jpn.* **59**, 563–567 (1986) [doi].

[5] D. B. Mitzi, C. A. Feild, W. T. A. Harrison, A. M. Guloy, Conducting tin halides with a layered organic-based perovskite structure, *Nature* **369**, 467–469 (1994) [doi].

[6] C. R. Kagan, D. B. Mitzi, C. D. Dimitrakopoulos, Organic-inorganic hybrid materials as semiconducting channels in thin-film field-effect transistors, *Science* **286**, 945–947 (1999) [doi].

[7] A. Kojima, K. Teshima, Y. Shirai, T. Miyasaka, Organometal halide perovskites as visible-light sensitizers for photovoltaic cells, *J. Am. Chem. Soc.* **131**, 6050–6051 (2009) [doi].

[8] I. Chung, B. Lee, J. He, R. P. H. Chang, M. G. Kanatzidis, All-solid-state dye-sensitized solar cells with high efficiency, *Nature* **485**, 486–489 [doi].

[9] H.-S. Kim, C.-R. Lee, J.-H. Im, K.-B. Lee, T. Moehl, A. Marchioro, S.-J. Moon, R. Humphry-Baker, J.-H. Yum, J. E. Moser, M. Grätzel, N.-G. Park, Lead iodide perovskite sensitized all-solid-state submicron thin film mesoscopic solar cell with efficiency exceeding 9%, *Sci. Rep.* 591 (2012) [doi].

[10] M. M. Lee, J. Teuscher, T. Miyasaka, T. N. Murakami, H. J. Snaith, Efficient hybrid solar cells based on meso-superstructured organometal halide perovskites, *Science* **338**, 643–647 (2012) [doi].

[11] I. C. Smith, E. T. Hoke, D. Solis-Ibarra, M. D. McGehee, H. I. Karunadasa, A layered hybrid perovskite solar-cell absorber with enhanced moisture stability, *Angew. Chem. Int. Ed.* **53**, 11232–11235 (2014) [doi].

[12] N. K. Noel, S. D. Stranks, A. Abate, C. Wehrenfennig, S. Guarnera, A.-A. Haghighirad, A. Sadhanala, G. E. Eperon, S. K. Pathak, M. B. Johnston, A. Petrozza, L. M. Herz, H. J. Snaith, Lead-free organic-inorganic tin halide perovskites for photovoltaic applications, *Energy Environ. Sci.* **7**, 3061–3068 (2014) [doi].

[13] M. H. Kumar, S. Dharani, W. L. Leong, P. P. Boix, R. R. Prabhakar, T. Baikie, C. Shi, H. Ding, R. Ramesh, M. Asta, M. Grätzel, S. G. Mhaisalkar, N. Mathews, Lead-free halide perovskite solar cells with high photocurrents realized through vacancy modulation, *Adv. Mater.* **26**, 7122–7127 (2014) [doi].

[14] F. Hao, C. C. Stoumpos, D. H. Cao, R. P. H. Chang, M. G. Kanatzidis, Lead-free solid-state organic-inorganic halide perovskite solar cells, *Nat. Photon.* **8**, 489–494 (2014) [doi].

[15] A. J. Lehner, H. Wang, D. H. Fabini, C. D. Liman, C.-A. Hébert, E. E. Perry, M. Wang, G. C. Bazan, M. L. Chabinyc, R. Seshadri, Electronic structure and photovoltaic application of BiI_3, *Appl. Phys. Lett.* **107**, 131109 (2015) [doi].

[16] A. J. Lehner, D. H. Fabini, H. A. Evans, C.-A. Hébert, S. R. Smock, J. Hu, H. Wang, J. W. Zwanziger, M. L. Chabinyc, R. Seshadri, Crystal and electronic structures of complex bismuth iodides $a_3bi_2i_9$ (a = k, rb, cs) related to perovskite: Aiding the rational design of photovoltaics, *Chem. Mater.* **27**, 7137–7148 (2015) [doi].

[17] C. C. Stoumpos, L. Frazer, D. J. Clark, Y. S. Kim, S. H. Rhim, A. J. Freeman, J. B. Ketterson, J. I. Jang, M. G. Kanatzidis, Hybrid germanium iodide perovskite semiconductors: Active lone pairs, structural distortions, direct and indirect energy gaps, and strong nonlinear optical properties, *J. Am. Chem. Soc.* **137**, 6804–6819 (2015) [doi].

[18] A. E. Maughan, A. M. Ganose, M. M. Bordelon, E. M. Miller, D. O. Scanlon, J. R. Neilson, Defect tolerance to intolerance in the vacancy-ordered double perovskite semiconductors Cs_2SnI_6 and Cs_2TeI_6, *J. Am. Chem. Soc.* **138**, 8453–8464 (2016) [doi].

[19] E. T. McClure, M. R. Ball, W. Windl, P. M. Woodward, Cs_2AgBiX_6 (X = Br, Cl): New visible light absorbing, lead-free halide perovskite semiconductors, *Chem. Mater.* **28**, 1348–1354 (2016) [doi].

[20] A. H. Slavney, T. Hu, A. M. Lindenberg, H. I. Karunadasa, A bismuth-halide double perovskite with long carrier recombination lifetime for photovoltaic applications, *J. Am. Chem. Soc.* **138**, 2138–2141 (2016) [doi].

[21] Z.-K. Tan, R. S. Moghaddam, M. L. Lai, P. Docampo, R. Higler, F. Deschler, M. Price, A. Sadhanala, L. M. Pazos, D. Credgington, F. Hanusch, T. Bein, H. J. Snaith, R. H. Friend, Bright light-emitting diodes based on organometal halide perovskite, *Nat. Nanotechnol.* **9**, 687–692 (2014) [doi].

[22] Y.-H. Kim, H. Cho, J. H. Heo, T.-S. Kim, N. S. Myoung, C.-L. Lee, S. H. Im, T.-W. Lee, Multicolored organic/inorganic hybrid perovskite light-emitting diodes, *Adv. Mater.* **27**, 1248–1254 (2015) [doi].

[23] G. Xing, N. Mathews, S. S. Lim, N. Yantara, X. Liu, D. Sabba, M. Grätzel, S. Mhaisalkar, T. C. Sum, Low-temperature solution-processed wavelength-tunable perovskites for lasing, *Nat. Mater.* **13**, 476–480 (2014) [doi].

[24] F. Deschler, M. Price, S. Pathak, L. E. Klintberg, D.-D. Jarausch, R. Higler, S. Hüttner, T. Leijtens, S. D. Stranks, H. J. Snaith, M. Atatüre, R. T. Phillips, R. H. Friend, High photoluminescence efficiency and optically pumped lasing in solution-processed mixed halide perovskite semiconductors, *J. Phys. Chem. Lett.* **5**, 1421–1426 (2014) [doi].

[25] C. C. Stoumpos, C. D. Malliakas, J. A. Peters, Z. Liu, M. Sebastian, J. Im, T. C. Chasapis, A. C. Wibowo, D. Y. Chung, A. J. Freeman, B. W. Wessels, M. G. Kanatzidis, Crystal growth of the perovskite semiconductor $CsPbBr_3$: A new material for high-energy radiation detection, *Cryst. Growth Des.* **13**, 2722–2727 (2013) [doi].

[26] Y. He, G. Galli, Perovskites for solar thermoelectric applications: A first principle study of $CH_3NH_3AI_3$ (A = Pb and Sn), *Chem. Mater.* **26**, 5394–5400 (2014) [doi].

[27] X. Y. Chin, D. Cortecchia, J. Yin, A. Bruno, C. Soci, Lead iodide perovskite light-emitting field-effect transistor, *Nat. Commun.* **6**, 7383 (2015) [doi].

[28] J. G. Labram, D. H. Fabini, E. E. Perry, A. J. Lehner, H. Wang, A. M. Glaudell, G. Wu, H. Evans, D. Buck, R. Cotta, L. Echegoyen, F. Wudl, R. Seshadri, M. L. Chabinyc, Temperature-dependent polarization in field-effect transport and photovoltaic measurements of methylammonium lead iodide, *J. Phys. Chem. Lett.* **6**, 3565–3571 (2015) [doi].

[29] F. Li, C. Ma, H. Wang, W. Hu, W. Yu, A. D. Sheikh, T. Wu, Ambipolar solution-processed hybrid perovskite phototransistors, *Nat. Commun.* **6**, 8238 (2015) [doi].

[30] Y. Mei, C. Zhang, Z. Vardeny, O. Jurchescu, Electrostatic gating of hybrid halide perovskite field-effect transistors: Balanced ambipolar transport at room-temperature, *MRS Commun.* **5**, 297–301 (2015) [doi].

[31] V. M. Goldschmidt, Die gesetze der krystallochemie, *Naturwissenschaften* **14**, 477–485

[32] J. C. Maxwell, On the calculation of the equilibrium and stiffness of frames, *Philos. Mag. Ser. 4* **27**, 294–299 (1864) [doi].

[33] I. Bersuker, On the origin of ferroelectricity in perovskite-type crystals, *Phys. Lett.* **20**, 589–590 (1966) [doi].

[34] I. B. Bersuker, Pseudo-Jahn–Teller effect—A two-state paradigm in formation, deformation, and transformation of molecular systems and solids, *Chem. Rev.* **113**, 1351–1390 (2013) [doi].

[35] U. V. Waghmare, N. A. Spaldin, H. C. Kandpal, R. Seshadri, First-principles indicators of metallicity and cation off-centricity in the IV-VI rocksalt chalcogenides of divalent Ge, Sn, and Pb, *Phys. Rev. B* **67**, 125111 (2003) [doi].

[36] G. W. Watson, S. C. Parker, G. Kresse, Ab initio calculation of the origin of the distortion of α-PbO, *Phys. Rev. B* **59**, 8481 (1999) [doi].

[37] R. Seshadri, G. Baldinozzi, C. Felser, W. Tremel, Visualizing electronic structure changes across an antiferroelectric phase transition: Pb_2MgWO_6, *J. Mater. Chem.* **9**, 2463–2466 (1999) [doi].

[38] R. Seshadri, N. A. Hill, Visualizing the role of Bi 6s "lone pairs" in the off-center distortion in ferromagnetic $BiMnO_3$, *Chem. Mater.* **13**, 2892–2899 (2001) [doi].

[39] R. Seshadri, Visualizing lone pairs in compounds containing heavier congeners of the carbon and nitrogen group elements, *J. Chem. Sci.* **113**, 487–496 (2001) [doi].

[40] M. W. Stoltzfus, P. M. Woodward, R. Seshadri, J.-H. Klepeis, B. Bursten, Structure and bonding in $SnWO_4$, $PbWO_4$, and $BiVO_4$: Lone pairs vs inert pairs, *Inorg. Chem.* **46**, 3839–3850 (2007) [doi].

[41] A. Walsh, D. J. Payne, R. G. Egdell, G. W. Watson, Stereochemistry of post-transition metal oxides: Revision of the classical lone pair model, *Chem. Soc. Rev.* **40**, 4455–4463 (2011) [doi].

[42] P. Hohenberg, W. Kohn, Inhomogeneous electron gas, *Phys. Rev.* **136**, B864–B871 (1964) [doi].

[43] W. Kohn, L. J. Sham, Self-consistent equations including exchange and correlation effects, *Phys. Rev.* **140**, A1133–A1138 (1965) [doi].

[44] K. W. Wagner, Erklärung der dielektrischen nachwirkungsvorgänge auf grund maxwellscher vorstellungen, *Archiv f. Elektrotechnik* **2**, 371–387 (1914) [doi].

[45] R. Sillars, The properties of a dielectric containing semiconducting particles of various shapes, *J. Inst. Electr. Eng.* **80**, 378–394 (1937) [**doi**].

[46] E. Billig, K. W. Plessner, A note on the dielectric dispersion in polycrystalline materials, *Proc. Phys. Soc. Sect. B* **64**, 362–363 (1951) [**doi**].

[47] C. G. Koops, On the dispersion of resistivity and dielectric constant of some semiconductors at audiofrequencies, *Phys. Rev.* **83**, 121–124 (1951) [**doi**].

[48] L. Van Beek, The Maxwell-Wagner-Sillars effect, describing apparent dielectric loss in inhomogeneous media, *Physica* **26**, 66–68 (1960) [**doi**].

[49] D. Fabini, Quantifying the potential for lead pollution from halide perovskite photovoltaics, *J. Phys. Chem. Lett.* **6**, 3546–3548 (2015) [**doi**].

[50] D. H. Fabini, G. Laurita, J. S. Bechtel, C. C. Stoumpos, H. A. Evans, A. G. Kontos, Y. S. Raptis, P. Falaras, A. Van der Ven, M. G. Kanatzidis, R. Seshadri, Dynamic stereochemical activity of the Sn^{2+} lone pair in perovskite $CsSnBr_3$, *J. Am. Chem. Soc.* **138**, 11820–11832 (2016) [**doi**].

[51] G. Laurita, D. H. Fabini, C. C. Stoumpos, M. G. Kanatzidis, R. Seshadri, Chemical tuning of dynamic cation off-centering in the cubic phases of hybrid tin and lead halide perovskites, *Chem. Sci.* **8**, 5628–5635 (2017) [**doi**].

[52] D. H. Fabini, T. Hogan, H. A. Evans, C. C. Stoumpos, M. G. Kanatzidis, R. Seshadri, Dielectric and thermodynamic signatures of low-temperature glassy dynamics in the hybrid perovskites $CH_3NH_3PbI_3$ and $HC(NH_2)_2PbI_3$, *J. Phys. Chem. Lett.* **7**, 376–381 (2016) [**doi**].

[53] D. H. Fabini, C. C. Stoumpos, G. Laurita, A. Kaltzoglou, A. G. Kontos, P. Falaras, M. G. Kanatzidis, R. Seshadri, Reentrant structural and optical properties and large positive thermal expansion in perovskite formamidinium lead iodide, *Angew. Chem. Int. Ed.* **55**, 15392–15396 (2016) [**doi**].

[54] D. H. Fabini, T. A. Siaw, C. C. Stoumpos, G. Laurita, D. Olds, K. Page, J. G. Hu, M. G. Kanatzidis, S. Han, R. Seshadri, Universal dynamics of molecular reorientation in hybrid lead iodide perovskites, *J. Am. Chem. Soc.* **139**, 16875–16884 (2017) [**doi**].

[55] M. A. Green, K. Emery, Y. Hishikawa, W. Warta, E. D. Dunlop, Solar cell efficiency tables (version 45), *Prog. Photovoltaics Res. Appl.* **23**, 1–9 (2015) [**doi**].

[56] J. Gong, S. B. Darling, F. You, Perovskite photovoltaics: Life-cycle assessment of energy and environmental impacts, *Energy Environ. Sci.* **8**, 1953–1968 (2015) [**doi**].

[57] N. Espinosa, L. Serrano-Luján, A. Urbina, F. C. Krebs, Solution and vapour deposited lead perovskite solar cells: Ecotoxicity from a life cycle assessment perspective, *Sol. Energ. Mat. Sol. Cells* **137**, 303–310 (2015) [**doi**].

[58] B. Hailegnaw, S. Kirmayer, E. Edri, G. Hodes, D. Cahen, Rain on methylammonium lead iodide based perovskites: Possible environmental effects of perovskite solar cells, *J. Phys. Chem. Lett.* **6**, 1543–1547 (2015) [**doi**].

[59] V. M. Fthenakis, H. C. Kim, E. Alsema, Emissions from photovoltaic life cycles, *Environ. Sci. Technol.* **42**, 2168–2174 (2008) [**doi**].

[60] J. D. Bergesen, G. A. Heath, T. Gibon, S. Suh, Thin-film photovoltaic power generation offers decreasing greenhouse gas emissions and increasing environmental co-benefits in the long term, *Environ. Sci. Technol.* **48**, 9834–9843 (2014) [**doi**].

[61] U.S. Environmental Protection Agency, EPA takes final step in phaseout of leaded gasoline (1996), accessed 7-20-15.

[62] U.S. Environmental Protection Agency, 2011 National Emissions Inventory, Technical report, U.S. Environmental Protection Agency (2015).

[63] C. Block, R. Dams, Lead contents of coal, coal ash and fly ash, *Water Air Soil Poll.* **5**, 207–211 (1975) [**doi**].

[64] R. J. Guidoboni, Determination of trace elements in coal and coal ash by spark source mass spectrometry, *Anal. Chem.* **45**, 1275–1277 (1973) [**doi**].

[65] U.S. Energy Information Administration, Annual Energy Review 2011, Technical report, U.S. Energy Information Administration (2012).

[66] U.S. Geological Survey, 2012 Minerals Yearbook: Lead, Technical report, U.S. Geological Survey (2015).

[67] C. C. Stoumpos, C. D. Malliakas, M. G. Kanatzidis, Semiconducting tin and lead iodide perovskites with organic cations: Phase transitions, high mobilities, and near-infrared photoluminescent properties, *Inorg. Chem.* **52**, 9019–9038 (2013) [**doi**].

[68] OpenEI, Transparent cost database, accessed 7-20-15.

[69] The New York Times, Coal ash spill revives issue of its hazards, Technical report (December 24, 2008).

[70] The Washington Post, After decade, still signs of coal slurry spill, Technical report (October 17, 2010).

[71] A. K. Geim, I. V. Grigorieva, Van der Waals heterostructures, *Nature* **499**, 419–425 (2013) [doi].

[72] D. B. Mitzi, Solution-processed inorganic semiconductors, *J. Mater. Chem.* **14**, 2355–2365 (2004) [doi].

[73] D. Nason, L. Keller, The growth and crystallography of bismuth tri-iodide crystals grown by vapor transport, *J. Cryst. Growth* **156**, 221–226 (1995) [doi].

[74] A. T. Lintereur, W. Qiu, J. C. Nino, J. Baciak, Characterization of bismuth tri-iodide single crystals for wide band-gap semiconductor radiation detectors, *Nucl. Instrum. Methods Phys. Res., Sect. A* **652**, 166–169 (2011) [doi].

[75] H. Han, M. Hong, S. S. Gokhale, S. B. Sinnott, K. Jordan, J. E. Baciak, J. C. Nino, Defect engineering of BiI_3 single crystals: Enhanced electrical and radiation performance for room temperature gamma-ray detection, *J. Phys. Chem. C* **118**, 3244–3250 (2014) [doi].

[76] S. S. Gokhale, H. Han, J. E. Baciak, J. C. Nino, K. A. Jordan, Growth, fabrication, and testing of bismuth tri-iodide semiconductor radiation detectors, *Radiat. Meas.* **74**, 47–52 (2015) [doi].

[77] A. Cuña, I. Aguiar, A. Gancharov, M. Pérez, L. Fornaro, Correlation between growth orientation and growth temperature for bismuth tri-iodide films, *Crys. Res. Technol.* **39**, 899–905 (2004) [doi].

[78] A. Cuña, A. Noguera, E. Saucedo, L. Fornaro, Growth of bismuth tri-iodide platelets by the physical vapor deposition method, *Crys. Res. Technol.* **39**, 912–919 (2004) [doi].

[79] I. Aguiar, S. Kröger, L. Fornaro, Bismuth tri-iodide polycrystalline films for X-ray direct and digital imagers, *Nucl. Instrum. Methods Phys. Res., Sect. A* **610**, 332–334 (2009) [doi].

[80] K. M. Boopathi, S. Raman, R. Mohanraman, F.-C. Chou, Y.-Y. Chen, C.-H. Lee, F.-C. Chang, C.-W. Chu, Solution-processable bismuth iodide nanosheets as hole transport layers for organic solar cells, *Sol. Energy Mater. Sol. Cells* **121**, 35–41 (2014) [doi].

[81] N.-G. Park, Perovskite solar cells: An emerging photovoltaic technology, *Mater. Today* **18**, 65–72 (2015) [doi].

[82] M. Ruck, Darstellung und kristallstruktur von fehlordnungsfreiem bismuttriiodid, *Z. Kristallogr.* **210**, 650–655 (1995) [doi].

[83] B. L. Evans, Optical properties of bismuth tri-iodide, *Proc. R. Soc. London, Ser. A* **289**, 275–286 (1966) [doi].

[84] Y. Kaifu, T. Komatsu, Optical properties of bismuth tri-iodide single crystals. II. Intrinsic absorption edge, *J. Phys. Soc. Jpn.* **40**, 1377–1382 (1976) [doi].

[85] S. Kowalczyk, L. Ley, F. McFeely, D. Shirley, A high-resolution X-ray photoemission study of the total valence-band densities of states of GaSe and BiI_3, *Solid State Commun.* **17**, 463–467 (1975) [doi].

[86] I. D. Turjanica, J. Horák, V. M. Benca, D. V. Čepur, The external photoeffect and a simple band scheme of A^VB_3 VII iodide crystals, *Czech. J. Phys.* **18**, 106–111 (1968) [doi].

[87] G. Margaritondo, J. Rowe, M. Schlüter, G. Wertheim, F. Levy, E. Mooser, Photoemission spectroscopy of layered halides: PbI_2 and BiI_3, *Phys. Rev. B* **16**, 2934–2937 (1977) [doi].

[88] G. Jellison, J. Ramey, L. Boatner, Optical functions of BiI_3 as measured by generalized ellipsometry, *Phys. Rev. B* **59**, 9718–9721 (1999) [doi].

[89] N. J. Podraza, W. Qiu, B. B. Hinojosa, H. Xu, M. A. Motyka, S. R. Phillpot, J. E. Baciak, S. Trolier-Mckinstry, J. C. Nino, Band gap and structure of single crystal BiI_3: Resolving discrepancies in literature, *J. Appl. Phys.* **114** (2013) [doi].

[90] T. R. Devidas, N. V. Chandra Shekar, C. S. Sundar, P. Chithaiah, Y. A. Sorb, V. S. Bhadram, N. Chandrabhas, K. Pal, U. V. Waghmare, C. N. R. Rao, Pressure-induced structural changes and insulator-metal transition in layered bismuth triiodide, BiI_3: A combined experimental and theoretical study, *J. Phys.: Condens. Matter* **26**, 275502 (2014) [doi].

[91] D. J. Singh, Structure and optical properties of high light output halide scintillators, *Phys. Rev. B* **82**, 155145 (2010) [doi].

[92] C. G. Van de Walle, R. M. Martin, Theoretical calculations of heterojunction discontinuities in the Si/Ge system, *Phys. Rev. B* **34**, 5621–5634 (1986) [doi].

[93] J. Brgoch, A. J. Lehner, M. Chabinyc, R. Seshadri, Ab initio calculations of band gaps and absolute band positions of polymorphs of $RbPbI_3$ and $CsPbI_3$: Implications for main-group halide perovskite photovoltaics, *J. Phys. Chem. C* **118**, 27721–27727 (2014) [doi].

[94] J. Heyd, G. E. Scuseria, M. Ernzerhof, Hybrid functionals based on a screened coulomb potential, *J. Chem. Phys.* **118**, 8207–8215 (2003) [doi].

[95] G. Kresse, J. Furthmüller, Efficient iterative schemes for ab initio total-energy calculations using a plane-wave basis set, *Phys. Rev. B* **54**, 11169–11186 (1996) [doi].

[96] G. Kresse, D. Joubert, From ultrasoft pseudopotentials to the projector augmented-wave method, *Phys. Rev. B* **59**, 1758–1775 (1999) [doi].

[97] A. Owens, A. Peacock, Compound semiconductor radiation detectors, *Nucl. Instrum. Methods Phys. Res., Sect. A* **531**, 18–37 (2004) [doi].

[98] M. Miao, J. Brgoch, A. Krishnapriyan, A. Goldman, J. A. Kurzman, R. Seshadri, On the stereochemical inertness of the auride lone pair: Ab initio studies of AAu (A = K, Rb, Cs), *Inorg. Chem.* **52**, 8183–8189 (2013) [doi].

[99] M.-H. Du, D. J. Singh, Enhanced Born charge and proximity to ferroelectricity in thallium halides, *Phys. Rev. B* **81**, 144114 (2010) [doi].

[100] P. Schulz, E. Edri, S. Kirmayer, G. Hodes, D. Cahen, A. Kahn, Interface energetics in organo-metal halide perovskite-based photovoltaic cells, *Energy Environ. Sci.* **7**, 1377–1381 (2014) [doi].

[101] S. Schols, *Device Architecture and Materials for Organic Light-emitting Devices: Targeting High Current Densities and Control of the Triplet Concentration*, Springer Science & Business Media (2011).

[102] J. Veres, S. Ogier, S. Leeming, B. Brown, D. Cupertino, Air stable, amorphous organic films and their applications to solution processable flexible electronics, *Mater. Res. Soc. Symp. Proc.* **708**, 1–8 (2001) [doi].

[103] Y. Zhang, S.-C. Chien, K.-S. Chen, H.-L. Yip, Y. Sun, J. A. Davies, F.-C. Chen, A. K.-Y. Jen, Increased open circuit voltage in fluorinated benzothiadiazole-based alternating conjugated polymers, *Chem. Comm.* **47**, 11026 (2011) [doi].

[104] S. De Wolf, J. Holovsky, S.-J. Moon, P. Löper, B. Niesen, M. Ledinsky, F.-J. Haug, J.-H. Yum, C. Ballif, Organometallic halide perovskites: Sharp optical absorption edge and its relation to photovoltaic performance, *J. Phys. Chem. Lett.* **5**, 1035–1039 (2014) [doi].

[105] J. L. Knutson, J. D. Martin, D. B. Mitzi, Tuning the band gap in hybrid tin iodide perovskite semiconductors using structural templating, *Inorg. Chem.* **44**, 4699–4705 (2005) [doi].

[106] T. Miyasaka, Organo-lead halide perovskite: Rare functions in photovoltaics and optoelectronics, *Chem. Lett.* **44**, 720–729 (2015) [doi].

[107] L.-M. Wu, X.-T. Wu, L. Chen, Structural overview and structure-property relationships of iodoplumbate and iodobismuthate, *Coord. Chem. Rev.* **253**, 2787–2804 (2009) [doi].

[108] D. B. Mitzi, Organic-inorganic perovskites containing trivalent metal halide layers: The templating influence of the organic cation layer, *Inorg. Chem.* **39**, 6107–6113 (2000) [doi].

[109] T. Kodzasa, H. Ushijima, H. Matsuda, T. Kamata, Preparation of thin film of layer structured bismuth iodide with a long chain alkylammonium and its nonlinear optical property, *Mol. Cryst. Liq. Cryst. Sci. Technol. A* **343**, 71–75 (2000) [doi].

[110] D. B. Mitzi, P. Brock, Structure and optical properties of several organic-inorganic hybrids containing corner-sharing chains of bismuth iodide octahedra, *Inorg. Chem.* **40**, 2096–2104 (2001) [doi].

[111] H. Dammak, A. Yangui, S. Triki, Y. Abid, H. Feki, Structural characterization, vibrational, optical properties and DFT investigation of a new luminescent organic–inorganic material: $(C_6H_{14}N)_3Bi_2I_9$, *J. Lumin.* **161**, 214–220 (2015) [doi].

[112] V. Sidey, Y. Voroshilov, S. Kun, E. Peresh, Crystal growth and X-ray structure determination of $Rb_3Bi_2I_9$, *J. Alloys Compd.* **296**, 53–58 (2000) [doi].

[113] C. Preitschaft, *Ternäre und quaternäre materialien mit komplexen thio-, selenido- und halogenid-anionen*, Ph.D. thesis, Universität Regensburg (2004).

[114] O. Lindquist, The crystal structure of caesium bismuth iodide, $Cs_3Bi_2I_9$, *Acta Chem. Scand.* **22**, 2943–2952 (1968) [doi].

[115] I. P. Aleksandrov, A. F. Bovina, O. A. Ageev, A. A. Sukhovskii, Incommensurate phase in the layered hexagonal crystal $Cs_3Bi_2I_9$, *Phys. Solid State* **39**, 991–994 (1997) [doi].

[116] S. V. Melńikova, A. I. Zaitsev, Ferroelectric phase transition in $Cs_3Bi_2I_9$, *Phys. Solid State* **39**, 1652–1654 (1997) [doi].

[117] A. Jorio, R. Currat, D. A. A. Myles, G. J. McIntyre, I. P. Aleksandrova, J. M. Kiat, P. Saint-Grégoire, Ferroelastic phase transition in $Cs_3Bi_2I_9$: A neutron diffraction study, *Phys. Rev. B* **61**, 3857–3862 (2000) [doi].

[118] A. Arakcheeva, G. Chapuis, M. Meyer, The LT phase of $Cs_3Bi_2I_9$, *Z. Kristallogr.* **216**, 199–205 (2001) [doi].

[119] F. Lazarini, Caesium enneabromodibismuthate(III), *Acta Crystallogr. B* **33**, 2961–2964 (1977) [doi].

[120] K. S. Aleksandrov, V. V. Beznosikov, Hierarchies of perovskite-like crystals (review), *Phys. Solid State* **39**, 695–715 (1997) [doi].

[121] B. Saparov, F. Hong, J.-P. Sun, H.-S. Duan, W. Meng, S. Cameron, I. G. Hill, Y. Yan, D. B. Mitzi, Thin-film preparation and characterization of $Cs_3Sb_2I_9$: A lead-free layered perovskite semiconductor, *Chem. Mater.* **27**, 5622–5632 (2015) [**doi**].

[122] A. V. Zamkov, A. I. Zaitsev, S. A. Parshikov, A. M. Sysoev, Acoustooptic properties of $Cs_3Bi_2I_9$ crystals, *Inorg. Mater.* **37**, 82–83 (2001) [**doi**].

[123] F. V. Motsnyi, E. Y. Peresh, O. M. Smolanka, Nontraditional temperature shift of the fundamental absorption edge for layered substances and the ferroelastic phase transition in $Cs_3Bi_2I_9$, *Solid State Commun.* **131**, 469–471 (2004) [**doi**].

[124] E. Y. Peresh, V. I. Sidei, O. V. Zubaka, I. P. Stercho, $K_2(Rb_2,Cs_2,Tl_2)TeBr_6(I_6)$ and $Rb_3(Cs_3)Sb_2(Bi_2)Br_9(I_9)$ perovskite compounds, *Inorg. Mater.* **47**, 208–212 (2011) [**doi**].

[125] E. Y. Peresh, V. I. Sidei, N. I. Gaborets, O. V. Zubaka, I. P. Stercho, I. E. Barchii, Influence of the average atomic number of the A_2TeC_6 and $A_3B_2C_9$ (A = K, Rb, Cs, Tl(I); B = Sb, Bi; C = Br, I) compounds on their melting point and band gap, *Inorg. Mater.* **50**, 111–116 (2014) [**doi**].

[126] R. E. Brandt, V. Stevanović, D. S. Ginley, T. Buonassisi, Identifying defect-tolerant semiconductors with high minority-carrier lifetimes: Beyond hybrid lead halide perovskites, *MRS Commun.* **5**, 265–275 (2015) [**doi**].

[127] A. A. Coelho, TOPAS-Academic V5 (2013).

[128] Bruker Analytical X-ray Systems, Inc. Madison WI, USA., SAINT*: Data Reduction and Frame Integration Program for the CCD Area-Detector System.* (1999).

[129] Siemens Industrial Automation Inc. Madison WI, USA, SADABS*: Area-Detector Absorption Correction* (1996).

[130] G. M. Sheldrick, SHELXS-97 - *Program for the Solution of Crystal Structures*, University of Göttingen, Germany (1997).

[131] G. M. Sheldrick, A short history of SHELX, *Acta Crystallogr. A* **64**, 112–122 (2008) [**doi**].

[132] K. Momma, F. Izumi, VESTA3 for three-dimensional visualization of crystal, volumetric and morphology data, *J. Appl. Crystallogr.* **44**, 1272–1276 (2011) [**doi**].

[133] M. N. Burnett, C. K. Johnson, ORTEP-III: Oak Ridge Thermal Ellipsoid Plot program for crystal structure illustrations (1996).

[134] ^{87}Rb dynamic-angle spinning NMR spectroscopy of inorganic rubidium salts, *J. Am. Chem. Soc.* **114**, 7489–7493 (1992) [doi].

[135] J. Tauc, R. Grigorovici, A. Vancu, Optical properties and electronic structure of amorphous germanium, *Phys. Stat. Sol.* **15**, 627–637 (1966) [doi].

[136] J. Tauc, Optical properties and electronic structure of amorphous Ge and Si, *Mater. Res. Bull.* **3**, 37–46 (1968) [doi].

[137] G. Kresse, J. Hafner, Ab initio molecular dynamics for liquid metals, *Phys. Rev. B* **47**, 558–561 (1993) [doi].

[138] G. Kresse, J. Hafner, Ab initio molecular-dynamics simulation of the liquid-metal-amorphous-semiconductor transition in germanium, *Phys. Rev. B* **49**, 14251–14269 (1994) [doi].

[139] G. Kresse, J. Furthmüller, Efficiency of ab-initio total energy calculations for metals and semiconductors using a plane-wave basis set, *Comput. Mater. Sci.* **6**, 15–50 (1996) [doi].

[140] P. E. Blöchl, Projector augmented-wave method, *Phys. Rev. B* **50**, 17953–17979 (1994) [doi].

[141] M. I. Aroyo, D. Orobengoa, G. de la Flor, J. M. Perez-Mato, H. Wondratschek, Brillouin-zone databases on the Bilbao Crystallographic Server, *Acta Crystallogr. A* **70**, 126–137 (2014) [doi].

[142] J. P. Perdew, K. Burke, M. Ernzerhof, Generalized gradient approximation made simple, *Phys. Rev. Lett.* **77**, 3865–3868 (1996) [doi].

[143] J. Heyd, G. E. Scuseria, M. Ernzerhof, Erratum: Hybrid functionals based on a screened coulomb potential, *J. Chem. Phys.* **124**, 219906 (2006) [doi].

[144] P. Giannozzi, S. Baroni, N. Bonini, M. Calandra, R. Car, C. Cavazzoni, D. Ceresoli, G. L. Chiarotti, M. Cococcioni, I. Dabo, A. D. Corso, S. de Gironcoli, S. Fabris, G. Fratesi, R. Gebauer, U. Gerstmann, C. Gougoussis, A. Kokalj, M. Lazzeri, L. Martin-Samos, N. Marzari, F. Mauri, R. Mazzarello, S. Paolini, A. Pasquarello, L. Paulatto, C. Sbraccia, S. Scandolo, G. Sclauzero, A. P. Seitsonen, A. Smogunov, P. Umari, R. M. Wentzcovitch, QUANTUM ESPRESSO: A modular and open-source software project for quantum simulations of materials, *J. Phys.: Condens. Matter* **21**, 395502 (2009) [doi].

[145] C. J. Pickard, F. Mauri, All-electron magnetic response with pseudopotentials: NMR chemical shifts, *Phys. Rev. B* **63**, 245101 (2001) [doi].

[146] J. R. Yates, C. J. Pickard, F. Mauri, Calculation of NMR chemical shifts for extended systems using ultrasoft pseudopotentials, *Phys. Rev. B* **76**, 024401 (2007) [**doi**].

[147] M. Profeta, F. Mauri, C. J. Pickard, Accurate first principles prediction of ^{17}O NMR parameters in SiO_2: Assignment of the zeolite ferrierite spectrum, *J. Am. Chem. Soc.* **125**, 541–548 (2003) [**doi**].

[148] F. Jollet, M. Torrent, N. Holzwarth, Generation of projector augmented-wave atomic data: A 71 element validated table in the XML format, *Comput. Phys. Comm.* **185**, 1246–1254 (2014) [**doi**].

[149] N. Holzwarth, A. Tackett, G. Matthews, A projector augmented wave (PAW) code for electronic structure calculations, Part I: *atompaw* for generating atom-centered functions, *Comput. Phys. Comm.* **135**, 329–347 (2001) [**doi**].

[150] E. Y. Peresh, V. B. Lazarev, S. V. Kun, I. E. Barchii, A. V. Kun, V. I. Sidei, Mixed halides $A_3B_2C_9$ (A = Rb, Cs; B = Sb, Bi; C = Br, I) and their solid solutions, *Inorg. Mater.* **33**, 362–365

[151] G. J. Wessel, D. J. W. Ijdo, The crystal structure of $Cs_3Cr_2Cl_9$, *Acta Crystallogr.* **10**, 466–468 (1957) [**doi**].

[152] A. Wosylus, U. Schwarz, M. Ruck, Die kristallstruktur von $Tl_3Bi_2I_9$: Eine komplexe ausdünnungs- und verzerrungsvariante des perowskit-typs, *Z. Anorg. Allg. Chem.* **631**, 1055–1059 (2005) [**doi**].

[153] D. H. Guthrie, G. Meyer, J. D. Corbett, Metal-metal repulsion and bonding in confacial bioctahedra. The crystal structures of cesium yttrium iodide ($Cs_3Y_2I_9$) and cesium zirconium iodide ($Cs_3Zr_2I_9$) and comparison with related phases, *Inorg. Chem.* **20**, 1192–1196 (1981) [**doi**].

[154] R. D. Shannon, Revised effective ionic radii and systematic studies of interatomic distances in halides and chalcogenides, *Acta Crystallogr. A* **32**, 751–767 (1976) [**doi**].

[155] D. H. Cao, C. C. Stoumpos, O. K. Farha, J. T. Hupp, M. G. Kanatzidis, 2D homologous perovskites as light-absorbing materials for solar cell applications, *J. Am. Chem. Soc.* **137**, 7843–7850 (2015) [**doi**].

[156] N. W. Ashcroft, N. D. Mermin, *Solid State Physics*, New York: Brooks/Cole (1976).

[157] J. Even, L. Pedesseau, J.-M. Jancu, C. Katan, Importance of spin-orbit coupling in hybrid organic/inorganic perovskites for photovoltaic applications, *J. Phys. Chem. Lett.* **4**, 2999–3005 (2013) [**doi**].

[158] M. H. Du, Efficient carrier transport in halide perovskites: Theoretical perspectives, *J. Mater. Chem. A* **2**, 9091 (2014) [doi].

[159] W. J. Yin, T. Shi, Y. Yan, Unique properties of halide perovskites as possible origins of the superior solar cell performance, *Adv. Mater.* **26**, 4653–4658 (2014) [doi].

[160] A. Walsh, Principles of chemical bonding and band gap engineering in hybrid organic-inorganic halide perovskites, *J. Phys. Chem. C* **119**, 5755–5760 (2015) [doi].

[161] L.-Y. Huang, W. R. L. Lambrecht, Electronic band structure, phonons, and exciton binding energies of halide perovskites $CsSnCl_3$, $CsSnBr_3$, and $CsSnI_3$, *Phys. Rev. B* **88**, 165203 (2013) [doi].

[162] B. Lee, C. C. Stoumpos, N. Zhou, F. Hao, C. Malliakas, C.-Y. Yeh, T. J. Marks, M. G. Kanatzidis, R. P. H. Chang, Air-stable molecular semiconducting iodosalts for solar cell applications: Cs_2SnI_6 as a hole conductor, *J. Am. Chem. Soc.* **136**, 15379–15385 (2014) [doi].

[163] G. Xing, N. Mathews, S. Sun, S. S. Lim, Y. M. Lam, M. Gratzel, S. Mhaisalkar, T. C. Sum, Long-range balanced electron- and hole-transport lengths in organic-inorganic $CH_3NH_3PbI_3$, *Science* **342**, 344–347 (2013) [doi].

[164] S. D. Stranks, G. E. Eperon, G. Grancini, C. Menelaou, M. J. P. Alcocer, T. Leijtens, L. M. Herz, A. Petrozza, H. J. Snaith, Electron-hole diffusion lengths exceeding 1 micrometer in an organometal trihalide perovskite absorber, *Science* **342**, 341–344 (2013) [doi].

[165] J. M. Frost, K. T. Butler, F. Brivio, C. H. Hendon, M. Van Schilfgaarde, A. Walsh, Atomistic origins of high-performance in hybrid halide perovskite solar cells, *Nano Lett.* **14**, 2584–2590 (2014) [doi].

[166] C. S. Ponseca, T. J. Savenije, M. Abdellah, K. Zheng, A. Yartsev, T. Pascher, T. Harlang, P. Chabera, T. Pullerits, A. Stepanov, J.-P. Wolf, V. Sundström, Organometal halide perovskite solar cell materials rationalized: Ultrafast charge generation, high and microsecond-long balanced mobilities, and slow recombination, *J. Am. Chem. Soc.* **136**, 5189–5192 (2014) [doi].

[167] L. M. Pazos-Outon, M. Szumilo, R. Lamboll, J. M. Richter, M. Crespo-Quesada, M. Abdi-Jalebi, H. J. Beeson, M. Vrucinic, M. Alsari, H. J. Snaith, B. Ehrler, R. H. Friend, F. Deschler, Photon recycling in lead iodide perovskite solar cells, *Science* **351**, 1430–1433 (2016) [doi].

[168] I. Chung, J.-H. Song, J. Im, J. Androulakis, C. D. Malliakas, H. Li, A. J. Freeman, J. T. Kenney, M. G. Kanatzidis, $CsSnI_3$: Semiconductor or metal? High electrical conductivity and strong near-infrared photoluminescence from a single material. High hole mobility and phase-transitions, *J. Am. Chem. Soc.* **134**, 8579–8587 (2012) [**doi**].

[169] C. E. Patrick, K. W. Jacobsen, K. S. Thygesen, Anharmonic stabilization and band gap renormalization in the perovskite $CsSnI_3$, *Phys. Rev. B* **92**, 201205 (2015) [**doi**].

[170] W. Siemons, M. A. McGuire, V. R. Cooper, M. D. Biegalski, I. N. Ivanov, G. E. Jellison, L. A. Boatner, B. C. Sales, H. M. Christen, Dielectric-constant-enhanced Hall mobility in complex oxides, *Adv. Mater.* **24**, 3965–3969 (2012) [**doi**].

[171] K. R. Knox, E. S. Bozin, C. D. Malliakas, M. G. Kanatzidis, S. J. L. Billinge, Local off-centering symmetry breaking in the high-temperature regime of SnTe, *Phys. Rev. B* **89**, 014102 (2014) [**doi**].

[172] E. S. Bozin, C. D. Malliakas, P. Souvatzis, T. Proffen, N. A. Spaldin, M. G. Kanatzidis, S. J. L. Billinge, Entropically stabilized local dipole formation in lead chalcogenides, *Science* **330**, 1660–1663 (2010) [**doi**].

[173] Y. Zhang, X. Ke, P. R. C. Kent, J. Yang, C. Chen, Anomalous lattice dynamics near the ferroelectric instability in PbTe, *Phys. Rev. Lett.* **107**, 175503 (2011) [**doi**].

[174] C. W. Li, J. Ma, H. B. Cao, A. F. May, D. L. Abernathy, G. Ehlers, C. Hoffmann, X. Wang, T. Hong, A. Huq, O. Gourdon, O. Delaire, Anharmonicity and atomic distribution of SnTe and PbTe thermoelectrics, *Phys. Rev. B* **90**, 214303 (2014) [**doi**].

[175] Y. Chen, X. Ai, C. A. Marianetti, First-principles approach to nonlinear lattice dynamics: Anomalous spectra in PbTe, *Phys. Rev. Lett.* **113**, 105501 (2014) [**doi**].

[176] L. Aggarwal, A. Banik, S. Anand, U. V. Waghmare, K. Biswas, G. Sheet, Local ferroelectricity in thermoelectric snte above room temperature driven by competing phonon instabilities and soft resonant bonding, *J. Materiomics* **2**, 196–202 (2016) [**doi**].

[177] T. Keiber, F. Bridges, B. C. Sales, Lead is not off center in PbTe: The importance of r-space phase information in extended X-ray absorption fine structure spectroscopy, *Phys. Rev. Lett.* **111**, 095504 (2013) [**doi**].

[178] K. V. Mitrofanov, A. V. Kolobov, P. Fons, M. Krbal, T. Shintani, J. Tominaga, T. Uruga, Local structure of the SnTe topological crystalline insulator: Rhombohedral distortions emerging from the rocksalt phase, *Phys. Rev. B* **90**, 1–6 (2014) [**doi**].

[179] K. M. Ø. Jensen, E. S. Božin, C. D. Malliakas, M. B. Stone, M. D. Lumsden, M. G. Kanatzidis, S. M. Shapiro, S. J. L. Billinge, Lattice dynamics reveals a local symmetry breaking in the emergent dipole phase of PbTe, *Phys. Rev. B* **86**, 085313 (2012) [**doi**].

[180] K. S. Knight, A high-resolution neutron powder diffraction investigation of galena (PbS) between 10 K and 350 K: No evidence for anomalies in the lattice parameters or atomic displacement parameters in galena or altaite (PbTe) at temperatures corresponding to the..., *J. Phys. Condens. Matter* **26**, 385403 (2014) [**doi**].

[181] S. Kastbjerg, N. Bindzus, M. Søndergaard, S. Johnsen, N. Lock, M. Christensen, M. Takata, M. A. Spackman, B. Brummerstedt Iversen, Direct evidence of cation disorder in thermoelectric lead chalcogenides PbTe and PbS, *Adv. Funct. Mater.* **23**, 5477–5483 (2013) [**doi**].

[182] E. Sawaguchi, Ferroelectricity versus antiferroelectricity in the solid solutions of $PbZrO_3$ and $PbTiO_3$, *J. Phys. Soc. Japan* **8**, 615–629 (1953) [**doi**].

[183] P. Baettig, R. Seshadri, N. A. Spaldin, Anti-polarity in ideal $BiMnO_3$, *J. Am. Chem. Soc.* **129**, 9854–9855 (2007) [**doi**].

[184] A. W. Hewat, Structure of rhombohedral ferroelectric barium titanate, *Ferroelectrics* **6**, 215–218 (1973) [**doi**].

[185] A. W. Hewat, Cubic-tetragonal-orthorhombic-rhombohedral ferroelectric transitions in perovskite potassium niobate: Neutron powder profile refinement of the structures, *J. Phys. C Solid State Phys.* **6**, 2559–2572 (1973) [**doi**].

[186] G. H. Kwei, S. J. L. Billinge, S.-W. Cheong, J. G. Saxton, Pair-distribution functions of ferroelectric perovskites: Direct observation of structural ground states, *Ferroelectrics* **164**, 57–73 (1995) [**doi**].

[187] B. Ravel, E. A. Stern, R. I. Vedrinskii, V. Kraizman, Local structure and the phase transitions of $BaTiO_3$, *Ferroelectrics* **206**, 407–430 (1998) [**doi**].

[188] I. Swainson, L. Chi, J.-H. Her, L. Cranswick, P. Stephens, B. Winkler, D. J. Wilson, V. Milman, Orientational ordering, tilting and lone-pair activity in the perovskite methylammonium tin bromide, $CH_3NH_3SnBr_3$, *Acta Crystallogr. Sect. B* **66**, 422–429 (2010) [**doi**].

[189] R. J. Worhatch, H. Kim, I. P. Swainson, A. L. Yonkeu, S. J. L. Billinge, Study of local structure in selected organic–inorganic perovskites in the $Pm\bar{3}m$ phase, *Chem. Mater.* **20**, 1272–1277 (2008) [**doi**].

[190] I. Swainson, R. Hammond, C. Soullière, O. Knop, W. Massa, Phase transitions in the perovskite methylammonium lead bromide, $CH_3ND_3PbBr_3$, *J. Solid State Chem.* **176**, 97–104 (2003) [doi].

[191] M. T. Weller, O. J. Weber, P. F. Henry, A. M. Di Pumpo, T. C. Hansen, Complete structure and cation orientation in the perovskite photovoltaic methylammonium lead iodide between 100 and 352 K, *Chem. Commun.* **51**, 4180–4183 (2015) [doi].

[192] J. J. Choi, X. Yang, Z. M. Norman, S. J. L. Billinge, J. S. Owen, Structure of methylammonium lead iodide within mesoporous titanium dioxide: Active material in high-performance perovskite solar cells, *Nano Lett.* **14**, 127–133 (2014) [doi].

[193] T. T. Tran, P. S. Halasyamani, Synthesis and characterization of $ASnF_3$ (A=Na^+, K^+, Rb^+, Cs^+), *J. Solid State Chem.* **210**, 213–218 (2014) [doi].

[194] J. Neuefeind, M. Feygenson, J. Carruth, R. Hoffmann, K. K. Chipley, The Nanoscale Ordered MAterials Diffractometer NOMAD at the Spallation Neutron Source SNS, *Nucl. Instr. Meth. Phys. Res. B* **287**, 68–75 (2012) [doi].

[195] X. Qiu, J. W. Thompson, S. J. L. Billinge, PDFgetX2: A GUI-driven program to obtain the pair distribution function from X-ray powder diffraction data, *J. Appl. Crystallogr.* **37**, 678–678 (2004) [doi].

[196] A. C. Larson, R. B. Von Dreele, General structure analysis system (GSAS), *Los Alamos Natl. Lab. Rep. LAUR* 86–748

[197] B. H. Toby, EXPGUI, a graphical user interface for GSAS, *J. Appl. Crystallogr.* **34**, 210–213 (2001) [doi].

[198] C. Farrow, P. Juhas, J. Liu, D. Bryndin, E. Božin, J. Bloch, T. Proffen, S. Billinge, PDFfit2 and PDFgui: Computer programs for studying nanostructure in crystals, *J. Phys. Condens. Matter* **19**, 335219 (2007) [doi].

[199] J. P. Perdew, A. Ruzsinszky, G. I. Csonka, O. A. Vydrov, G. E. Scuseria, L. A. Constantin, X. Zhou, K. Burke, Restoring the density-gradient expansion for exchange in solids and surfaces, *Phys. Rev. Lett.* **100**, 136406 (2008) [doi].

[200] H. J. Monkhorst, J. D. Pack, Special points for Brillouin-zone integrations, *Phys. Rev. B* **13**, 5188–5192 (1976) [doi].

[201] M. Gajdoš, K. Hummer, G. Kresse, J. Furthmüller, F. Bechstedt, Linear optical properties in the projector-augmented wave methodology, *Phys. Rev. B* **73**, 1–9 (2006) [doi].

[202] M.-H. Chen, A. Emly, A. Van der Ven, Anharmonicity and phase stability of antiperovskite Li_3OCl, *Phys. Rev. B* **91**, 214306 (2015) [**doi**].

[203] B. J. Campbell, H. T. Stokes, D. E. Tanner, D. M. Hatch, ISODISPLACE: A web-based tool for exploring structural distortions, *J. Appl. Crystallogr.* **39**, 607–614 (2006) [**doi**].

[204] C. J. Howard, H. T. Stokes, Group-theoretical analysis of octahedral tilting in perovskites, *Acta Crystallogr. Sect. B Struct. Sci.* **54**, 782–789 (1998) [**doi**].

[205] H. T. Stokes, D. M. Hatch, FINDSYM: Program for identifying the space-group symmetry of a crystal, *J. Appl. Crystallogr.* **38**, 237–238 (2005) [**doi**].

[206] T. Chatterji, P. F. Henry, R. Mittal, S. L. Chaplot, Negative thermal expansion of ReO_3: Neutron diffraction experiments and dynamical lattice calculations, *Phys. Rev. B* **78**, 3–8 (2008) [**doi**].

[207] E. E. Rodriguez, A. Llobet, T. Proffen, B. C. Melot, R. Seshadri, P. B. Littlewood, A. K. Cheetham, The role of static disorder in negative thermal expansion in ReO_3, *J. Appl. Phys.* **105** (2009) [**doi**].

[208] T. Egami, S. J. L. Billinge, *Underneath the Bragg Peaks: Structural Analysis of Complex Materials*, Oxford, UK: Elsevier Ltd. (2003).

[209] E. S. Božin, P. Juhás, S. J. L. Billinge, Local structure of bulk and nanocrystalline semiconductors using total scattering methods, in C. Lamberti, G. Agostini (Editors), *Characterization of Semiconductor Heterostructures and Nanostructures*, 229–257, Elsevier B.V., 2nd edition (2013).

[210] K. Page, T. Proffen, M. Niederberger, R. Seshadri, Probing local dipoles and ligand structure in $BaTiO_3$ nanoparticles, *Chem. Mater.* **22**, 4386–4391 (2010) [**doi**].

[211] M. S. Senn, D. A. Keen, T. C. A. Lucas, J. A. Hriljac, A. L. Goodwin, Emergence of long-range order in $BaTiO_3$ from local symmetry-breaking distortions, *Phys. Rev. Lett.* **116**, 207602 (2016) [**doi**].

[212] R. E. Cohen, Origin of ferroelectricity in perovskite oxides, *Nature* **358**, 136–138 (1992) [**doi**].

[213] W. Zhong, R. D. King-Smith, D. Vanderbilt, Giant LO-TO splittings in perovskite ferroelectrics, *Phys. Rev. Lett.* **72**, 3618–3621 (1994) [**doi**].

[214] M. Posternak, R. Resta, A. Baldereschi, Role of covalent bonding in the polarization of perovskite oxides: The case of $KNbO_3$, *Phys. Rev. B* **50**, 8911–8914 (1994) [**doi**].

[215] P. Ghosez, J.-P. Michenaud, X. Gonze, Dynamical atomic charges: The case of ABO_3 compounds, *Phys. Rev. B* **58**, 6224–6240 (1998) [doi].

[216] R. D. Shannon, C. T. Prewitt, Effective ionic radii in oxides and fluorides, *Acta Crystallogr. Sect. B Struct. Crystallogr. Cryst. Chem.* **25**, 925–946 (1969) [doi].

[217] B. Silvi, A. Savin, Classification of chemical bonds based on topological analysis of electron localization functions, *Nature* **371**, 683–686 (1994) [doi].

[218] P. Ghosez, E. Cockayne, U. V. Waghmare, K. M. Rabe, Lattice dynamics of $BaTiO_3$, $PbTiO_3$ and $PbZrO_3$: A comparative first-principles study, *Phys. Rev. B* **60**, 9 (1999) [doi].

[219] B. K. Greve, K. L. Martin, P. L. Lee, P. J. Chupas, K. W. Chapman, A. P. Wilkinson, Pronounced negative thermal expansion from a simple structure: Cubic ScF_3, *J. Am. Chem. Soc.* **132**, 15496–15498 (2010) [doi].

[220] K. P. O'Donnell, X. Chen, Temperature dependence of semiconductor band gaps, *Appl. Phys. Lett.* **58**, 2924–2926 (1991) [doi].

[221] H. Oga, A. Saeki, Y. Ogomi, S. Hayase, S. Seki, Improved understanding of the electronic and energetic landscapes of perovskite solar cells: High local charge carrier mobility, reduced recombination, and extremely shallow traps, *J. Am. Chem. Soc.* **136**, 13818–13825 (2014) [doi].

[222] T. J. Savenije, C. S. Ponseca, L. Kunneman, M. Abdellah, K. Zheng, Y. Tian, Q. Zhu, S. E. Canton, I. G. Scheblykin, T. Pullerits, A. Yartsev, V. Sundström, Thermally activated exciton dissociation and recombination control the carrier dynamics in organometal halide perovskite, *J. Phys. Chem. Lett.* **5**, 2189–2194 (2014) [doi].

[223] R. L. Milot, G. E. Eperon, H. J. Snaith, M. B. Johnston, L. M. Herz, Temperature-dependent charge-carrier dynamics in $CH_3NH_3PbI_3$ perovskite thin films, *Adv. Funct. Mater.* **25**, 6218–6227 (2015) [doi].

[224] Q. Dong, Y. Fang, Y. Shao, P. Mulligan, J. Qiu, L. Cao, J. Huang, Electron-hole diffusion lengths ¿175 μm in solution-grown $CH_3NH_3PbI_3$ single crystals, *Science* **347**, 967–970 (2015) [doi].

[225] D. Shi, V. Adinolfi, R. Comin, M. Yuan, E. Alarousu, A. Buin, Y. Chen, S. Hoogland, A. Rothenberger, K. Katsiev, Y. Losovyj, X. Zhang, P. A. Dowben, O. F. Mohammed, E. H. Sargent, O. M. Bakr, Low trap-state density and long carrier diffusion in organolead trihalide perovskite single crystals, *Science* **347**, 519–522 (2015) [doi].

[226] M. Zhang, H. Yu, M. Lyu, Q. Wang, J.-H. Yun, L. Wang, Composition-dependent photoluminescence intensity and prolonged recombination lifetime of perovskite $CH_3NH_3PbBr_{3-x}Cl_x$ films, *Chem. Commun.* **50**, 11727–11730 (2014) [doi].

[227] X.-Y. Zhu, V. Podzorov, Charge carriers in hybrid organic–inorganic lead halide perovskites might be protected as large polarons, *J. Phys. Chem. Lett.* **6**, 4758–4761 (2015) [doi].

[228] T. M. Brenner, D. A. Egger, A. M. Rappe, L. Kronik, G. Hodes, D. Cahen, Are mobilities in hybrid organic-inorganic halide perovskites actually "high"?, *J. Phys. Chem. Lett.* **6**, 4754–4757 (2015) [doi].

[229] A. Filippetti, A. Mattoni, C. Caddeo, M. I. Saba, P. Delugas, Low electron-polar optical phonon scattering as a fundamental aspect of carrier mobility in methylammonium lead halide $CH_3NH_3PbI_3$ perovskites, *Phys. Chem. Chem. Phys.* **18**, 15352–15362 (2016) [doi].

[230] C. Quarti, E. Mosconi, F. De Angelis, Interplay of orientational order and electronic structure in methylammonium lead iodide: Implications for solar cell operation, *Chem. Mater.* **26**, 6557–6569 (2014) [doi].

[231] J. Ma, L.-w. Wang, Nanoscale charge localization induced by random orientations of organic molecules in hybrid perovskite $CH_3NH_3PbI_3$, *Nano Lett.* **15**, 248–253 (2015) [doi].

[232] C. Motta, F. El-Mellouhi, S. Kais, N. Tabet, F. Alharbi, S. Sanvito, Revealing the role of organic cations in hybrid halide perovskite $CH_3NH_3PbI_3$, *Nat. Commun.* **6**, 7026 (2015) [doi].

[233] A. N. Beecher, O. E. Semonin, J. M. Skelton, J. M. Frost, M. W. Terban, H. Zhai, A. Alatas, J. S. Owen, A. Walsh, S. J. L. Billinge, Direct observation of dynamic symmetry breaking above room temperature in methylammonium lead iodide perovskite, *ACS Energy Lett.* **1**, 880–887 (2016) [doi].

[234] F. Zheng, L. Z. Tan, S. Liu, A. M. Rappe, Rashba spin–orbit coupling enhanced carrier lifetime in $CH_3NH_3PbI_3$, *Nano Lett.* **15**, 7794–7800 (2015) [doi].

[235] P. Azarhoosh, S. McKechnie, J. M. Frost, A. Walsh, M. van Schilfgaarde, Research update: Relativistic origin of slow electron-hole recombination in hybrid halide perovskite solar cells, *APL Mater.* **4**, 091501 (2016) [doi].

[236] O. Delaire, J. Ma, K. Marty, A. F. May, M. A. McGuire, M.-H. Du, D. J. Singh, A. Podlesnyak, G. Ehlers, M. D. Lumsden, B. C. Sales, Giant anharmonic phonon scattering in PbTe, *Nat. Mater.* **10**, 614–619 (2011) [doi].

[237] T. Shiga, J. Shiomi, J. Ma, O. Delaire, T. Radzynski, A. Lusakowski, K. Esfarjani, G. Chen, Microscopic mechanism of low thermal conductivity in lead telluride, *Phys. Rev. B* **85**, 1–5 (2012) [doi].

[238] S. Lee, K. Esfarjani, T. Luo, J. Zhou, Z. Tian, G. Chen, Resonant bonding leads to low lattice thermal conductivity, *Nat. Commun.* **5**, 3525 (2014) [doi].

[239] A. Pisoni, J. Jaćimović, O. S. Barišić, M. Spina, R. Gaál, L. Forró, E. Horváth, Ultra-low thermal conductivity in organic–inorganic hybrid perovskite $CH_3NH_3PbI_3$, *J. Phys. Chem. Lett.* **5**, 2488–2492 (2014) [doi].

[240] M. Mori, H. Saito, An X-ray study of successive phase transitions in $CsSnBr_3$, *J. Phys. C Solid State Phys.* **19**, 2391 (1986) [doi].

[241] M. H. Kuok, E. L. Saw, C. T. Yap, A Mössbauer study of the phase transitions in $CsSnBr_3$, *Phys. Status Solidi* **132**, K89–K92 (1992) [doi].

[242] J.-C. Zheng, C. H. A. Huan, A. T. S. Wee, M. H. Kuok, Electronic properties of $CsSnBr_3$: Studies by experiment and theory, *Surf. Interface Anal.* **28**, 81–83 (1999) [doi].

[243] D. E. Scaife, P. F. Weller, W. G. Fisher, Crystal preparation and properties of cesium tin(ii) trihalides, *J. Solid State Chem.* **9**, 308–314 (1974) [doi].

[244] A. M. Glazer, The classification of tilted octahedra in perovskites, *Acta Crystallogr. Sect. B Struct. Crystallogr. Cryst. Chem.* **28**, 3384–3392 (1972) [doi].

[245] I. D. Brown, Bond valences—A simple structural model for inorganic chemistry, *Chem. Soc. Rev.* **7**, 359–376 (1978) [doi].

[246] I. D. Brown, Recent developments in the methods and applications of the bond valence model, *Chem. Rev.* **109**, 6858–6919 (2009) [doi].

[247] N. E. Brese, M. O'Keeffe, Bond-valence parameters for solids, *Acta Crystallogr. Sect. B Struct. Sci.* **47**, 192–197 (1991) [doi].

[248] J. Young, J. M. Rondinelli, Octahedral rotation preferences in perovskite iodides and bromides, *J. Phys. Chem. Lett.* **7**, 918–922 (2016) [doi].

[249] E. H. Smith, N. A. Benedek, C. J. Fennie, Interplay of octahedral rotations and lone pair ferroelectricity in $CsPbF_3$, *Inorg. Chem.* **54**, 8536–8543 (2015) [doi].

[250] P. Berastegui, S. Hull, S. Eriksson, A low-temperature structural phase transition in $CsPbF_3$, *J. Phys. Condens. Matter* **13**, 5077–5088 (2001) [doi].

[251] M. Saliba, T. Matsui, J.-Y. Seo, K. Domanski, J.-P. Correa-Baena, M. K. Nazeeruddin, S. M. Zakeeruddin, W. Tress, A. Abate, A. Hagfeldt, M. Grätzel, Cesium-containing triple cation perovskite solar cells: Improved stability, reproducibility and high efficiency, *Energy Environ. Sci.* **9**, 1989–1997 (2016) [**doi**].

[252] S. Gupta, T. Bendikov, G. Hodes, D. Cahen, $CsSnBr_3$, a lead-free halide perovskite for long-term solar cell application: Insights on SnF_2 addition, *ACS Energy Lett.* **1**, 1028–1033 (2016) [**doi**].

[253] L. Ma, F. Hao, C. C. Stoumpos, B. T. Phelan, M. R. Wasielewski, M. G. Kanatzidis, Carrier diffusion lengths of over 500 nm in lead-free perovskite $CH_3NH_3SnI_3$ films, *J. Am. Chem. Soc.* **138**, 14750–14755 (2016) [**doi**].

[254] W. Liao, D. Zhao, Y. Yu, C. R. Grice, C. Wang, A. J. Cimaroli, P. Schulz, W. Meng, K. Zhu, R.-G. Xiong, Y. Yan, Lead-free inverted planar formamidinium tin triiodide perovskite solar cells achieving power conversion efficiencies up to 6.22%, *Adv. Mater.* **28**, 1–8 (2016) [**doi**].

[255] A. M. Ganose, C. N. Savory, D. O. Scanlon, Beyond methylammonium lead iodide: Prospects for the emergent field of ns^2 containing solar absorbers, *Chem. Commun.* **53**, 20–44 (2017) [**doi**].

[256] C. C. Stoumpos, M. G. Kanatzidis, The renaissance of halide perovskites and their evolution as emerging semiconductors, *Acc. Chem. Res.* **48**, 2791–2802 (2015) [**doi**].

[257] C. C. Stoumpos, M. G. Kanatzidis, Halide perovskites: Poor man's high-performance semiconductors, *Adv. Mater.* **28**, 5778–5793 (2016) [**doi**].

[258] H. Tsai, W. Nie, J.-C. Blancon, C. C. Stoumpos, R. Asadpour, B. Harutyunyan, A. J. Neukirch, R. Verduzco, J. J. Crochet, S. Tretiak, L. Pedesseau, E. Even, M. A. Alam, G. Gupta, J. Lou, P. M. Ajayan, M. J. Bedzyk, M. G. Kanatzidis, A. D. Mohite, High-efficiency two-dimensional Ruddlesden–Popper perovskite solar cells, *Nature* **536**, 312–316 (2016) [**doi**].

[259] C. Wehrenfennig, G. E. Eperon, M. B. Johnston, H. J. Snaith, L. M. Herz, High charge carrier mobilities and lifetimes in organolead trihalide perovskites, *Adv. Mater.* **26**, 1584–1589 (2014) [**doi**].

[260] H. Zhu, M. T. Trinh, J. Wang, Y. Fu, P. P. Joshi, K. Miyata, S. Jin, X.-Y. Zhu, Organic cations might not be essential to the remarkable properties of band edge carriers in lead halide perovskites, *Adv. Mater.* **29**, 1603072 (2016) [**doi**].

[261] T. Chen, B. J. Foley, B. Ipek, M. Tyagi, J. R. D. Copley, C. M. Brown, J. J. Choi, S.-H. Lee, Rotational dynamics of organic cations in the $CH_3NH_3PbI_3$ perovskite, *Phys. Chem. Chem. Phys.* **17**, 31278–31286 (2015) [**doi**].

[262] H. Zhu, K. Miyata, Y. Fu, J. Wang, P. P. Joshi, D. Niesner, K. W. Williams, S. Jin, X.-Y. Zhu, Screening in crystalline liquids protects energetic carriers in hybrid perovskites, *Science* **353**, 1409–1413 (2016) [doi].

[263] O. Yaffe, Y. Guo, L. Z. Tan, D. A. Egger, T. Hull, C. C. Stoumpos, F. Zheng, T. F. Heinz, L. Kronik, M. G. Kanatzidis, J. S. Owen, A. M. Rappe, M. A. Pimenta, L. E. Brus, Local polar fluctuations in lead halide perovskite crystals, *Phys. Rev. Lett.* **118**, 136001 (2017) [doi].

[264] M. Kulbak, D. Cahen, G. Hodes, How important is the organic part of lead halide perovskite photovoltaic cells? Efficient $CsPbBr_3$ cells, *J. Phys. Chem. Lett.* **6**, 2452–2456 (2015) [doi].

[265] G. E. Eperon, G. M. Paternò, R. J. Sutton, A. Zampetti, A. A. Haghighirad, F. Cacialli, H. J. Snaith, Inorganic caesium lead iodide perovskite solar cells, *J. Mater. Chem. A* **3**, 19688–19695 (2015) [doi].

[266] R. E. Beal, D. J. Slotcavage, T. Leijtens, A. R. Bowring, R. A. Belisle, W. H. Nguyen, G. Burkhard, E. T. Hoke, M. D. McGehee, Cesium lead halide perovskites with improved stability for tandem solar cells, *J. Phys. Chem. Lett.* **7**, 746–751 (2016) [doi].

[267] W. G. Zeier, A. Zevalkink, Z. M. Gibbs, G. Hautier, M. G. Kanatzidis, G. J. Snyder, Thinking like a chemist: Intuition in thermoelectric materials, *Angew. Chem. Int. Ed.* **55**, 6826–6841 (2016) [doi].

[268] Y. Kawamura, H. Mashiyama, K. Hasebe, Structural study on cubic-tetragonal transition of $CH_3NH_3PbI_3$, *J. Phys. Soc. Jpn.* **71**, 1694–1697 (2002) [doi].

[269] W. Kwestroo, P. Vromans, Preparation of three modifications of pure tin (II) oxide, *J. Inorg. Nucl. Chem.* **29**, 2187–2190 (1967) [doi].

[270] A. P. Hammersley, S. O. Svensson, M. Hanfland, A. N. Fitch, D. Häusermann, Two-dimensional detector software: From real detector to idealised image or two-theta scan, *High Pressure Res.* **14**, 235–248 (1996) [doi].

[271] M. I. Aroyo, J. M. Perez-Mato, D. Orobengoa, E. Tasci, G. De La Flor, A. Kirov, Crystallography online: Bilbao Crystallographic Server, *Bulg. Chem. Commun.* **43**, 183–197

[272] M. I. Aroyo, J. M. Perez-Mato, C. Capillas, E. Kroumova, S. Ivantchev, G. Madariaga, A. Kirov, H. Wondratschek, Bilbao Crystallographic Server: I. Databases and crystallographic computing programs, *Zeit. Krist.* **221**, 15–27 (2006) [doi].

[273] M. I. Aroyo, A. Kirov, C. Capillas, J. M. Perez-Mato, H. Wondratschek, Bilbao Crystallographic Server. II. Representations of crystallographic point groups and space groups, *Acta Crystallogr. A* **62**, 115–128 (2006) [doi].

[274] Y. Takahashi, R. Obara, Z.-Z. Lin, Y. Takahashi, T. Naito, T. Inabe, S. Ishibashi, K. Terakura, Charge-transport in tin-iodide perovskite $CH_3NH_3SnI_3$: origin of high conductivity, *Dalton Trans.* **40**, 5563 (2011) [doi].

[275] N. Onoda-Yamamuro, T. Matsuo, H. Suga, Calorimetric and IR spectroscopic studies of phase transitions in methylammonium trihalogenoplumbates (II), *J. Phys. Chem. Solids* **51**, 1383–1395 (1990) [doi].

[276] Z. Tang, J. Guan, A. M. Guloy, Synthesis and crystal structure of new organic-based layered perovskites with 2,2′-biimidazolium cations, *J. Mater. Chem.* **11**, 479–482 (2001) [doi].

[277] Y. Y. Li, C. K. Lin, G. L. Zheng, Z. Y. Cheng, H. You, W. D. Wang, J. Lin, Novel $\langle 110 \rangle$-oriented organic–inorganic perovskite compound stabilized by N-(3-aminopropyl)imidazole with improved optical properties, *Chem. Mater.* **18**, 3463–3469 (2006) [doi].

[278] Y. Takahashi, R. Obara, K. Nakagawa, M. Nakano, J. Tokita, T. Inabe, Tunable charge transport in soluble organic–inorganic hybrid semiconductors, *Chem. Mater.* **19**, 6312–6316 (2007) [doi].

[279] M. D. Smith, A. Jaffe, E. R. Dohner, A. M. Lindenberg, H. I. Karunadasa, Structural origins of broadband emission from layered Pb-Br hybrid perovskites, *Chem. Sci.* **8**, 4497–4504 (2017) [doi].

[280] A. J. Neukirch, W. Nie, J.-C. Blancon, K. Appavoo, H. Tsai, M. Y. Sfeir, C. Katan, L. Pedesseau, J. Even, J. J. Crochet, G. Gupta, A. D. Mohite, S. Tretiak, Polaron stabilization by cooperative lattice distortion and cation rotations in hybrid perovskite materials, *Nano Lett.* **16**, 3809–3816 (2016) [doi].

[281] S. Hirotsu, J. Harada, M. Iizumi, K. Gesi, Structural phase transitions in $CsPbBr_3$, *J. Phys. Soc. Japan* **37**, 1393–1398 (1974) [doi].

[282] N. Onoda-Yamamuro, T. Matsuo, H. Suga, Dielectric study of $CH_3NH_3PbX_3$ (X = Cl, Br, I), *J. Phys. Chem. Solids* **53**, 935–939 (1992) [doi].

[283] L.-Y. Huang, W. R. L. Lambrecht, Lattice dynamics in perovskite halides $CsSnX_3$ with X = I, Br, Cl, *Phys. Rev. B* **90**, 195201 (2014) [doi].

[284] Q. Lin, A. Armin, R. C. R. Nagiri, P. L. Burn, P. Meredith, Electro-optics of perovskite solar cells, *Nat. Photon.* **9**, 106–112 (2015) [doi].

[285] S. Stemmer, S. James Allen, Two-dimensional electron gases at complex oxide interfaces, *Annu. Rev. Mater. Res.* **44**, 151–171 (2014) [doi].

[286] K. A. Müller, H. Burkard, $SrTiO_3$: An intrinsic quantum paraelectric below 4 K, *Phys. Rev. B* **19**, 3593 (1979) [doi].

[287] H. P. R. Frederikse, W. R. Thurber, W. R. Hosler, Electronic transport in strontium titanate, *Phys. Rev.* **134**, A442–A445 (1964) [doi].

[288] A. Spinelli, M. A. Torija, C. Liu, C. Jan, C. Leighton, Electronic transport in doped $SrTiO_3$: Conduction mechanisms and potential applications, *Phys. Rev. B* **81**, 155110 (2010) [doi].

[289] S. J. Allen, B. Jalan, S. Lee, D. G. Ouellette, G. Khalsa, J. Jaroszynski, S. Stemmer, A. H. MacDonald, Conduction-band edge and Shubnikov–de Haas effect in low-electron-density $SrTiO_3$, *Phys. Rev. B* **88**, 045114 (2013) [doi].

[290] W.-J. Yin, T. Shi, Y. Yan, Unusual defect physics in $CH_3NH_3PbI_3$ perovskite solar cell absorber, *Appl. Phys. Lett.* **104**, 063903 (2014) [doi].

[291] A. Zakutayev, C. M. Caskey, A. N. Fioretti, D. S. Ginley, J. Vidal, V. Stevanovic, E. Tea, S. Lany, Defect tolerant semiconductors for solar energy conversion, *J. Phys. Chem. Lett.* **5**, 1117–1125 (2014) [doi].

[292] M. Kim, J. Im, A. J. Freeman, J. Ihm, H. Jin, Switchable $S = 1/2$ and $J = 1/2$ Rashba bands in ferroelectric halide perovskites, *Proc. Natl. Acad. Sci. USA* **111**, 6900–6904 (2014) [doi].

[293] D. Niesner, M. Wilhelm, I. Levchuk, A. Osvet, S. Shrestha, M. Batentschuk, C. Brabec, T. Fauster, Giant Rashba splitting in $CH_3NH_3PbBr_3$ organic-inorganic perovskite, *Phys. Rev. Lett.* **117**, 126401 (2016) [doi].

[294] N. J. Jeon, J. H. Noh, W. S. Yang, Y. C. Kim, S. Ryu, J. Seo, S. I. Seok, Compositional engineering of perovskite materials for high-performance solar cells, *Nature* **517**, 476–480 (2015) [doi].

[295] O. Knop, R. E. Wasylishen, M. A. White, T. S. Cameron, M. J. M. V. Oort, Alkylammonium lead halides. Part 2. $CH_3NH_3PbX_3$ (X = Cl, Br, I) perovskites: Cuboctahedral halide cages with isotropic cation reorientation, *Can. J. Chem.* **68**, 412–422 (1990) [doi].

[296] M. Maeda, M. Hattori, A. Hotta, I. Suzuki, Dielectric studies on $CH_3NH_3PbX_3$ (X = Cl and Br) single cystals, *J. Phys. Soc. Jpn.* **66**, 1508–1511 (1997) [doi].

[297] R. E. Wasylishen, O. Knop, J. B. Macdonald, Cation rotation in methylammonium lead halides, *Solid State Commun.* **56**, 581–582 (1985) [doi].

[298] Q. Xu, T. Eguchi, H. Nakayama, N. Nakamura, M. Kishita, Molecular motions and phase transitions in solid $CH_3NH_3PbX_3$ (X = C1, Br, I) as studied by NMR and NQR, *Z. Naturforsch. A* **46**, 240–246 (1991) [**doi**].

[299] J.-H. Lee, N. C. Bristowe, P. D. Bristowe, A. K. Cheetham, Role of hydrogen-bonding and its interplay with octahedral tilting in $CH_3NH_3PbI_3$, *Chem. Commun.* **51**, 6434–6437 (2015) [**doi**].

[300] M. T. Weller, O. J. Weber, J. M. Frost, A. Walsh, Cubic perovskite structure of black formamidinium lead iodide, α-$[HC(NH_2)_2]PbI_3$, at 298 K, *J. Phys. Chem. Lett.* **6**, 3209–3212 (2015) [**doi**].

[301] C. Eames, J. M. Frost, P. R. F. Barnes, B. C. O'Regan, A. Walsh, M. S. Islam, Ionic transport in hybrid lead iodide perovskite solar cells, *Nat. Commun.* **6**, 7497 (2015) [**doi**].

[302] P. Dixon, L. Wu, S. Nagel, B. Williams, J. Carini, Scaling in the relaxation of supercooled liquids, *Phys. Rev. Lett.* **65**, 1108–1111 (1990) [**doi**].

[303] C. A. Angell, Formation of glasses from liquids and biopolymers, *Science* **267**, 1924–1935 (1995) [**doi**].

[304] P. Lunkenheimer, A. Loidl, Dielectric spectroscopy of glass-forming materials: α-relaxation and excess wing, *Chem. Phys.* **284**, 205–219 (2002) [**doi**].

[305] U. Schneider, P. Lunkenheimer, R. Brand, A. Loidl, Broadband dielectric spectroscopy on glass-forming propylene carbonate, *Phys. Rev. E* **59**, 6924–6936 (1999) [**doi**].

[306] C. Kittel, H. Kroemer, *Thermal Physics*, San Francisco: W. H. Freeman and Company, 2nd edition (1980).

[307] N. Onoda-Yamamuro, T. Matsuo, H. Suga, Thermal, electric, and dielectric properties of $CH_3NH_3SnBr_3$ at low temperatures, *J. Chem. Thermodyn.* **23**, 987–999 (1991) [**doi**].

[308] A. Sokolov, R. Calemczuk, B. Salce, A. Kisliuk, D. Quitmann, E. Duval, Low-temperature anomalies in strong and fragile glass formers, *Phys. Rev. Lett.* **78**, 2405–2408 (1997) [**doi**].

[309] B. C. Melot, R. Tackett, J. O'Brien, A. L. Hector, G. Lawes, R. Seshadri, A. P. Ramirez, Large low-temperature specific heat in pyrochlore $Bi_2Ti_2O_7$, *Phys. Rev. B* **79**, 224111 (2009) [**doi**].

[310] V. Lubchenko, P. G. Wolynes, The origin of the boson peak and thermal conductivity plateau in low-temperature glasses., *Proc. Natl. Acad. Sci. U. S. A.* **100**, 1515–1518 (2003) [**doi**].

[311] D. Safarik, R. Schwarz, M. Hundley, Similarities in the C_p/T^3 peaks in amorphous and crystalline metals, *Phys. Rev. Lett.* **96**, 195902 (2006) [doi].

[312] A. I. Chumakov, G. Monaco, A. Monaco, W. A. Crichton, A. Bosak, R. Rüffer, A. Meyer, F. Kargl, L. Comez, D. Fioretto, H. Giefers, S. Roitsch, G. Wortmann, M. H. Manghnani, A. Hushur, Q. Williams, J. Balogh, K. Parliski, P. Jochym, P. Piekarz, Equivalence of the boson peak in glasses to the transverse acoustic van Hove singularity in crystals, *Phys. Rev. Lett.* **106**, 225501 (2011) [doi].

[313] X. Liu, H. V. Löhneysen, Specific-heat anomaly of amorphous solids at intermediate temperatures (1 to 30 K), *Europhys. Lett.* **33**, 617–622 (1996) [doi].

[314] P. Jain, N. S. Dalal, B. H. Toby, H. W. Kroto, A. K. Cheetham, Order–disorder antiferroelectric phase transition in a hybrid inorganic–organic framework with the perovskite architecture, *J. Am. Chem. Soc.* **130**, 10450–10451 (2008) [doi].

[315] T. Besara, P. Jain, N. S. Dalal, P. L. Kuhns, A. P. Reyes, H. W. Kroto, A. K. Cheetham, Mechanism of the order–disorder phase transition, and glassy behavior in the metal-organic framework $[(CH_3)_2NH_2]Zn(HCOO)_3$, *Proc. Natl. Acad. Sci. U. S. A.* **108**, 6828–6832 (2011) [doi].

[316] J. N. Sherwood (Editor), *The plastically crystalline state: Orientationally disordered crystals*, Wiley: Chichester, U.K. (1979).

[317] J. Even, M. Carignano, C. Katan, Molecular disorder and translation/rotation coupling in the plastic crystal phase of hybrid perovskites, *Nanoscale* **8**, 6222–6236 (2016) [doi].

[318] A. A. Bakulin, O. Selig, H. J. Bakker, Y. L. Rezus, C. Mller, T. Glaser, R. Lovrincic, Z. Sun, Z. Chen, A. Walsh, J. M. Frost, T. L. C. Jansen, Real-time observation of organic cation reorientation in methylammonium lead iodide perovskites, *J. Phys. Chem. Lett.* **6**, 3663–3669 (2015) [doi].

[319] I. P. Swainson, Tilt and acoustic instabilities in abx_4, a_2bx_4 and abx_3 perovskite structure types: Their role in the incommensurate phases of the organic–inorganic perovskites, *Acta Crystallogr. Sect. B Struct. Sci.* **61**, 616–626 (2005) [doi].

[320] B. V. Lotsch, New light on an old story: Perovskites go solar, *Angew. Chem. Int. Ed.* **53**, 635–637 (2014) [doi].

[321] H. T. Stokes, E. H. Kisi, D. M. Hatch, C. J. Howard, Group-theoretical analysis of octahedral tilting in ferroelectric perovskites, *Acta Crystallographica Section B* **58**, 934–938 (2002) [doi].

[322] H.-H. Fang, F. Wang, S. Adjokatse, N. Zhao, J. Even, M. A. Loi, Photoexcitation dynamics in solution-processed formamidinium lead iodide perovskite thin films for solar cell applications, *Light Sci. Appl.* **5**, e16056 (2016) [**doi**].

[323] A. D. Wright, C. Verdi, R. L. Milot, G. E. Eperon, M. A. Pérez-Osorio, H. J. Snaith, F. Giustino, M. B. Johnston, L. M. Herz, Electron–phonon coupling in hybrid lead halide perovskites, *Nat. Commun.* **7**, 11755 (2016) [**doi**].

[324] W. Zhang, Y. Cai, R.-G. Xiong, H. Yoshikawa, K. Awaga, Exceptional dielectric phase transitions in a perovskite-type cage compound, *Angew. Chem. Int. Ed.* **49**, 6608–6610 (2010) [**doi**].

[325] O. J. Weber, B. Charles, M. T. Weller, Phase behaviour and composition in the formamidinium-methylammonium hybrid lead iodide perovskite solid solution, *J. Mater. Chem. A* **4**, 15375–15382 (2016) [**doi**].

[326] Y. Rakita, S. R. Cohen, N. K. Kedem, G. Hodes, D. Cahen, Mechanical properties of $APbX_3$ (A = Cs or CH_3NH_3; X = I or Br) perovskite single crystals, *MRS Commun.* **5**, 623–629 (2015) [**doi**].

[327] A. L. Goodwin, M. Calleja, M. J. Conterio, M. T. Dove, J. S. O. Evans, D. A. Keen, L. Peters, M. G. Tucker, Colossal positive and negative thermal expansion in the framework material $Ag_3[Co(CN)_6]$, *Science* **319**, 794–797 (2008) [**doi**].

[328] B. Saparov, D. B. Mitzi, Organic–inorganic perovskites: Structural versatility for functional materials design, *Chem. Rev.* **116**, 4558–4596 (2016) [**doi**].

[329] D. H. Fabini, J. G. Labram, A. J. Lehner, J. S. Bechtel, H. A. Evans, A. Van der Ven, F. Wudl, M. L. Chabinyc, R. Seshadri, Main-group halide semiconductors derived from perovskite: Distinguishing chemical, structural, and electronic aspects, *Inorg. Chem.* **56**, 11–25 (2016) [**doi**].

[330] E. Purcell, Nuclear resonance in crystals, *Physica* **17**, 282–302 (1951) [**doi**].

[331] D. E. Woessner, B. S. S. Jr., Proton spin–lattice relaxation temperature dependence in ammonium bromide, *J. Chem. Phys.* **47**, 378–381 (1967) [**doi**].

[332] R. Blinc, J. Seliger, J. Dolinšek, D. Arčon, Two-dimensional ^{13}C NMR study of orientational ordering in solid C_{60}, *Phys. Rev. B* **49**, 4993–5002 (1994) [**doi**].

[333] A. Poglitsch, D. Weber, Dynamic disorder in methylammoniumtrihalogenoplumbates (II) observed by millimeter-wave spectroscopy, *J. Chem. Phys.* **87**, 6373–6378 (1987) [**doi**].

[334] I. Anusca, S. Balciunas, P. Gemeiner, a. Svirskas, M. Sanlialp, G. Lackner, C. Fettkenhauer, J. Belovickis, V. Samulionis, M. Ivanov, B. Dkhil, J. Banys, V. V. Shvartsman, D. C. Lupascu, Dielectric response: Answer to many questions in the methylammonium lead halide solar cell absorbers, *Adv. Energy Mater.* 1700600 (2017) [**doi**].

[335] Y. Guo, O. Yaffe, D. W. Paley, A. N. Beecher, T. D. Hull, G. Szpak, J. S. Owen, L. E. Brus, M. A. Pimenta, Interplay between organic cations and inorganic framework and incommensurability in hybrid lead-halide perovskite $CH_3NH_3PbBr_3$, *Phys. Rev. Materials* **1**, 042401(R) (2017) [**doi**].

[336] I. P. Swainson, C. Stock, S. F. Parker, L. Van Eijck, M. Russina, J. W. Taylor, From soft harmonic phonons to fast relaxational dynamics in $CH_3NH_3PbBr_3$, *Phys. Rev. B* **92**, 100303 (2015) [**doi**].

[337] A. M. A. Leguy, J. M. Frost, A. P. McMahon, V. G. Sakai, W. Kockelmann, C. Law, X. Li, F. Foglia, A. Walsh, B. C. O'Regan, J. Nelson, J. T. Cabral, P. R. F. Barnes, The dynamics of methylammonium ions in hybrid organic–inorganic perovskite solar cells, *Nat. Commun.* **6**, 7124 (2015) [**doi**].

[338] K. Drużbicki, R. S. Pinna, S. Rudić, M. Jura, G. Gorini, F. Fernandez-Alonso, Unexpected cation dynamics in the low-temperature phase of methylammonium lead iodide: The need for improved models, *J. Phys. Chem. Lett.* **7**, 4701–4709 (2016) [**doi**].

[339] B. Li, Y. Kawakita, Y. Liu, M. Wang, M. Matsuura, K. Shibata, S. Ohira-Kawamura, T. Yamada, S. Lin, K. Nakajima, S. F. Liu, Polar rotor scattering as atomic-level origin of low mobility and thermal conductivity of perovskite $CH_3NH_3PbI_3$, *Nat. Commun.* **8**, 16086 (2017) [**doi**].

[340] B. A. Rosales, L. Men, S. D. Cady, M. P. Hanrahan, A. J. Rossini, J. Vela, Persistent dopants and phase segregation in organolead mixed-halide perovskites, *Chem. Mater.* **28**, 6848–6859 (2016) [**doi**].

[341] C. Roiland, G. Trippe-Allard, K. Jemli, B. Alonso, J.-C. Ameline, R. Gautier, T. Bataille, L. Le Polles, E. Deleporte, J. Even, C. Katan, Multinuclear NMR as a tool for studying local order and dynamics in $CH_3NH_3PbX_3$ (X = Cl, Br, I) hybrid perovskites, *Phys. Chem. Chem. Phys.* **18**, 27133–27142 (2016) [**doi**].

[342] W. M. J. Franssen, S. G. D. van Es, R. Derviolu, G. A. de Wijs, A. P. M. Kentgens, Symmetry, dynamics, and defects in methylammonium lead halide perovskites, *J. Phys. Chem. Lett.* **8**, 61–66 (2017) [**doi**].

[343] J. Gong, M. Yang, X. Ma, R. D. Schaller, G. Liu, L. Kong, Y. Yang, M. C. Beard, M. Lesslie, Y. Dai, B. Huang, K. Zhu, T. Xu, Electron–rotor interaction in organic–inorganic lead iodide perovskites discovered by isotope effects, *J. Phys. Chem. Lett.* **7**, 2879–2887 (2016) [doi].

[344] M. A. Carignano, Y. Saeed, S. A. Aravindh, I. S. Roqan, J. Even, C. Katan, A close examination of the structure and dynamics of $HC(NH_2)_2PbI_3$ by MD simulations and group theory, *Phys. Chem. Chem. Phys.* **18**, 27109–27118 (2016) [doi].

[345] J. S. Bechtel, R. Seshadri, A. Van der Ven, Energy landscape of molecular motion in cubic methylammonium lead iodide from first-principles, *J. Phys. Chem. C* **120**, 12403–12410 (2016) [doi].

[346] J.-H. Lee, N. C. Bristowe, J. H. Lee, S.-H. Lee, P. D. Bristowe, A. K. Cheetham, H. M. Jang, Resolving the physical origin of octahedral tilting in halide perovskites, *Chem. Mater.* **28**, 4259–4266 (2016) [doi].

[347] J. H. Lee, J.-H. Lee, E.-H. Kong, H. M. Jang, The nature of hydrogen-bonding interaction in the prototypic hybrid halide perovskite, tetragonal $CH_3NH_3PbI_3$, *Sci. Rep.* **6**, 21687 (2016) [doi].

[348] T. Chen, B. J. Foley, C. Park, C. M. Brown, L. W. Harriger, J. Lee, J. Ruff, M. Yoon, J. J. Choi, S.-H. Lee, Entropy-driven structural transition and kinetic trapping in formamidinium lead iodide perovskite, *Sci. Adv.* **2**, e1601650 (2016) [doi].

[349] S. Sun, Z. Deng, Y. Wu, F. Wei, F. Halis Isikgor, F. Brivio, M. W. Gaultois, J. Ouyang, P. D. Bristowe, A. K. Cheetham, G. Kieslich, Variable temperature and high-pressure crystal chemistry of perovskite formamidinium lead iodide: A single crystal X-ray diffraction and computational study, *Chem. Commun.* **53**, 7537–7540 (2017) [doi].

[350] P. Whitfield, N. Herron, W. Guise, K. Page, Y. Cheng, I. Milas, M. Crawford, Structures, phase transitions and tricritical behavior of the hybrid perovskite methyl ammonium lead iodide, *Sci. Rep.* **6**, 35685 (2016) [doi].

[351] A. Marronnier, H. Lee, B. Geffroy, J. Even, Y. Bonnassieux, G. Roma, Structural instabilities related to highly anharmonic phonons in halide perovskites, *J. Phys. Chem. Lett.* **8**, 2659–2665 (2017) [doi].

[352] E. M. Hutter, R. J. Sutton, S. Chandrashekar, M. Abdi-Jalebi, S. D. Stranks, H. J. Snaith, T. J. Savenije, Vapour-deposited cesium lead iodide perovskites: Microsecond charge carrier lifetimes and enhanced photovoltaic performance, *ACS Energy Lett.* **2**, 1901–1908 (2017) [doi].

[353] F. J. Owens, C. P. Poole, Jr., H. A. Farach (Editors), *Magnetic Resonance of Phase Transitions*, Academic Press, Inc.: New York (1979).

[354] Q. Xu, T. Eguchi, H. Nakayama, Molecular motions in solid $CD_3NH_3PbBr_3$ as studied by ^{1}H NMR, *Bull. Chem. Soc. Jpn.* **65**, 2264–2266 (1992) [doi].

[355] S. Senthil Kumaran, K. Ramesh, J. Ramakrishna, Proton NMR T_1 studies in methylammonium trichloro stannate (II) ($CH_3NH_3SnCl_3$), *Phase Transit.* **75**, 597–605 (2002) [doi].

[356] G. Kieslich, A. C. Forse, S. Sun, K. T. Butler, S. Kumagai, Y. Wu, M. R. Warren, A. Walsh, C. P. Grey, A. K. Cheetham, Role of amine–cavity interactions in determining the structure and mechanical properties of the ferroelectric hybrid perovskite $[NH_3NH_2]Zn(HCOO)_3$, *Chem. Mater.* **28**, 312–317 (2016) [doi].

[357] N. Abhyankar, J. J. Kweon, M. Orio, S. Bertaina, M. Lee, E. S. Choi, R. Fu, N. S. Dalal, Understanding ferroelectricity in the Pb-free perovskite-like metal–organic framework $[(CH_3)_2NH_2]Zn(HCOO)_3$: Dielectric, 2D NMR, and theoretical studies, *J. Phys. Chem. C* **121**, 6314–6322 (2017) [doi].

[358] A. Bielecki, D. P. Burum, Temperature dependence of ^{207}Pb MAS spectra of solid lead nitrate. An accurate, sensitive thermometer for variable-temperature MAS, *J. Magn. Reson., Ser A* **116**, 215 – 220 (1995) [doi].

[359] T. A. Siaw, S. A. Walker, B. D. Armstrong, S.-I. Han, Inductively coupled NMR probe for versatile dynamic nuclear polarization operation at 7 T: Observation of $61\pm2\%$ ^{1}H polarization at 4 K, *J. Magn. Reson.* **221**, 5–10 (2012) [doi].

[360] T. A. Siaw, A. Leavesley, A. Lund, I. Kaminker, S. Han, A versatile and modular quasi optics-based 200 GHz dual dynamic nuclear polarization and electron paramagnetic resonance instrument, *J. Magn. Reson.* **264**, 131–153 (2016) [doi].

[361] M. Newville, T. Stensitzki, D. B. Allen, A. Ingargiola, LMFIT: Non-linear least-square minimization and curve-fitting for python (2014).

[362] K. Page, C. E. White, E. G. Estell, R. B. Neder, A. Llobet, T. Proffen, Treatment of hydrogen background in bulk and nanocrystalline neutron total scattering experiments, *J. Appl. Crystallogr.* **44**, 532–539 (2011) [doi].

[363] N. Bloembergen, E. M. Purcell, R. V. Pound, Relaxation effects in nuclear magnetic resonance absorption, *Phys. Rev.* **73**, 679–712 (1948) [doi].

[364] D. Kubicki, D. Prochowicz, A. Hofstetter, P. Péchy, S. M. Zakeeruddin, M. Grätzel, L. Emsley, Cation dynamics in mixed-cation $(MA)_x(FA)_{1-x}PbI_3$ hybrid perovskites from solid-state NMR, *J. Am. Chem. Soc.* **139**, 10055–10061 (2017) [doi].

[365] C. N. R. Rao, Effect of deuteration on hydrogen bonds, *J. Chem. Soc., Faraday Trans. 1* **71**, 980–983 (1975) [**doi**].

[366] K. Yamada, K. Mikawa, T. Okuda, K. S. Knight, Static and dynamic structures of $CD_3ND_3GeCl_3$ studied by TOF high resolution neutron powder diffraction and solid state NMR, *Dalton Trans.* 2112–2118 (2002) [**doi**].

[367] T. Steiner, Hydrogen-bond distances to halide ions in organic and organometallic crystal structures: Up-to-date database study, *Acta Crystallogr. Sect. B* **54**, 456–463 (1998) [**doi**].

[368] M. R. Linaburg, E. T. McClure, J. D. Majher, P. M. Woodward, $Cs_{1-x}Rb_xPbCl_3$ and $Cs_{1-x}Rb_xPbBr_3$ solid solutions: Understanding octahedral tilting in lead halide perovskites, *Chem. Mater.* **29**, 3507–3514 (2017) [**doi**].

[369] M. Sherwin, Applied physics: Terahertz power, *Nature* **420**, 131–133 (2002) [**doi**].

[370] A. M. Lindenberg, S. L. Johnson, D. A. Reis, Visualization of atomic-scale motions in materials via femtosecond X-ray scattering techniques, *Annu. Rev. Mater. Res.* **47**, 425–449 (2017) [**doi**].

[371] H. Mizoguchi, H. W. Eng, P. M. Woodward, Probing the electronic structures of ternary perovskite and pyrochlore oxides containing Sn^{4+} or Sb^{5+}, *Inorg. Chem.* **43**, 1667–1680 (2004) [**doi**].

[372] F. Wei, Z. Deng, S. Sun, F. Xie, G. Kieslich, D. M. Evans, M. A. Carpenter, P. D. Bristowe, A. K. Cheetham, The synthesis, structure and electronic properties of a lead-free hybrid inorganic-organic double perovskite $(MA)_2KBiCl_6$ (MA = methylammonium), *Mater. Horiz.* **6**, 328–332 (2016) [**doi**].